Structure- and fluid-dynamics in piezo inkjet printheads

Samenstelling promotiecommissie:

Prof. dr. ir. L. van Wijngaarden, voorzitter	Universiteit Twente
Prof. dr. rer. nat. D. Lohse, promotor	Universiteit Twente
Prof. dr. rer. nat. F. G. Mugele	Universiteit Twente
Prof. dr. ir. H. Tijdeman	Universiteit Twente
Prof. dr. ir. J. Huétink	Universiteit Twente
Prof. dr. ir. M. E. H. van Dongen	Technische Universiteit Eindhoven
Prof. dr. F. Toschi	Technische Universiteit Eindhoven
Prof. dr. ir. D. J. Rixen	Technische Universiteit Delft
Ir. H. Reinten, referent	Océ Technologies B.V.

The research described in this thesis was carried out at the Research and Development department of Océ Technologies B.V.

Nederlandse titel:
Dynamica van constructies en vloeistoffen in piezo inkjet printkoppen

Publisher:
Herman Wijshoff, Océ Technologies B.V., Venlo,
P.O. Box 101, 5900 MA Venlo, The Netherlands
www.oce.com
Cover design: Herman Wijshoff
Background cover illustration: A MEMS-based printhead structure, the future.
Front cover illustration: The models describing the complete printhead operation, the upper two represent the solid mechanics and the lower two the fluid mechanics part of the thesis.
Back cover illustration: Cover of the oldest publication in this field, anno 1749.
Print: Gilde Print B.V., Enschede

ISBN 978-90-365-2582-4

Structure- and fluid-dynamics in piezo inkjet printheads

PROEFSCHRIFT

ter verkrijging van
de graad van doctor aan de Universiteit Twente,
op gezag van de rector magnificus,
prof. dr. W. H. M. Zijm,
volgens besluit van het College voor Promoties
in het openbaar te verdedigen
op vrijdag 25 januari 2008 om 16.45 uur

door

Herman Wijshoff
geboren op 3 september 1961

te Grevenbicht

Dit proefschrift is goedgekeurd door de promotor:
prof. dr. rer. nat. Detlef Lohse

Contents

1 Introduction **1**
- 1.1 Historical overview on inkjet technology . . . 1
- 1.2 Printing principles . . . 9
- 1.3 Printhead operation . . . 11
  - 1.3.1 Working principle . . . 11
  - 1.3.2 Printhead testing . . . 14
- 1.4 Guide through the thesis . . . 17

2 Structure dynamics **19**
- 2.1 Actuating . . . 19
  - 2.1.1 Piezoelectricity . . . 19
  - 2.1.2 Bump mode actuation . . . 22
  - 2.1.3 Actuation efficiency . . . 26
- 2.2 Local cross-talk . . . 27
  - 2.2.1 Electrical cross-talk . . . 27
  - 2.2.2 Direct cross-talk . . . 28
  - 2.2.3 Pressure-induced cross-talk . . . 31
- 2.3 Printhead dynamics . . . 33
  - 2.3.1 Modeling setup . . . 34
  - 2.3.2 Structural resonances . . . 35
- 2.4 Concluding remarks . . . 39

3 Channel acoustics **41**
- 3.1 Narrow channel theory . . . 41
  - 3.1.1 Governing equations . . . 41
  - 3.1.2 Frequency characteristics . . . 44
  - 3.1.3 Traveling wave principle . . . 48
- 3.2 Nozzle boundary . . . 51
  - 3.2.1 Nozzle pressure . . . 51
  - 3.2.2 Drop size and speed . . . 54
- 3.3 Cross-talk . . . 56
  - 3.3.1 Local cross-talk . . . 56
  - 3.3.2 Printhead resonances . . . 59

3.3.3 Acoustic cross-talk . . . 62
3.4 Residual vibrations . . . 65
3.4.1 Refill . . . 65
3.4.2 Drop on demand frequency oscillations . . . 68
3.4.3 Interaction with local cross-talk . . . 70
3.5 Concluding remarks . . . 72

4 Drop dynamics 73
4.1 Drop formation . . . 73
4.1.1 Drop shape and properties . . . 73
4.1.2 Impact on acoustics . . . 77
4.2 Break-off mechanism . . . 81
4.2.1 Impact of ink properties . . . 81
4.2.2 Secondary tail . . . 83
4.2.3 Tail-end speed . . . 85
4.3 Satellite drop formation . . . 87
4.3.1 Mist of droplets . . . 87
4.3.2 Rayleigh breakup . . . 89
4.3.3 Fast satellites . . . 91
4.3.4 Slow satellites . . . 92
4.4 Drop size modulation . . . 94
4.4.1 Pulse width and fill-before-fire-level . . . 94
4.4.2 Acoustic resonances . . . 96
4.4.3 Break pulses . . . 98
4.4.4 Meniscus and drop formation oscillations . . . 99
4.5 Concluding remarks . . . 100

5 Wetting dynamics 103
5.1 Wetting of the nozzle plate . . . 103
5.1.1 Origin of wetting . . . 103
5.1.2 Wetting regimes and visualization . . . 106
5.2 A wetted nozzle . . . 107
5.2.1 Jetting nozzle . . . 107
5.2.2 Non-jetting nozzle . . . 111
5.3 A wetted nozzle plate . . . 114
5.3.1 Long-range phenomena . . . 114
5.3.2 Driving mechanisms . . . 115
5.3.3 Complete wetting . . . 118
5.3.4 Marangoni flow . . . 120
5.4 Impact on drop formation . . . 121
5.4.1 Drop properties . . . 121
5.4.2 Channel acoustics . . . 122
5.5 Concluding remarks . . . 123

6 Bubble dynamics **125**
6.1 Stability . . . 125
6.1.1 Dirt and air entrapment . . . 125
6.1.2 Acoustic detection of air bubbles . . . 126
6.2 Air entrainment . . . 128
6.2.1 Wetting layer . . . 128
6.2.2 Small dirt particles . . . 129
6.3 The oscillating bubble . . . 134
6.3.1 Size dynamics . . . 134
6.3.2 Impact on channel acoustics . . . 134
6.3.3 Impact on drop formation . . . 136
6.4 The moving bubble . . . 139
6.4.1 Balance of forces . . . 139
6.4.2 Net displacements . . . 140
6.5 The growing bubble . . . 141
6.5.1 Rectified diffusion and dissolution . . . 141
6.5.2 Influence of the actuation . . . 143
6.5.3 Impact on channel acoustics . . . 145
6.5.4 Impact on drop formation . . . 146
6.6 Concluding remarks . . . 147

7 Conclusions **149**

References **153**

Summary **165**

Samenvatting **169**

Acknowledgements **173**

List of publications **175**

About the author **177**

Chapter 1

Introduction

In this chapter an overview is presented of the main inkjet developments to clarify the importance of inkjet technology as key-technology for today's industry. Besides printing onto paper, many other application have emerged the last years. The requirements to meet the needs in many areas justify the intensive research program. The basic printing principles are outlined and the main printhead operation issues are presented. Finally a guide through the chapters of this thesis is given.

1.1 Historical overview on inkjet technology

Inkjet printing is an important technology in color document production [133]. The rapid development of inkjet technology started off around the late fifties. Since then, many inkjet devices have seen the light of day. In this overview, the attention is mainly restricted to the development towards the most important inkjet concepts of today, namely continuous, piezoelectric, and thermal inkjet.

The first inkjet-like recording device, using electrostatic forces, was invented by William Thomson, later Lord Kelvin, in 1858. This was the Siphon recorder as shown in figure 1.1. The apparatus was used for automatic recordings of telegraph messages and was patented in 1867 (UK Patent 2147/1867). A siphon produces a continuous stream of ink onto a moving web of paper and a driving signal moves the siphon horizontally back and forth. The first experiments on manipulating a stream of droplets even goes back to 1749. That year, Abbé Nollet published his investigations on the effects of static electricity on a drop stream [122, 123].

In 1822 the equations to describe the motion of fluids were formulated by the French engineer and physicist Claude Navier [121], seventy years after Euler had published his equation for ideal liquids without viscosity [53]. Navier also formulated the general theory of elasticity in a mathematically usable form in 1821. George Stokes introduced his equations for the motion of liquids in 1845 [145]. Hence the name Navier-Stokes equations for the application of classical mechanics to a continuum under the assumption of a stress that is linear with the strain rate.

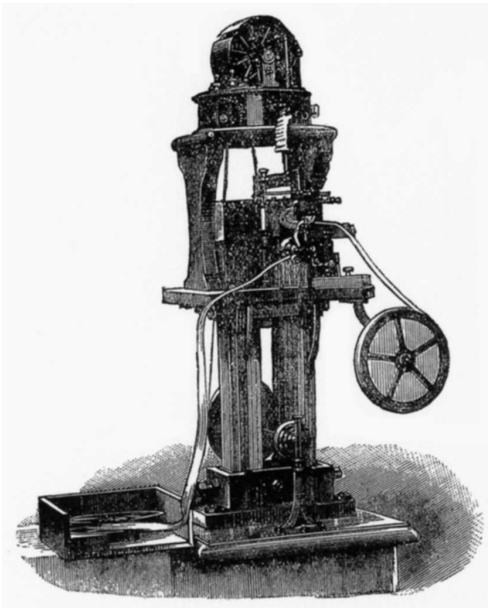

(a)

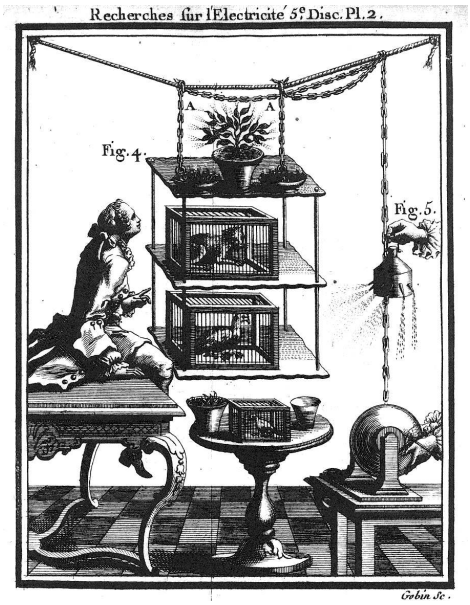

(b)

Figure 1.1: (a) The Siphon recorder is the first practical continuous inkjet device. It was used for automatic recordings of telegraph messages and invented by William Thomson in 1858 (UK Patent 2147/1867). (b) An illustration from Abbé Nollet showing the first experiments on the effect of static electricity on a drop stream, published in 1749 [122].

The foundation of modern inkjet technology is attributed to the Belgian physicist Joseph Plateau and English physicist Lord Rayleigh. Plateau was the very first to publish on this field with his article *On the recent theories of the constitution of jets of liquid issuing from circular orifices* in 1856 [132]. He derived the relationship of jet diameter to drop size in 1865. Lord Rayleigh published a series of founding papers starting with *Instability of jets* in 1878 [136]. The experimental foundation of this work started in 1833, when Savart published his observations on drop break-up [138]. He was the first one who recognized that the break-up of liquid jets is governed by laws, independent of the circumstance under which the jet is produced. He used acoustic energy to form uniform drops. What was missing in his work was the realization that surface tension is the driving force behind drop break-up. The groundwork for the description of the role of surface tension forces was laid by Young in 1804 [172] and Laplace in 1805 [96].

Still, it took many decades before applications of the physical principles of drop formation were used in commercial working devices. In 1951, Elmqvist of the Siemens-Elema company patented the first practical continuous inkjet device (US Patent 2,566,433), which was based on the Rayleigh breakup [97]. This resulted

in the Mingograph, which was released in 1952. Instead of being an inkjet printer, it was merely a medical voltage recorder (e.g. for ECG and EEG). The deflecting of the drops was driven through analog voltages from a sensor, quite similar to current seismic apparatus.

In the early 1960s Sweet of Stanford University demonstrated that, by applying a pressure wave pattern to an orifice, the ink stream could be broken into droplets of uniform size and spacing [147]. When the drop break-up mechanism was controlled, the drops could be charged selectively and reliably as they emerged out of the continuous ink stream. The charged drops were deflected, when passing through an electric field, to form an image on the substrate. The uncharged drops were captured by the gutter and re-circulated in the system. This version of the printing process is known as the Continuous Inkjet (CIJ) printing process (US Patent 3,596,275), with the Inkjet Oscillograph as first device. This device was elaborated for use by the Stanford Research Institute (SRI) for inkjet bar coding work for Recognition Equipment Incorporated (REI). The A.B. Dick Company elaborated Sweets invention to be used for character printing. With their Videojet 9600 in 1968, it was the first commercial CIJ printing product.

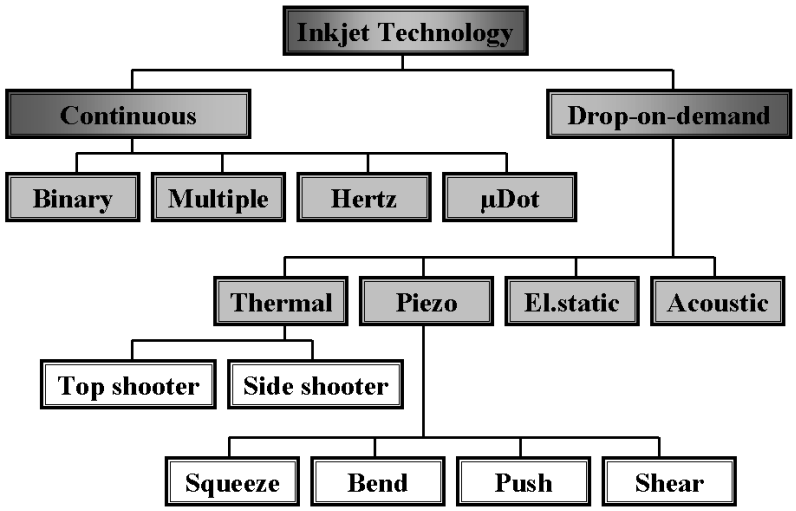

Figure 1.2: Classification of inkjet printing technologies, adapted from [97].

The binary deflection was further developed, not only for bar code printing, but also for advertising purposes, with the so-called DIJIT printer, introduced in 1973 by the Mead company. Developments were boosted by the huge research efforts of IBM in the 1970s, which resulted in 1976 in the IBM 6640, a word processing hardcopy-output peripheral application [27]. Two companies were involved in the multiple drop deflection, the Sharp and the Applicon company. The former released their Jetpoint in 1973, the latter their color image printer in 1977. In the same period Hertz of the Lund University of Technology in Sweden developed

several continuous inkjet techniques, which enabled gray-scale printing by varying the number of drops per pixel. His methods were adopted by Iris Graphics and Stork to produce high-quality color images for the prepress color hardcopy market [69].

Instead of continuously firing drops it is also possible to create drops only when an actuation pulse is provided: drop-on-demand. Major advantages of drop-on-demand (DOD) printers over CIJ printers include the fact that there is no need for break-off synchronization, charging electrodes, deflection electrodes, guttering, and re-circulation systems, high pressure ink-supplies and complex electronic circuitry. The first pioneering work in that direction was performed in the late 1940s by Hansell of the Radio Corporation of America (RCA), who invented the first drop-on-demand device as shown in figure 1.3. By means of a piezoelectric disc, pressure waves could be generated that caused a spray of ink drops. However, this invention, intended for use as a writing mechanism in a pioneering RCA facsimile concept, was never developed into a commercial product [133].

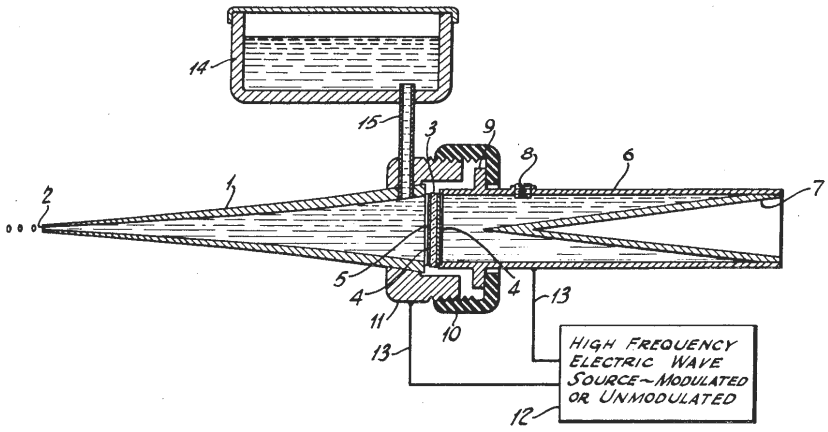

Figure 1.3: Drawing of the first drop-on-demand piezo inkjet device, which was patented in 1950 but not further developed into a commercial product (US Patent 2,512,743). A piezoelectric disc (5) generates pressure waves in the solid cone (1), which cause a spray of ink drop from the nozzle (2).

The first DOD technique, that really emerged, was the electrostatic pull inkjet in the 1960s. The basic working principle comprises the following. Conductive ink is held in a nozzle by negative pressure. By application of a high voltage pulse to an electrode located outside the nozzle, a charged droplet of ink is pulled out. By application of the appropriate deflection field, the droplet can be located on the substrate. Companies developing electrostatic pull inkjet devices were the Casio, Teletype, and Paillard company. The Inktronic Teletype machine in the late 1960s was marketed by the Teletype company. With the model 500 Typuter, the Casio company released a printer of this type in 1971. In the 1970s, the

DOD electrostatic pull principle was abandoned due to poor printing quality and reliability, although research activities continues until today [153, 154].

Generally, the basis of piezoelectric inkjet (PIJ) printers is attributed to three patents in the 1970s. Common denominator of these three patents is the use of a piezoelectrical unit to convert an electrical driving voltage into a mechanical deformation of a ink chamber, which generates the pressure required for the drop formation from a nozzle. The first one is that of Zoltan of the Clevite company in 1972 (US Patent 3,683,212), proposing a squeeze mode of operation [28]. In this mode, a hollow tube of piezoelectric material is used. When a voltage is applied on the piezoelectric material, the ink chamber is squeezed and a drop is forced out of a nozzle.

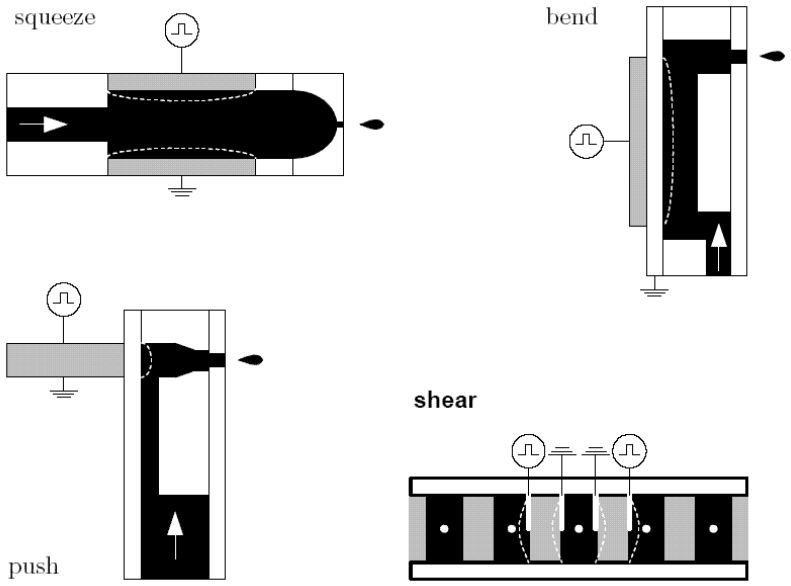

Figure 1.4: Classification of piezo inkjet (PIJ) printhead technologies by the deformation mode used to generate the drops.

The second patent of Stemme of the Chalmers University in 1973 (US Patent 3,747,120) utilizes the bend mode of piezoelectric operation. In this mode, the bending of a wall of the ink chamber is used to eject a drop. The third patent of Kyser and Sears of the Silonics company in 1976 (US Patent 3,946,398) also used the bend mode operation. Both bend-mode patents were filed in the same year. The minor difference between the two is that Stemme used a flat disc of piezoelectric material to deform a rear wall of an ink chamber and that Kyser and Sears used a rectangular plate to deform the roof of an ink chamber. The first PIJ printer to reach the market was in 1977 with the Siemens PT-80, which used the squeeze mode. Silonics was the second company to introduce a piezoelectric

DOD printer, namely the Quietype in 1978, which used the bend mode The bend mode is also referred to as bimorph or unimorph mode. Obviously, the main discriminator between the PIJ patents is the used dominating deformation mode of the piezoelectric material, together with the geometry of the ink channels.

The patent of Stuart Howkins (US Patent 4,459,601) of the Exxon company in 1984, describing the push mode version, and the patent of Fischbeck (US Patent 4,584,590), who proposed the shear mode, completed the now commonly adapted categorization of printhead configurations. With the push mode, also referred to as bump mode, a piezo electric element pushes against an ink chamber wall to deform the ink chamber. In the shear mode the strong shear deformation component in piezo electric materials is used to deform a ink chamber wall. So in general, four types of PIJ printheads are distinguished, the squeeze, push, bend, and shear mode, see figure 1.4.

With sudden steam printing, figure 1.5, a researcher from the Sperry Rand Company basically invented another DOD technique, thermal inkjet printing, in the 1960s. By boiling aqueous ink at certain time instances, a drop of ink could be generated. The strength of this design clearly was not immediately acknowledged, since the company did not elaborate this idea into a commercial product. The idea was abandoned until the late 1970s when Canon and Hewlett Packard (HP) picked it up.

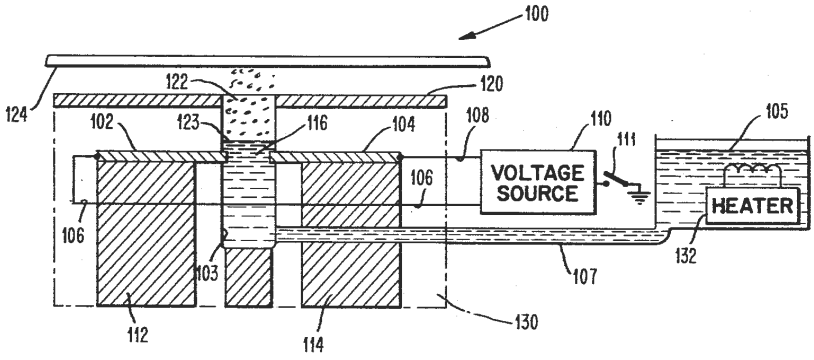

Figure 1.5: Sudden steam printing, the first drop-on-demand thermal inkjet device, which was patented in 1965, but not further developed into a commercial product (US Patent 3,179,042). An electric current from the electrodes (102 and 104) passes through a portion of the ink (116). The ink is preheated (132) nearly to its boiling temperature and the extra heat from electric current generates the steam that ejects the drops form the nozzle.

In 1979 Endo and Hara of the Canon company re-invented the drop-on-demand printheads actuated by a water vapor bubble, called bubblejet, with the first printer launched in 1981. In the same period also HP developed their thermal inkjet technology leading to the first successfull low-cost inkjet printer in 1984.

The invention of thermal inkjet (TIJ) fundamentally changed inkjet research. By the replacement of the piezoelectric by a thermal transducer, the main bottleneck concerning miniaturization was resolved. The thermal transducer became a simple, small, and cheap resistor, figure 1.6.

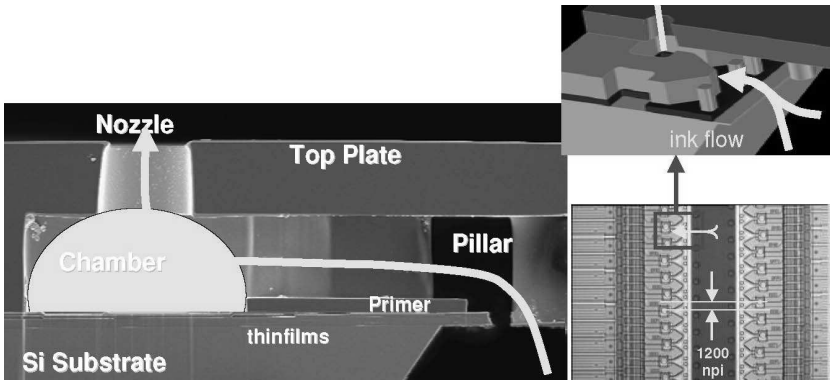

Figure 1.6: Side view of HP's SPT printhead, showing the state of the art technology in thermal inkjet printing [8]. The outlet diameter of the nozzle is 18 μm, the ink chamber height is 18 μm. The nozzle pitch in a single row is 42.3 μm and both nozzle rows are shifted a half nozzle pitch with respect to each other. This results in a nozzle resolution of 1200 npi.

TIJ can be manufactured using mass-production based on IC manufacturing technologies. This made the cost per nozzle much lower than the cost per nozzle of a piezoelectric printhead. Both the fact that inkjet printers now could be miniaturized and its low cost of manufacturing made TIJ the superior inkjet technology at that time. HP solved the reliability problem of the thermal drop on demand printheads by the concept of disposable heads and increased the performance of their thermal printheads continuously as shown in figure 1.7. HP claims that TIJ jets everything that nucleates like toluene, silver suspensions, and even functional proteins. Currently thermal inkjet, with top-shooters of HP, Canon, Lexmark and Olivetti and side-shooters of Canon (the first series) and Xerox, dominates the low-end home/office color printer market. Océ also applies thermal drop-on-demand inkjet in its wide format color printing systems with printheads of various manufacturers.

After the introduction and immense success of TIJ, PIJ research efforts were largely diminished. However, critical in TIJ is the spreading and intercolor bleeding of water based inks. This requires special coatings on the media surface. At high productivity cockling and drying of the media is another problem. Therefore, solid inks (hot-melt or phase-change ink), which require piezo actuation, remained important.

Only a few companies continued their research into PIJ. New initiatives with a bump-mode design were taken in 1984 by Howtek and Exxon, later acquired by

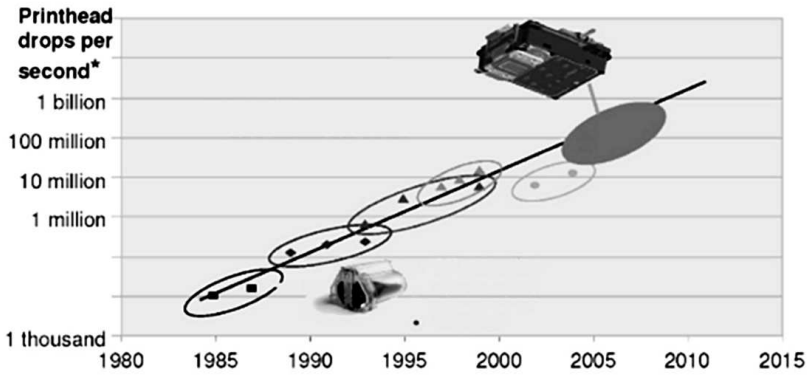

Figure 1.7: HP Moores law: inkjet printhead performance as printhead drops per second (the number of nozzles times the maximum drop-on-demand frequency) doubles every 18 months for the past 20 years. It started with 12 nozzles in a single color glass chip in 1984. Via different printer series (the different markers), this evolved into the 3900 nozzles in a six color single silicon chip in 2006, the Scalable Printhead Technology (SPT).

Dataproducts. Now the bump mode actuation is used by Hitachi (which acquired Dataproducts), Trident, Brother and Epson [155]. The bend mode is used by Tektronix (acquired by Xerox), Brother/Kyocera and Epson [119, 175]. The shear-mode design came into the field in 1984 with Spectra, a with Xerox licenses formed company, and later with Brother. Spectra is acquired by Markem, later by Dimatix and finally by FujiFilm [114, 118]. A special version of the shear mode is the shared wall design of Xaar. This company started in 1990 for commercializing the work of the Cambridge researchers [15, 95, 109, 111, 173, 174]. Other companies which use this concept are Brother/Kodak, ToshibaTEC and MicroFab [3].

At present, both TIJ and PIJ printing have evolved into the two most important technologies when it comes to printing. The initial advantages of TIJ over PIJ have been leveled over the years by further development of the PIJ technology. A fundamental strength of the PIJ technology is its ability to deposit a wide variety of materials on various substrates in well-defined patterns. Recently many other applications than printing onto paper emerged [13, 106, 116, 140, 142, 167, 168].

In the display market, inkjet technology is used to manufacture Flat Panel Displays (FDP), Liquid Crystal Displays (LCD), color filters (a part of LCDs), Polymer Light Emitting Diodes (PLED), and flexible displays. The accompanying performance criteria are among the major driving forces behind much research and development efforts [11, 67]. Within the chemical market, the inkjet technology is mainly used as tool for research purposes. The unique capacity of the technology for dispensing small doses of liquids makes it very useful for this market. Applications include material and substrate development as well as coating purposes [92, 120, 127].

In the electronic market, inkjet printheads are used to create functional electrical traces using conductive fluids on both rigid and flexible substrates. One of the first applications of inkjet technology within this field was that for the production of Printed Circuit Boards (PCB). Other applications include the fabrication of electric components and circuits such as Radio Frequency Identification (RFID) tags, wearable electronics, solar cells, fuel cells, and batteries. Challenges for the inkjet technology within this field include the spreading of the ink and the required guarantees of continuity of the jetted lines [68, 91, 99, 148].

Three-dimensional mechanical printing claims the inkjet technology as tool for rapid prototyping, small volume production, and the production of small sensors [158, 160, 170]. Jetting of UV-curable optical polymers is a key technology for the cost-effective production of micro-lenses. These tiny lenses are used in devices from fiber optic collimators to medical systems. The ability of inkjet technology to precisely jet spheres in variable, but consistent, drop sizes provides opportunities for the cost reduction of existing optical components and innovative new designs [16, 36, 41].

The life science market is rapidly expanding with new requirements for precise dispensing of DNA and protein substances [6]. The high costs of these fluids make inkjet technology with its precision placement and tight flow control an excellent dispensing tool. Applications include the use for DNA research, various medical purposes such as dosing of drugs, and food science. A quite futuristic application is the use of inkjet printing for the fabrication of living tissue [31, 32, 40, 79, 135].

1.2 Printing principles

The graphic printing applications require certain performance criteria to be met. For an inkjet printhead, an important set of requirements is related to the resulting drop properties, namely:

- Drop-speed: the resulting droplets are required to have a certain speed, typically several m/s. A high drop speed results in a short time of flight. The sensitivity for disturbing influences like variations in the printhead-substrate distance will be less, thus the dot position errors will be smaller.

- Drop-volume: depending on the application under consideration, the performance requirement concerning volume typically varies now from 2 to 32 picoliter. For some applications, it is required that the drop-size can be varied during operation. For example, for large areas that need to be covered large drops are desired, whereas for high resolution printing small drops are desirable. This is referred to as drop-size modulation.

- Drop speed and volume consistency: the variations in drop volume and speed must stay within a certain percentage band, typically around 2 percent. This is to avoid irregularities in the printed object.

- Drop-shape: the shape of the dots on a substrate is negatively influenced by the formation of tails or satellite drops. These are highly undesirable for the quality of the print.

- Jet straightness: the droplets have to be deposed in a straight line towards the substrate, typically within 10 mrad accuracy.

Productivity and stability are important requirements, which are closely related to the jetting process. The productivity of an inkjet printhead is mainly determined by the jetting frequency, defined as the number of drops that a channel jets within a certain time f_{dod}, and by the number of nozzles N_{noz}, defined by the integration density or nozzles per inch and the printhead width. A high integration density has a lot of consequences for the functionality and the producibility. For the productivity of an inkjet printer, the firing power P_{jet} of the printheads is the key number. The productivity in m^2/s is given by:

$$P_{jet} = \frac{N_{noz} f_{dod}}{dpi^2} \times (24.4 \cdot 10^{-3})^2 \tag{1.1}$$

with dpi the number of dots per inch [2]. This results in a print time t_{print} for an area A_{print} of a printer of:

$$t_{print} = \frac{A_{print}}{\eta P_{jet}} \tag{1.2}$$

with η the efficiency of the printer, which plays a very important role in a scanning system. Most inkjet printers use a carriage with several printheads which moves over the full width of the paper. Between the strokes of the carriage, or print swaths, the paper is transported over a certain distance to cover the full area. At higher frequencies the carriage turn-time and the paper step give more and more limitations. These limitations result in an optimum DOD-frequency for the productivity of scanning printer systems [26]. For productivity the maximum applicable DOD-frequency for 600 dpi prints in most scanning printer concepts is $30 - 40\ kHz$.

High productivity single pass printing requires a page-wide array with thousands of nozzles as explored by Spectra [152, 179] and Brother-Kyocera [75], and used by Xerox/Tektronix in their Phaser printer series. Another way to increase the number of nozzles is to use multiple nozzles per channel as explored by Trident [180].

The number of dots per inch is important for print cost and print quality. Print cost is directly related to the thickness of the ink layer or amount of ink/m^2. As a first order approximation, the required drop volume for a 600 dpi dot is about 32 pl and for a 1200 dpi dot about 4 pl, since volume scales as the third power of the spatial resolution. The total volume for a 600 dpi dot with four 1200 dpi drops becomes 16 pl instead of 32 pl with a single 600 dpi drop. Print quality is better with smaller dots at a high resolution. Finer detail can be represented and also the graininess of the print is much less with small dots. For water based inks

the less amount of ink with smaller drops results in shorter drying time, another drive to move towards smaller drops. So there is a trade-off between productivity and print quality/cost. Drop size modulation is a way to meet both requirements. The small drops are used for achieving a high print quality and the large drops for productivity.

Stability of the jetting process is one of the most important performance requirements for inkjet printheads. Typically, it is required that at most one failure occurs per certain number of jetted drops. For printing onto paper this is typical one billion, but in some industrial applications no failure at all is allowed.

Additional, more general, requirements include the lifespan of the printhead (typically more than ten billion actuations per channel, a fundamental strength of PIJ over TIJ), the materials compatibility (a wide variety of inks must be deposable (again a strength of PIJ over TIJ), the maintainability, and the cost of production and manufacturability of the printhead (a weakness of PIJ).

1.3 Printhead operation

1.3.1 Working principle

The final goal of the printhead operation is firing billions of drops. Before a drop is fired, a lot of processes must take place. In the case of hotmelt inks it starts with the melting of the ink in the melting unit (a), figure 1.8. This unit must have enough capacity. A good heat transfer and draining of the melted ink at a given maximum temperature like 135 $^{\circ}C$ is necessary, taking into account some overshoot and time delay. Another task is filtering (b) the ink. The next unit is the reservoir (c), which must have enough volume, while keeping the total printhead dimensions within certain limits. Important aspects concerning the reservoir are:

- filtering with non-woven filters with high dirt holding capacity
- removal of air bubbles
- temperature control
- closing static pressure, for example supplied with hose (d)
- ink-level sensing.

The lower part of the printhead is the central part (e) where drop formation takes place. This part is the subject of this thesis and is shown in more detail in figure 1.9. The main components in the central part are:

- a last filter (k), to remove the dirt particles from the ink
- the channel block (h), in which the ink channels (l) are made
- the nozzle plate (g), where the drops are formed

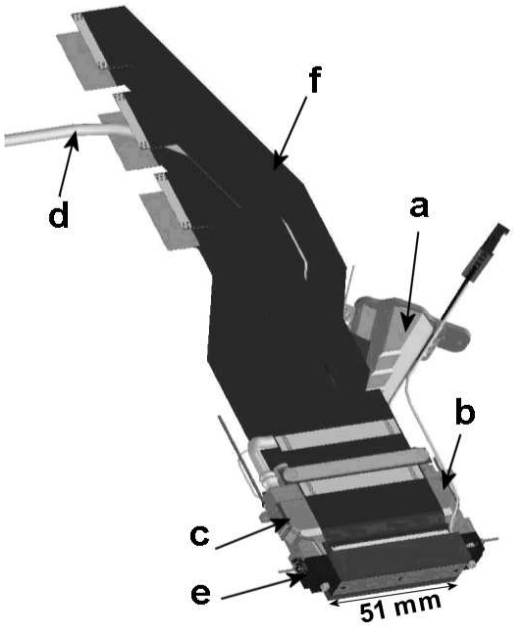

Figure 1.8: 3D CAD drawing of a printhead prototype showing (a) the melting unit, (b) the filter units, (c) the reservoir, (d) the static pressure hose, (e) the central part, and (f) the electronic driving supply.

- the actuator foil (i), which covers the ink channels in the channel block. The foil is also connected to:
- the actuator plate with piezo elements and substrate (j). Here the driving force for the drop formation process is generated. The required electric voltage is supplied by the electronic flex (f), figure 1.8.

The ink path from the reservoir and last filter to the nozzle can be divided into a supply channel, a pressure channel and a connection channel. The actuation takes place in the pressure channel, which is shown in figure 1.9 in a front view of a channel. When a voltage is applied on a piezo element, this element will change its shape. This deforms the ink channel, which generates the pressure waves to fire a drop. The reaction force is supplied by the substrate, which is connected to the channel block via passive piezo elements.

Typical dimensions are length $5-20\ mm$ for the total ink channel with a cross-section of $0.01-0.05\ mm^2$. The channel block material is graphite with shaped channels, or a metal like brass or silicon with etched channels. The actuator foil has a thickness of $5-50\ \mu m$ and we use poly-imide, metal, glass, or silicon as material. The actuator plate is a piezo-ceramic material with a height of typical $500\ \mu m$ with diced elements. In most cases we use a substrate to support the element structure. The substrate is several millimeter longer than the piezo elements, to

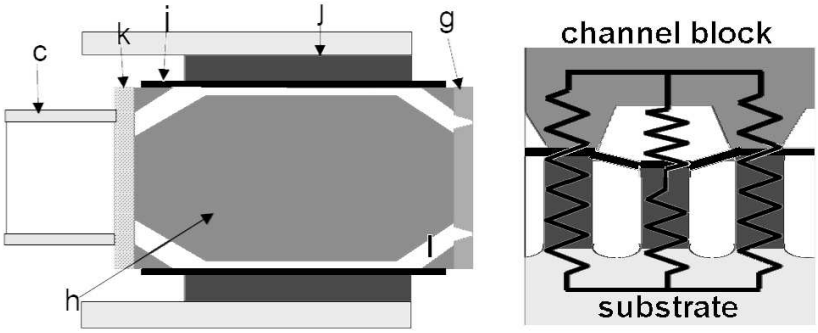

Figure 1.9: Side view of channel structure and front view with actuation principle as explained in section 2.1.2., with (c) the reservoir, (g) the nozzle plate, (h) the channel block, (i) the actuator foil, (j) the actuator with piezo elements and the substrate, (k) a last filter, and (l) the ink channel.

enable the connection of the electronic flex. The nozzle plate thickness ranges from $30 - 125\ \mu m$ and nozzle diameters from $18 - 50\ \mu m$. Different nozzle shapes are made in nozzle plates of nickel, tantalum, poly-imide or silicon.

A long ink channel with a nozzle at the right side and a large reservoir at the left side is the simplified geometry of the inkjet device like in [17], figure 1.10. A piezo actuator element drives each channel. To fire a droplet, an electric voltage is applied and the channel cross-section will be deformed by the inverse piezo-electric effect. This results in a negative pressure wave inside the channel. The pressure waves propagates in the channel direction and will be reflected when the characteristic acoustic impedance Z of the channel changes. The acoustic impedance of the channel depends on the size of the channel cross-section A and the speed of sound c as:

$$Z = \frac{\rho c}{A} \tag{1.3}$$

with ρ the density of the ink. The speed of sound is influenced by the compliance of the channel cross-section, see section 3.1.3. The reflection and transmission coefficients at the interface between domain 1 and domain 2 are:

$$R = \frac{Z_2 - Z_1}{Z_1 + Z_2} \qquad T = \frac{2Z_2}{Z_1 + Z_2} \tag{1.4}$$

When the compliance does not change, the following relationship holds:

$$R = \frac{A_1 - A_2}{A_1 + A_2} \qquad T = \frac{2A_1}{A_1 + A_2} \tag{1.5}$$

At the large reservoir ($A_2 \gg A_1$) the transmission coefficient is zero and the reflection coefficient equals -1. This means that the pressure wave will be completely reflected and the amplitude of the wave will change from a negative to a positive pressure wave.

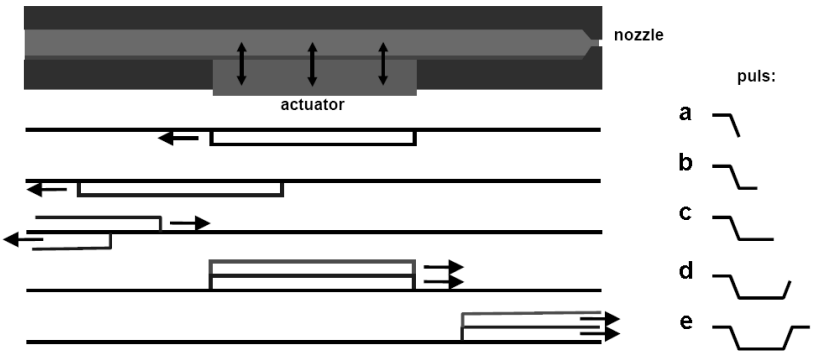

Figure 1.10: Schematic drawing of the actuation principle. An electric voltage on a piezo element enlarges the channel and a negative pressure is generated. After reflection at the reservoir this becomes a positive pressure pressure wave. The positive pressure wave is amplified by the second slope of the driving waveform to get a large positive pressure peak at the nozzle, which fires a drop.

The charging of the piezo element (a) enlarges the channel cross-section and the resulting negative pressure wave will be reflected at the reservoir at the left (b). The large reservoir acts as an open-end and the acoustic wave returns as a positive pressure wave (c). The de-charging of the piezo element reduces the channel cross-section to its original size. This will amplify the positive pressure wave when tuned to the travel time of this acoustic wave (d). The channel structure and driving pulse are designed to get a large incoming positive pressure peak at the nozzle (e), which drives the ink through the nozzle. Acceleration of the ink movement in the small cross-section of the nozzle (conservation of mass and incompressibility) results in drop formation.

1.3.2 Printhead testing

Droplets are measured by means of optical methods [1] like stroboscopic illumination at drop formation rate and high-speed camera recordings up to 160,000 images/sec with a Phantom V7 camera from Vision Research or up to 1 million images/sec with a Shimadzu HPV-1 camera. The basic setup for the optical measurements is outlined in figure 1.11. The setup can be divided into a part which controls the printhead and a part to visualize the droplets.

The required reference temperature is reached by a PID controller (Eurotherm 2408), which measures the temperature of the printhead with thermocouples and controls the input voltages for the heating elements. The printhead is mounted in vertical direction with the nozzles faced down, similar to its position in an inkjet printer. To avoid that the ink simply flows out of the nozzles under the influence of gravity, an air pressure unit (TS 9150G) makes sure that the pressure

in the ink reservoir remains 8 *mbar* below the ambient pressure. The setup is connected to a personal computer that is equipped with National Instruments IMAQ PCI 1409 and PCI GPIB cards for image capturing and processing and for communication, respectively. A Newport MM3000 motion controller is used for automatic positioning of the printheads in the measuring positions with Newport xy-tables.

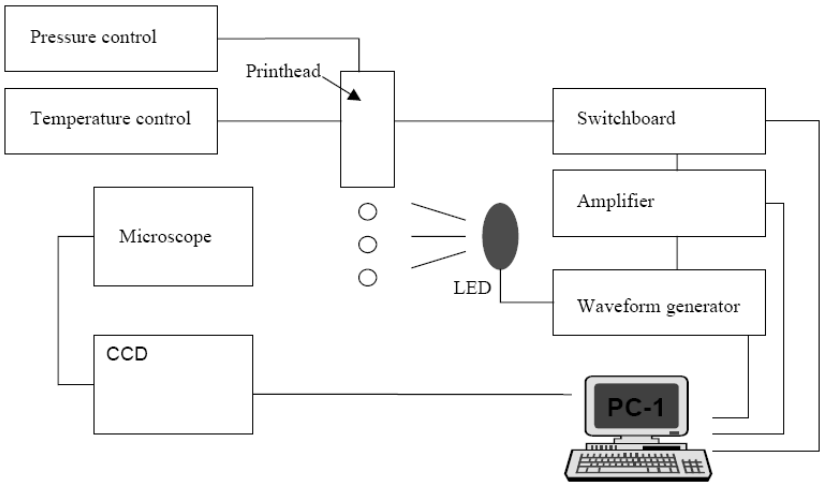

Figure 1.11: Outline of experimental setup with printhead control, driving electronics and optical recording equipment.

We use Labview software to control the measurements and the measuring results can be directly exported to for example Excel for further analysis. After defining the actuation signal, it is sent to an arbitrary waveform generator (Philips PM 5150/Wavetek 75A). The waveform generator sends the signal to an amplifier (Krohn-Hite 7602). From the amplifier, the signal is fed to a so-called switch-board. The switch-board is controlled by the personal computer and determines which channels are provided with the appropriate actuation signals.

We use a standard CCD-camera (for example Sony SSC-M370CE or Watek LCL902K) to capture the images from an Olympus SZH-10 microscope of the drop formation with a frame rate 25 images/sec. A led produces flashes of 100 ns and the strobe frequency is the same as the drop repetition rate or DOD-frequency. We will only see the reproducible part of the drop formation, because the images are integrated over many (depending on the DOD-frequency up to several hundred) droplets. Drop properties can be derived very easily from these images. The drop speed is calculated from the distance of adjacent drops and the known repetition time. The drop size is calculated from the number of pixels, or by weighting a certain number of captured drops. Drop direction is calculated from the centers of mass. To capture non-reproducible phenomena we use high-speed camera recordings. In a certain time frame (up to typical 1 s) all drops are recorded with

1-10 μs time intervals, using a trigger signal to read back the relevant time frame.

With laser-Doppler interferometry (Ono Sokki laser vibrometer LV1500) we record meniscus movements without drop formation. The measuring principle is based on mixing an undisturbed and a Doppler-shifted laser beam. The Doppler effect, the frequency shift Δf, of the reflected beam is given by:

$$\triangle f = \frac{2v}{c} f_0 = \frac{2v}{\lambda} \tag{1.6}$$

with f_0 the frequency of the undisturbed laser beam, λ the wavelength of the laser beam, c the speed of light, and v the normal speed of the surface which reflects the laser beam. The meniscus speed is derived from the interference pattern of the reflected beam with the reference beam and the frequency characteristics are recorded with a HP 3585A spectrum analyzer. With laser-Doppler it is also possible to measure actuator displacements with an accuracy of 20 nm [178]. Another setup for the latter is a speckle interferometer.

All these measurements give details on the ink flow outside the printhead and the deformations of the exterior of the printhead. The phenomena inside the channels are difficult to measure. Only when using special transparent printheads, e.g. channels in or covered by a glass plate, and flow tracing particles the flow inside can be measured [117]. The only suitable method for the opaque heads uses the actuator also as a sensor. As generally known, a piezo can be used as actuator or as sensor, see e.g. [159]. For that, one uses the piezos inverse (actuator) and direct (sensor) piezo-electric effect. The former comprises the following. If an electrical voltage V is applied to the piezo unit, a displacement y of the piezo unit results. The latter refers to the following phenomenon. If a force F is applied to a piezos surface, an electric charge Q results. Together, this behavior can be described as:

$$\begin{bmatrix} y \\ Q \end{bmatrix} = \begin{bmatrix} d & 1/k \\ C & d \end{bmatrix} \begin{bmatrix} V \\ F \end{bmatrix} \tag{1.7}$$

with C the capacity, d the piezoelectric charge constant, and k the stiffness of the piezo, see chapter 2 for more details.

Switching the piezo elements from the electronic driving circuit to a measuring circuit gives an accurate recording of the average pressure inside the ink channel, which we from now on call the "Paint" signal (Piezo-Acoustic sensing of INk channels in the Time domain), figure 1.12. First the driving waveform is applied, which takes $5 - 20$ μs. After that the current from the piezo element can be measured until the next actuation cycle starts. The piezo must be completely de-charged before the acoustic measurement starts. The problem for this setup is that the amplitude of the Paint signal is only 0.1 mA, while the current for charging and de-charging the piezo is about 10 mA. The acoustic measurement also enables monitoring of jetting stability [85] and feed-forward control of the driving waveform [65].

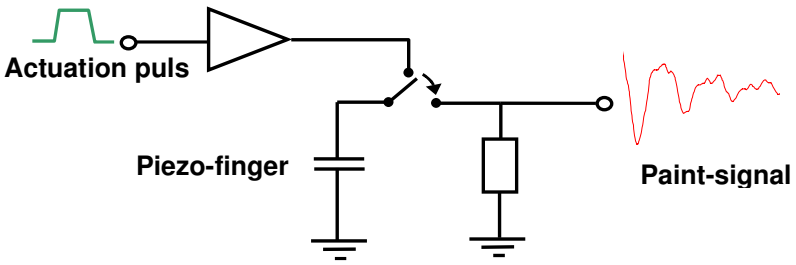

Figure 1.12: Outline of Paint measurement. Switching the piezo elements between an electronic driving circuit and a measuring circuit enables both. The actuation of the channels and the measurement of the pressure variation inside the channels.

1.4 Guide through the thesis

The aim of the research described is this thesis is to explore the processes which lead to the final goal, the stable and reproducible formation of billions of drops. We need more information on the phenomena preceding the drop formation for a better understanding of the operating principles of the piezo printhead. This enables a faster and better development of new printheads [166].

The first step is the actuation. The transformation of an electric voltage to a deformation of the ink channels is described in chapter 2. The deformations inside the printhead cannot be measured and modeling with the commercial finite element code Ansys plays an important role [162]. The deformation of the channel cross-section results in pressure waves.

The acoustic properties of the ink channels are the subject of chapter 3. The pressure waves play a central role in the printhead operation. They connect the electrical/mechanical domain of the actuator to the fluid dynamic domain in and outside the nozzles. Measurements are done with the laser-Doppler setup and the acoustic measurement. Details on ink flow and acoustic pressure waves inside the ink channel are available through modeling. The acousto-elastic interaction plays an important role in the "narrow-channel" model. Acoustic modeling with Ansys gives the details of the interactions with the structure dynamics of the printhead.

Another approach, modeling the complete printhead operation with one model in a multi-physics approach [177], leads to a very long calculation time and is not considered in this thesis.

The drop formation is the final goal of the printhead operation. The pressure waves in the ink channels are the driving force behind the drop formation process. In chapter 4 the details of the drop formation process are described. Optical measurements and modeling provide the information we need. For the modeling of the free surface flow with surface tension, and its impact on channel acoustics, we use the commercial volume of fluid code Flow3D, an approach used also by Dimatix/Spectra [113] and other competitors.

Also the flow phenomena on the nozzle plate are important. Wetting of the nozzle plate can influence the drop formation process. The material interactions, which determine the wetting properties, are not known in detail. Therefore, an experimental study of the wetting phenomena is performed. This is described in chapter 5.

Wetting can also result in air entrainment. Air bubbles play an important role in the jetting stability. The theoretical and experimental research on the generation and the behavior of air bubbles and their impact on the printhead performance is the subject of chapter 6. The acoustic measurement is an indirect measuring tool for the existence of air bubbles. Transparent heads are developed for direct visual measurements. Modeling is done with different numerical models.

In the last chapter the results are summarized, conclusions are drawn and an outlook on further developments is presented.

The experiments are done with printheads developed at Océ Technologies B.V. For the research described in this thesis a transparent test ink is used with a viscosity of about 10 $mPa.s$ at the jetting temperature of 130 $^{\circ}C$, a surface tension of 30 mN/m, a density of 1000 kg/m^2 and a speed of sound of 1250 m/s.

Chapter 2

Structure dynamics

In this chapter the driving force in piezoelectric printheads is discussed. The actuator design for the printhead will be presented, which is based on the bump mode actuation. The deformation of the channels to generate the pressure waves for firing droplets from the nozzles can also result in local cross-talk effects, like the direct and the pressure induced cross-talk effect, as will be shown with numerical simulations. Exciting many channels at the same time excites also resonances in the printhead structure.

2.1 Actuating

2.1.1 Piezoelectricity

The driving force to fire a droplet with a piezo inkjet printhead is generated by the actuator, which deforms the structure through the inverse piezo-electric effect.

The piezoelectric effect (electricity from an applied mechanical stress) was first discovered by Pierre and Jacques Curie in 1880. Their experimental demonstration consisted of a conclusive measurement of surface charges appearing on specially prepared crystals, which were subjected to mechanical stress. In 1881, Lippmann deduced mathematically the inverse piezoelectric effect (stress in response to an applied electric field). The Curie brothers immediately confirmed the existence of this property [25]. In the following years, the twenty natural crystal classes in which piezoelectric effects occur and all possible macroscopic piezoelectric coefficients were defined [5].

Barium titanate ($BaTiO_3$), the first piezoelectric ceramic with a perovskite structure (a tetragonal/rhombohedral structure very close to cubic), was found around 1943. S. Roberts detected the piezoelectric effect in $BaTiO_3$ in 1947. In 1954, the discovery of the piezoelectric ceramic $Pb(Zr_xTi_{1-x})O_3$, lead zirconate titanate (PZT), was reported by B. Jaffe (US Patent 2,708,244). In the following years PZT became the main industrial product in piezoelectric ceramic materials.

Ceramic perovskites have a cubic structure that is stable at temperatures above their Curie temperature, as seen in figure 2.1. When the temperature decreases

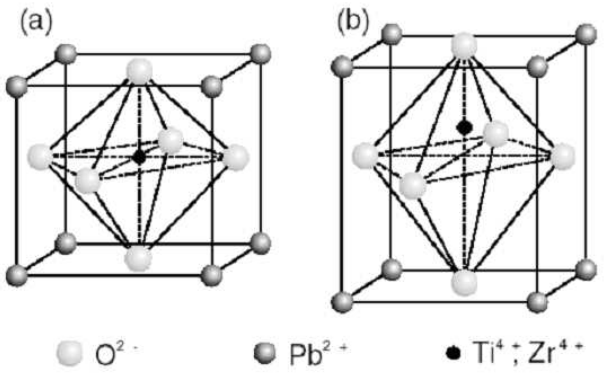

Figure 2.1: The elementary cell of PZT (a) above the Curie temperature and (b) below the Curie temperature. At a high temperature, the electric charges coincide in a cubic structure and there is no piezo-electricity. Below the Curie-temperature the electric charges do not coincide anymore. This results in a piezoelectric effect.

and falls below the Curie temperature, the structure changes and in the case of PZT, the O^{2-} and the Pb^{2+} -ions are moved from their cubic positions and the Ti^{4+} and Zr^{4+} ions are moved from the center of the cube. The positive and negative charge sites do not coincide anymore, which results in a dipole and a structure that is no longer cubic but rather tetragonal. An electric field will therefore tend to deform the structure and this results in the inverse piezo-electric effect.

In general, a uniform alignment of the electric dipoles only occurs in certain regions of a crystal, while in other regions the polarization may be in the reverse direction. Such regions are called ferroelectric domains. When a ferroelectric ceramic is produced, it shows no piezoelectricity. Because of the random orientation of the different domains, there is no net polarization. In order for the material to become piezoelectric it has to be poled. Poling is the imposition of a DC-voltage across the material. The ferroelectric domains align to the field resulting in a net piezoelectric effect. Not all the domains become exactly aligned. Some of them align only partially and some do not align at all. The number of domains that do align depends upon the electric poling field, the temperature, and the time the electric field is held on the material. During poling the material permanently increases in dimension between the poling electrodes. The material can be de-poled by reversing the poling voltage, increasing the temperature beyond the Curie temperature or by inducing a large mechanical stress.

A ferroelectric hysteresis loop for a piezoelectric ceramic is a plot of the polarization P developed against the field E applied to that device at a given frequency. A typical hysteresis loop is shown in figure 2.2. Applying a small electric field, we only get the linear relationship between P and E (1→2), because the field is not large enough to switch any domain and the sample will behave as a normal

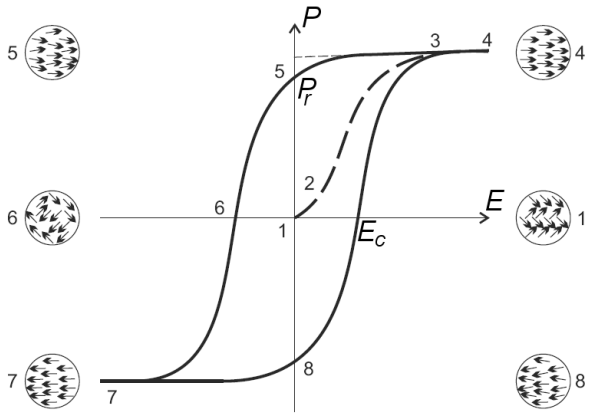

Figure 2.2: P-E hysteresis loop for a ferroelectric material. A plot of the polarization P developed against the field E applied to that device at a given frequency. (1-2) A small electric field does not align the domains but (3-4) a large electric switches the domain in one direction resulting in (5) a net polarization of the material. (6) A large electric field in the opposite direction de-polarizes the material and (7-8) can even reverse the polarization.

dielectric material. As the electric field strength increases (2→3), a number of the negative domains (which have a polarization opposite to the direction of the field) will be switched over in the positive direction and the polarization will increase rapidly until all domains are aligned in the positive direction (4). As the field strength decreases, the polarization will generally decrease but not return back to zero. When the field is reduced to zero (5), some of the domains will remain aligned in the positive direction, and the ferroelectric sample will exhibit a remnant polarization P_r.

The remnant polarization P_r in a ferroelectric sample cannot be removed until the applied field in the opposite (negative) direction reaches a certain value. The strength of the field required to reduce the polarization P to zero (6) is called the coercive field strength E_c. Further increasing of the field in the negative direction will cause a complete alignment of the dipoles in this direction (7). Reversing the field direction once again can complete the hysteresis cycle. The piezoelectric PIC251 material has a Curie temperature of 200 $°C$. The coercive field strength at room temperature is 1.2 kV/m and only the half at an operating temperature of 130 $°C$.

Balance of angular momentum requires that the stress tensor is symmetric and the six remaining components of the stress matrix are written as a vector with six components, $\underline{T} = (\tau_x x, \tau_y y, \tau_z z, \tau_{yz}, \tau zx, \tau xy)^T$. The same is done for the strain matrix. We use linear relationships for describing the piezoelectric effect. The matrices with the piezoelectric coefficients $\underline{\underline{d}}$ for the piezoelectric and the inverse

piezoelectric effect are equal:

$$\underline{S} = \underline{\underline{d}}\ \underline{E} \qquad \underline{D} = \underline{\underline{d}}^T\ \underline{T} \tag{2.1}$$

in which $\underline{D}$ is the electric displacement field (or the charge density), and $\underline{E}$ is the applied electrical field. Combining the piezoelectric equations with the equations describing dielectric relation with $\underline{\underline{\varepsilon}}$ the matrix with the dielectric constants:

$$\underline{D} = \underline{\underline{\varepsilon}}\ \underline{E} \tag{2.2}$$

and the elastic equation with $\underline{\underline{s}}$ the compliance matrix:

$$\underline{S} = \underline{\underline{s}}\ \underline{T} \tag{2.3}$$

we get the matrix equations describing the complete electromechanical behavior of a material:

$$\underline{S} = \underline{\underline{s}}\ \underline{T} + \underline{\underline{d}}\ \underline{E} \tag{2.4}$$

$$\underline{D} = \underline{\underline{d}}^T\ \underline{T} + \underline{\underline{\varepsilon}}\ \underline{E} \tag{2.5}$$

2.1.2 Bump mode actuation

The actuator of the printhead is a bump mode actuator. A side view and a front view is already given in figure 1.9. The actuation movement is directed along the polarization of the piezo material and the corresponding axis along the height h_p of the piezo element is the y-axis as shown in figure 2.3. The z-direction is taken in the direction of the channel and the length l_p of the piezo element.

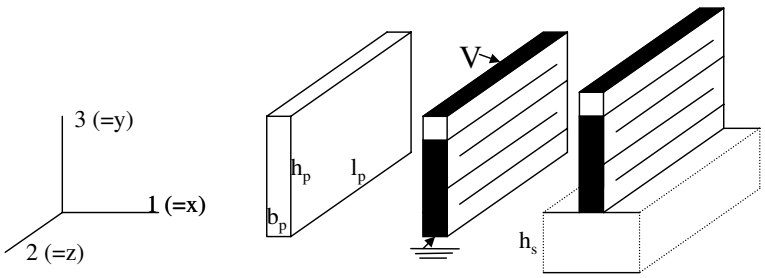

Figure 2.3: Configuration of the bump mode actuator with definition of the x-, y- and z-directions. The y-direction is the actuation and polarization direction of a piezo element with height h_p, width b_p and length l_p, supported by a substrate with thickness h_s.

To identify the directions in a piezoelectric ceramic element, the orthogonal axes are termed 1, 2 and 3. The 3 axis is taken parallel to the direction of

polarization within the ceramic. For the orthotropic PZT-material the matrices with the polarization in the y-direction become:

$$\underline{\underline{s}} = \begin{bmatrix} s_{11} & s_{13} & s_{12} & 0 & 0 & 0 \\ s_{13} & s_{33} & s_{13} & 0 & 0 & 0 \\ s_{12} & s_{13} & s_{11} & 0 & 0 & 0 \\ 0 & 0 & 0 & s_{44} & 0 & 0 \\ 0 & 0 & 0 & 0 & s_{66} & 0 \\ 0 & 0 & 0 & 0 & 0 & s_{44} \end{bmatrix} \tag{2.6}$$

$$\underline{\underline{d}} = \begin{bmatrix} 0 & d_{13} & 0 \\ 0 & d_{33} & 0 \\ 0 & d_{13} & 0 \\ 0 & 0 & d_{15} \\ 0 & 0 & 0 \\ d_{15} & 0 & 0 \end{bmatrix} \quad \underline{\underline{\varepsilon}} = \begin{bmatrix} \varepsilon_{11} & 0 & 0 \\ 0 & \varepsilon_{22} & 0 \\ 0 & 0 & \varepsilon_{33} \end{bmatrix} \tag{2.7}$$

The displacement of a free piezo element with height h_p, that is without any mechanical stresses, in the y-direction is:

$$\frac{\Delta y}{h_p} = d_{33} E_3 = d_{33} \frac{V}{h_p} \tag{2.8}$$

with V the driving voltage. So the free displacement is $\Delta y = d_{33} V$ see also equation 1.7. With d_{33} about 400 pm/V for most PZT materials, the displacement of the piezo element is 0.4 nm/V. As we will see in chapter 3 the volume displacement of the actuator should be about twice the drop volume. To fire a drop of 25 pl with a channel of 10 mm length and a width of 250 μm, the displacement of the piezo element should be 20 nm. This requires a driving voltage of 80 V.

For driving electronics, a driving voltage of less than 40 V is preferred. A simple way to reduce the required driving voltage is to use a multi-layer stack as shown in figure 2.3. The piezo element is divided in n layers with thickness $d_{layer} = h_p/n$. So the free displacement is $\Delta y = n d_{33} V$. The required driving voltage in the previous example becomes now $80/n$.

A limitation is the maximum electric current I_{max}, which has to be supplied during the charging time t_p by the driving electronics:

$$I_{max} = \frac{Q}{t_p} \tag{2.9}$$

A faster charging of the piezo element, i.e. a smaller t_p, is only possible when the total charge Q at the electrodes of the piezo element remains within certain limits. The total charge of a free piezo element is:

$$Q = l_p \cdot b_p \; D = A_p D = \varepsilon_{33} A_p E_3 = \frac{\varepsilon_{33} A_p}{h_p} V = CV \tag{2.10}$$

see also equation 1.7. With n layers the total area of the electrodes becomes nA_p and the electric field E_3 becomes nV/h_p. So the total capacitance of the piezo element becomes:

$$C = \frac{n^2 \varepsilon_{33} A_p}{h_p} \tag{2.11}$$

With equations 2.9, 2.10, 2.11, and the fact that the required driving voltage scales with $1/n$ we can see that the maximum electric current increases with n. This limits the maximum applicable number of layers within a piezo element.

In order to be capable of deforming an ink channel, the piezo elements have to be supported by a substrate, which supplies the reaction force. An important consequence of this is that mechanical stresses will be generated, which influence the piezoelectric behavior of the piezo element. The stresses result from the d_{13} deformation mode of the piezoelectric material. With a d_{13} coefficient of -180 pm/V (which is a typical value for many PZT materials), a 10 mm long piezo element would have an increase in length of 400 nm, while the actuation displacement is only 20 nm. Connected to a substrate this elongation will be counteracted.

As a first order approximation we assume that the support by a substrate results in homogeneous mechanical stresses T_1 and T_2 in the x- and z-direction, respectively, throughout the complete piezo element, so the strain in the y-direction becomes:

$$S_3 = s_{13} T_1 + s_{13} T_2 + d_{33} E_3 = d_{eff} E_3 \tag{2.12}$$

Assuming isotropic material properties in the x- and z-directions in the piezo element and the substrate, $T_1 = T_2$, we get for the strain in the x- and z-direction in the piezo element:

$$S_1 = S_2 = s_{11} T_1 + s_{12} T_2 + d_{13} E_3 = (s_{11} + s_{12}) T_1 + d_{13} E_3 \tag{2.13}$$

For the strain in the substrate in the x- or z-direction we get with the isotropic compliances $s_{11} = s_s$ and $s_{12} = -\nu s_s$ of the substrate material:

$$S_s = s_s T_s - \nu_s T_s = s_s (1 - \nu_s) T_s \tag{2.14}$$

with ν the Poisson ratio of the substrate material. Both materials are connected, so the strain in the x- and z-direction in the piezo element and the substrate are equal. The forces in the piezo element are opposite to the forces in the substrate. For the x-direction this results in:

$$\sum F_1 = 0 = h_p T_1 + h_s T_s \tag{2.15}$$

Substituting equation 2.15 in equation 2.14 we get:

$$S_s = S_1 = -\frac{s_s (1 - \nu_s)}{h_s} h_p T_s \tag{2.16}$$

With equations 2.13 and 2.12 this results in the following equation for the effective piezo electric constant:

$$d_{eff} = d_{33}\left(1 - \frac{2d_{13}s_{13}/d_{33}}{s_{11} + s_{12} + \frac{s_s(1-\nu_s)}{h_s}h_p}\right) \tag{2.17}$$

The substrate is 1 mm thick and the material(AlOx) has an E-modulus of 110 GPa and a Poisson ratio of 0.35. With PZT as piezo material with an E-modulus of 60 GPa this results in a loss of about 50 % for the effective piezoelectric constant. This is shown in figure 2.4.

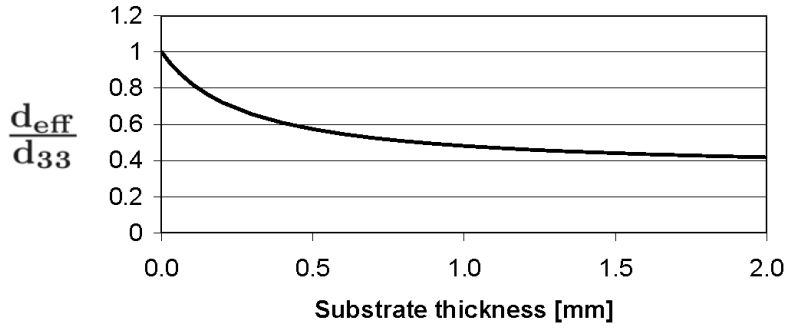

Figure 2.4: Ratio between d_{eff} and d_{33} as function of substrate thickness. The mechanical constraints from the substrate reduce the effective piezo electricity by a factor of two.

One way to reduce the loss in effective piezoelectricity is to make use of the shape factor. At least one dimension in the x- or z-direction of the piezo element should be much less than the height of the element. Then, the mechanical constraints from the substrate only extend over a similar small part of the piezo element height and the loss in effective piezoelectricity will be much less. The most extreme version of this approach is used by Trident in their PixelPro printhead [37]. Also Epson uses in their MLP printheads [149] a high aspect ration between the height and the length and width of the piezo elements. In the printheads of Océ the piezo height is 500 μm, the width less than 100 μm and the length several millimeters to actuate ink channels of the same length. The loss in effective piezoelectricity is reduced to 30 %.

The strain in the piezo element is now inhomogeneous and we use finite element simulations to solve the complex behavior. To include all structural details like glue menisci, without getting very large CPU times, we use static linear analysis with a two-dimensional plain strain model in the x- and y-directions. The commercial finite element code Ansys is used with standard full structural PLANE82 elements and piezo-electric PLANE13 elements, which solve the above mentioned equations 2.4 and 2.5. The parametric models are written in APDL (Ansys Parametric Design Language).

2.1.3 Actuation efficiency

The efficiency is defined as the volume displacement in the ink chamber per volt driving amplitude on the electrodes of the piezo element. The volume displacement per volt must be as high as possible. The effective piezo electric coefficient gives the change in channel height as function of the electric voltage, equation 2.17. Mechanical constraints result not only from the substrate but also from the channels, which are covered with a foil. Some basic actuator design rules can be derived with simple formulas for the stiffness in the actuation direction of block-shaped components with height h_0, width b_0 and length l_0. The equations for the elongation k_e, bending k_b and shear stiffness k_s in the y-direction of the components with elasticity modulus E and Poisson ratio ν are:

$$k_e = \frac{Eb_0l_0}{h_0} \qquad k_b = \frac{Eh_0^3l_0}{b_0^3} \qquad k_s = \frac{Gh_0l_0}{b_0} \tag{2.18}$$

with the shear modulus $G = E/2(1+\nu)$. The elongation stiffness is important for the piezo elements . The stiffness increases proportional to the piezo width b_p and varies from 100-200 MN/m for 85-170 μm piezo width of an element of 500 μm height and 10 mm length.

For the 25 μm tantalum foil between the actuating piezo and the channel wall, see figure 2.5a, the bending stiffness and the shear stiffness are both important. The bending and shear stiffness can be considered as two springs acting in series. The width of the foil between the piezo element and the channel spacing is $b_f = (b_{ch} - b_p)/2$. The bending stiffness is the lowest for a large distance between the piezo element and channel wall. The bending stiffness determines mainly the total stiffness, which varies therefore with the third power of the piezo width. For a small foil width ($b_f < \sqrt{2}(1+\nu)h_f$) the shear stiffness is the lowest. The total stiffness is mainly determined by the shear stiffness, which varies proportional to the piezo width. For a 220 μm wide channel the stiffness of the foil varies from 100 MN/m to 500 MN/m, with the bending stiffness the lowest with a 85 μm wide piezo element and the shear stiffness the lowest with a 170 μm wide piezo element. For a 270 μm wide channel the foil stiffness varies from 40 MN/m to 150 MN/m.

The stiffness of the piezo element and the foil increases with the width of the piezo element. For a large displacement the stiffness of the foil must be low and the stiffness of the piezo element must be high. This means that there will be an optimum in piezo width for the efficiency as shown in figure 2.5b. The calculated volume displacement in a 10 mm long channel is shown as function of piezo element width for a double layer PZT element. For a 220 μm wide channel the optimum piezo element width is about 90 μm and for a 270 μm wide channel about 150 μm. The efficiency is not the only criterion. The influence on neighboring channels is another important design criterion. The will be discussed in the next subsection.

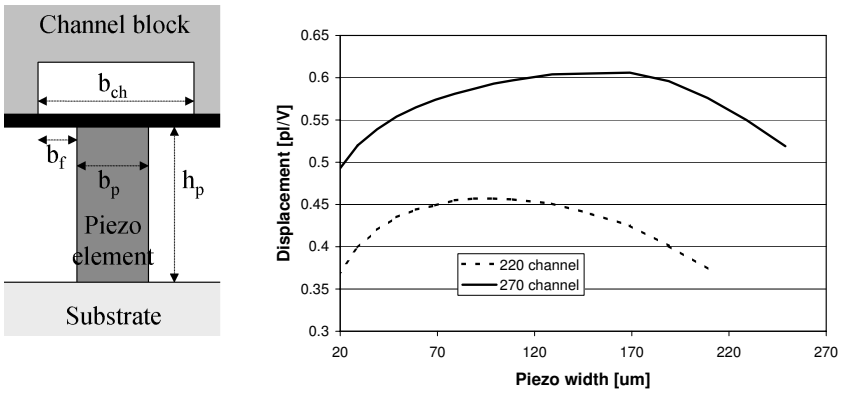

(a) (b)

Figure 2.5: (a) Drawing of a single piezo element supported by a substrate and connected via a foil to an ink channel. (b) Calculated volume displacement in a 220 μm and a 270 μm wide channel, covered with a 25 μm tantalum foil. The channel length is 10 mm. The double-layer piezo element height is 500 μm. The results of the Ansys calculations show the optimum piezo element width.

2.2 Local cross-talk

2.2.1 Electrical cross-talk

The use of a passive support reduces the effective piezoelectric constant in the bump mode actuator. A high aspect ratio between the height of the piezo elements and the other dimensions reduces this loss. Another way to reduce the loss in effective piezoelectricity is to use a substrate of the same piezoelectric material. The external electrodes are the ground electrodes to prevent electrical effects in the other parts of the printhead. The voltage is applied to the inner electrode on the interface between the two piezo layers, figure 2.6. The strain from the d_{13} mode is the same in both piezo layers so no mechanical stresses are generated in the xz-plane. There will be no loss in effective piezoelectricity.

The calculated distribution of the electric field and the resulting deformation are shown in figure 2.6. A voltage of 100 V is applied on the inner electrode of the piezo element in the middle. All outer electrodes and the inner electrodes of the other piezo element are kept at 0 V. 100 V on one element of PZT59 material results in a contraction of that piezo element in the y-direction of 54 nm. The height of the piezo elements is 500 μm, diced to get distinct elements, on a 1000 μm piezo layer, which acts as the substrate.

The electric field is not restricted to one element. As a consequence also the substrate and the neighboring piezo elements will deform because of the inverse piezoelectric effect and this results in a large cross-talk effect. The substrate and the neighboring elements are lifted 10 nm in the y-direction, opposite to

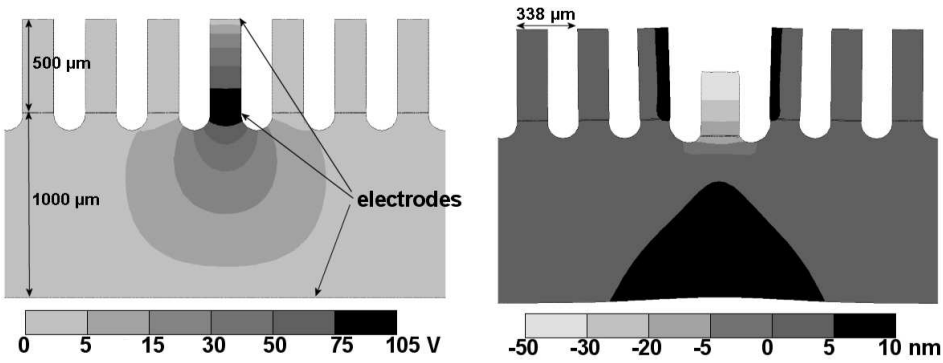

(a) V (b) u_y

Figure 2.6: (a) Calculated electric potential in the xy-plane of an actuator with piezo material as substrate and 75 elements per inch (element width and spacing is 169 μm, which results in a pitch of 338 μm). (b) The resulting displacement in the y-direction u_y. The electric voltage is applied on the electrode between the central element and the substrate. The electric field is not restricted to one element and this results in a large cross-talk effect.

the actuation direction. The remaining displacement of the foil of the actuated channel is reduced to 44 nm. This loss in net actuation displacement and the large cross-talk effect of 23% on both neighboring elements are the reason that for the substrate a passive material is used.

The expansion of the electric field towards the neighboring elements via the ferroelectric substrate is just one example of electrical cross-talk. Other electrical cross-talk effects from for example parasitic capacitances in the electronic driving circuit have to be avoided too.

2.2.2 Direct cross-talk

To prevent electrical cross-talk an actuator is used with 500 μm high PZT elements on a 1 mm AlOx substrate. The actuator is attached to a channel block with channels at the same resolution as the piezo elements. With a resolution of 75 channels per inch the reasonable channel width b_{ch} varies between 170 μm and 270 μm. The stiffness of a 25 μm tantalum foil, which covers a 220 μm wide channel, is 150 MN/m for a 10 mm long channel. This foil has to be displaced over several tens of nanometers.

With the 169 μm wide piezo elements supported by a substrate, the reaction force of the substrate will be guided to the non-actuated elements. The channels that are not actuated will deform too, as shown in figure 2.7a. for a 120 μm high channel, made in brass. This results in a direct cross-talk effect.

The resulting deformation of the neighboring channels is opposite to the de-

formation which is necessary for firing a drop. In figure 2.7a the actuation results in a displacement of 27 nm of the foil of the actuated channel, but the foil in the first neighboring channels lifted over 13 nm in the opposite direction, which means a cross-talk effect of almost 50%. The drop speed will be lower when a neighboring channels is actuated simultaneously. This is shown in figure 2.7b for a 270 μm wide channel. The resulting measured drop-speed of channel zero is depicted when in turn neighboring channels are actuated. When the neighboring channel at the right of channel zero is actuated, the drop-speed of channel zero drops from 5 to 2.2 m/s.

A thin substrate results in an even larger cross-talk effect on the first neighboring channels, but the cross-talk effect is now restricted to only a few channels. The total stiffness (bending and shear) of a 1 mm thick substrate with a length of 10 mm over a distance of eight elements (2.7 mm), as calculated with equations 2.18, is about 150 MN/m. This is of the same order as the stiffness of the foil, which covers the channel. The stiffness of a 0.5 mm substrate is the same over a distance of 4 elements. So the range of the direct cross-talk effect can be estimated by the balance between the stiffness of the substrate and the stiffness of the foil. The total cross-talk effect is about the same with a thin or a thick substrate. Actuating all channels simultaneously would results in a complete fall out of the drop formation.

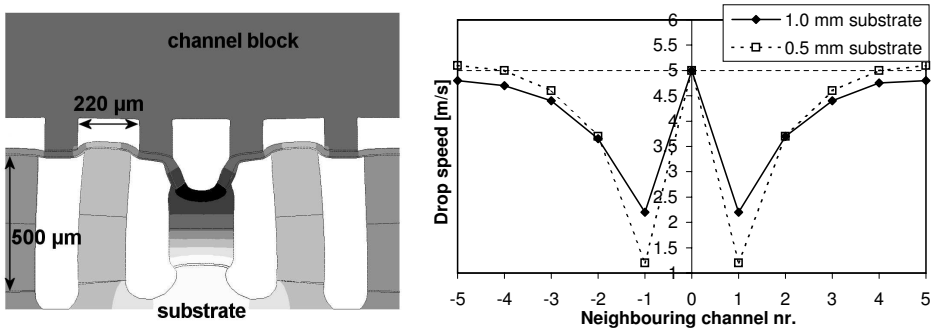

(a) (b)

Figure 2.7: (a) Front view of the channel structure and the calculated deformation of the channel structure. The color scale light→dark is 13 $nm \rightarrow -27$ nm, the deformation is magnified 2000 times in the plot of the deform ed structure. The reaction force of the substrate is guided to the neighboring elements and this results in an opposite deformation of the neighboring channels. (b) The measured resulting lowering of the drop speed for a 1 mm and a 0.5 mm thick substrate. A thin substrate results in a more localized cross-talk effect.

The reaction force of the substrate has to be guided to another part of the printhead to suppress the direct cross-talk effect. A simple way is to use the channel spacings. With 220 μm wide channels there is enough space for doubling

the piezo element resolution. The number of piezo elements is doubled by reducing the piezo element width and spacing from 169 μm to 84.5 μm. One half of the piezo elements is used as actuators and the other half as supports against the channel walls. This creates a force loop as already shown in figure 1.9.

The stiffness of the force loop must be much higher than the stiffness of the channel structure, which has to be deformed. With 220 μm wide channels made in graphite, which has an E-modulus of 14 GPa, the stiffness of the channel spacings becomes comparable with the stiffness of the piezo elements. This results in a stiffness of the force loop of 100 MN/m. The distance between the piezo elements and the channel spacing is 68 μm. The stiffness of a 25 μm tantalum foil is of the same order as the stiffness of force loop. The resulting lowering in drop speed when a neighboring channel is actuated simultaneously is shown in figure 2.8a. The stiffness of a 50 μm silicon foil is 200 MN/m and the stiffness of a 20 μm poly-imide foil, which has an E-modulus of only 9 GPa, is 10 MN/m. The consequences for the lowering in the drop speed are also shown in figure 2.8a.

With a 10 μm thin polyimide foil the stiffness of the foil in the actuation direction becomes less than 1 MN/m and the direct cross-talk effect can even be eliminated. This is shown in figure 2.8b. The actuation of piezo element results in 40 nm displacement of the foil of the actuated channel. The displacements in the neighboring channels are less than 1 nm.

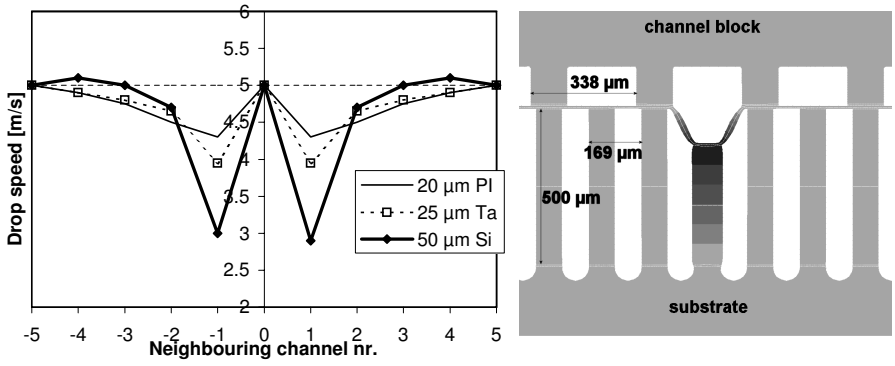

(a) (b)

Figure 2.8: (a) The resulting lowering of the drop speed with a double piezo element resolution for a 50 μm silicon foil, a 25 μm tantalum foil, and a 20 μm poly-imide foil. (b) Front view of the channel structure and the calculated deformation, of 220 μm wide channels in graphite, covered with a 10 μm poly-imide foil. The color scale corresponds to a displacement range of 0 nm to 60 nm. The deformations are in the plot magnified 2000x. The reaction force of the substrate is guided to the channel walls and this eliminates the direct cross-talk effect.

2.2.3 Pressure-induced cross-talk

The actuation of a channel results in pressure waves with an amplitude of 1-2 bar as we will see in chapter 3. These pressure waves deform the structure, too. In figure 2.9a, the deformation is shown of 220 μm wide channels in graphite, covered with a 25 μm tantalum foil. A positive pressure inside the actuated channel results in a deformation of all channels, which is called the pressure induced cross-talk effect.

The deformation of the channels has two main components, an elongation and a bending component. The actuator is pushed away from the channels, an action, which is counteracted by the piezo elements, which are connected to the channel walls. The elongation stiffness in the y-direction of this force loop is about 100 MN/m with 10 mm long channels. The elongation component of the channel deformation results in an enlargement of all channels, thus in a lowering of the channel pressure and the drop speed is lowered for all channels.

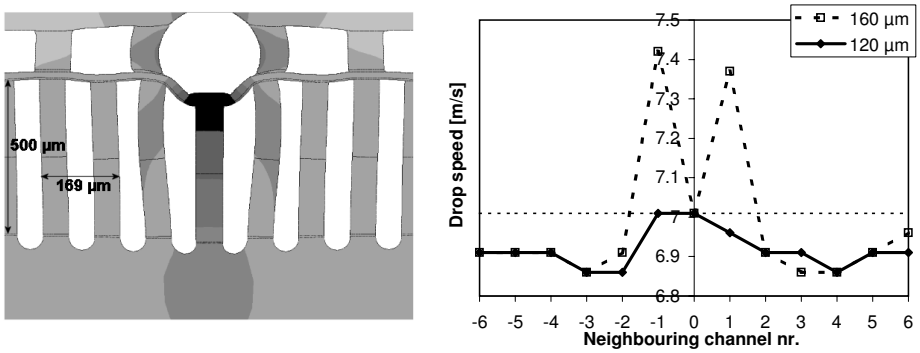

(a) (b)

Figure 2.9: (a) Front view of the channel structure and the calculated deformation, magnified 10000 times, of 220 μm wide channels in graphite covered with a 25 μm tantalum foil. The pressure in the middle channel is 1 bar. The resulting displacement of the foil in the y-direction is about 2 nm/bar. (b) The measured resulting lowering of the drop speed with a 10 μm poly-imide foil for a channel height of 120 μm and 160 μm. The bending of a high channel walls in the first neighboring channels can compensate for the elongation of the channel spacing. This results in an increase of the drop speed with 160 μm high channels.

The amount of elongation depends on the stiffness in the y-direction of the foil between the piezo elements and the channel spacings. A 25 μm tantalum foil has a stiffness comparable to the elongation stiffness of the piezo elements and the channel spacings. The channel spacings and piezo elements will be deformed a lot as shown in figure 2.9a. With a 10 μm poly-imide foil, the stiffness of the foil is much lower. The pressure waves will deform mainly the foil of the channel itself. The resulting lowering of the drop speed is only $0.1 - 0.2$ m/s, as shown in figure

2.9b.

The deformation of the thin flexible poly-imide foil is large and this results in a very compliant channel cross-section. For the actuated channels the compliance of the channel has a large impact on the channel acoustics as we will see in chapter 3. The efficiency will be reduced and the effective speed of sound in the ink will be much lower.

For the pressure induced cross-talk effect the bending stiffness in the x-direction of the channel wall is important too. The bending stiffness in the x-direction of the piezo elements is negligible. For a channel spacing of 120x120 μm the bending stiffness is about 70 MN/m. This bending component reduces the cross-section of the first neighboring channel and can compensate the effect of the elongation deformation component as shown in figure 2.9b for a 160 μm high channel. The bending component has a larger effect in the first neighboring channel than the elongation component and this results in an increase of the drop speed, when the first neighboring channel is actuated at the same time.

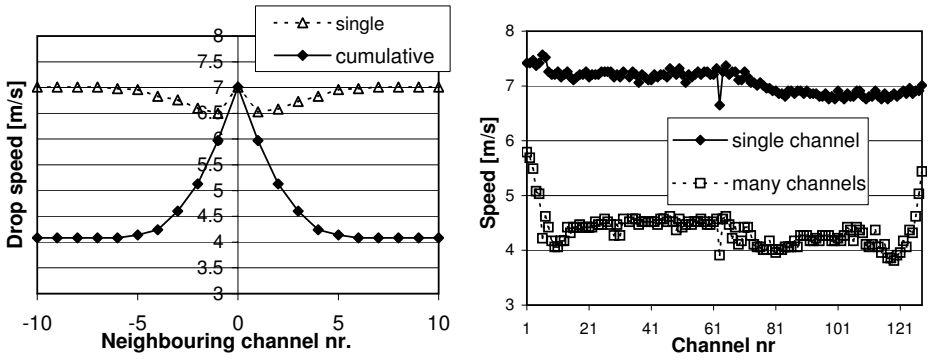

(a) (b)

Figure 2.10: (a) The measured lowering of the velocity of the drop with one neighboring channel firing simultaneously and the cumulative effect of firing more channels simultaneously. (b) Total measured lowering of the drop speed when all channels in an array of 128 channels are firing simultaneously. Depicted for all channels are the drop speed when only one channel is actuated (solo) and when all channels are actuated (many). The channels are 220 μm wide, made in graphite and covered with a 20 μm poly-imide foil. The lowering in drop speed of $0.1 - 0.5$ m/s, with one neighboring channel firing at the same time, will add to a total decrease in drop speed of about 3 m/s when all channels are firing.

The lowering in drop speed will add to a total decrease in drop speed of several m/s, when more channels are firing simultaneously. In figure 2.10a the lowering of the drop speed of a 220 μm wide channel covered with a 20 μm poly-imide foil is shown. When only one neighboring channel is firing simultaneously the lowering in the drop speed is $0.1 - 0.5$ m/s. The cumulative effect of actuating

more channels simultaneously leads to a lowering in the drop speed of 3 m/s. The maximum effect is also shown in 2.10b, with all 128 channels of the array firing simultaneously. The drop speed of the outmost channels decreases less because there are less neighboring channels.

The actuation of a piezo element does not only change the channel cross-section of the actuation channel, but also the channel cross-sections of the neighboring channels. The dynamic deformation of the piezo element can also excite resonances in the printhead structure. The effect of the actuation will than be spread over the whole printhead, as will be discussed in the next section.

2.3 Printhead dynamics

To generate pressure waves in the ink channels, the speed of the deformation of the printhead must be on the same time scale as the channel acoustics. In chapter 3 we will see that this requires a driving waveform at frequencies of several tens of kilohertz. However, the fast movement of the piezo elements can also excite resonances in the printhead structure.

The 8 mm long ink channels are located at both sides of a channel block, see figure 1.9. In figure 2.11, the response of a meniscus surface on the actuation of all 128 channels at the other side of the channel block is depicted. The channels are actuated with a sinusoidal driving waveform with an amplitude of 10% of the nominal driving amplitude. The speed of the meniscus movement in a nozzle in the middle of printhead is measured with the laser-Doppler equipment.

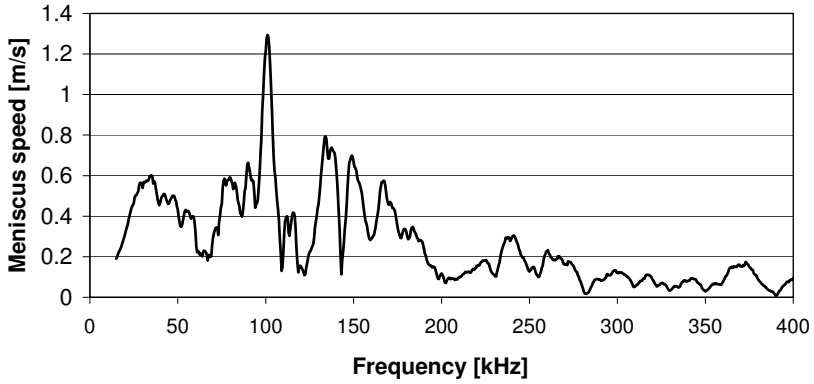

Figure 2.11: The meniscus speed as function of the frequency of the harmonic actuation of all 128 channels at the other side of the channel block. The meniscus speed of nozzle 64 is measured with laser-Doppler. The actuation of many piezo elements results in resonances in the printhead structure, especially at frequencies up to 200 kHz.

Exciting many channels at one side of the printhead influences the movement of

the meniscus surface of a nozzle at the other side of the channel block. Especially at frequencies around 35 kHz and at a frequency range between 60 kHz and 180 kHz. This can only be caused by resonances in the printhead structure.

2.3.1 Modeling setup

The deformations inside the printhead cannot be measured. Therefore, the dynamic response of the printhead structure is simulated with a 3D model of the complete printhead structure. A 3D CAD model of the printhead without the melting unit, the filters and the electronic driving supply, see figure 1.8, is imported into Ansys as basis of the finite element model. Because of the very small and thin parts in the structure, a very fine grid would be required and the number of grid elements would be very large. So a first simplification of the model is to strip all the small parts. It is not likely that these small parts will have any effect. Secondly, the meshing with the Ansys SOLID45 (standard full structural elements) and SOLID5 (including piezo-electricity) is simplified by replacing small round geometries with rectangular geometries.

$\underline{F}$ is the load vector and $\underline{\underline{m}}$, $\underline{\underline{c}}$ and $\underline{\underline{k}}$ are the structural mass, damping and stiffness matrices. The equation of motion for the displacement vector $\underline{x}$ is:

$$\underline{F} = \underline{\underline{m}}\,\underline{\ddot{x}} + \underline{\underline{c}}\,\underline{\dot{x}} + \underline{\underline{k}}\,\underline{x} \tag{2.19}$$

However, solving this equation in a full transient analysis with a model of the complete printhead would require a huge computational effort. Therefore, we start with a modal analysis and perform a mode superposition analysis to get the complete transient behavior.

From experience we know that the amount of damping in the printhead structure is much less than the damping in the ink channels. The damping will be neglected in the modal analysis of the printhead structure. For a linear system, free vibrations will be harmonic of the form $\underline{x} = \underline{\phi}_i \cos(\omega_i t)$, where $\underline{\phi}_i$ is the shape of the eigenmode at angular frequency ω_i. The equation of motion without a load vector, which resolves the eigenmodes, reduces for each mode to:

$$(-\omega_i^2 \underline{\underline{m}} + \underline{\underline{k}})\underline{\phi}_i = 0 \tag{2.20}$$

The mesh element sizes are maximized with the frequency range as criterion. Only modes with a frequency less than 250 kHz are expected to have an impact on the channel acoustics and the drop formation. The corresponding minimum wavelengths of the relevant modes are about 1 mm. With the criterion that at least 10 elements are required to capture the shape of the modes, the maximum element size becomes 100 μm. The smallest elements are necessary to describe the smallest details, e.g. the foil, which has a thickness of 25 μm.

The voltage on all electrodes is set to zero in the modal analysis. With the modal analysis all resonances in the printhead structure are identified. Now we have to calculate which modes are excited the most. First the deformation, which

results from the electrical loading (the voltage applied on the piezo elements) and the mechanical loading (the constraints from the substrate and the channel block), is translated into a pure mechanical loading. This is done, because a mode-superposition analysis is in Ansys not possible with piezo-electric elements. The deformation $\underline{S}$ as the sum of the mechanical and piezoelectric strain (equation 2.4), is translated into an elastic stress $\underline{T}$ with:

$$\underline{T} = \underline{\underline{s}}^{-1} \, \underline{S} \tag{2.21}$$

Only the components of the stress acting in the actuation direction on the top and the bottom of the piezo elements have a significant contribution. These normal components of the elastic stress are multiplied with the surface area to get the load vector $\underline{F}$.

The displacement $\underline{x}$ in the printhead structure can be written as:

$$\underline{x} = \sum_i \xi_i \underline{\phi}_i \tag{2.22}$$

with ξ_i the modal coordinates, or the contribution of every eigenmode to the resulting deformation of the printhead. With the orthogonal condition:

$$\underline{\phi}_j^T \underline{\underline{m}} \, \underline{\phi}_i = 0 \qquad j \neq i \tag{2.23}$$

$$\underline{\phi}_j^T \underline{\underline{k}} \, \underline{\phi}_i = 0 \qquad j \neq i \tag{2.24}$$

and the normalization:

$$\underline{\phi}_i^T \underline{\underline{m}} \, \underline{\phi}_i = 1 \tag{2.25}$$

The modal coordinates can be resolved in the time domain with the following equation:

$$\ddot{\xi}_i + \omega_i^2 \xi_i = f_i \tag{2.26}$$

where f_i is defined as:

$$f_i = \underline{\phi}_i^T \cdot \underline{F} \tag{2.27}$$

After resolving the modal coordinates ξ_i and the eigenmodes $\underline{\phi}_i$, the transient response of the printhead structure can be resolved with equation 2.22, the mode superposition analysis.

2.3.2 Structural resonances

The modal analysis of the complete model results in about 1000 modes with frequencies less than 250 kHz. To reduce the calculation time, the printhead is made symmetric with respect to the xz- and yz-plane in the middle of the head. This requires only some minor changes in small exterior parts of the printhead body, which will not affect the dynamic behavior. Modal analysis with the complete model show that all modes can be described with a 1/4 model with symmetric and anti-symmetric boundary conditions on the xz- and yz-planes in the middle

of the head. Four analyses with a 1/4 model take much less CPU time than a single analysis with a complete model.

The modes with the lowest resonance frequency are the bending modes around the x- and z-axis of the complete printhead at frequencies of $2 - 6\ kHz$. The bending around the z-axis is shown in figure 2.12a. When actuating all channels the maximum displacement with this mode is 1 nm.

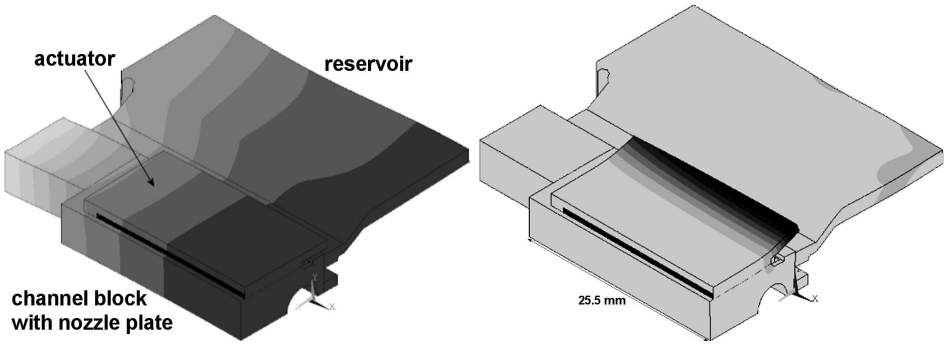

(a) (b)

Figure 2.12: (a) The bending of the printhead around the z-axis in the middle of the printhead. The upper-left quarter of the printhead is shown (the complete printhead model is visible in figure 2.14). The frequency of this mode is 6 kHz and the color range ($light \rightarrow dark$) indicates the displacement of $0 \rightarrow 1\ nm$ when all channels are actuated. (b) The participation of the free bending of the substrate at 33 kHz has a maximum displacement of 77 nm.

The mode with the largest amplitude of the participation is the free bending of the substrate. The substrate is 4 mm longer than the piezo elements to facilitate the electric connection. The base mode of the free bending resonance has a frequency of 33 kHz and is shown in figure 2.12b. Higher harmonics of this mode can be found at 40, 52, 69 and 93 kHz. The free bending of the substrate is excited very strongly because this mode is not hindered by any other parts of the printhead structure. The maximum displacement with the base mode at 33 kHz when actuating all channels is 77 nm.

At frequencies around 100 kHz a range of bending modes can be found. The shape of the base mode at 60 kHz is shown in figure 2.13a. Higher order modes of this resonance have frequencies of $60 - 150kHz$ and amplitudes ranging from a few nanometers up to almost twenty nanometers. Especially the modes around 100 kHz are strongly excited.

These modes are excited because of the shape of the actuation, see figure 2.13b. The piezo elements not only contract in the y-direction because of the d33 mode, but also tend to elongate in the x- and z-directions because of the d13 mode. Without a substrate, this elongation would become in the z-direction about 100 nm. With a 1 mm substrate of AlOx this elongation is now restricted

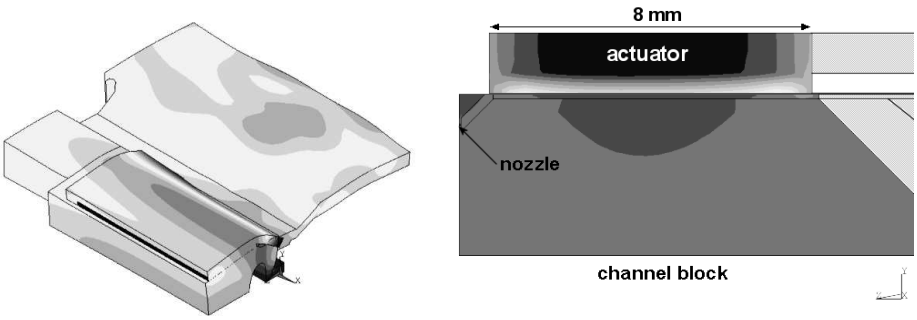

(a) (b)

Figure 2.13: (a) The bending of the actuator at a frequencies 60 kHz. The bending modes of the actuator cover a frequency range of $60 - 150$ kHz. The modes are excited well because of the shape of the actuation. (b) The shape of the actuation in the yz-plane. The 4 mm long extension of the substrate and the reservoir at the right are deleted to make the bimorph shape of the actuation clearly visible.

to 30 nm. This reduces the effective dielectric constant as described in section 2.1.2. Another effect is that the whole structure bends, which is the bimorph effect. This effect is used in other printhead designs as the primary actuation mode [134], but in our case this effect is hindering the actuation. The y-displacement from the bending alone is 12 nm, reducing the actuation displacement from 44 nm to 32 nm, a reduction of almost 30 %.

Furthermore, because of the bimorph shape of the actuation, resonances with a bending component of the substrate are excited very effectively when actuating all piezo elements. When actuating only a few elements, the bimorph shape of the actuation and the excitation of the bending resonances diminishe and only the range of free bending modes of the substrate remains as relative strongly excited modes.

To calculate the transient behavior of the printhead a transient mode superposition analysis is performed. However, in Ansys a mode superposition analysis is only possible with standard structural elements. Therefore, the piezoelectric deformation is replaced by a thermal deformation. The complete strain matrix with the structural elements in Ansys reads:

$$\underline{S} = \underline{\underline{s}}\ \underline{T} + \underline{\underline{k}} P + \underline{\alpha} \Delta T \tag{2.28}$$

and with:

$$\underline{\alpha} \Delta T = \underline{\underline{d}}\ \underline{E} \tag{2.29}$$

we find for the thermal expansion coefficients:

$$\alpha_{x,z} = d_{13}/h_p \qquad \alpha_y = d_{33}/h_p \tag{2.30}$$

to get $|\Delta T| = |V|$. The temperature is imposed homogeneous on the complete piezo element and thermal conductivity is set to zero. The only difference with the real ferroelectric case is that the d_{15} shear mode is lacking and that there is no coupling as described by equation 2.5. Modal analysis with the two cases show that the differences are very small. The maximum deviations remain within 2-5% amplitude variations and a maximum shift in frequency of 0.3 kHz.

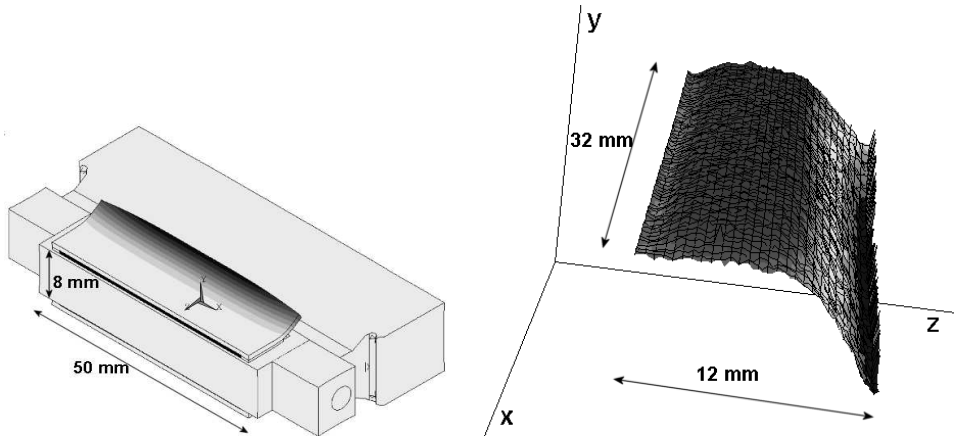

(a) (b)

Figure 2.14: (a) The free bending of the substrate with a maximum displacement of 77 nm dominates the deformation of the printhead. The maximum deformation is magnified 5000 times in the drawing. Depicted are the channel block with reservoir and actuator with jetting direction towards the lower left corner. (b) The measured displacement of the substrate as response of a small sinusoidal actuation at 33 kHz in a 12x32 mm^2 area in the xy-plane, which covers about 3/4 of the substrate surface. The measured displacement pattern matches with the calculated shape of the free bending resonance of the substrate at 33 kHz.

The deformation of the printhead at 16 μs after the start of the actuation is shown in figure 2.14. The free bending of the substrate dominates the picture of the transient deformation of the complete printhead.

The displacement of an outer surface can also be measured with speckle-interferometry. The measured displacement of the outer substrate surface is shown in figure 2.14b for an area of 25x32 mm^2, which covers about the half of the total substrate. The actuation in this measurement is done with a small sinusoidal signal at all piezo elements with a frequency of 33 kHz, the resonance frequency of the free bending mode. The shape of this mode is clearly visible in the measured displacement of the substrate surface.

The measurement of the influence of the printhead resonances on the meniscus movement shows the largest effects at frequencies of $60 - 150$ kHz, figure 2.11. Most likely the bending modes of the actuator are causing the meniscus movement.

We need to model the acoustic pressure waves inside the ink channels to confirm this.

2.4 Concluding remarks

In this chapter, we have seen that with a piezoelectric bump mode actuator design an efficient transformation of electric potential to mechanical deformations is possible. Mechanical constraints result from the channel structure and the substrate. The channels must be deformed to generate the pressure waves, which have to drive the drop formation process. The substrate provides the reaction force. The mechanical constraints result in a complicated deformation pattern with local cross-talk as negative consequence. Doubling the number of piezo elements reduces the local cross-talk. The extra piezo elements can guide the reaction force to the channel walls. When actuating many channels simultaneously, resonances in the printhead structure can be excited. These resonances can have an influence on the printhead performance. To resolve the possible influence of local cross-talk and printhead resonances on the functional behavior of the printhead, the acoustics in the ink channels must be taken into account. The channel acoustics are the subject of the next chapter.

Chapter 3

Channel acoustics

In this chapter the pressure waves inside in the ink channels are discussed. The acoustic properties of the ink channels play a central role in the printhead operation. The dynamics of the printhead structure are coupled through the acoustics to the drop formation process in the nozzle. The derivation of the governing equations of the channel acoustics is given and the resulting frequency characteristics and the application of the traveling wave principle is presented. The interface with the nozzle, treated here as a boundary condition, is the starting point of the next chapter on drop formation. In this chapter the required pressure, the acoustic coupling and the resulting drop size and drop speed of the printhead are presented. The coupling with local cross-talk effects and printhead resonances is described, i.e. the interaction with the printhead structure. Other cross-talk effect described in this chapter are restricted to the ink domain, i.e. acoustic cross-talk, refill and residual vibrations.

3.1 Narrow channel theory

3.1.1 Governing equations

The Navier-Stokes equation of motion and the continuity equation are the starting point for the derivation of the narrow channel equations. The derivation is similar to the derivation of the narrow gap equations [150], which was originally developed for rigid rectangular plates [9], but now extended for acoustic domains restricted in two directions [10]. Instead of using the more general solutions of the references for the specific problem given by the inkjet channel configuration, the underlying equations can also be simplified using the specific geometry constraints of the channel in the printhead.

The continuity equation results from the balance between the change in mass and the flux of mass in a control volume:

$$\frac{\partial \rho}{\partial t} + \nabla \cdot (\rho \underline{u}) = 0 \tag{3.1}$$

with ρ the density and $\underline{u}$ the velocity vector.

The Navier-Stokes equation is the continuum version of Newton's second law, with on the left side the inertial acceleration terms (unsteady acceleration and convective acceleration) and on the right side the external forces and internal forces:

$$\rho\left(\frac{\partial \underline{u}}{\partial t} + \underline{u} \cdot \nabla \underline{u}\right) = \underline{f} + \nabla \cdot \underline{\underline{T}} \tag{3.2}$$

with $\underline{f}$ the external forces and $\underline{\underline{T}}$ the stress tensor. Without any other external forces only gravity remains. The diameter d of the channel is about 100 μm. The Bond number, expressing the balance of gravity and capillary effects, is very small:

$$Bo = \frac{g\Delta\rho d^2}{\gamma} = 3 \cdot 10^{-3} \tag{3.3}$$

with the difference in density between the ink and air $\Delta\rho \approx 1000\ kg/m^3$ and the surface tension $\gamma \approx 30\ mN/m$. This means that gravity is negligible with respect to the surface tension forces. The Galileo number, expressing the balance of gravity and viscous effects, is small, too:

$$Ga = \frac{gd^3\rho^2}{\eta^2} = 9 \cdot 10^{-2} \tag{3.4}$$

with the viscosity $\eta \approx 10mPa.s$. This means that gravity is also small with respect to viscous forces. Finally, the Froude number, expressing the balance of inertia and gravity, is large:

$$Fr = \frac{u}{\sqrt{gd}} = 30 \tag{3.5}$$

even with an ink speed $u \approx 1\ m/s$ in a 100 μm cross-section. This means that gravity is also negligible with respect to inertia. So for the channel acoustics we can neglect gravity.

For the ink properties we take isotropic homogeneous properties with a Newtonian (shear rate independent) viscosity. The internal forces in the Navier-Stokes equation can be split into a pressure term, a deformation term and a dilatation term [7]:

$$\rho(\frac{\partial \underline{u}}{\partial t} + \underline{u} \cdot \nabla \underline{u}) = -\nabla p + \eta\nabla^2\underline{u} + \frac{1}{3}\eta\nabla(\nabla \cdot \underline{u}) + (\frac{2}{3}\eta + \lambda)\nabla(\nabla \cdot \underline{u}) \tag{3.6}$$

with p the pressure and λ the second viscosity coefficient ($\xi = \frac{2}{3}\eta + \lambda$ is also referred to as volume or bulk viscosity). The dilatational term can be neglected for flow through narrow channels. Without mean flow and the convective acceleration playing no role [10], the equation of motion reduces to:

$$\rho\frac{\partial \underline{u}}{\partial t} = -\nabla p + \eta\nabla^2\underline{u} + \frac{1}{3}\eta\nabla(\nabla \cdot \underline{u}) \tag{3.7}$$

The pressure p is considered as an acoustic variation around a zero static value. With only small perturbations of the density around the mean value only the linear

terms will be used ($\rho = \rho_0 + \Delta\rho$, and $\Delta\rho \ll \rho_0$)). With the adiabatic modulus of a fluid ρc^2, the linearized approach with small perturbations of the density results in:

$$p = (\rho_0 + \Delta\rho)c_0^2 \frac{\Delta V}{V_0} = \rho_0 \frac{\Delta V}{V_0} c_0^2 = \rho c_0^2 \tag{3.8}$$

With a channel cross-section much smaller than the length of the channels, the flow components perpendicular to the channel direction are very small and can be neglected. The equation of motion reduces to one component of the velocity u_z in the z-direction, which is taken along the channel [150]:

$$\rho_0 \frac{\partial u_z}{\partial t} = -\frac{\partial p}{\partial z} + \eta \left(\frac{\partial^2 u_z}{\partial x^2} + \frac{\partial^2 u_z}{\partial y^2} \right) \tag{3.9}$$

With only a significant pressure change in the channel direction ($p = p(z)$), the continuity equation reduces to:

$$\frac{\partial p}{\partial t} + \rho_0 c_0^2 \left(\frac{\partial u_x}{\partial x} + \frac{\partial u_y}{\partial y} + \frac{\partial u_z}{\partial z} \right) = 0 \tag{3.10}$$

Substituting harmonic perturbations for u and p:

$$\underline{u} = \underline{\hat{u}} e^{i\omega t} \qquad p = \hat{p} e^{i\omega t} \tag{3.11}$$

we obtain two differential equations in the frequency domain. From the conservation of momentum we find:

$$i\omega\rho_0 \hat{u}_z = -\frac{\partial \hat{p}}{\partial z} + \eta \left(\frac{\partial^2 \hat{u}_z}{\partial x^2} + \frac{\partial^2 \hat{u}_z}{\partial y^2} \right) \tag{3.12}$$

From the conservation of mass we get:

$$i\omega\hat{p} + \rho_0 c_o^2 \left(\frac{\partial \hat{u}_x}{\partial x} + \frac{\partial \hat{u}_y}{\partial y} + \frac{\partial \hat{u}_z}{\partial z} \right) = 0 \tag{3.13}$$

Now we write the components of the velocity in the z-direction as:

$$\hat{u}_z = -\frac{\partial p(z)}{\partial z} H(x, y) \tag{3.14}$$

with $H(x, y)$ describing the shape of the velocity profile in the channel cross-section. After substitution of equation 3.14 in equation 3.12, we get a partial differential equation (PDE) for the velocity profile:

$$i\omega\rho_0 H(x, y) - \eta \left(\frac{\partial^2 H(x, y)}{\partial x^2} + \frac{\partial^2 H(x, y)}{\partial y^2} \right) = 1 \tag{3.15}$$

Now we define a function B_{ch} as the integral of the velocity profile over the channel cross-section A_{ch}:

$$B_{ch} = \frac{i\omega\rho_0}{A_{ch}} \int_{A_{ch}} H(x, y) dA_{ch} \tag{3.16}$$

and integrate equation 3.13 over the channel cross-section to get the narrow channel equation for the pressure [10]:

$$B_{ch}\frac{\partial^2\hat{p}}{\partial z^2}+\frac{\omega^2}{c_0^2}\hat{p}=-\rho_0\omega^2\frac{\Delta A}{A_0} \tag{3.17}$$

The solution of B_{ch} for rectangular cross-sections in the frequency domain is [10]:

$$B_{ch}=\frac{i\omega\rho_0}{\eta}\sum_{n=1,3,\ldots}^{\infty}\frac{8}{(n\pi k)^2}\left(\frac{2(1-\cosh(kh_0))}{kh_0\sinh(kh_0)}+1\right) \tag{3.18}$$

with

$$k^2=\left(\frac{i\omega\rho_o}{\eta}+(\frac{n\pi}{b_0})^2\right) \tag{3.19}$$

and h_0 the channel height and b_0 the channel width.

3.1.2 Frequency characteristics

The narrow channel equations 3.17-3.19 are used for the actuation principle, described in figure 1.10. Therefore the channel cross-sections are transformed to rectangular cross-sections with the same area A and contour length C. The effective channel height h_0 and channel width b_0 in the hypothetical rectangular cross-section geometry can be calculated as:

$$h_0=\frac{1}{4}\left(C-\sqrt{C^2-16A}\right)\qquad b_0=\frac{1}{4}\left(C+\sqrt{C^2-16A}\right) \tag{3.20}$$

with a square cross-section as the geometry with the smallest contour length.

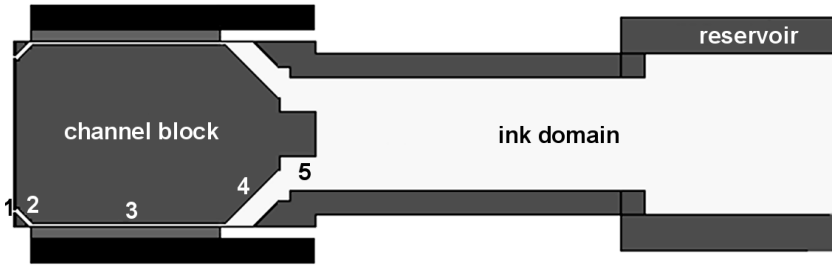

Figure 3.1: Side view on the yz-plane in the middle of an ink channel. (1) The nozzle, (2) the 1 mm long connection channel, (3) the 8 mm long pressure channel, (4) the supply channel, and (5) the reservoir. The nozzle, connection channel and the last part of the pressure channel are shown in more detail in figure 3.2.

The geometry of the ink channel has not only different shapes of the cross-section but also slanting channel section and corners at various angles. In figure 3.1 the complete ink domain in the reservoir and channel block is shown. These

geometric variations cannot be modeled with the one dimensional narrow channel equations.

Therefore, acoustic calculations are done with a 3D finite element model of the ink domain in Ansys. The ink domain is modeled with FLUID80 elements. These elements are standard structural elements, extended with an extra equation to incorporate viscous stresses. The cross-sections are made rectangular too. The mesh resolution is adapted to the velocity profile as predicted by the shear wave number [10] to keep the CPU time as low as possible.

By using a symmetry boundary condition at the middle of the channel in the yz-plane, only half of the channel geometry has to be modeled. The other yz-wall is taken as a rigid boundary. To minimize the CPU time, only the nozzle, the connection channel, and the pressure channel segments are taken of one channel, with zero pressure as boundary condition on the external xy-planes. That are, the meniscus in the nozzle and the start of the supply channel at the other side. On the upper xz-plane of the pressure channel spring elements are used to add the channel compliance as calculated with a 2D model in the xy-plane, section 2.1.2. The lower xz-plane moves in accordance with the deformation, which results from the actuation, section 2.2.3.

The acoustic analysis with the 3D ink domain model in Ansys show that different shapes of the 1 mm long connection channel (as shown in figure 3.2) only have influence at frequencies above 1 MHz. These high frequencies can be neglected regarding the drop formation process. All printheads have a 1 mm long connection channel.

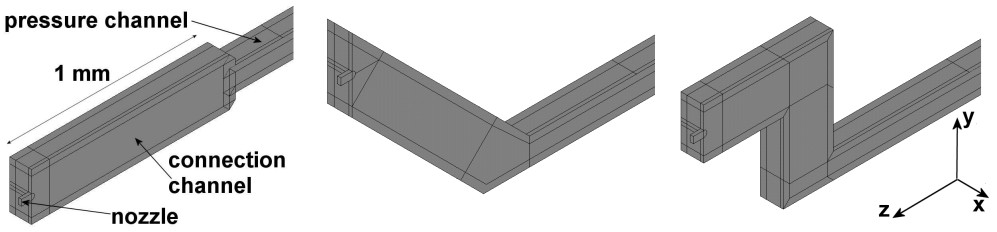

(a) (b) (c)

Figure 3.2: The connection channel geometries as tested with the 3D ink domain model in Ansys. The last part of the pressure channel, the 1 mm long connection channel and the nozzle at the lower left corner are shown. (a) in line, (b) the mostly used connection channel at an angle of 45 degrees, which is also shown as part of the total printhead model in figure 3.1, and (c) a connection channel with corners. The different shapes have no significant effect on the channel acoustics.

The change in channel cross-section results from the actuation with an electric voltage V applied on the piezo element, see section 2.1.2, and from the pressure amplitude p in the channel, see section 2.2.3. The actuation efficiency α and the

compliance β of the channel cross-section are defined as:

$$\frac{\Delta A}{A_0} = \alpha V + \beta p \tag{3.21}$$

From now on the symbol p is used for the pressure amplitude in the frequency domain. The narrow-gap equation 3.17 becomes:

$$B_{ch}\frac{\partial^2 p}{\partial z^2} + \left(\frac{\omega^2}{c_0^2} + \rho_0\omega^2\beta\right)p = -\rho_0\omega^2\alpha V \tag{3.22}$$

At the large reservoir and in the small nozzle, with the meniscus as free surface, the change in pressure is zero ($p = 0$). The response of the meniscus movement resulting from a small sinusoidal actuation of the piezo element, 10 % of the nominal driving amplitude, is shown in figure 3.3.

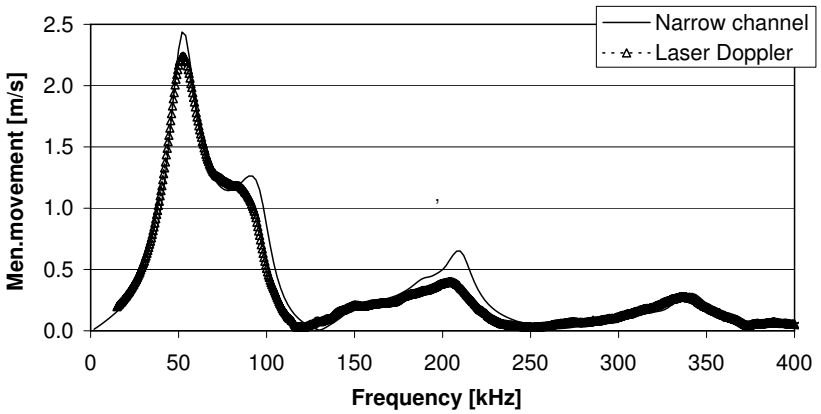

Figure 3.3: The maximum meniscus speed as function of the frequency of a small sinusoidal actuation with an amplitude of 10 % of the nominal driving amplitude. The pressure channel length is 6.7 mm and the nozzle has a diameter of 35 μm nozzle in a 100 μm thick electroformed nickel nozzle plate. The calculated results agree well with the experimental results, which are measured with the laser-Doppler equipment.

The strongest peak in figure 3.3 is the main channel resonance between the nozzle and the reservoir at a frequency of $f = 54\ kHz$. This frequency scales with the total channel length (pressure and connection channel segments), with the nozzle as one boundary and the reservoir with supply channel as the other boundary. In figure 3.4a the variation of the main frequency with pressure channel length is shown.

At low frequencies the ink domain acts more as a $\frac{1}{2}\lambda$ resonator. The pressure waves are reflected with a p=0 boundary condition at the meniscus surface in the nozzle and at the large reservoir with supply channel. The first mode has one

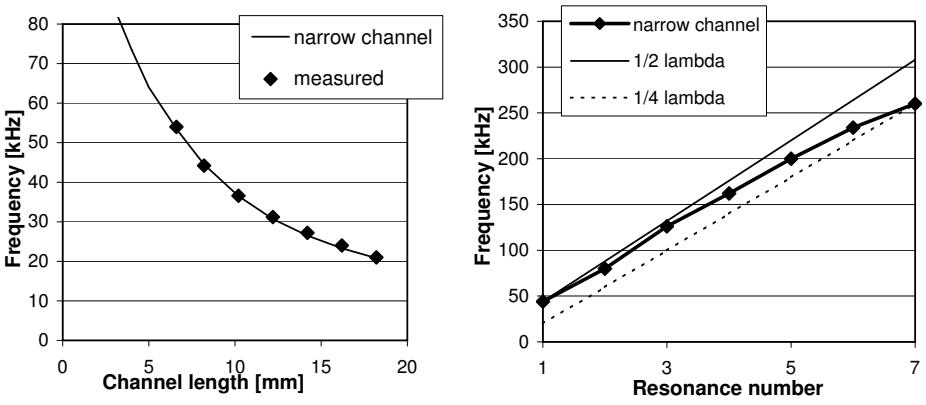

(a) (b)

Figure 3.4: (a) The calculated and the measured resonance frequency of the first mode as function of the length of the pressure channel. (b) The frequencies of the first 7 modes of a 8 mm long pressure channel and the $\frac{1}{2}\lambda$ assumption starting with the first mode and the $\frac{1}{4}\lambda$ assumption ending with the seventh mode.

large pressure peak (anti-node) over the whole length of the pressure channel and the connection channel. This shape fits very well with the shape of the actuation. The major part of the ink domain, the pressure channel, is actuated over the full length.

The second mode however has two pressure anti-nodes over the whole length of the pressure and connection channel. With an actuation over the full length of the pressure channel the positive and negative anti-nodes will cancel out. The second harmonic is therefore hardly excited. At higher harmonics the wavelength will be more comparable with the length of the connection channel and the whole picture becomes more complicated. Another important effect plays a large role at high frequencies, that is the increase of the acoustic impedance of the nozzle. The acoustic impedance of the nozzle at the end of the channel $Z(\omega)$ is defined as the ratio of the pressure at the entrance of the nozzle p_n over the average speed $\overline{u}_{ch}$ in the channel:

$$Z(\omega) = \frac{p_n}{\overline{u}_{ch}} \tag{3.23}$$

With the continuity equation:

$$\overline{u}_{ch} A_{ch} = \overline{u}_n A_n \tag{3.24}$$

and with equations 3.14 and 3.16:

$$\overline{u} = \frac{1}{A}\int_A \underline{u} = -\frac{1}{A}\frac{\partial p}{\partial z}\int_A H(x,y)dA = \frac{iB}{\omega\rho_0}\frac{\partial P}{\partial z} \tag{3.25}$$

we get after the linearization of the pressure gradient over the length of the nozzle, $\frac{\partial P}{\partial z} = \frac{p_n}{L_n}$, for the acoustic impedance of the nozzle:

$$Z(\omega) = -\frac{A_{ch}}{A_n}\frac{\omega \rho_0 L_n}{iB_n} \tag{3.26}$$

So at higher frequencies the nozzle will act more and more as a closed boundary because of the increasing acoustic impedance. The higher modes shift towards a $\frac{1}{4}\lambda$ resonator. This is shown in figure 3.4b for the first seven modes of a 8 mm long pressure channel and a straight nozzle with a diameter of 32 μm and a length of 36 μm.

With the specific impedance as a criterion, various nozzle shapes can be described with straight nozzles with the same diameter, but with a length adapted to get the same impedance. The concave nozzle shapes in electroformed nickel, with the curvature the same as the nozzle plate thickness, the length becomes 36 μm for nozzles in a 100 μm nozzle plate and 21 μm for nozzles in a 50 μm nozzle plate.

The anti-resonances at 125 kHz and 250 kHz in figure 3.3 are a result of a destructive interference. The whole actuator can be considered as a range of point sources. When the wavelength of the pressure wave is the same as the length of the actuator, these sources can be grouped as pairs at $\frac{1}{2}\lambda$ distance of each other. Pressure waves from these pairs of sources will have a phase difference of a half oscillation period at positions outside the actuation region. The pressure waves will cancel each other out and no pressure waves are transmitted into the channel outside the actuation region. So no meniscus movement is visible at these frequencies after a few cycles, when the initial effects are faded away because of damping.

3.1.3 Traveling wave principle

The most efficient and direct way to generate a high pressure amplitude at the entrance of the nozzle is not to use the channel resonance, described in the previous section, but to amplify the first negative pressure wave after this wave is reflected at the reservoir boundary of the pressure channel. This principle is already described in section 1.3.1 and illustrated in figure 1.10. For maximum efficiency, the width of a trapezoidal shaped driving waveform must be tuned to the travel time of the pressure wave from the center of the active piezo length to the end of the pressure channel at the reservoir side and back. The most efficient pulse width as function of the channel length is shown in figure 3.5.

A consequence of the compliance β of the channel cross-section is the reduction of the effective speed of sound c_{eff}, which follows directly from equation 3.22:

$$c_{eff} = c\sqrt{B_c h} = \sqrt{B_c h}\sqrt{\frac{c_0^2}{1 + \rho c_0^2 \beta}} \tag{3.27}$$

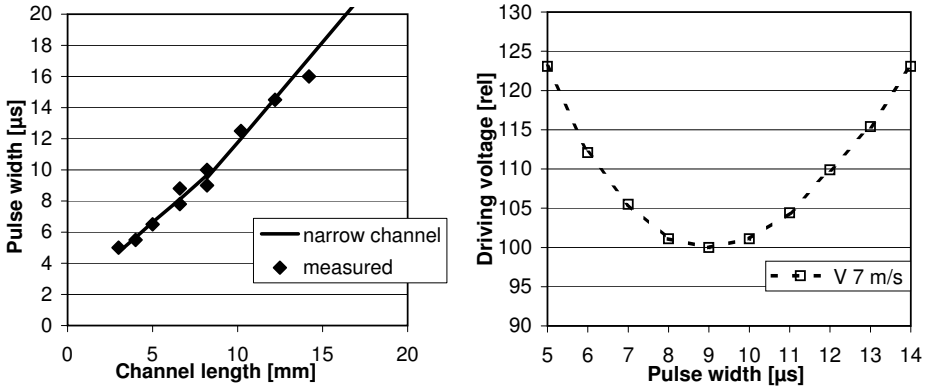

(a) (b)

Figure 3.5: (a) The most efficient driving pulse width as function of the length of the pressure channel. (b) The measured driving voltage to get a drop speed of 7 m/s with an 8 mm long pressure channel as function of the pulse width, showing the most efficient pulse width.

The B_ch term has only a very small effect on the effective speed of sound, so only the channel compliance has to be taken into account [46]. This results with $\beta \approx 7.5 \cdot 10^{-10} m^2/N$ for channels of 220x120 μm in graphite covered with a 25 μm poly-imide foil in a typical effective speed of sound inside the channel of 850 m/s instead of 1250 m/s (the speed of sound of the ink itself). The effective speed of sound can also be derived from figure 3.5. The optimal pulse width is 9.5 μs with a 8 mm long channel, which results with $c_{eff} = L_{ch}/t_{travel}$ in an effective speed of sound of 842 m/s. Also from the minimum in the frequency characteristics as shown in figure 3.3 we can derive the effective speed of sound. With a minimum at 120 kHz with a 6.7 mm channel, which corresponds to the wavelength, we get with $c = f \cdot \lambda$ a speed of sound of 838 m/s.

To get the acoustic pressure in the time domain, the frequency characteristics are multiplied with the actuation driving waveform in the frequency domain. Then, with inverse Fourier transform we get the pressures inside the channel as function of time, figure 3.6a. Direct measurements of this pressure are not possible. Only with the Paint measurement, see section 1.3.2, we can get a measure of the pressure inside the ink channel after the voltage of the driving waveform is zero again. Using the piezo element as a sensor we get a charge proportional to the total force on the piezo element, equation 1.7. The total force is generated by the pressure inside the channel integrated over the area of the piezo element. This charge is measured as an electrical current through the measuring circuit as shown in figure 3.6b.

The differences between the measurement and the simulation of the Paint signal are mainly in the high frequency range i.e. $f > 200$ kHz. In the narrow

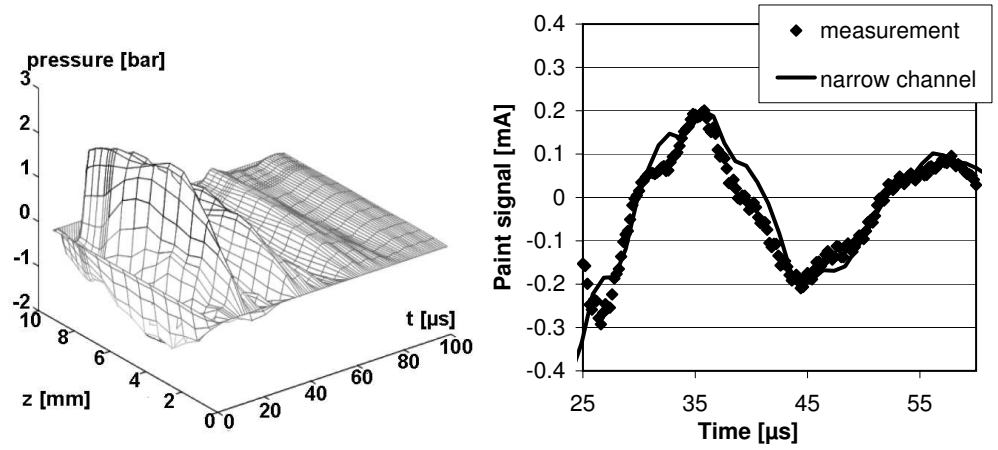

(a) (b)

Figure 3.6: (a) The calculated pressure inside the ink channel as function of time and position. The reservoir is located at the lower right corner and the nozzle at the upper left corner. (b) Measured and calculated Paint signal. There is a reasonable agreement between the calculation and the Paint measurement.

channel model a constant compliance of the channel cross-section is assumed. This is only valid when the deformation of the channel structure by the actuation and the acoustics is small and slower than the dynamic effects of the printhead structure itself. However, in section 2.3, we have seen that this is not always the case and that dynamic effects of the printhead structure can influence the acoustics inside the ink channels.

The most important effect on single channel level is the limited deformation speed in the printhead structure. With a speed of sound of typically 1000-5000 m/s for most solids it will take 0.1-1 μs to deform the channel structure with the actuation force loop over the whole cross-sectional area of 300x2000 μm. In figure 3.7a the calculated dynamic change of the channel cross-section is shown. At t=0 an electric voltage step is applied to the piezo element. The calculations are done with a 2D Ansys model in the xy-plane of the channel structure, see section 2.1.2.

The change in channel cross-section dA can be described with an exponential relaxation:

$$dA = \left(1 - e^{-t/\tau}\right) dA_{stat} \tag{3.28}$$

with a relaxation time τ of 0.15 μs for the best fit. The high frequency oscillations are neglected. With the 3D Ansys models of the ink domain, it is also possible to apply a relaxation time as boundary condition by using COMBIN14 elements at the upper channel wall. The upper channel wall is then fixed via parallel spring and dashpot elements, by which the compliance and the relaxation can be defined. The effect of a relaxation time on the pressure at the entrance of the

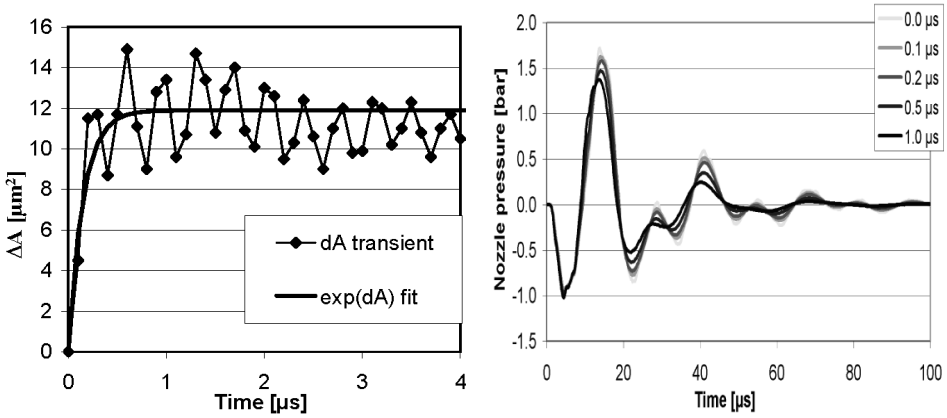

(a) (b)

Figure 3.7: (a) The calculated change of the channel cross-section after an electric voltage is applied at t=0. This is calculated with a 2D Ansys model in the xy-plane of the printhead structure. (b) The impact of a relaxation time on the calculated pressure at the entrance of the nozzle. This is calculated with the 3D Ansys model of the ink domain. A longer relaxation time results in lower pressure amplitudes and more damping.

nozzle is shown in figure 3.7b. The most important effect is the increased damping. This also explains the major part of the differences between the measured and the calculated frequency characteristics of the meniscus movement as shown in figure 3.3. The meniscus movement is driven by the pressure at the entrance of the nozzle.

3.2 Nozzle boundary

3.2.1 Nozzle pressure

Ink movement in the nozzle is driven through the pressure at the entrance of the nozzle. The required pressure for firing a drop with a speed of 7 m/s from a nozzle with a diameter of 32 μm in a 100 μm electroformed nickel nozzle plate is shown in figure 3.8a. In this case the piezo element is charged during 5 μs, which enlarges the channel cross-section and a negative pressure is generated. This negative pressure wave also reaches the nozzle. After 10 μs the charge from the piezo element is removed, which reduces the channel cross-section to its original size. Meanwhile the negative pressure wave is reflected at the reservoir and is became a positive pressure wave. This pressure wave will be amplified and a large positive pressure peak is generated, which reaches the nozzle after 10-15 μs. This large positive pressure peak will drive the ink through the nozzle. The resulting

meniscus speed and position are shown in figure 3.6b.

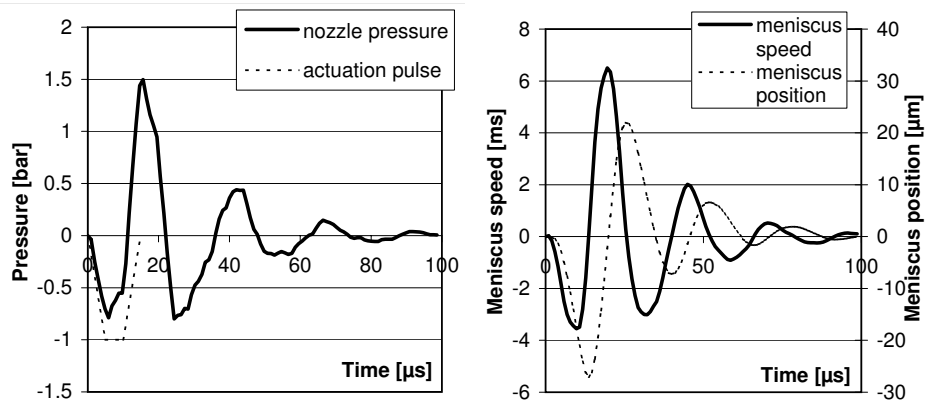

(a) (b)

Figure 3.8: The calculated pressure at the entrance of the nozzle. The shape of the driving waveform is depicted with the dotted line. (b) The resulting average meniscus speed and position. The channel length is 8 mm and the nozzle diameter is 32 μm. Actuation is done with a 10 μs wide trapezoidal pulse with a rise time of 5 μs.

To fire droplets, the average meniscus speed u must be of the same order as the final drop speed, typically 5-10 m/s. To generate a drop, the pressure at the entrance of the nozzle has to overcome steady and unsteady inertia, the viscous forces and forces resulting from the surface tension of the ink. An estimation for the required pressure to overcome inertia is given by the Bernoulli pressure p_b:

$$p_b = \frac{1}{2}\rho u^2 \tag{3.29}$$

With the density of the ink $\rho = 1000\ kg/m^{-3}$, the Bernoulli pressure becomes about 0.25 bar. The ink accelerates in 5 μs (the rise time of the driving waveform) to the required speed. The unsteady pressure p_i (Newton's second law):

$$p_i = \rho L_n \frac{du}{dt} \tag{3.30}$$

generated during this pressure is about 0.5 bar. The surface tension of the ink γ generates a capillary pressure p_c:

$$p_c = \frac{2\gamma cos\theta}{R_n} \tag{3.31}$$

with $cos\theta$ equal to 1 at the nozzle exit with sharp edges. This gives a pressure of 0.05 bar. The viscous resistance can be estimated assuming a Poiseuille flow

profile, which results is a pressure term of:

$$p_v = \frac{8\pi\eta L_n u}{A_n} \tag{3.32}$$

With the viscosity of the ink $\eta = 10\ mPa.s$, this pressure becomes 0.7 bar. The total nozzle pressure $p_n = p_b + p_i + p_c + p_v$ is roughly 1.5 bar, in agreement with the pressure peak in figure 3.8, which is calculated with the narrow channel equations.

The shape of the pressure peak is affected by the acoustic coupling. For an approximation we start with an incoming pressure wave p^+ with a constant amplitude. At the nozzle entrance, a nozzle pressure p_n (the transmitted pressure wave), and a reflected pressure wave p^- are generated:

$$p_n = p^+ + p^- = \rho c(u^+ - u^-) \tag{3.33}$$

where we used the plane wave relation between pressure and speed, $p = \rho c u$. With $u_{ch} = u^+ + u^-$ and the continuity equation 3.24 we get for the nozzle pressure:

$$p_n = \rho c \left(2u^+ - u_n \frac{A_n}{A_{ch}}\right) = \rho L_n \frac{\partial u_n}{\partial t} \tag{3.34}$$

The last term is Newton's second law describing the acceleration of the ink in the nozzle. The solution for the nozzle pressure reads:

$$p_n = 2p^+ e^{-t/\tau} \qquad \tau = \frac{L_n}{c}\frac{A_{ch}}{A_n} \tag{3.35}$$

This result indicates that at t=0 the incoming pressure wave will be reflected as at a closed boundary because the ink in the nozzle is at rest. The nozzle pressure starts to move the ink, which results in less reflection. The nozzle pressure decreases with a characteristic time τ to zero. For a straight nozzle with a diameter of 32 μm and a length of 36 μm, the acoustic equivalent of the nozzle used in figure 3.8, the characteristic time is about 1 μs.

For nozzles with a small diameter, the characteristic time increases. The shape of the nozzle pressure peak changes as shown in figure 3.9a. Here the pressure peak at the beginning of nozzles in a 50 μm electroformed nickel nozzle plate is shown. The nozzle diameter varies from 19 μm to 38 μm. For nozzles with a diameter of 20 μm, the shape of the pressure peak becomes almost the same as the shape of the amplified pressure wave, which results directly from the shape of the driving waveform. The nozzle acts more as a closed boundary. For nozzles with a diameter of 30 μm, the pressure is the same during the first microsecond, but decreases then exponentially to zero.

For a maximum efficiency in terms of required driving voltage for a given meniscus or drop speed, there are two important effects. First, a smaller nozzle area will accelerate the ink movement more, according to the continuity equation 3.24. This would result in a continuously decreasing driving voltage when the nozzle area becomes smaller. The second effect is the acoustic coupling. The

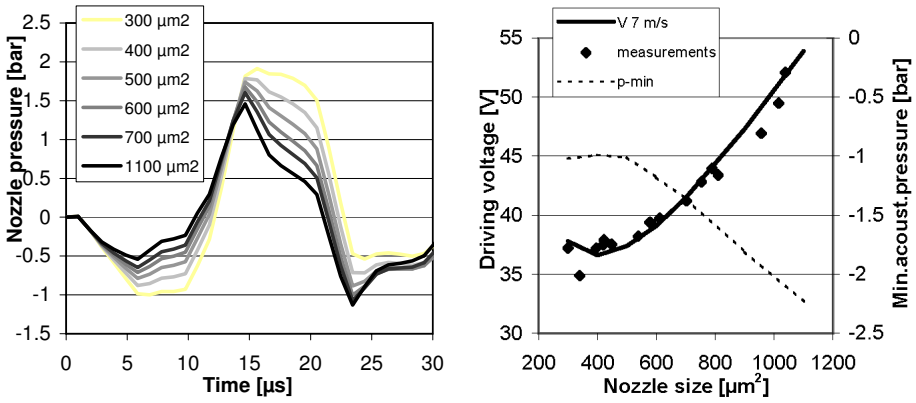

(a) (b)

Figure 3.9: (a) The calculated pressure at the entrance of the nozzle. The nozzle area varies from 300 μm^2 to 1100 μm^2 and the driving voltage is kept constant. (b) The calculated minimum acoustic pressure and the required driving voltage for a drop speed of 7 m/s as function of the nozzle area. The measurements of the driving voltage are also shown. The pressure channel length is 8 mm and the actuation is done with a 10 μs wide pulse with a rise time of 5 μs. There is an optimal nozzle area of 450 μm^2.

transmission coefficient of plane waves, see also equation 1.5, is proportional to the nozzle area for nozzles which are much smaller than the channel cross-section. This would result in a continuously increasing driving voltage when the nozzle area becomes smaller. Both effects together result in an optimal nozzle area with respect to the required driving voltage as shown in figure 3.9b.

The amplitudes of the acoustic pressure waves at the minimum driving voltage are also minimal. This results in the smallest negative acoustic pressure, with the optimal nozzle area. This is important for the jetting stability, as we will see in chapter 6.

3.2.2 Drop size and speed

For an estimate of the drop size range with the current printhead design and the traveling wave principle, we take a cylinder as the shape of the ink column transported outside. The volume of this column is equal to the nozzle area times the length of the cylinder. So the **nozzle area** is the first parameter. The length of the cylinder equals the drop speed times drop formation time. So **drop speed** is the next parameter. Parameters for the drop formation time are the **width of the driving waveform** (which is for maximum efficiency tuned to the travel time of the acoustic wave), the **nozzle shape** (through its impact on the acoustic impedance) and ink properties as **viscosity** and **surface tension**. The travel

time of the acoustic wave is given by the **channel length**, the **inlet geometry** of the supply (because of the phase shift of the reflected wave, in our case a half period) and the effective speed of sound inside the channel. The effective speed of sound is given by the **speed of sound** of the ink itself and the **compliance of the channel cross-section**, see equation 3.27. These parameters can be used for defining an empirical relationship which contains all relevant parameters. A similar approach can be found in [137].

A simple calculation of the drop size and speed, based on the speed of the ink in the nozzle as derived with acoustic calculations, is given by Dijksman in [48]. The ink outside the nozzle is assumed to keep moving with the same speed as the ink inside the nozzle. The criterion for drop formation is that a drop is formed when the kinetic energy of the ink volume outside the nozzle becomes equal to the integral over time of the kinetic energy at the nozzle exit, minus the surface energy of the ink outside the nozzle. The drop size is calculated as nozzle area times the integral over time of the average ink speed, which is based on acoustic calculations. The drop speed is calculated from the resulting kinetic energy with corrections for breakup and the viscous losses to form a spherical drop. A comparable approach, which is based on a balance of forces, can be found in [39]. An even simpler approach is based on a range of numerical calculations with Flow3D as used in chapter 4 of this thesis [54]. In this reference, the drop size is taken as a constant fraction, typical 0.8-0.9, of the amount of ink transported outside the nozzle during the whole drop formation cycle.

In chapter 4 detailed numerical simulations of the drop formation process will be presented. In this section we will compare the measurements with calculations based on the energy balance of Dijksman and the narrow channel model. The measured and the calculated drop sizes as a function of drop speed, channel length and nozzle area are shown in figure 3.10. The channel cross-section is 220x120 μm for all geometries, shaped in a graphite channel-block and covered with a 25 μm poly-imide foil. The pulse width is in all cases the most efficient pulse width. The channels are always connected via an 1 mm long connection channel with a diameter of 250 μm to a nozzle in a 50 or 100 μm electroformed nickel nozzle plate.

In figure 3.10a we see a good match between the calculations and measurements at a drop speed of 5 m/s and a repetition rate of 2 kHz. The drop size increases about 3 pl when the nozzle area increases with 100 μm^2. With an increase in drop speed from 5 m/s to 7 m/s the drop size increases with 25 %. The driving voltage varies with 10 % for each m/s change in drop speed. Measurements at a repetition rate of 10 kHz show $2-5$ pl larger drop sizes as predicted by the calculations. In section 3.4.1 we will see that the deviation at 10 kHz is caused by a refill effect.

The measurements at 10 kHz further show no difference between the nozzles in a 100 μm nozzle plate and a 50 μm nozzle plate. The nozzles in the thick nozzle plate have a higher acoustic impedance. This results in a higher driving voltage to get the same drop speed, but at the same drop speed there is no effect of the

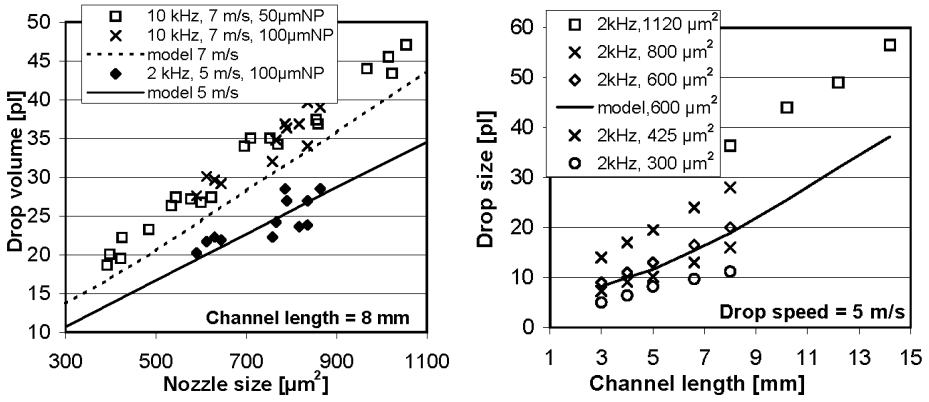

(a) (b)

Figure 3.10: The calculated and measured drop volumes with a repetition frequency of 2 kHz and 10 kHz at a drop speed of 5 m/s or 7 m/s with different nozzle areas and channel lengths. (a) The drop volume as function of the nozzle area in a 50 μm and a 100 μm electroformed nickel nozzle plate for a channel length of 8 mm. (b) The drop volume at a repetition rate of 2 kHz and a drop speed of 5 m/s as function of the channel length for different nozzle areas between 300 μm^2 and 1120 μm^2. The calculations are done with the narrow channel model and the energy balance of the drop formation.

nozzle shape on the drop volume.

The measured drop volumes at a repetition rate of 2 kHz and a drop speed of 5 m/s are shown in the second figure 3.10b. The channel length varies from 3 mm to 14 mm and the nozzle area varies from $300 - 1100$ μm^2. This results in a drop size range of $5 - 55$ pl. The calculated results are only shown for a nozzle area of 600 μm^2. From the calculations with the narrow channel model also the volume displacements by the actuator are known. The corresponding actuator displacements vary from 10 pl for the smallest drop sizes to 100 pl for the largest drop sizes. The actuator displacement is about two times the resulting drop volume for the whole drop size range.

These calculations translate the actuation of a channel to the resulting drop size and drop speed. The same approach can also be used to take into account the cross-talk effects as we will see in the next sections.

3.3 Cross-talk

3.3.1 Local cross-talk

The change in channel cross-section ΔA can be expressed as function α of the actuation voltage V and as function β of the pressure in the channel p, see section

3.1.2, equation 3.21. The actuation efficiency and the channel compliance are calculated with a 2D Ansys model in the xy-plane, see chapter 2. Not only the actuated channel is deformed but also the neighboring channels deform. The resulting deformations of all channel cross-sections ΔA_i can be written as the sum of all contributions of the neighboring channels from the direct cross-talk effect α_{ij}, see section 2.2.2, and the pressure induced cross-talk effect β_{ij}, see section 2.2.3:

$$\frac{\Delta A_i}{A_0} = \sum_j \alpha_{ij} V_j + \beta_{ij} p_j \tag{3.36}$$

Using this expression in the narrow channel equation 3.17, we get a set of M coupled partial differential equations for an array of M channels. All individual channels are divided in N segments, so we have to solve a NxM matrix of coupled partial differential equations. The coupling between the M channels is given by equation 3.36 and the coupling between the N segments of a channel is given by pressure and flux boundary conditions.

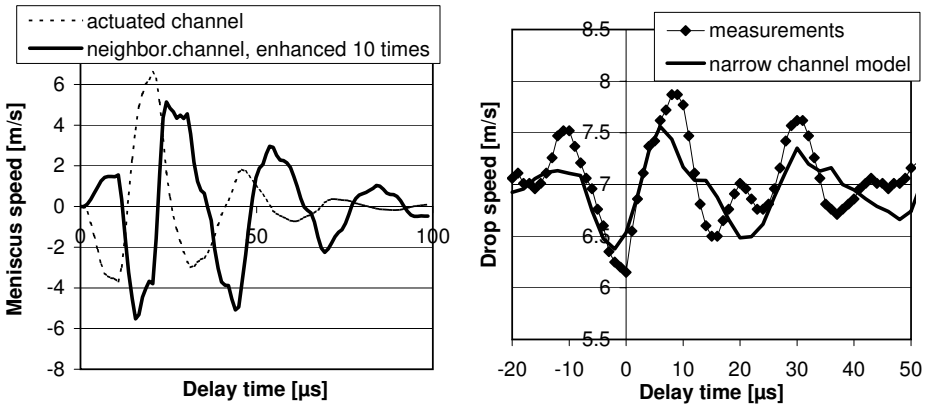

(a) (b)

Figure 3.11: (a) The calculated meniscus speed as function of time in the nozzle of the actuated channel and the neighboring channel. The meniscus speed in the neighboring channel is 10 times enhanced in the picture to show more clearly that this meniscus moves in the opposite direction. This results in a lower drop speed when both channels are actuated simultaneously. (b) Calculated and measured effect on drop speed of a delay time between the reference and the first neighboring channel. The delay time has a large impact on the local cross-talk. The channel length is 8 mm and the nozzle diameter is 32 μm.

After solving this set of partial differential equations, we get the speed of the meniscus in all channels. Not only in the nozzle of the actuated channel but also in the non-actuated neighboring channels. This is shown in figure 3.11a. The meniscus in the neighboring channel moves approximately in the opposite

direction of the meniscus in the actuated channel, which explains the lower drop velocities when more channels are firing simultaneously, see figures 2.9 and 2.10. The channel cross-section of the 8 mm long pressure channel is 220x120 μm, shaped in a graphite channel-block and covered with a 25 μm poly-imide foil. The nozzle has a diameter of 32 μm in a 50 μm electroformed nickel nozzle plate.

The meniscus speed in all channels resonates with the channel resonance frequency. With a time delay between the start of the actuation in neighboring channels we get a large effect on the drop speed as shown in figure 3.11b. With a time delay corresponding to a half period of the channel resonance, 11 μs for an 8 mm channel with a resonance frequency of 44 kHz, the meniscus movement in the neighboring channel will be in-phase with the meniscus movement in the actuated channel and even a higher drop velocity will result from the local cross-talk effect. A time delay corresponding to one fourth of a period of the channel resonance eliminates the effect of local cross-talk on drop speed. Hitachi uses this to minimize the dot positioning errors on the paper [77]. The positioning errors of the dots in a scanning printer concept are proportional to the differences in the speed of the drops.

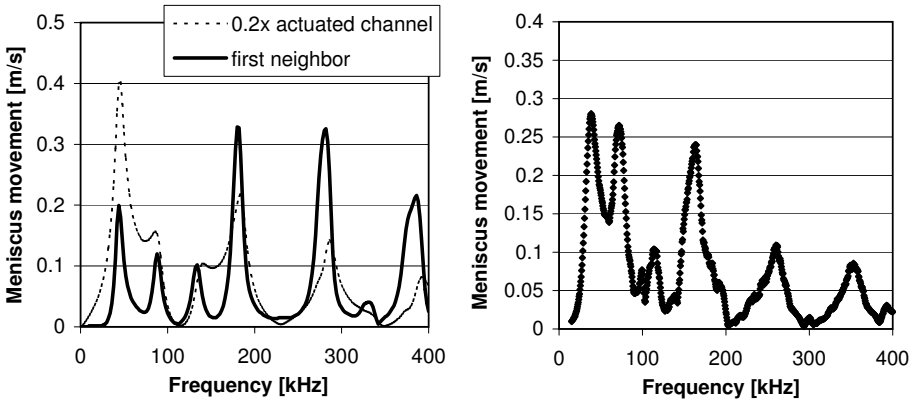

(a) (b)

Figure 3.12: (a) The maximum meniscus speed as function of the frequency of a small sinusoidal actuation with an amplitude of 1 % of the nominal driving amplitude at the piezo element of the same channel and at the piezo element of the first neighboring channel. The amplitude of the actuated channel is reduced 5 times in the picture to make a comparison more easily. (b) The measured meniscus speed of the first neighboring channel. The meniscus response of the first neighboring channels shows more higher frequency components.

There are more high frequency components visible in the meniscus speed of the neighboring channel. This is better visible in the frequency characteristics as shown in figure 3.12. In figure 3.12a the calculated frequency response of the meniscus movement is shown. Depicted is the maximum meniscus speed as

function of the frequency of a small sinusoidal actuation with an amplitude of 1 % of the nominal driving amplitude. Both at the piezo element of the same channel and at the piezo element of the first neighboring channel. The latter is also measured with the laser Doppler equipment, figure 3.12b, which shows a reasonable agreement. The main resonance frequencies remain the same, but the higher frequencies are excited more effective. The dynamic behavior of the printhead structure is not incorporated in the calculations so far. This will be done in the next section.

3.3.2 Printhead resonances

The dynamic behavior of the printhead structure plays a role on single channel level, on local cross-talk level and on total printhead level. This is not incorporated in the narrow channel model. The first example was the finite deformation speed of the printhead, section 3.1.3, which results in a relaxation time in the change of the channel cross-section. As a consequence of this, there is more damping in the channel acoustics, see figure 3.7.

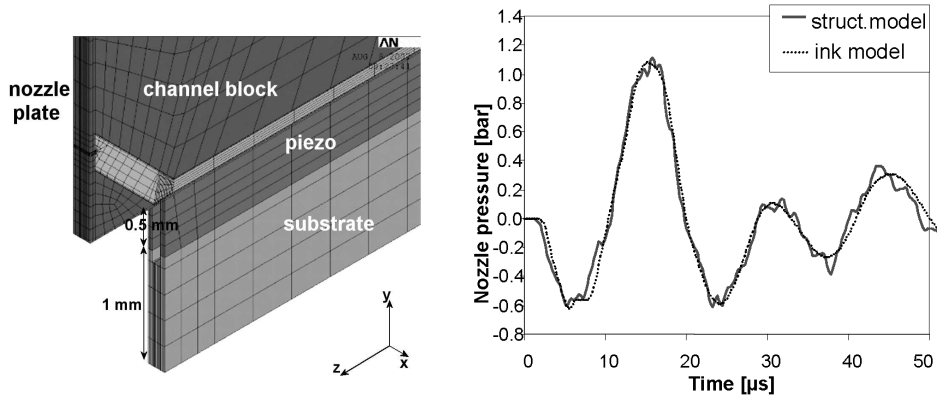

(a) (b)

Figure 3.13: (a) Modular setup of the 3D Ansys model of a single channel geometry, including the ink domain and the printhead structure. (b) The impact of printhead resonances on the pressure at the entrance of the nozzle. This pressure is either calculated with the ink domain only (dotted line) or and with the ink domain extended with the corresponding part of the printhead structure (solid line). The resonances in the printhead structure on single channel scale results in a high frequency ($f = 1\ MHz$) distortion, which will have no impact on the drop formation.

On single channel level also structural resonances are excited. This can be modeled with a 3D Ansys model of a single channel. This is the ink domain model described in section 3.1.2, extended with the printhead structure at that level, i.e. the corresponding part of the channel plate, foil and actuator. The model

is composed with modules of a half channel geometry with boundary conditions on the yz-plane at the center of the channel and actuating piezo element and at the yz-plane at the center of the channel spacing and supporting piezo element, see figure 3.13a. The pressure at the entrance of the nozzle is now calculated with the ink domain model and the extended version, see figure 3.13b. The channel length is 8 mm, and the nozzle has a diameter of 32 μm nozzle in a 100 μm thick electroformed nozzle plate. Only a small high frequency distortion ($f = 1\ MHz$) on the pressure at the entrance of the nozzle is visible, so printhead resonances at single channel level have only a minor contribution. This will have no influence on the meniscus movement and the drop formation.

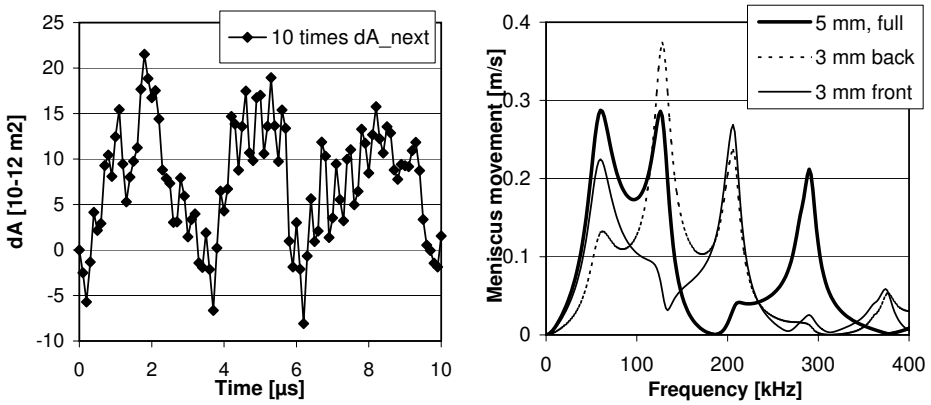

(a) (b)

Figure 3.14: (a) The dynamic change in the channel cross-section of the first neighboring channel after an electric voltage is applied stepwise at t=0. The channel dimensions are $220x120\ \mu m$ in graphite, covered with a 25 μm poly-imide foil. (b) The maximum meniscus speed as function of a small sinusoidal actuation with an amplitude of 1 % of the nominal driving voltage. The channel length is 5 mm and the nozzle diameter is 24 μm in a 50 μm thick electroformed nozzle plate. Actuation is done over the full length, over 3 mm at the supply side of the channel (back), and at the nozzle side of the channel (front). The length over which the channel is actuated has a large effect on the frequency characteristics of the meniscus movement.

On local cross-talk level, resonance frequencies become more important. This can be seen in the change in the channel cross-section of the first neighboring channel. To get a first indication, the change in channel cross-section of the first neighboring channel as a response to a stepwise increase of the driving voltage is calculated with a 2D Ansys model in the xy-plane of the channel structure, figure 3.14a. Not only a relaxation time is visible, (similar to the same calculation for the actuated channel in figure 3.7), but also oscillations with frequencies of $100 - 400\ kHz$ are visible. This is the main reason for the differences between the

measurement and the narrow channel calculation in figure 3.11.

The frequency characteristics of the channel are also important for the acoustic coupling between resonances of the printhead structure and their impact on the meniscus movement and drop formation. The frequency characteristics of the meniscus movement are strongly affected by the length over which the pressure channel is actuated. To demonstrate this, the frequency response of the meniscus movement is calculated with the narrow channel model, figure 3.14b. The channel is actuated over the full length (5 mm), over only 3 mm at the beginning of the channel, and over 3 mm at the end of the channel. This results in complete different frequency characteristics.

The frequency characteristics are important for the acoustic coupling with the resonances in the printhead structure. In section 2.3.2 the resonances in the structure of the printhead are calculated. To model the impact of the resonances in the printhead structure on the pressure waves inside the ink channels, we use the 3D Ansys model of the ink domain, see section 3.1.2. Normally, the deformation of the channel cross-section by the actuated piezo element is the boundary condition for the lower xz-plane of the ink domain model. Now, the deformation of the channel walls from the modal analysis and the mode superposition analysis is used as boundary condition. The resulting pressure at the entrance of the nozzle from the mode superposition analysis is shown in figure 3.15. During one actuation cycle a pressure of almost 0.05 bar at the entrance of the nozzle is generated by the excited printhead resonances. Inside the channel the maximum pressure becomes even higher.

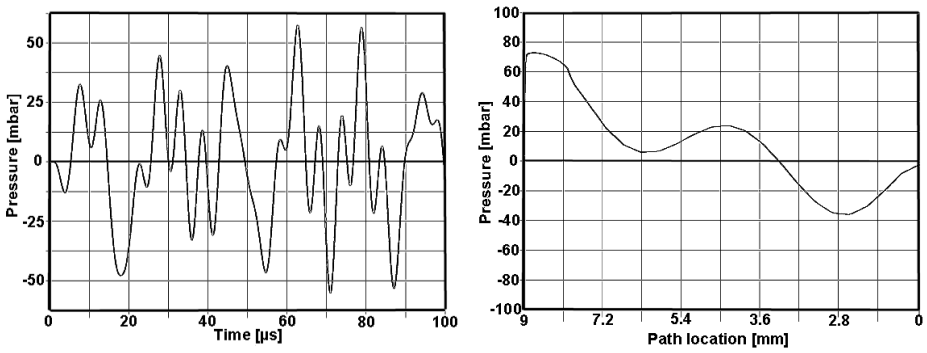

(a) (b)

Figure 3.15: (a) The pressure at the entrance of the nozzle from the mode superposition analysis. The resonances in the printhead structure, excited during one drop formation cycle, generate a maximum pressure of 0.05 bar. (b) The pressure over the channel length at 28 μs after the start of the actuation. The beginning of the supply channel is the origin at the right side and the nozzle is located at 9 mm at the left side. The maximum pressure inside the ink channel is 0.07 bar.

To determine which modes are contributing to this pressure the resulting channel wall deformations per mode are now taken as boundary condition. The strongest excited mode, the free bending of the substrate with a frequency of 33 kHz has almost no contribution, whereas the bending modes around 100 kHz have the largest contribution. The cause of that can be seen in figure 3.16. Here the acceleration of the walls of the pressure channel segment is depicted for these two modes.

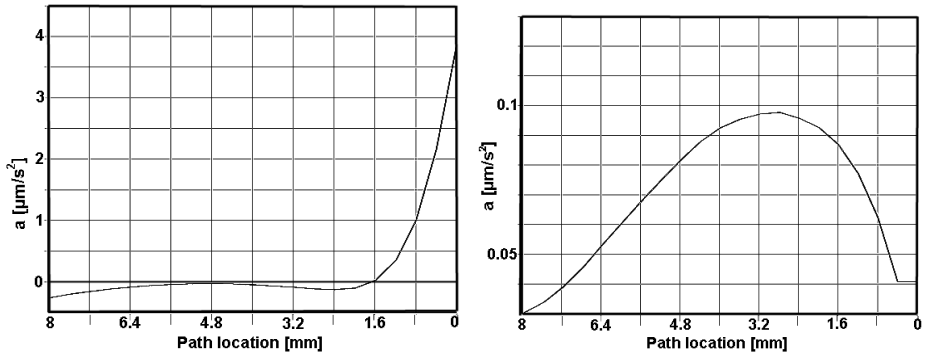

(a) (b)

Figure 3.16: The acceleration of the channel walls from (a) the free bending mode at 33 kHz and (b) from a bending mode at 102.7 kHz. Only the deformation in the pressure channel segment is shown with the supply at the right. The free bending mode deforms the channel only near the supply, whereas the bending modes around 100 kHz deform the pressure channel segment over the whole length.

The free bending of the substrate results in a channel deformation only very close to the supply channel. This is very close to the compliant supply channel, section 3.3.3, and therefore almost no pressure waves are generated. The bending modes around 100 kHz deform the pressure channel over the whole length and this generates pressure waves inside the channel very effectively. This explains the observed high amplitude of the meniscus movement around 100 kHz as shown in figure 2.11.

So far the crosstalk effect from other parts of the printhead structure on the pressure waves in a single channel are discussed. Crosstalk effects can also result from other parts of the ink domain (acoustic cross-talk) or from the ink channel itself (refill and residual vibrations). This will be discussed in the next sections.

3.3.3 Acoustic cross-talk

With the traveling wave principle, a complete reflection of the pressure waves at the supply is very important. Without a complete reflection of the pressure waves, a part of the pressure waves will travel through the supply and the reservoir. This

transmitted part of the pressure waves will also reach the neighboring channels, leading to an acoustic cross-talk effect. Therefore, the acoustic impedance of the supply must be as low as possible.

Since the acoustic impedance is inversely proportional to the cross section of the channel, the supply channel must have much larger dimensions than the pressure channel. A first step is not to use separate supply channels for all individual channels, but one large supply for all channels. The 3D Ansys model of the ink domain is based on modules of half channel segments (nozzle, connection channel, pressure channel and supply channel). With these modules one model is generated. This model contains multiple channels, connected to each other via a common supply, figure 3.17.

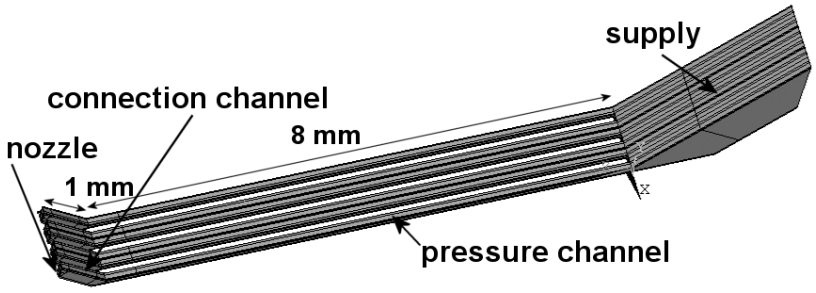

Figure 3.17: The 3D Ansys model of the ink domain with multiple channels connected via an ink supply slit. Depicted are 6 half channel modulus generating two complete and two half channels, with symmetry at outer yz-planes of the half channels. The nozzles are located at the left.

The minimal height of the supply in order to reduce the acoustic cross-talk is calculated with this model. When only a few channels are actuated, a 1 mm high supply is sufficient to get an almost complete reflection, see figure 3.18a. When all channels are actuated, a significant part of the pressure wave is transmitted to the supply as shown in figure 3.18b-d. Only the difference in height between the pressure channel and the supply can now contribute to a difference in acoustic impedance. For channel cross-sections of 220 μm x 120 μm the height of the supply must be of the order of 10 mm to reduce the transmitted pressure wave to less than 1 % of the incoming wave. This is not possible, since the dimensions of the printhead must remain within certain limits.

In figure 3.19b the pressure wave from acoustic cross-talk is shown when half of the channels with a 1 mm high supply slit are actuated. In the actuated channels, the pressure wave is generated over the whole length of the pressure channel, figure 3.19a. With acoustic cross-talk, the transmitted, negative, pressure waves from the actuated channels will enter all other channels as a traveling wave from the supply side of the channels, figure 3.19c. The amplitude of the pressure wave from acoustic cross-talk with all channels actuated is about 10 % of the amplitude of

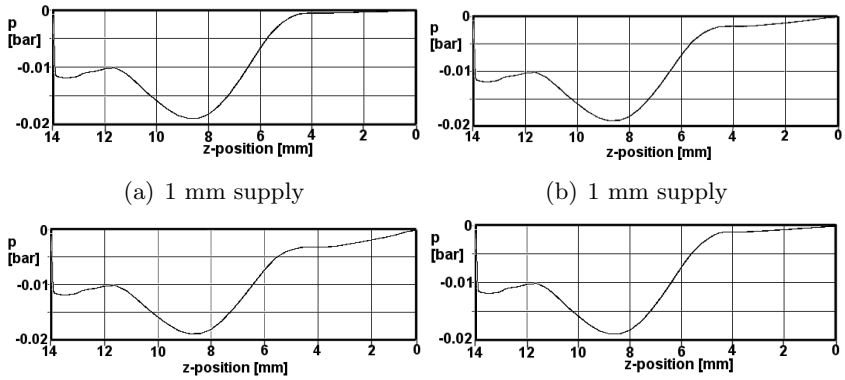

(a) 1 mm supply (b) 1 mm supply

(c) 0.5 mm supply (d) 2 mm supply

Figure 3.18: The acoustic pressure p at 4 μs after the start of the actuation in the 5 mm supply, 8 mm pressure, and 1 mm connection channel. The reservoir is located at 0 mm and the nozzle 14 mm at the left. (a) 1 of 4 channels actuated, (b-d) all channel actuated. The height of the supply must be more than 2 mm to prevent acoustic cross-talk, when all channels are actuated.

the pressure from the actuation. This has an impact of about 1 m/s on the drop speed.

Another way to reduce the impedance of the supply is to increase the compliance of the supply, see equations 1.3 and 3.27. The most simple way to increase the compliance is to cover the supply with a thin foil. The compliant foil will deform when a pressure wave reaches the supply. With a supply of 1 mm height at an angle of 45 degrees, the compliant foil covers a gap of 1.4 mm. A 25 μm poly-imide foil deflects 300 nm when a pressure wave with an amplitude of 0.8 bar reaches the supply, figure 3.20a. This movement can compensate the complete displacement of the acoustic pressure wave, eliminating the acoustic pressure (as would happen with a very large supply). A compliant foil is also used by Dimatix/Spectra to prevent acoustic cross-talk [50, 115].

The effect of the compliance is the same as adding extra volume V_c to the volume of the supply channel V_s. With the bulk compliance ρc^2 of the liquid in the supply and the compliance defined with respect to the undeformed volume of the supply V_s we get for the added volume:

$$V_c = \beta \rho c^2 V_s \tag{3.37}$$

With a 25 μm poly-imide foil over a gap of 1.5 mm, the compliance is $4{\cdot}10^{-9} m^2/N$, and the extra volume from the compliance V_c is six times larger than the volume of the supply V_s itself.

Another option is to use a closed boundary. With a very small inlet at the supply, acoustic cross-talk can be eliminated, too. In figure 3.20b the dimensions of a restriction at the beginning of the pressure channel are shown, which transmit

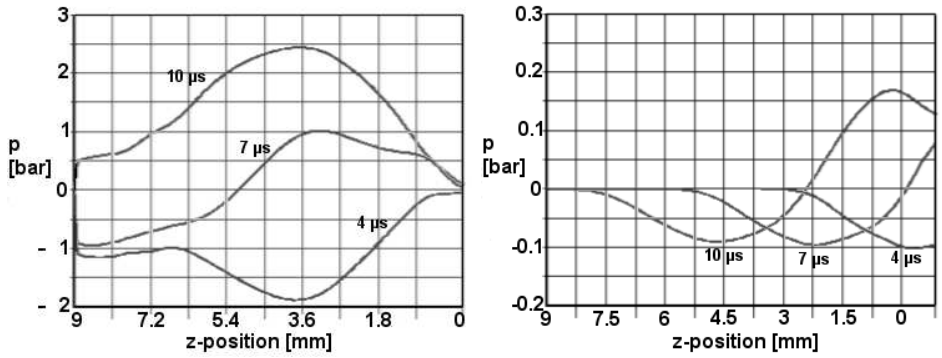

(a) (b)

Figure 3.19: The acoustic pressure p in the pressure and connection channel at 4, 7, and 10 μs after the start of the actuation. (a) In the actuated channel without acoustic cross-talk and (b) the acoustic pressure in the first neighboring channel with 1 of 2 channels actuated and a 1 mm high supply. The pressure waves with normal actuation are generated over the whole length of the pressure channel. The pressure waves from acoustic cross-talk enters the channel through the supply channel.

1 % of the pressure waves. The cross-sectional area of the inlet must be smaller or the length must be larger to prevent acoustic cross-talk. This option is used by Xerox/Tektronix [29] in their pagewide array's [12, 30], by Epson [90], by Dimatix/Spectra in their M-class heads [18, 101, 146] and by Hitachi [124]. A small inlet at the beginning of the pressure channel leads to complete other acoustic properties. Standing waves or Helmholtz resonances as described in [49] are the preferred acoustic principle in these devices.

3.4 Residual vibrations

3.4.1 Refill

In order to fire many drops continuously, the nozzle has to get filled again after one drop formation cycle. At short time scales, that is as long as the acoustic pressure waves are not damped out, the asymmetric acceleration of the ink in the nozzle is the main driving force behind the refill of the nozzle. Before a positive pressure peak reaches the nozzle, the meniscus surface is retracted, and the small mass of ink in the nozzle gets a large acceleration outward. Before a negative pressure peak reaches the nozzle, the meniscus surface is displaced outward, and the large mass of ink in the nozzle gets a small acceleration inward. This results in a net displacement outward, which fills the nozzle at a short time scale. With a 8 mm long pressure channel this refill mechanism plays a role during the first 100 μs,

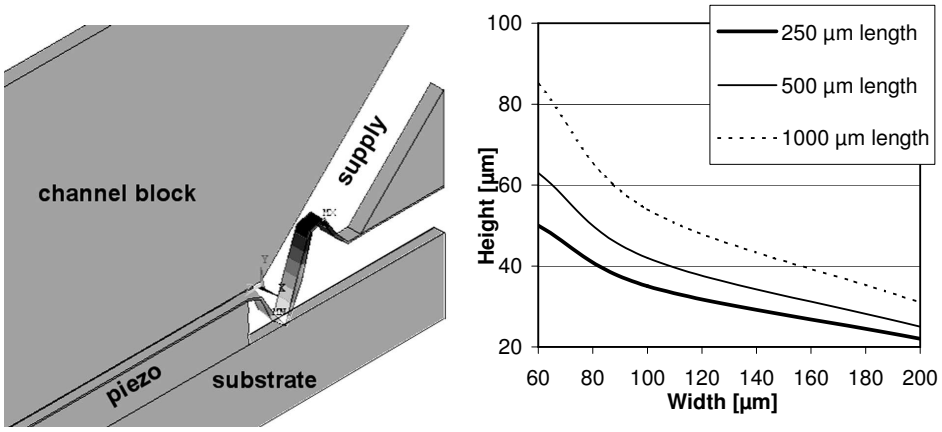

(a) (b)

Figure 3.20: (a) Deformation of the compliant foil when a pressure wave reaches the supply, calculated with a 3D Ansys model of a single channel. A 25 μm polyimide foil covers a gap of 1.4 mm and bends almost 300 nm when an acoustic pressure wave of with an amplitude of 0.8 *bar* reaches the supply. This results in a complete reflection of the acoustic pressure wave. The ink domain is deleted from the plot to make the movement of the foil clearly visible. (b) The maximum cross-sectional area of a small inlet between the supply and the pressure channel, to reduce the acoustic cross-talk to less than 1 %. Another option to reduce acoustic cross-talk is to apply a small inlet instead of a large supply. The calculations with a 3D Ansys model of the ink domain with multiple channels are done for an inlet length of 250 μm, 500 μm, and 1000 μm.

the time period over which the pressure waves come to rest, see for example figure 3.8.

In the narrow channel equations, the nozzle is considered to be completely filled the whole time. The mass of ink in the nozzle remains constant. For a straight nozzle with length L_n, and area A_n, the simple expression $\rho L_n A_n$ gives the mass of ink in the nozzle. The acceleration inward and outward is the same, and there is no refill of the nozzle. There is also no drop formation. The resulting drop properties are calculated as postprocessing of the acoustic calculations.

In order to take into account the variable mass of the ink inside the nozzle, we have to solve the following expression for the meniscus position $z_n(t)$, which is Newton's second law applied on the mass of ink inside the nozzle:

$$p_n(t) = \rho A_n (L_n + z_n(t)) \frac{\partial^2 z_n(t)}{\partial t^2} \tag{3.38}$$

The position $z_n(t)$ is zero at the nozzle exit and $-L_n$ at the entrance of the nozzle.

The capillary pressure, see equation 3.31, is another driving force behind the refill of the nozzle. This pressure will drive the meniscus surface to its equilibrium

position. Assuming a Poiseuille flow profile, equation 3.32, we get the Washburn equation for the meniscus position:

$$\frac{\partial z_n(t)}{\partial t} = \frac{\gamma R_n cos\theta}{4\eta(L_n + z_n(t))} \tag{3.39}$$

with R_n the nozzle radius. Both equations are used to calculated the meniscus position. The nozzle pressure from the narrow channel model is the input for these calculations. In figure 3.21a the meniscus position is shown for different channel lengths and nozzle areas. The refill mechanism from the asymmetric acceleration of the variable mass of ink inside the nozzle results in an overfilling of the nozzle, which disappears slowly after the pressure waves are faded away.

The overfilling disappears more quickly with short channels, because the pressure waves are damped out on a shorter time scale. With a smaller nozzle area there is less overfilling. Because of the increased damping, as we will see in the next section, there are less ongoing pressure waves to overfill the nozzle through the variable mass effect.

In figure 3.21b a top-view of a firing nozzle at a repetition rate of 10 kHz (cycle time of 100 μs) is shown, showing the overfilled nozzle. A accurate quantitative measurement of the amount of overfilling is not possible.

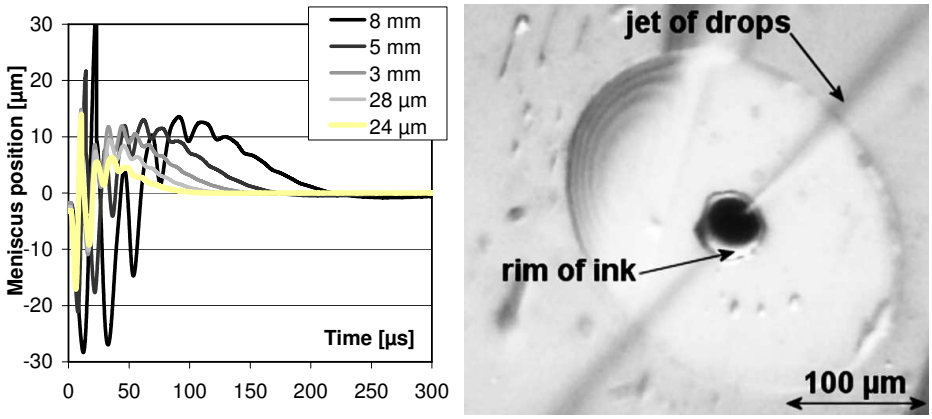

(a) (b)

Figure 3.21: (a) The calculated meniscus position as function of time for a channel length of 8, 5 and 3 mm and a nozzle with a diameter of 32 μm in a 50 μ nozzle plate. The 3 mm channel length is also calculated with 28 μm and 24 μm nozzles. (b) Top-view of a firing 32 μm nozzle at a cycle time of 100 μs with an 8 mm channel. The overfilling results in a rim of ink, accumulated around the nozzle opening (b).

The overfilling results in larger and faster drops if the next drops are fired before the meniscus has reached its equilibrium position. This is shown in figure

3.22. With a 8 mm long channel and a 32 μm nozzle, the drop size increases with 7 pl from 27.5 to 34.5 pl and the drop speed increases by about 1 m/s. The narrow channel model predicts no refill, since the nozzle is assumed to be completely filled at all times. The refill model predicts the global trend very well. The drop properties are calculated with the energy balance as postprocessing of the narrow gap calculations, with the nozzle length adapted to the position according to the calculations with the refill model.

At a cycle time of about 200 μs, the measured drop speed is almost 0.5 m/s slower. The refill model does not predict this minimum in drop speed at 200 μs. The minimum is related to the shape of the meniscus surface as we will see in section 4.1.2. In the refill model only the average position of the meniscus surface is taken into account.

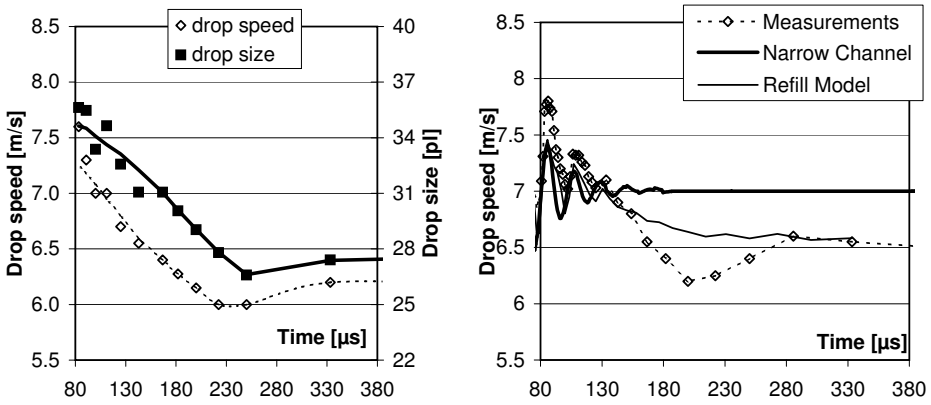

(a) (b)

Figure 3.22: (a) Measured drop size and drop speed as function of the cycle time (the time between consecutive drops), for a 8 mm long channel and a nozzle with a diameter of 32 μm. Because of overfilling, the drop size increases by 7 pl and the drop speed increases by 1 m/s at a short cycle time. (b) The measured and calculated resulting drop speed for an 8 mm channel with a 32 μm nozzle as function of the cycle time. The narrow channel predicts no refill at all and the refill model predicts the major trend well.

3.4.2 Drop on demand frequency oscillations

The gradual change in drop size and drop speed at a time interval of $100 - 400$ μs between consecutive drop is related to the meniscus position as shown in the previous section. Another effect appears when the next droplet is fired before the acoustic pressure waves have come to rest. In figure 3.8 we can see that this takes about 100 μs for a 8 mm long channel. The next drop formation cycle will then start with a non-zero velocity of the meniscus surface. Depending on whether

the residual movement of the meniscus is in-phase or out-of-phase with the next drop formation cycle, the drop speed of the next droplet will be higher or lower, respectively. This results in an oscillation in drop speed and drop size at a time scale below 100 μs. This can also be seen in figure 3.22, but it is better shown in figure 3.23a. In this figure, the drop speed is shown as a function of the repetition rate for a 8 mm long pressure channel.

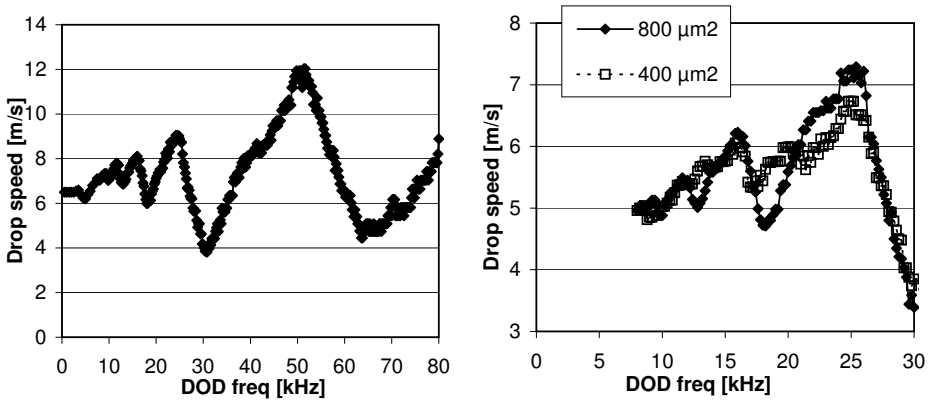

(a) (b)

Figure 3.23: (a) Measured drop speed as function of the drop repetition (drop on demand (DOD) frequency). The largest peak corresponds to the channel resonance frequency. The pressure channel length is 8 mm with a cross-section of $240x100$ μm^2 and covered with a 25 μm ploy-imide foil. The nozzle diameter is 32 μm in a 50 μm thick electroformed nickel nozzle plate. (b) The impact of a smaller nozzle area, showing smaller amplitudes in the oscillation because of increased damping from the viscous dissipation in the nozzle.

The frequency at which the drop speed reaches the highest value corresponds to the channel resonance frequency. The other peaks are found at fractions ($\frac{1}{n}$, $n = 1, 2, 3...$) of the resonance frequency, corresponding to a time period between the consecutive drops of n resonance periods respectively. The channel resonance frequency scales with the channel length as shown in figure 3.4a and is almost 50 kHz for this 8 mm pressure channel geometry.

The amplitude of the oscillations is mainly determined by the amount of damping in the channel acoustics. The most important contribution to the damping is the viscous dissipation in the nozzle, when a pressure wave reflects at the nozzle side. Traveling through the channels gives only a minor contribution because the speed of the ink in the large channel cross-section is much lower than the speed in the small nozzle cross-section. Therefore, the nozzle area and the nozzle length have a large impact on damping, thus on the amplitude of the oscillations in drop speed. In figure 3.23b the impact of a smaller nozzle area is shown. The amplitude of the oscillation in the drop speed at a frequency of 25 kHz is 2.5 m/s with the

large nozzle area and 1.5 m/s with the small nozzle area.

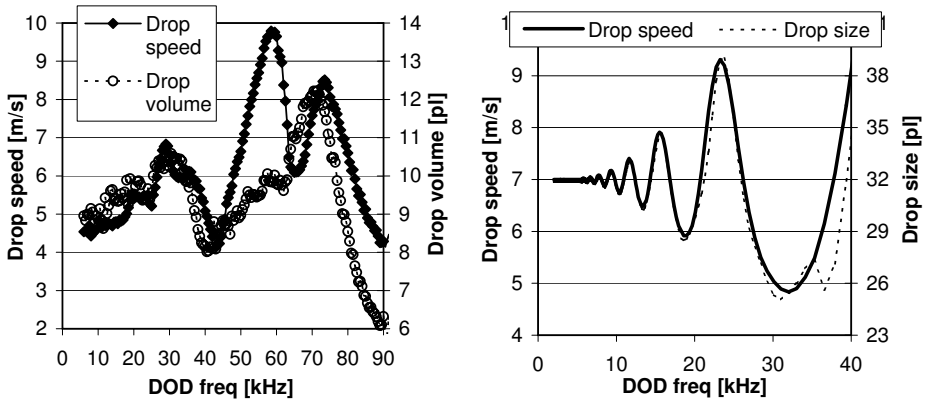

(a) (b)

Figure 3.24: (a) Measured drop speed and drop volume as function of the drop repetition or drop on demand (DOD) frequency. The pressure channel length is 4.5 mm with a cross-section of 200x140 μm^2 and covered with a 15 μm ploy-imide foil. The pressure channel is connected via a 1 mm connection channel to a nozzle with a diameter of 24 μm in a 50 μm thick electroformed nickel nozzle plate. The drop volume shows another dependency on frequency, which is not predicted by the narrow channel model and energy balance of the drop formation, the results of which are depicted in figure (b).

The drop size shows another dependence on the drop repetition rate. In figure 3.24a, the dependence of drop speed and drop volume is shown for a 4.5 mm pressure channel with a cross-section of 200x140 μm^2 covered with a 15 μm poly-imide foil. The nozzle has a diameter of 24 μm. The drop speed shows two large peaks at 60 and 75 kHz, whereas the drop volume only has one peak at 72 kHz. So apparently the drop formation process itself is also affected. For the modeling of this effect we have to resolve the complete fluid dynamic behavior like the drop formation process itself as is done in the next chapter. The narrow channel model with the energy balance for a first order approximation of the resulting drop properties gives an identical dependence for the drop speed and the drop volume as shown in figure 3.24b. Only a meniscus speed effect is then taken into account and the model shows a more harmonic shape of the peaks. The measurements show a more asymmetric and triangular shape of the peaks in the drop speed.

3.4.3 Interaction with local cross-talk

The impact of residual vibrations on the drop properties is also influenced by local cross-talk effects. In figure 3.25a the drop speed as function of drop repetition rate is shown for a single channel and for the same channel when many other channels

are firing simultaneously. If many channels are firing simultaneously, the peaks are shifted by 5 kHz to lower frequencies. This is a direct consequence of the larger compliance when the neighboring channels are also actuated, as reflected by equation 3.36. The larger compliance results in a lower effective speed of sound as given by equation 3.27.

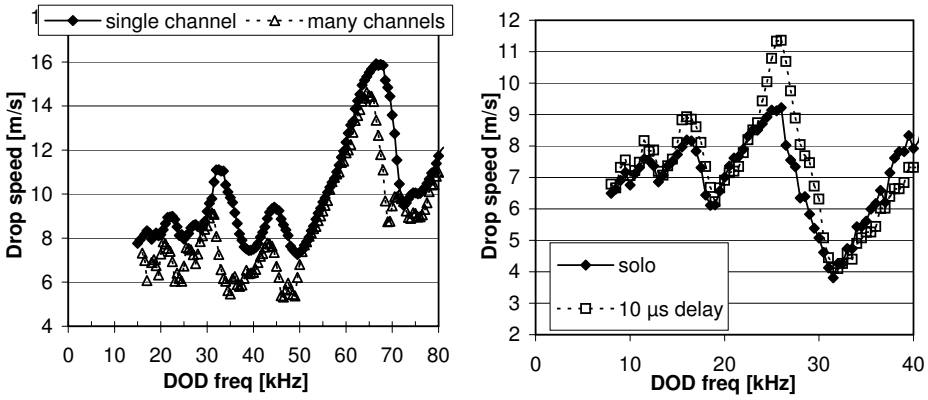

(a) (b)

Figure 3.25: (a) The measured drop speed as function of the drop repetition rate for a single channel and the same channel with many channels firing simultaneously. The peaks are shifted by about 5 kHz to lower frequencies because of the increased compliance when many channels are actuated. (b) The measured effect of one neighboring channel fired at a delay time corresponding to one fourth of the channel resonance period. This eliminates the effect of local cross-talk at low drop repetition rates. However, residual vibrations and local cross-talk do influence each other, which still can give large differences in drop speed at high drop repetition rates.

With only one neighboring channel firing, with a time delay corresponding with one fourth of the channel resonance period, the effect of local cross-talk can be eliminated as described in section 3.3.1. There should be no difference between a single channel and the same channel with the neighbor also firing. However, the residual vibrations and local cross-talk do influence each other. This results in a large difference of 2 m/s in drop speed at 25 kHz between a single channel and the same channel with the neighbor firing as well. The channel length is 8 mm and the nozzle has a diameter of 32 μm, A similar effect is described by Spectra for their printheads [50].

3.5 Concluding remarks

In chapter 2 is descried how an electric voltage results in a deformation of the ink channels. The deformation of the channels results in pressure waves, which is the subject of chapter 3. The traveling wave principle is used as an efficient acoustic mechanism to generate the required pressure for the drop formation process. Many effects play a role. The compliance of the channel cross-section influences the effective speed of sound of the traveling pressure waves. The acoustic impedance of the nozzle must match with the acoustic impedance of the channel. A thin foil, which results in a high compliance of the ink supply, eliminates the acoustic cross-talk. Local cross-talk and resonances in the printhead structure result in variations of the pressure waves. The residual vibrations and the variable mass of ink in the nozzle result in a strong refill mechanism. However, the residual vibrations have an influence on the drop properties at high drop repetition rates. The variations of the drop properties can become large when the residual vibrations interfere with local cross-talk effects. The parameters that determine the resulting drop size are presented. The drop formation process itself is the subject of the next chapter. The pressure at the entrance of the nozzle, as determined in this chapter, is the link to the next chapter.

Chapter 4

Drop dynamics

In this chapter, the flow phenomena outside the ink channel are discussed. The free surface flow, resulting in drop formation, is the ultimate goal of the inkjet process. The dynamics of the drop formation process and their impact on channel acoustics will be discussed. The details of the tail break-off, which lead to the drop formation, show the formation of long tails and secondary tails with a large impact of ink properties as viscosity and surface tension. Surface tension is the driving force behind most of the phenomena encountered in this chapter. The disturbing satellite drop formation mechanisms are discussed i.e. the mist of droplets from the secondary tail, the satellite drops from the Rayleigh break-up of the long tails, the fast satellite drop from a supercritical acceleration, and the slow satellite drops from a bad distribution of mass. Finally, an important application is shown, the drop size modulation. Eight mechanisms for drop size modulation will be identified at the end of this chapter.

4.1 Drop formation

4.1.1 Drop shape and properties

The traveling wave principle to generate drops is discussed in the previous chapter. First a negative acoustic pressure is generated, which retracts the meniscus, see figure 3.8. This action is also known as the fill-before-fire action. Another description found in literature is pull-push action [119, 149], which refers directly to the movement of the meniscus surface. The negative pressure wave from the first rise time of the driving pulse retracts the meniscus, the pull action, and ink is attracted from the reservoir, the fill action. The negative pressure wave reflects at the reservoir and becomes positive. The de-charging of the piezo element amplifies the positive pressure wave, section 3.1.3. The resulting large positive pressure peak drives the drop formation, which is the push or fire action. With a 8 mm long channel the fill-before-fire action takes $15 - 20$ μs. This time period corresponds to the total travel time of this pressure wave.

After $15 - 20\ \mu s$ the head of the drop appears outside the nozzle with a high speed. This can be seen in figure 4.1, where the measured drop formation is shown for an 8 mm long channel. The speed of the head when the ink is just coming outside the nozzle is the same as the meniscus speed, which is then at its maximum speed of 20 m/s. The head of the drop drags a long tail along. This slows down the head of the drop to the final drop speed of 7 m/s. The tail breaks off after $55 - 60\ \mu s$ resulting in a several hundred micrometers long tail. The drop size in this case is 32 pl.

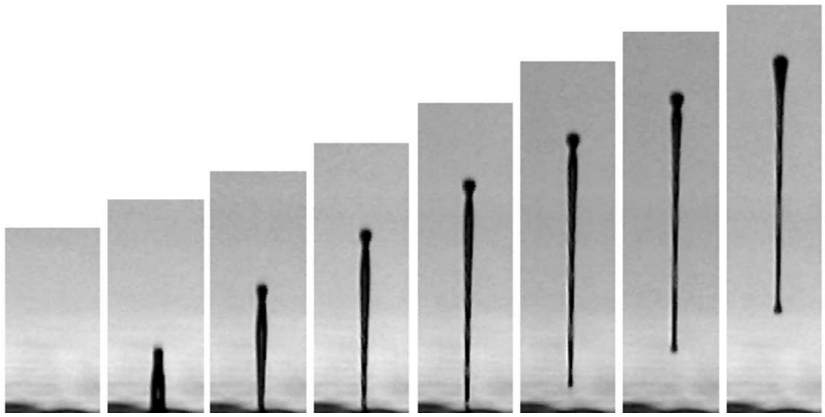

Figure 4.1: Measured drop formation at 10, 20 . . . 80 μs after the start of the actuation. The channel is 8 mm long channel and the nozzle has a diameter of 32 μm. The drop drags a long tail along, which slows down the speed of the head from the initial maximum meniscus speed of 20 m/s to a final drop speed of 7 m/s.

To model the details of the drop formation process we use the volume of fluid (VOF) method [76] as implemented in the commercial code Flow3D(R) [164]. The core of the Flow3D code solves the continuity and the momentum equations and uses an extra variable, which specifies the fraction of fluid within the elements. The code uses a structured Eulerian grid and a finite difference discretization method. The Reynolds transport theorem is used to transfer the equations from the Lagrangian approach by control mass (the mesh coupled to the particles like in the finite element code Ansys) to the control volume field approach.

To reduce the CPU time we use a 2D rotational symmetric model with symmetry on the nozzle axis. So we only consider perpendicular firing jets. The model is restricted to a single nozzle with the last 300 μm of the connection channel. The channel pressure at the beginning of the last 300 μm of the channel serve as one-way coupling between the acoustic modeling and the modeling of the drop formation. The pressure is calculated with the narrow channel model or the Ansys acoustic models, chapter 3. The space outside the nozzle is treated as a void. The only interaction of the ink with the surrounding air is the surface tension of

the ink. With a speed of sound of the ink of 1250 m/s, the wavelengths of the acoustic waves for frequencies less than 1 MHz is more than 1 mm, much more than the spatial dimensions involved, so the flow is treated as incompressible. At the channel and nozzle walls the no-slip condition is used.

In Flow3D, typically 10 grid cells are required for an accurate simulation of the spatial details. The nozzle diameters vary from 18 μ to 50 μm, but the smallest spatial dimensions result from the fluid flow itself. The viscous length scale L_γ is the characteristic length scale of the internal flow properties [52]:

$$L_\eta = \frac{\eta^2}{\rho\gamma} \tag{4.1}$$

with γ the surface tension, η the viscosity, and ρ the density. For the transparent test ink, the viscous length scale is only 3 μm. To capture the internal flow properties with Flow3D simulations a grid size of 0.3 μm is required.

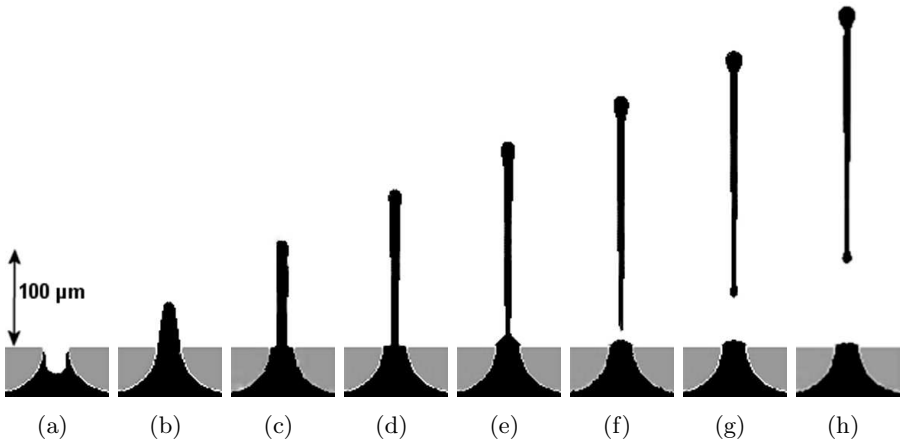

Figure 4.2: Calculated drop formation at 10, 20 . . . 80 μs after the start of the actuation. The channel length is 8 mm and the nozzle diameter 32 μm. The calculated drop formation correlates well with the measured drop formation. Now also information on the retracted meniscus and the internal distribution of ink speed is available.

This grid resolution results in typical $10^5 - 10^6$ elements and the CPU time for one drop formation cycle is of the order of several hours on a dual core 64 bits platform. The calculated drop formation for an 8 mm long channel, figure 4.2, looks identical to the measured drop formation, figure 4.1. The correlation is also good for multiple drop formation cycles at a high repetition rate. In [85] we show an example at a repetition rate of 20 kHz.

The simulations also provide information on the retracted meniscus and the internal flow properties, like the distribution of the velocity. Also the overfilling just

after one drop formation cycle is visible. For a comparison with an experimental recording of the overfilled meniscus shape see figure 3.21b in section 3.4.1.

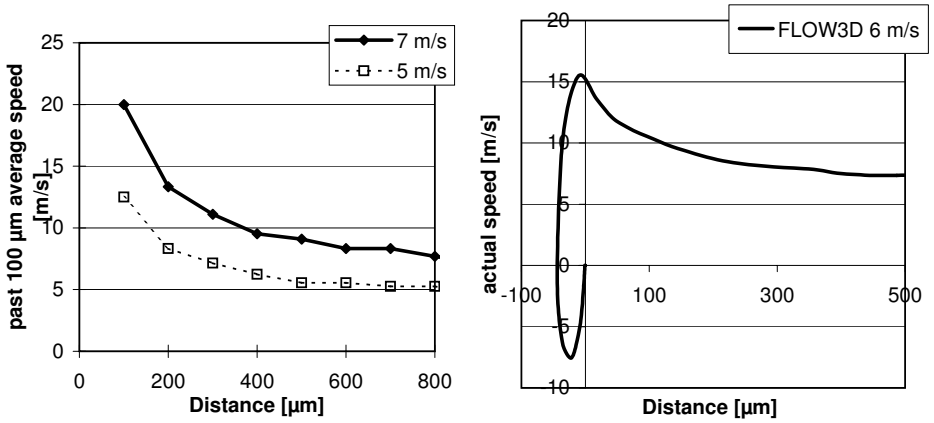

(a) (b)

Figure 4.3: (a) The measured speed of the head of the drop as function of the distance to the nozzle with a final drop speed of 5 m/s and 7 m/s. The values are averaged over a distance of 100 μm. (b) The calculated speed of the head of the drop as function of the distance to the nozzle for a final drop speed of 6 m/s. The speed of the head is at its maximum 2 to 3 times higher than the final drop speed. The calculations show also that the meniscus retracts almost 50 μm with a maximum speed of -7 m/s.

The speed of the head of the drop is important for the dot positioning. Not only the final drop speed, but the variation of the drop speed as a function of the distance to the nozzle is important, since this will determine the total time of flight of the drop. The measured speed of the head of the drop as a function of the distance to the nozzle with a final drop speed of 5 and 7 m/s is given in figure 4.3a. In figure 4.3b the calculated results are depicted for a final drop speed of 6 m/s.

The speed of the drop varies gradually. The high frequency components in the pressure signal are smoothed out. Only frequency components of the pressure signal lower than 200 kHz have an influence on the drop formation process. The speed at the beginning of the drop formation is 2 to 3 times higher than the final drop speed. The lowering of the speed of the head is mainly caused by the drag from the tail and by the flow of ink from the tail to the head. The tail itself is moving with a lower speed of about 6 m/s, see also section 4.2.3. When ink from the tail flows to the head of the drop, the head will slow down.

During the fill-before-fire action, the meniscus surface moves 47 μm inwards with a maximum speed of -7 m/s. The meniscus retraction, which takes $15 - 20$ μs, also contributes to the total time of flight i.e. the time required to reach a

certain distance. The time of flight for a distance of 1 mm with a final drop speed of 6 m/s is 150 μs and varies with 50 μs per m/s drop speed. In many applications the printhead moves with a speed of typical 1 m/s with respect to the substrate. Therefore, a variation in drop speed of 1 m/s results in a dot positioning error of 50 μm. Compare this with the dot size of 42 μm in 600dpi prints, a common print resolution in high quality document printing. So the variations in the drop speed must be much smaller than 1 m/s to have good dot positioning.

4.1.2 Impact on acoustics

The mass of ink in the nozzle has a direct impact on the acoustic properties. More ink in the nozzle results in a higher acoustic impedance of the nozzle. The reflection of the acoustic pressure waves will change towards a reflection at a closed end. The refill, as described in section 3.4.1, and of course the drop formation itself, will change the amount of ink. The impact on the acoustic properties is not included in the acoustic modeling used in chapter 3. With the acoustic modeling the nozzle is completely filled all the time. There is only an one-way coupling to the models, which calculate the resulting drop properties.

To model the effect of refill and the drop formation on the acoustic properties, an acoustic model is also developed in Flow3D. This model includes the average position, which determines the refill, the movement, which determines the effect of residual vibrations, and the shape of the meniscus surface.

The pressure channel, the connection channel and the nozzle are a part of the acoustic Flow3D model, see figure 4.4. A 2D rotational symmetric model is not possible. The keep the number of grid elements in the 3D model within reasonable limits, the grid size is taken as large as possible. In the nozzle the minimum grid element size is taken 0.1 times the nozzle diameter, which results in a lower grid size limit of 3 μm. This is enough to describe the shape of the meniscus surface in the nozzle and the resulting drop outside the nozzle, with an accuracy of about 10 % of the actual volume displacements. The grid resolution is not fine enough to capture the details of the complete drop formation process. Therefore the drop formation has to be calculated again with the drop formation model, but the two-way coupling, i.e. the impact of the flow phenomena in the nozzle on the acoustic properties of the channel, are now incorporated in the pressure signal.

The upper grid size limit is set to 0.1 times the minimum channel length. With a 1 mm connection channel this results in an upper grid element size of 100 μm. The pressure channel, connection channel and the nozzle are put in one line with a symmetry plane in the middle. Now only one half of the geometry has to be modeled.

The acoustic pressure waves are simulated in the Flow3D model by adding an extra equation to the continuity and momentum equations. This equation is based on the adiabatic modulus of a fluid, see also equation 3.8:

$$\frac{\partial \rho}{\partial t} = \frac{1}{c^2} \frac{\partial p}{\partial t} \tag{4.2}$$

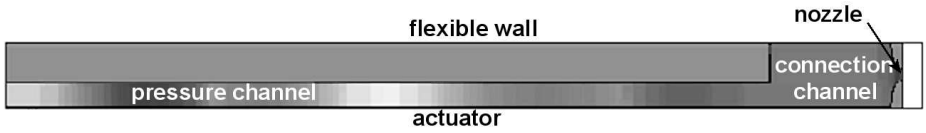

(a)

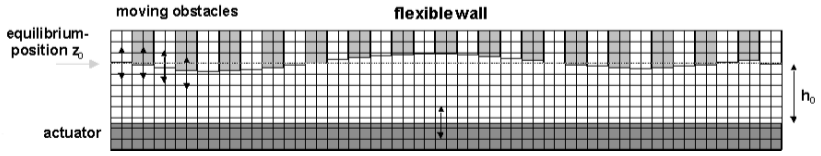

(b)

Figure 4.4: The acoustic Flow3D model. (a) From left to right the $3-8$ mm long pressure channel, the 1 mm long connection channel, and the nozzle. The amplitude of the pressure wave in the channel is visible as a variation in the grey scale. (b) The pressure channel, with a moving lower wall as actuator and a flexible upper wall. The compliance β of the channel cross-section is taken into account through locally pressure dependent adjustments op the upper wall segment positions. Actuation is done with a movement of the lower wall according to the driving voltage and actuation efficiency α.

The acoustic waves are generated with a moving wall, the lower wall in figure 4.4. This wall is the actuator in this model, which moves according to the shape of the driving waveform, with driving amplitude V:

$$\frac{z-z_0}{h_0} = \alpha V \tag{4.3}$$

with h_0 the height of the channel and z_0 the position of the lower wall without actuation. The actuation efficiency α is defined in section 3.1.1, equation 3.21.

The compliance of the channel cross-section has a very large impact on channel acoustics however, see section 3.1.3. However, the Flow3D code cannot handle physical properties of solids such as wall flexibility. In order to incorporate wall flexibility, a user routine is written for the Flow3D model, which applies a moving wall boundary condition to the upper pressure channel wall. This routine moves the upper wall to its new equilibrium position z:

$$\frac{z-z_0}{h_0} = \beta p \tag{4.4}$$

with z_0 the position at ambient pressure and β the compliance of the channel. To enable a local pressure dependent deformation of the upper wall, this wall is divided into segments of $100-200$ μm length. On each segment the moving boundary condition is applied independently.

Instead of moving the upper wall within one time step to the position corresponding to the pressure and channel compliance, the movement is spread over several time steps. Like with the acoustic models in the finite element code Ansys, see section 3.1.3, a relaxation time τ is therefore introduced as:

$$\frac{\partial z}{\partial t} = \frac{\beta p h_0 - z_0}{\tau} \tag{4.5}$$

The limited speed of the upper channel wall results in a change in channel cross-section dA according to:

$$dA = \left(\frac{t/\tau}{1 + t/\tau} \right) dA_{stat} \tag{4.6}$$

This equation gives with a value of $\tau = 0.1\ \mu s$ a comparable change of the channel cross-section as the exponential relation 3.28 used in the Ansys acoustic models with $0.15\ \mu s$. These values give the best fit for the dynamic behavior of the printhead structure, see section 3.1.3.

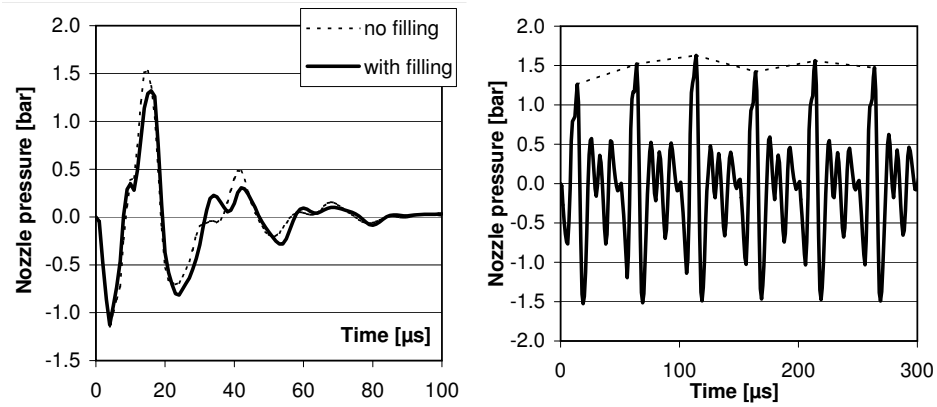

(a) (b)

Figure 4.5: The calculated pressure at the entrance of a nozzle with a diameter of 28 μm in a 50 μm electroformed nickel nozzle plate with a 6.7 mm long pressure channel. (a) The effect of the variable filling of the nozzle during one drop formation cycle. The variable filling results in a lower positive pressure peak. (b) The effect of the overfilling of the nozzle during the first six drop formation cycles at a repetition rate of 20 kHz. The pressure amplitude increases with 20%.

In figure 4.5a the effect of the variable filling of the nozzle is shown. The pressure at the entrance of the nozzle is calculated during one drop formation cycle. The curve without the filling effect is calculated with a small amplitude of the driving waveform, so the nozzle remained almost completely filled all the time. In a postprocessing step, the resulting pressure is multiplied with the same ratio. Now we compare it with the pressure resulting from a normal actuation.

The first negative pressure peak remains the same, because the meniscus surface is at rest when the first negative pressure wave reaches the nozzle. The first positive pressure peak gets a lower amplitude, because the meniscus is retracted when the positive pressure wave reaches the nozzle. The smaller mass of ink results in a more open reflection of this pressure wave, thus in a lower pressure amplitude. When the second negative pressure wave reaches the nozzle, the meniscus is moved outside the nozzle. The larger mass of ink results in a more closed reflection of this pressure wave, so the next negative pressure peak becomes larger. The asymmetric reflection of the pressure waves is the main cause for the non-harmonic shape of the peaks in the measured curves of drop speed versus repetition rate in section 3.4.2.

Just after one drop formation cycle the nozzle will be overfilled. The effect of the larger mass of ink in the nozzle is shown in figure 4.5b. The amplitude of the pressure at the entrance of the nozzle increases 20 % during the first drop formation cycles at a repetition rate of 20 kHz. This would result in an increase in drop speed of 2 m/s, see section 3.2.2. However, the larger amount of ink results also in a higher resistance against the movement, mainly because of inertia. The net increase in drop speed, which remains, is about 1 m/s, in agreement with the measured refill effect shown in section 3.4.1.

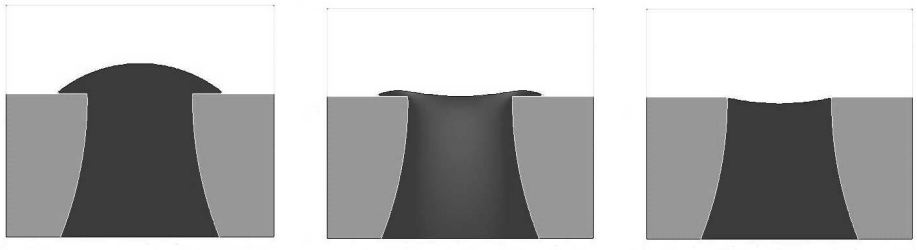

(a) $t = 100 - 150\ \mu s$ (b) $t = 150 - 250\ \mu s$ (c) $t > 250\ \mu s$

Figure 4.6: The calculated shape of the meniscus, after the pressure waves have come to rest. Only the last 30 μm of the nozzle shape is shown. The nozzle plate is 100 μm thick. (a) The shape at 100-150 μs after start of the last actuation cycle. (b) The shape during the transition from overfilling towards the equilibrium position at 150-250 μs. (c) The shape of the equilibrium position after 250 μs. The shape of the free surface during the transition from overfilling to equilibrium results in a minimum drop speed at a repetition rate of 5 kHz.

With an 8 mm long pressure channel it takes 100 μs before the pressure waves are faded away. At repetition rates higher than 10 kHz, the ongoing movement of the ink in the nozzle results in oscillations in the drop speed, see section 3.4.2. Just after the pressure waves are faded away, the meniscus protrudes outside the nozzle plate surface because of the overfilling of the nozzle, as shown in figure 4.6a. A good quantitative measurement is not available, but in figure 3.21b the rim of

ink around the nozzle during the drop formation at 10 kHz is clearly visible. The equilibrium shape, figure 4.6c, is bent inwards because of the static pressure of 8 $mbar$ below the ambient pressure to prevent leakage of ink.

Before the meniscus returns to its equilibrium position, the surface in the center of the nozzle is already almost at this position while there is still a considerable amount of ink accumulated as a rim around the nozzle opening, figure 4.6b. In the transition phase, the pressure waves are almost normal again, because the pressure waves are reflected mainly at the mass of ink inside the nozzle. There is no larger pressure amplitude anymore, but the extra amount of ink around the nozzle opening results in an increased resistance for the drop formation process. This causes the minimum in the drop speed as shown in figure 3.22. So not only the average position of the meniscus has influence, but also the shape of the meniscus.

4.2 Break-off mechanism

4.2.1 Impact of ink properties

A drop is formed when the tail pinches off from the meniscus in the nozzle. Tail properties and pinch-off are mainly determined by ink properties, such as surface tension, density and viscosity. Surface tension is the driving force behind pinch-off and viscosity is the most important parameter for the characteristic length scale of the internal flow phenomena in the fluid. The shape of the tail is affected by the viscosity of the ink, and not by the shape of the driving waveform or the channel and nozzle geometries [52]. Highly viscous inks show long symmetric tail shapes with the minimum neck radius somewhere in the middle of the tail, moderately viscous inks show long asymmetric tail shapes with the minimum neck radius close to the meniscus or head of the drop, and low viscous inks show only short tails.

Pinch-off will occur at the position with the largest curvature because at this position the capillary pressure is the largest. One principle radius of curvature corresponds to the radius of the tail, which remains almost constant over the length of the tail. The tail itself has a conical shape with a very large second principle radius of curvature. The capillary pressure is relative low in this part of the tail. The second principle radius of curvature becomes also small at the transitions of the tail to the meniscus or to the head of the drop. There is a large curvature at the transition to the head of the drop and at the transition to the meniscus in the nozzle. The capillary pressure will be the largest at these two positions. With drop-on-demand inkjet the radius of the head of the drop is smaller than the nozzle radius, thus the largest curvature is at the transition to the meniscus in the nozzle. Pinch-off will occur at the meniscus, as shown in figures 4.1 and 4.2. With a large drop falling from a faucet or drops forming from a jet, like in continuous inkjet, the largest curvature is at the transition from the tail to the head of the drops. Pinch-off will occur at the head of the drops in these cases [176].

The pinch-off time shifts with channel length: 45 μs (52 μs, 59 μs) for heads with channel length of 3 mm (5 mm, 8 mm). With these channel lengths the head

of the drop appears at 9 μs (12 μs, 16 μs) after the start of the actuation. This means that at drop repetition rates above 28 kHz (25 kHz, 23 kHz), respectively, the next drop appears before the tail of the previous drop has been pinched off. At slightly higher repetition rates, the tail of the previous drop will be captured by the next drop as shown in figure 4.7. The point of largest curvature is no longer at the meniscus, but at one of the heads of the two consecutive drops, like in continuous inkjet. The head of the first drop is larger, because ink flows from the tail to the head of the drops. The curvature will be larger at the head of the first drop and the tail now breaks off from the head of the first drop.

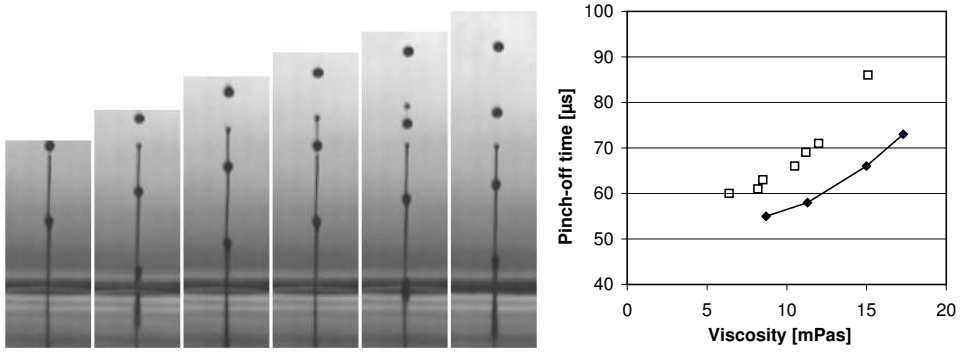

(a) (b)

Figure 4.7: (a) Measured drop formation at a drop repetition rate of 28 kHz with a 8 mm long channel showing the capturing of the tail by the next drop. The ink viscosity is 10 $mPas$ and the surface tension is 22 mN/m. (b) Measured influence of ink viscosity and surface tension on pinch-off-time. The black markers are for inks with $\gamma = 35\ mN/m$ and the open markers for inks with $\gamma = 22\ mN/m$. Pinch-off time is longer with a higher viscosity or a lower surface tension of the ink.

The driving waveform, the channel cross-sectional geometry, and the nozzle geometry have no influence on the pinch-off time. Ink properties such as viscosity and surface tension do have an influence. This influence can be described by means of the characteristic time scales of the fluid flow i.e. the capillary and viscous time scales t_γ and t_η:

$$t_\gamma = \sqrt{\frac{\rho L^3}{\gamma}} \qquad t_\eta = \frac{\rho L^2}{\eta} \tag{4.7}$$

At tail break-off the characteristic length is determined by the viscous length scale L_η [52], see equation 4.1. With $L = L_\eta$, both time scales of the fluid flow are equal:

$$t_\gamma = t_\eta = \frac{\eta^3}{\rho\gamma^2} \tag{4.8}$$

With the transparent test ink, the characteristic time scale at break-off is typically

1 μs. A higher viscosity or a lower surface tension will result in a longer characteristic time scale and pinch-off time will be longer, as shown in figure 4.7 for a range of modified inks. In this example, the characteristic time scale increases from 0.5 μs to 4.5 μs with the high surface tension inks and from 0.5 μs to 7 μs for the low surface tension inks.

4.2.2 Secondary tail

At pinch-off, a secondary tail is formed [165], see figure 4.8. The diameter of the secondary tail is about 1 μm, which is close to the optical resolution of the measurement setup. The secondary tail is visible during 5-10 μs between the main tail and the meniscus in the nozzle. The small secondary tail first breaks off at the meniscus and then at the end of the main tail. The small secondary is generated because ink cannot flow from the main tail into the secondary tail, which has a radius much smaller than the viscous length scale [94].

To capture the formation of the secondary tail with Flow3D calculations, a very small grid size is necessary. The secondary tail has a width smaller than the viscous length scale. A grid size of 0.1 μm is necessary to capture the formation of the secondary tail. The correlation with the measurements is good. However, the CPU time is very large, because of the large amount of grid cells and the very small time steps required to resolve the motion of liquid through a 0.1 μm grid. The formation of a secondary tail is also reported for large drops dripping from a faucet [94], but in that case the secondary tail is visible between the tail and the head of the drop. Also in the reference the diameter of the secondary tail is about 1 μm. It is not known which mechanisms are determining this value. Any influence of the surrounding air can be ruled out for tail diameters larger than 0.05 μm [103].

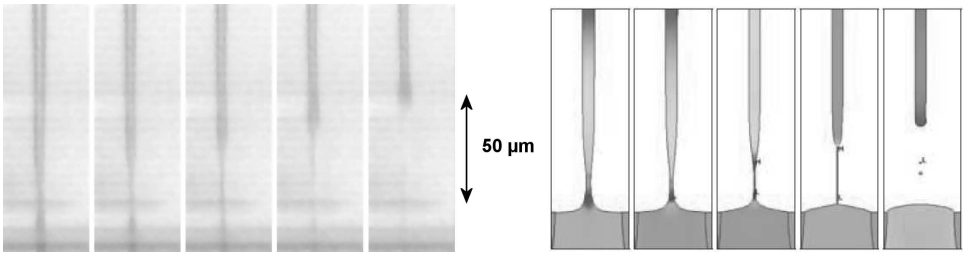

(a) (b)

Figure 4.8: Measured and calculated formation of a secondary tail at 56 μs, 58 μs, 60 μs, 62 μs, and 64 μs after the start of the actuation of a 8 mm long pressure channel. The grey scale range light-dark indicate a velocity range of $0 - 6$ m/s.

At tail break-up for a large drop falling from a faucet sometimes even a cascade of structures can be seen as described in [141]. The flow regime determines what kind of drop formation is observed. From low to high flow rates the drop

formation regimes are: dripping drops, drops on demand, continuous drops and atomization. The cascade of structures with dripping drops can be characterized by the different length scales involved [20, 35]. In our experiments only the formation of a secondary tail is observed.

The thinning of the tail is characterized by three flow-regimes with different dominating forces. In the analysis of the break-off mechanism the minimum tail radius R_{min} is the key number and a power-law relationship is often used [78]:

$$R_{min} = k(t_0 - t)^m \tag{4.9}$$

with t_0 the pinch-off time and k and m constants. When the tail is just formed only viscous forces and surface tension forces play a role like in high viscous flows. A high viscous flow shows a long tail with a minimum radius somewhere in the middle and a low value of the exponent $m \leq 0.5$ in the power-law relationship 4.9. Sometimes even a plateau shows up in the curve of R_{min} versus time [105, 131]. The minimum tail radius decreases slowly.

At some point before break-off inertia will become important at the position of the minimum tail radius. Three forces play a role now [34] and the fluid enters the inertial-viscous flow regime at this position. In the one-dimensional analysis of Eggers [52] the symmetric similarity solution for high viscous flow with $Re = 0$ transients into the asymmetric asymptotic solution for moderate viscosity with $Re = 1$. The relationship for the minimum neck radius becomes in these analysis:

$$R_{min} = 0.0304\frac{L_\eta(t_o - t)}{t_\eta} \tag{4.10}$$

which is also the only experimentally observed relationship by others [21]. The tail radius decreases much faster now, with the exponent $m = 1$ in the power-law relationship 4.9.

The last microseconds before pinch-off, only surface tension forces and inertia are important [130]. The viscous flow regime becomes an inviscid or potential flow regime [125]. The exponent m in the power-law relationship 4.9 can now be derived from the Weber number $We = \rho u^2 R/\gamma$ as non-dimensional grouping of the balance of the two remaining forces. The scaling for the speed u can be derived from the transformation of a sphere with radius R to a cylinder with radius R and length $L = u \cdot t$. Conservation of mass requires both volumes to be equal:

$$\frac{4}{3}\pi R^3 = \pi R^2 u \cdot t \tag{4.11}$$

which results in a scaling for the speed $u = R/t$ [47]. The Weber number with the speed u replaced by R/t becomes:

$$We = \frac{\rho u^2 R}{\gamma} \propto \frac{\rho R^3}{\gamma t^2} \tag{4.12}$$

This results in $m = \frac{2}{3}$ for the exponent in the power-law relationship 4.9. This indicates a slow decrease in tail width. That the inviscid flow regime applies for the

last microseconds before pinch-off is reported be many others. The most striking evidence of an inviscid flow regime is the observation of a double cone structure. The surface with the largest curvature overturns in the potential flow regime, which results in a larger cone-shaped free surface around the smaller cone-shaped tail [47, 51]. This is also reported for viscous liquids [125]. However, this structure is smaller than the optical resolution of our measurement setup. Modeling with Flow3D would require even smaller grid cells than needed to resolve the secondary tail. This is not pursued because of the excessive long calculation time. Only special Navier-Stokes solvers developed for handling very small details can resolve the double cone structure [34].

4.2.3 Tail-end speed

After pinch-off, the end of the tail moves away with a certain speed as predicted by the scaling laws of Eggers. The double cone structure at pinch-off cannot be resolved with the one-dimensional analysis like the one of Eggers [51, 52]. But except for the pinch-off moment itself the one-dimensional modeling is capable of predicting the shape of the tails and even of complete drops. These analysis show the inviscid decline of the minimum tail radius until a singularity occurs [22]. After pinch-off the shape of the tail can also be described by these analysis.

Because the initial tip is very small, the capillary pressure is very high. The end of the tail moves away with a high speed. The tip of the tail becomes larger, thus the capillary pressure becomes lower. The speed of the end of the tail slows down according to the formula [52]:

$$v_{tip} = 3c\frac{\sqrt{t_\eta}}{2\sqrt{t}(1 + t_\eta/L_\eta)} \tag{4.13}$$

with t the time after pinch-off. The constant $c = 17.452$ for the side with the smallest curvature before pinch-off and $c = 0.4476$ for the side with the largest curvature before pinch-off. In our sequence, the end of the tail is first the tip of the secondary tail which pinched-off from the meniscus surface. The end of the tail is the side with the smallest curvature before pinch-off. A few microseconds later the secondary tail breaks off from the main tail. The end of the tail is now the tip of the main tail, which is the side with the largest curvature before pinch-off. Both events, and the resulting speed of the end of the tail as calculated with equation 4.13, are shown in figure 4.9a, together with the results of a Flow3D calculation.

The tail-end moves with the speed of the ink in the nozzle before pinch-off. At $t = 0\ \mu s$ the secondary tail pinches off from the meniscus. The tail-end of the secondary tail accelerates to the speed predicted by equation 4.13 for the side with smallest curvature before pinch-off. At $t = 4\ \mu s$ the main tail pinch off from the secondary tail. The tail-end of the main tail tends to slow down to the speed predicted for the side with largest curvature before pinch-off. After $t = 6\ \mu s$ the end of the tail accelerates again because of the formation of a drop at the tail-end. The speed of the end of the tail averaged over a time period of at least 15 μs,

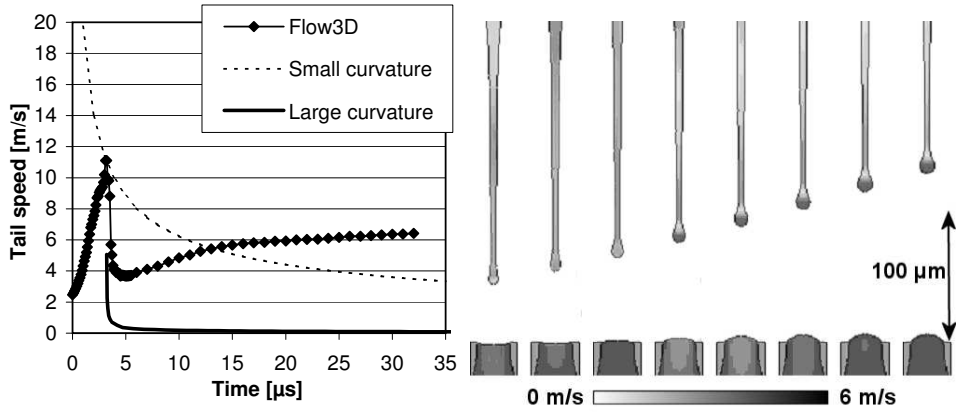

(a) (b)

Figure 4.9: (a) Calculated speed of the end of the tail after pinch-off. The Flow3D results are shown together with the results of Eggers' scaling laws (denoted as "Large curvature" and "Small curvature"). The scaling laws are applied first for the side with the smallest curvature before pinch-off (the secondary tail after 0 μs) and then for the side with largest curvature before pinch-off (the main tail after 4 μs). (b) Flow3D simulation of the formation of a tail-end-drop. The whole sequence of events results in a constant tail-end speed, when averaged over a time period of at least 15 μs.

which corresponds to a distance of 100 μm, becomes constant at about 6 m/s. This is in agreement with the measurements.

This whole sequence is an independent behavior of the end of the tail. As a consequence of this, at higher driving voltage the velocity of the head increases but the tail is not affected at all. This can be seen in figure 4.10, where the position of the end of the tail remains the same while the faster head is moved further away. This is also in agreement with observations by others [105, 131].

This means that with a speed of the head of the drop of more than 6 m/s, very long tails will be formed. With a lower speed of the head, the tail will catch up and this can be seen in the measured speed of the head in figure 4.10c. After 800 μm the tail with the tail-end-drop merges with the head of the drop and increases the speed of the head by more than 1 m/s.

So far the regular drop formation process is described, i.e. the formation of a drop as a result of the actuation of a piezo element. We will look now at the formation of extra drops, which are called satellite drops.

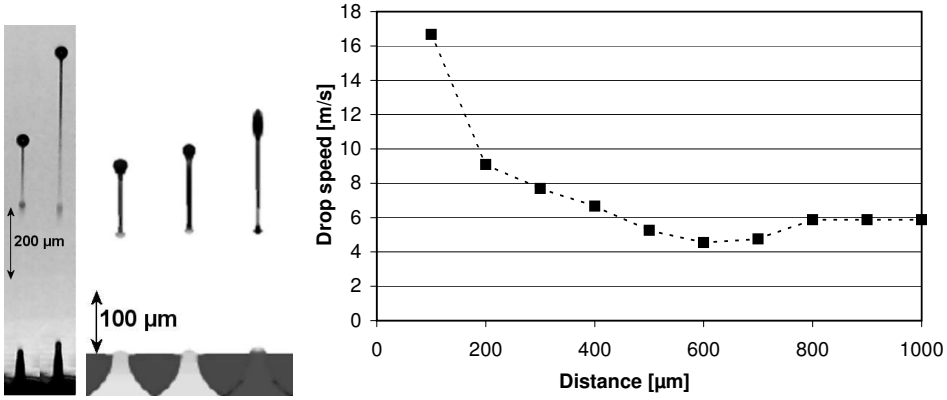

(a) (b) (c)

Figure 4.10: (a) Measured and (b) calculated shape of the drop at the same time after the start of the actuation with different actuation amplitudes. The head of the drop has moved further away at higher driving amplitude because of the higher drop speed. The tail-end remains at the same position, showing the independent behavior of the tail. (c) The measured speed of the head of the drop as function of the distance to the nozzle plate. The tail merges with the head of the drop at a distance of 800 μm. The tail-end has a higher speed than the head of the drop. This results in an increase in the drop speed when the tail-end merges with the head of the drop.

4.3 Satellite drop formation

4.3.1 Mist of droplets

For most applications it is very important that only a single drop is generated. However, occasionally extra drops are generated. These drops are called satellite drops. The first satellite drops are generated from the secondary tail, immediately after pinch-off from the main tail. Droplets of less than 1 pl are formed within 1-2 μs. This can be seen in figure 4.11a-e, where a high speed camera recording is shown with 1 million frames per second.

The micro-droplets are dragged along with the main drop formation, as shown in figure 4.11f-k, with only one of every five frames shown. In the recording of figure 4.11 there are five micro-droplets as indicated with the white boxes in frame (f). These drops are dragged along with the main drop formation. The micro-droplets will result in a mist of droplets around the main drop on the substrate. For graphical printing applications this is no problem because the resulting micro-dots are too small to be visible.

The drag force results from an induced air flow along with continuous jetted

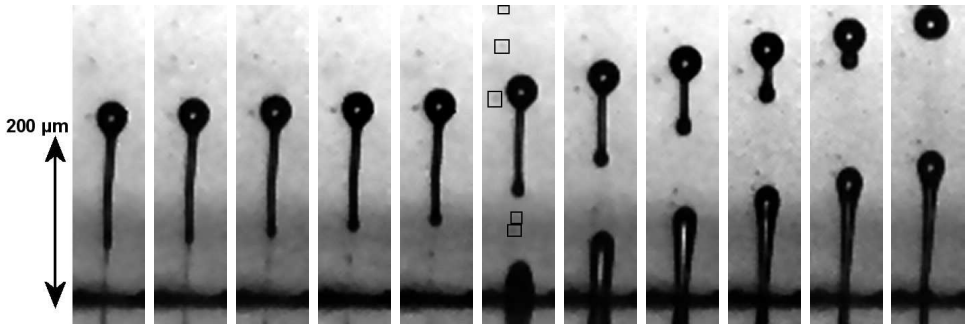

(a)	(b)	(c)	(d)	(e)	(f)	(g)	(h)	(i)	(j)	(k)
$t - t_0 = 1\ \mu s$	$2\ \mu s$	$3\ \mu s$	$4\ \mu s$	$5\ \mu s$	$10\ \mu s$	$15\ \mu s$	$20\ \mu s$	$25\ \mu s$	$30\ \mu s$	$35\ \mu s$

Figure 4.11: The measured generation of micro-droplets from the secondary tail. The frame rate of the Shimadzu HPV-1 camera recording is 1 Mfps. In (a)-(e) every frame is depicted showing the formation of a micro-droplet within 1-2 μs. In (f)-(k) only one of five frames is depicted illustrating that the micro-droplets are dragged along with the main drops. The drop speed is only 3 m/s, so the main tail merges with the head of the drop at 35 μs after pinch-off.

drops [98, 139]. This air flow also influences the drop flight of large drops. In figure 4.12, which is taken from [14], the impact on drops of the same size as the jetted drops is shown. Drops of 32 pl are jetted at a repetition rate of 20 kHz with a drop speed of 7 m/s. These drops transfer momentum to the surrounding air and the air will be accelerated along with the jetted drops. This can de seen in the high speed camera recording with 10.000 frames per second. Two drops of the same size pass by slowly and horizontally. One drop is very close to the jetted drops, it is nearly in focus. The depth of field in this high speed camera recording is only 20 μm. The other drop is out of focus, thus not so close to the jetted drops. Each frame shows two successive jetted drops in vertical direction. The induced air flow drags the drop, which is close to the jetted drops, along with the jetted drops.

The horizontally moving drop which is in focus, is at a distance of at most 20 μm from the jetted drops. From analysis of the captured images we get a maximum acceleration a_d of the horizontally moving drops of about 1000 m/s^2. With Stokes' law for the drag force F_D on a sphere with radius r_d:

$$F_D = 6\pi\eta_a(v_a - v_d)r_d = m_d a_d \tag{4.14}$$

with η_a the viscosity of air (0.02 mPa.s) and v_a and v_d the velocities of the air and the drop with mass m_d, respectively. The resulting air speed is 4 m/s. This is 60 % of the jetted drop velocity of 7 m/s.

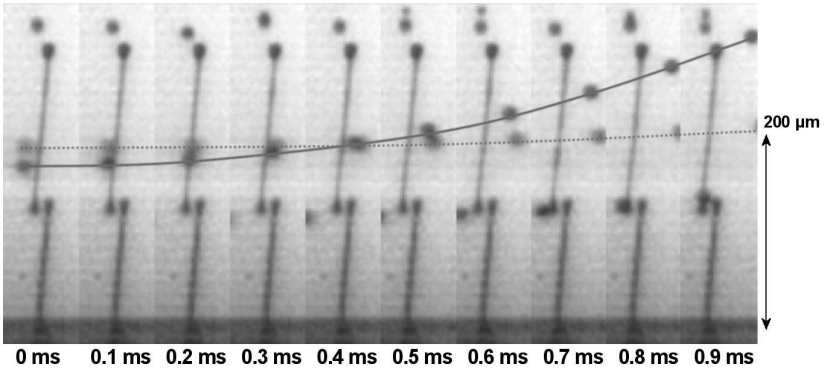

Figure 4.12: The measured drag of horizontally passing drops. The frame rate of the Phantom V7 high speed camera recording is 10 $kfps$. Drops of the same size are jetted continuously. Each frame show two successive jetted drops in vertical direction. This induces an air flow. Based on the limited depth of field it is determined that the drop which comes close to the jetted drops (continuous line) is dragged along more than the drop further away (dashed line). Taken from [14].

4.3.2 Rayleigh breakup

A second satellite drop formation mechanism results from the long tail itself. The end of the tail moves with an averaged speed of 6 m/s, see section 4.2.3. For many applications a high drop speed is required, so long tails will be formed at a drop speed higher than 6 m/s. However, a long tail will not be stable. We take a cylinder with radius R and length L as the tail. This tail will break-up in n drops with radius r with the same volume as a cylinder:

$$n\frac{4}{3}\pi r^3 = \pi R^2 L \tag{4.15}$$

The total surface energy of the n drops becomes smaller than the surface area of the cylinder when:

$$n \cdot 4\pi r^2 < 2\pi RL \tag{4.16}$$

This is the case when the radius r of the drops becomes at least 1.5 times the radius of the cylinder [63]. The total surface energy will be reduced when a cylinder of liquid breaks up into several droplets which have a radius of at least 1.5 times the radius of the cylinder or tail. A liquid column will therefore always breakup at some time into drops with a radius of at least 1.5 times the radius of the column.

The break-up process is initiated by thermal noise. The noise excites surface tension driven capillary waves. The surface tension driven capillary waves have to overcome inertia and viscous forces to break-up the tail in many small droplets. This break-up process is well known as the Rayleigh instability. For inviscid fluids with a one-dimensional analysis of the balance between internal pressure and the

pressure from surface tension and the principal radii of curvature the optimal reduced wave number for Rayleigh instability can be derived [52]:

$$X_R = \frac{2\pi R}{\lambda} = 0.697 \tag{4.17}$$

This results in an optimal wavelength for the Rayleigh instability of about 9R. The radius of the satellite becomes 1.9 times the radius of the tail.

For viscous liquids another expression for the optimal reduced wave number is derived [52]:

$$X_R = \frac{1}{(2 + \sqrt{18}/Re)} \tag{4.18}$$

In our case the Reynolds number, which is based on the nozzle radius, varies between 2 and 20. The optimal wavelength becomes 14R-24R and the radius of the satellite becomes 2.2-2.6 times the radius of the tail. The measured and calculated Rayleigh break-up is shown in figure 4.13.

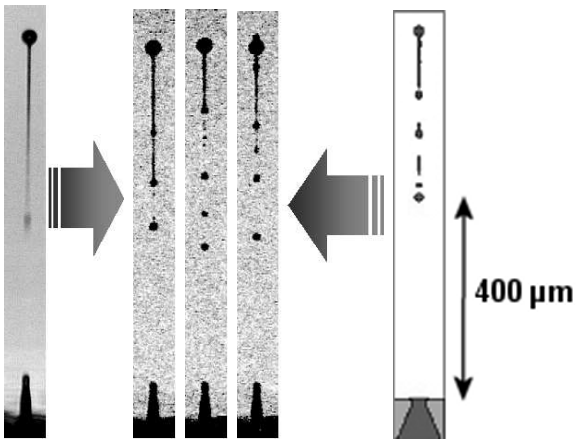

Figure 4.13: The break-up of a long tail. The drop speed is 7 m/s and the tail length about 400 μm. (a) The shape of the drop recorded with a stroboscopic illumination. This recording shows the average of many drops. (b-d) Recording of single drops with 100 ns flashes and the same camera. These recordings show the non-reproducible break-up of the long tail. (e) The calculated shape of the tail, which breaks up in small droplets. The calculation was done with Flow3D for the same geometry. A channel with a length of 8 mm and a nozzle with a diameter of 32 μm.

With the often used stroboscopic illumination at the drop repetition rate the pictures consist of averages of several hundred drops. The CCD camera captures 25 frames per second and the drop repetition rate is $10kHz$. The non-reproducible

break-up process appears now as a smooth tail as shown in figure 4.13a. By recording single drops the real non-reproducible nature of the break-up becomes visible, figure 4.13b-d. The recordings are now made with the stroboscopic illumination at camera frame rate. Another option is to use high-speed camera recordings. The flow3D calculations show a good correlation with the experimental observed breakup, figure 4.13e. The Rayleigh break-up in the calculations is initiated by numerical noise. The real nature of the noise source is not important. The noise only initiates the Rayleigh break-up, and is responsible for the non-reproducible nature of the breakup process.

With visco-elastic fluids, the satellite droplets become even larger [60]. In particle laden fluids such as pigment based inks new break-up modes can be observed [55, 56]. With our transparent Newtonian test inks, these effects do not play a role. In continuous inkjet a controlled break-up of the jet is used. One way is through thermal modulation of the surface tension, which results in Marangoni flow. Then, the jet breaks up at well defined points of minimum surface tension and not at the non-reproducible points resulting from the thermal noise [57, 58].

4.3.3 Fast satellites

The third type of satellite drop formation occurs at a high drop speed. A part of the drop moves away in front of the head of the drop. This is a reproducible process as can be seen in figure 4.14. The mist of droplets from the secondary tail and the droplets from Rayleigh break-up of the long main tail are formed non-reproducible.

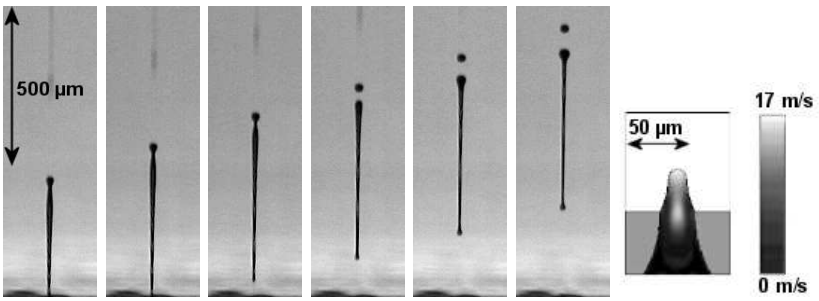

(a) 40 μs (b) 50 μs (c) 60 μs (d) 70 μs (e) 80 μs (f) 90 μs (g) 20 μs

Figure 4.14: (a-f) The reproducible formation of a fast satellite drop at 40, 50. . . 90 μs after the start of the actuation. The recordings are made with a stroboscopic illumination at drop repetition rate. (g) The calculated distribution of the speed in the z-direction at 20 μs after the start of the actuation. This shows two maxima inside the drop. The normal maximum right behind the head of the drop and another right in front of the head, indicating that this part of the head keeps moving away.

The formation of a fast satellite out of the head of the drop results from a supercritical acceleration at the start of the drop formation process. When the ink starts to come out of the nozzle, the acceleration of the ink has to stay below a critical level. When the first acceleration of the ink exceeds this level, surface tension forces are no longer capable of holding the ink together. This can be seen in figure 4.14g. In the figure the distribution of the speed in the jetting direction inside the drop is given. Normally, a maximum occurs only behind the head of the drop, meaning that ink flows from the tail into the head of the drop to form a spherical drop. However, with a supercritical acceleration, a maximum in the distribution remains also at the front of the head. This indicates that this part of the head keeps moving away from the rest of the drop. With a 8 mm long channel, the first ink comes out of the nozzle at 15-20 μs after the start of the actuation. At this point it is already determined whether a fast satellite drop will be formed or not.

The speed above which fast satellite drops are formed, the splitting speed, depends on the shape of the driving waveform. The driving waveform consists of a rise time of 1, 3 or 5 μs during which the piezo element is charged. The voltage remains then a certain time at the same value and 7-13 μs after the start of the actuation, the electrical charge is removed during the same time period as the charging time. The pulse width is time difference between the start of the charging and the de-charging. For a simple single trapezoidal shaped driving waveform the influence of the rise time and pulse width is shown in figure 4.15a.

A pulse width close to the most efficient pulse width results in the lowest splitting speed. A shorter rise time of the trapezoidal-shaped driving waveform also result in a lower splitting speed. The influence of the driving waveform can be explained with variation of the pressure at the entrance of the nozzle. A shorter rise time of the driving waveform result in a faster increase of the positive pressure peak, with more initial acceleration as an important effect. This causes a lower splitting speed. The first negative pressure peak, which determines the amount of ink at the start of the outward movement of the ink, and the amplitude of the main positive pressure peak determine the fast satellite drop formation mechanism.

With a longer pulse-width, the amplitude of the positive pressure peak decreases as shown in figure 4.15b. This would result in less acceleration and a higher splitting speed. However, the meniscus retraction increases with a longer pulse-width, as shown in figure 4.17a. The smaller mass of ink at the beginning of the outward movement would result in a larger initial acceleration and a lower splitting speed. Together, both effects result in a minimum in the splitting speed as function of driving pulse width.

4.3.4 Slow satellites

Another satellite drop formation mechanism results in slow satellites, formed reproducibly from the tail of the drop when the distributions of mass and momentum in the tail of the drop are not optimal, figure 4.16. Now the tail breaks off from

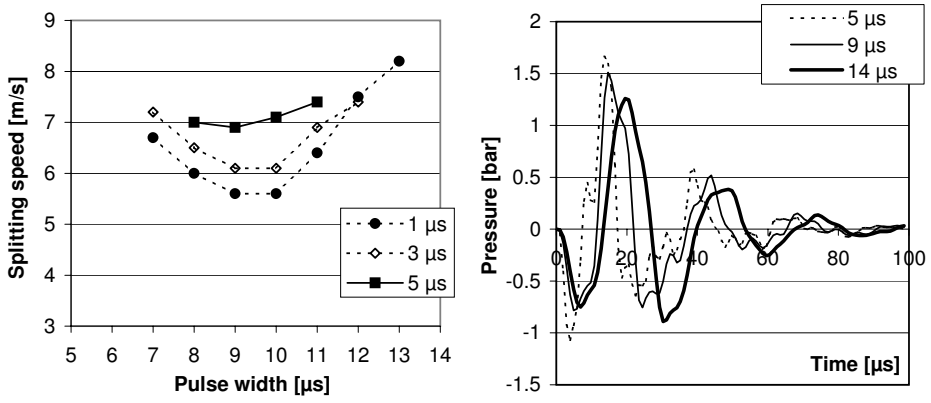

(a) (b)

Figure 4.15: (a) Measured splitting speed as function of the driving pulse width with a rise time of 1, 3 and 5 μs. The channel length is 8 mm and the nozzle diameter is 28 μm in a 100 μm electroformed nickel nozzle plate. (b) The calculated pressure at the entrance of the nozzle for a drop speed of 7 m/s. The rise time is 3 μs and the pulse width 5, 9 and 14 μs. The calculations are done with the narrow-channel model. The amplitude of the positive pressure peak is one of the two parameters, which determines the splitting speed.

the head and forms a slower moving satellite droplet.

The shape of the pressure wave after the main positive pressure peak is important for this mechanism. When after the first positive pressure peak a large second positive pressure peak is generated, a minimum in the tail width is generated. This minimum in the tail width is now localized somewhere between the head of the drop and a part further on the tail. Due to the higher capillary pressure at this minimum tail width, the tail will pinch-off at this position. This leads to the separation of the main part of the tail from the head of the drop.

This situation occurs for example with a very long driving pulse, as shown in figure 4.16. Normally, the de-charging of the piezo element amplifies the positive pressure wave from the charging of the piezo element. This generates one big positive pressure peak, see section 3.1.3. With a very long pulse, the de-charging comes too late. The negative pressure wave from the charging of the piezo is already reflected at the reservoir and has reached the nozzle as a positive pressure peak. The positive pressure wave from the de-charging of the piezo element reaches the nozzle now as a second positive pressure peak.

So there are four satellite drop formation mechanisms. Satellite drops can have a negative impact on the print quality. The generation of satellite drops must be avoided as much as possible. With the knowledge of the drop formation mechanisms it is not only possible to suppress the formation of satellite drops, but also the options for changing the drops size can be identified [163]. For graphical

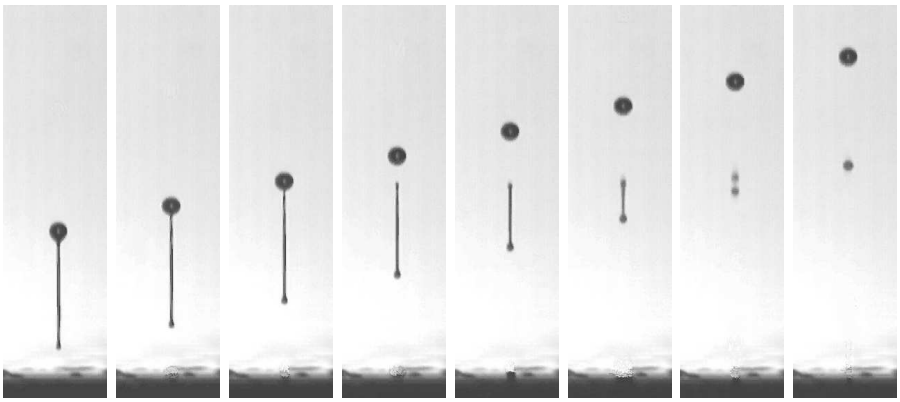

(a) 70 μs (b) 80 μs (c) 90 μs (d) 100 μs (e) 110 μs (f) 120 μs (g) 130 μs (h) 140 μs

Figure 4.16: The measured reproducible formation of a slow satellite drop. The 8 mm long channel is actuated with a 18 μs long driving pulse. The main drop has a speed of 7 m/s and the satellite drop has a speed of 5 m/s.

printing applications, changing the drop size fired with the same printhead geometry, drop size modulation, is an important option to improve the print quality and productivity. The drop size modulation mechanisms are described in the next section.

4.4 Drop size modulation

4.4.1 Pulse width and fill-before-fire-level

The first option is already mentioned in section 3.1.3. By changing the time delay between the rise time and the fall time of a trapezoidal shaped driving waveform, the drop formation time is modulated. With a larger width of the driving waveform, the time over which ink is transported outward increases, see figure 4.17a. The resulting drop size will become larger. However, when the timing of the rise time and the fall is not tuned to the travel time of the acoustic wave, the pressure wave will be less effectively amplified. This results in higher driving voltages for the same drop speed.

In figure 4.17b, the measured drop size at a drop speed of 7 m/s and the relative driving voltage (driving voltage with most efficient pulse width is 100 V) are shown. The channel length is 8 mm and the nozzle diameter is 36 μm. The drop size increases by almost 2 pl for each μs pulse width. The drop volume can be changed from 36 pl to 54 pl by increasing the pulse width from 5 μs to 14 μs. The increase of the driving voltage remains within 20%. For a head with a 5 mm long channel and a nozzle with a diameter of 24 μm, the drop size can be adjusted between 10 and 16 pl at a drop speed of 6 m/s. The pulse width varies from 3 μs

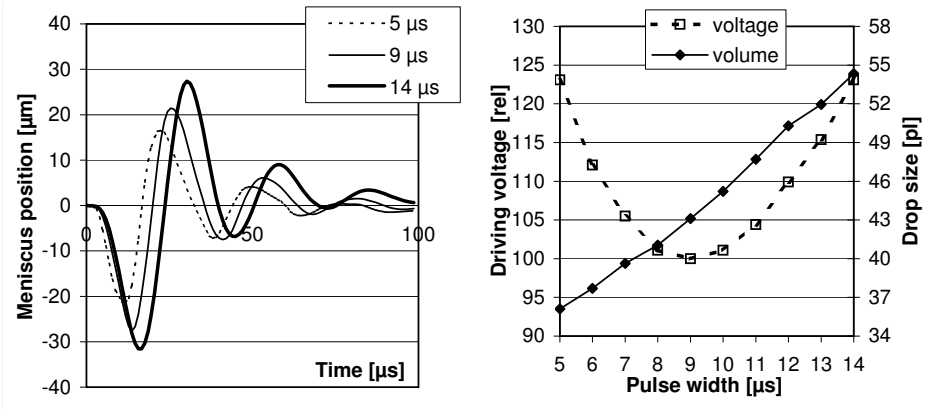

(a) (b)

Figure 4.17: (a) The meniscus position with a 5, 9 and 14 μs wide driving pulse (the rise time is 3 μs). The calculations are done with the narrow-channel model. A larger pulse width results in a longer time period during which the ink is transported outward. (b) Measured driving voltage and drop volume for a drop speed of 7 m/s as function of the pulse width. The channel length is 8 mm and the nozzle diameter 36 μm. The drop volume increases with a larger pulse width and the driving voltage increases when the pulse width is not tuned to the travel time of the pressure wave.

to 8 μs with this case. With this 5 mm geometry the other options for drop size modulation are further investigated.

With only two slopes in a driving waveform, as described in the previous sections, a maximum fill-before-fire action is achieved. The meniscus is retracted as much as possible when the positive pressure peak, which fires the drop, reaches the nozzle. This results in a minimum mass of ink in the nozzle when the ink starts to move outward to form a drop. The volume of the generated drop is relative small. Both slopes have the same contribution to the required amplitude of the positive pressure peak.

With a smaller amplitude of the first slope, the fill-before-fire action will be less. The smaller amplitude of the first slope must be compensated with a larger amplitude of the second slope to generate the same amplitude of the positive pressure peak. The electric voltage on the actuator changes in sign after the second slope. This results in a double-sided driving waveform amplitude and the total amplitude (peak-peak amplitude) of the driving waveform increases. The variation of the fill-before-fire level also requires a third slope in the driving waveform to remove the electric voltage from the actuator. The shape of a double-sided driving waveform is shown in figure 4.18a.

The variation of the fill-before-fire level is often used for a better control of the meniscus movement [88]. The variation can also be used for changing the

drop size. With a lower fill-before-fire level, the meniscus retraction will be less when the positive pressure peak reaches the nozzle. This is shown in figure 4.18a. Because of the larger amount of ink in the nozzle when the ink starts to move outward, the drop size will be larger.

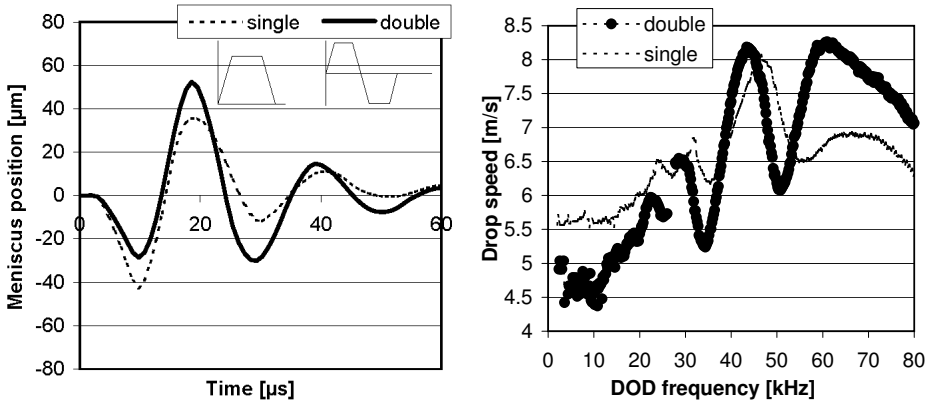

(a) (b)

Figure 4.18: (a) The meniscus position with a single- and a symmetric double-sided driving waveform. The calculations are done with the narrow-channel model for one drop formation cycle. The meniscus retraction with the double waveform is much smaller. (b) The measured drop speed as function of the drop repetition rate (drop on demand (DOD) frequency) with a single- and a double-sided driving waveform. The double-sided driving waveform results in more variations of the drop speed at higher drop repetition rates. The channel length is 5 mm and the nozzle diameter is 24 μm.

With the negative driving amplitude as large as the positive driving amplitude, a symmetric two-sided driving waveform, the total driving amplitude becomes 50 % higher. With a 5 mm long channel, the drop size range can be extended from 10-16 pl to 10-22 pl when applying the symmetric two-side driving waveform.

With the maximum fill-before-fire the main channel resonance is excited during only a half time period. With the symmetric two-sided driving waveform, the main channel resonance is excited during the complete time period. The acoustic resonances in the ink channel are much more excited. The higher level of residual vibrations, section 3.4.2, leads to more variations of the drop speed at higher drop repetition rates as shown in figure 4.18b.

4.4.2 Acoustic resonances

Pre-actuation of the meniscus with a small driving waveform (typical 1 % of the nominal driving amplitude) can be used for conditioning the ink by mixing the ink components [88]. Pre-actuation with driving waveforms of order 10 % of the

nominal driving amplitude can be used for reducing the required driving voltage [45]. A small pulse before the main actuation pulse can also create extra ink just in front of the nozzle. This amount of ink will be dragged along with the main drop formation process as shown in figure 4.19. A pre-pulse increases the total drop volume up to 10 pl when the timing of the pre-pulse is in phase with the channel resonance. With the 5 mm channel geometry the drop size range can be extended to 10-26 pl.

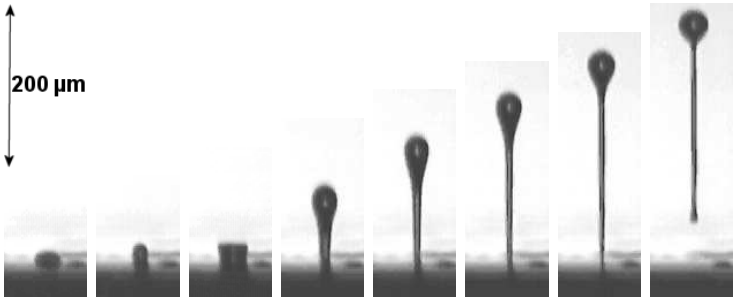

(a) 10 μs (b) 20 μs (c) 30 μs (d) 40 μs (e) 50 μs (f) 60 μs (g) 70 μs (h) 80 μs

Figure 4.19: The measured formation of a large drop after pre-actuation of the meniscus at 10, 20. . . 80 μs after the start of the actuation. The channel length is 5 mm and the nozzle diameter is 24 μm. With a small pulse before the main pulse extra ink in front of the nozzle is created. This amount of ink is dragged along with the main drop formation, which results in up to 10 pl larger drops. The head of the drop deforms a lot when colliding with the extra amount of ink, as can be seen in frame c.

When the main drop collides with the extra amount of ink in front of the nozzle, the head of the drop deforms a lot. The head of the drop recovers its spherical shape within a few microseconds. With a pre-pulse, the required driving voltage for larger drops does not increase as with the variation of the pulse-width or fill-before-fire level. However, the driving waveform will be longer and will not fit in the time window of high drop repetition rates. This is also the case with the next option.

When firing drops at a high repetition rate, the acoustic waves of the preceding drop formation cycle will not come to rest when the next cycle starts. The residual vibrations result in drop speed variations, see figure 3.23. When firing the next drop at a timing, which corresponds to a maximum in the frequency-speed curve, the next drops will move faster and merge with the first drop as shown in figure 4.20.

The driving waveforms will be long. For the 5 mm channel geometry the timing between the multiple pulses must be 13.5 μs, which corresponds to the highest maximum in the frequency-volume curve and a local maximum in the frequency-

speed curve, figure 3.24. We can extend the drop size range to drop sizes of 36, 50 or 65 *pl* with bursts of 2, 3 or 4 drops. However, the length of the driving waveform must fit in the time window of the drop repetition rate. Depending on the maximum drop on demand frequency, the length of the burst will be limited. With the timing of the 5 *mm* channel geometry, four drops can be fired within a burst up to a frequency of 20 kHz, and up to 40 kHz only a burst of two drops can be fired.

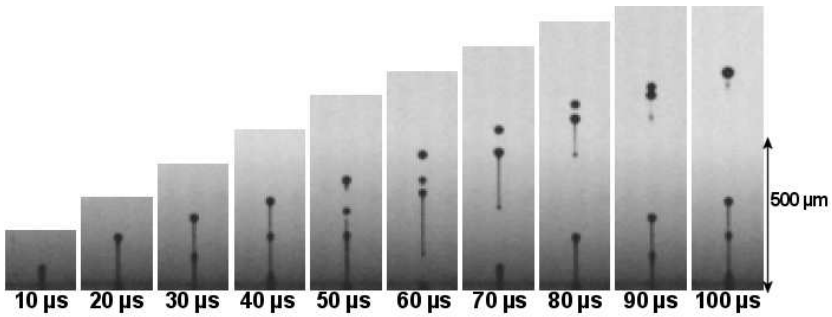

Figure 4.20: The measured drop formation at 10, 20. . . 100 μs after the start of the actuation when firing a burst of three drops. For the 5 *mm* channel geometry the timing between the adjacent drops is 13.5 μs corresponding to a maximum in the DOD frequency-drop volume relationship and the three drops merge to one big drop after 95 μs.

4.4.3 Break pulses

The opposite of pre-actuation is the use of a break pulse just after the main pulse. This can be a pulse of the same polarity after a half period of the channel resonance or of the opposite sign after a whole period. This dampens the residual vibrations [156]. When a break pulse starts when the main part of the drop is still leaving the nozzle, several pl of drop volume can be held back. With a break pulse after a half period with an amplitude of 50% of the main pulse, the smallest drop size with the 5 *mm* channel geometry can be reduced from 10 *pl* to 7 *pl* with a drop formation which looks the same as the normal drop formation.

A break pulse also reduces residual vibrations, especially when there is only one dominant frequency in the channel acoustics. For more complex situations with more than one important frequency, iterative learning control can identify suitable break waveforms [64]. A disadvantage of a strong break pulse is that refill of the nozzle will be less. Refill is driven by the variable mass effect and the channel acoustics, see section 3.4.1. With more damping less pressure waves remain to drive the filling of the nozzle.

Another way the generate smaller drop is to use the fast satellite drop formation mechanism as described in section 4.3.3. First actuation pulse is applied,

which generates a fast satellite drop, the so-called split pulse. This pulse generates a supercritical acceleration at the beginning of the drop formation, section 4.3.3. The best way is to use a short rise time for the split pulse. The first part of the ink cannot be captured anymore by the surface tension forces. With a 5 mm long channel this is the case after 15 μs. Then we start with a second counter pulse that blocks the main drop formation. As a result only the fast satellite drop will be jetted away as a small drop with a volume of 7 pl. This is shown in figure 4.21.

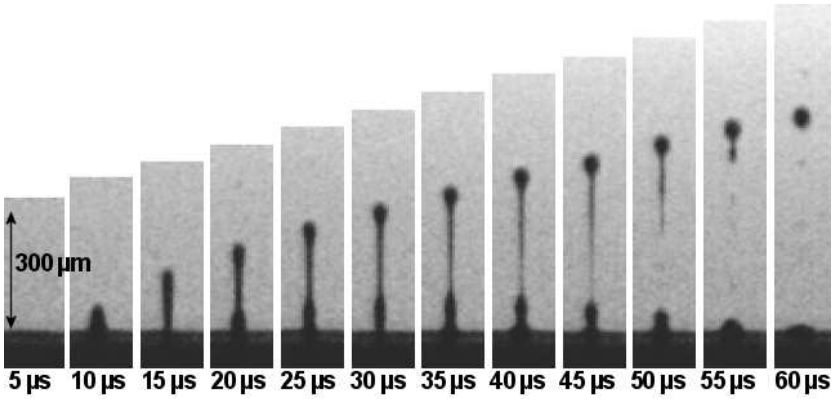

Figure 4.21: The measured drop formation at 5, 10, 15. . . 60 μs after the start of the actuation with a split pulse, followed by a counter pulse. The channel length is 5 mm and the nozzle diameter is 24 μm. The counter pulse blocks the main drop formation, which is visible close to the nozzle plate surface. The fast satellite cannot be captured and remains as a small drop.

With these mechanisms the drop size range with the 5 mm channel geometry is 7-36 pl with a maximum drop on demand frequency of 40 kHz, 7-50 pl with a maximum frequency of 30 kHz, and 7-65 pl with a maximum frequency of 20 kHz.

4.4.4 Meniscus and drop formation oscillations

Exciting resonances in the meniscus surface can result in a higher order drop formation. This results in small drops when using the third mode of the meniscus resonance [29].

In order to excite a higher order meniscus resonance, the second strong peak in the frequency characteristics of the meniscus movement in our printheads is used, see figure 3.3. With a 8 mm long geometry this peak is at a frequency of 170 kHz and with the 5 mm long channel at 220 kHz.

In a 8 mm long channel, a burst of three pulses at 170 kHz excites the third mode resonance, which results in 3 pl drops with a speed of 3 m/s. This is shown in figure 4.22. Numerical simulations with Flow3D show the same results. However,

the jetting stability is poor. Only at a very low drop speed (below 4 m/s), the drop formation remains stable. In addition, there are problems with wetting and satellite drop formation. With the 5 mm channel geometry the drop size looked to be of order 1 pl, but the jetting performance was too poor to get good quantitative data.

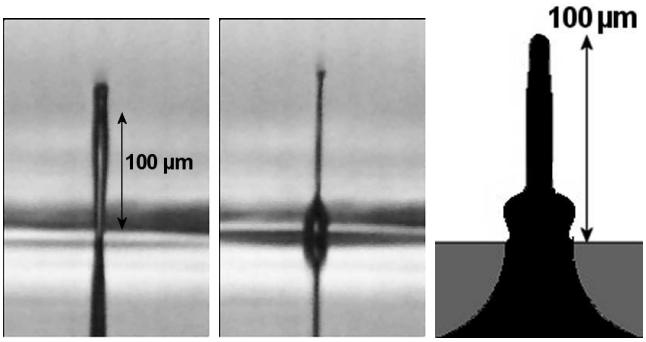

(a) (b) (c)

Figure 4.22: The measured drop formation 25 μs after the start of the actuation. The channel length is 8 mm and the nozzle diameter 32 μm. (a) Withe the normal driving waveform. (b) With a triple burst at 170 kHz, which results in a 3 pl drop instead of a 32 pl drop. (c) The calculated drop formation with the triple burst at 170 kHz.

Finally, exciting oscillations in nozzle flow of the drop formation process is also a possibility for firing small droplets from a large nozzle [33]. For this mechanism the Ohnesorge number, balancing the viscous effects on one side and inertial and surface tension effects on the other side, should be of order 0.1 and the rise time of the driving waveform about 0.03 times the capillary time scale. The capillary time scale is about 10 μs in our case. Under these conditions an oscillation in the flow inside the nozzle generates small drops. In the reference [33] a drop size reduction by a factor of 10 was reported for a default drop size of 40 pl. In our printhead geometries the capacitance of the piezo-electric actuator is too high to apply a rise time of order of 0.3 μs.

4.5 Concluding remarks

In the previous chapter we have seen how pressure waves inside the ink channels are generated. These pressure waves drive the drop formation process, which is described in this chapter.

The traveling wave principle leads to a drop formation process, which takes several tens of microseconds. Because of the viscosity of the ink, a tail is formed,

which slows down the speed of the head of the drop from 20 to 7 m/s. At tail break-off a secondary tail is formed. The secondary tail forms a mist of very small droplets. The mist of droplets is dragged along with the main drop formation, because of an induced air flow. The resulting tail-end behavior is mainly determined by the ink properties. The actuation amplitude has no impact on the tail-end speed. The tail breaks off after $45 - 60$ μs and long tails will be formed when the speed of the head exceeds the tail-end speed. The long tail will break-up non-reproducible in small satellite droplets by the Rayleigh break-up.

The fill-before-fire action retracts the meniscus during the first $10 - 20$ μs. The small mass of ink in the nozzle can result in a supercritical acceleration. This results in the reproducible formation of a fast satellite drop out of the head of the drop. The formation of slow satellites out of the tail of the drop is another satellite drop formation mechanism. This occurs when the distribution of mass in the tail has a minimum between the head of the drop and a point in the middle of the tail.

An important application is drop size modulation. With the knowledge of the drop formation process up to eight drop size modulation techniques are identified. The mechanisms are varying the driving pulse width and the fill-before-fire level, using pre-actuation, multiple drops or break pulses, the fast satellite drop formation mechanism with a split pulse and a block pulse, exciting meniscus oscillations and drop formation oscillations. With a selection from these mechanisms we can vary the drop size by a factor of ten.

The four satellite drop formation mechanisms, which are discussed in this chapter, are an example of possible disturbing phenomena in inkjet printing. Another disturbing phenomenon is the wetting of the nozzle plate. This is the subject of the next chapter.

Chapter 5

Wetting dynamics

In this chapter the wetting phenomena on the nozzle plate are discussed. Wetting of the nozzle plate is determined by the material interactions between the ink and the nozzle plate material, which result either in a partial wetting regime or a complete wetting regime. Detailed knowledge of the material interactions is not available. Therefore, a phenomenological investigation of the flow phenomena is performed. The flow patterns in the ink layer and the influence of the actuation of the nozzles will be described. In the jetting situation with a wetted nozzle, two flow patterns are observed. A Couette flow and a sink flow, with sometimes de-wetting of the nozzle plate. In the non jetting situation no activity is seen at very low driving voltages, a source flow at moderate driving voltages, a small sink flow regime at high repetition rates, and a dipole flow at driving voltages just below the jetting threshold. Then, the flow patterns at nozzle plate scale will be described. The precursor film and Marangoni flow, resulting from the changing surface tension of the ink, determine the flow patterns. Finally, the effect of the ink layer around the nozzle on the drop formation and the channel acoustics is discussed.

5.1 Wetting of the nozzle plate

5.1.1 Origin of wetting

Free surface flow in the nozzle and the acoustics in the ink channels are designed to give a good refill of the nozzle. This makes high drop repetition rates possible. However, a strong refill process results also in overfilling of the nozzle, see section 3.4.1. Overfill of the nozzle can result in wetting of the nozzle plate, especially when the area around the nozzles has mechanical and chemical defects like scratches or depositions of ink components. Large grooves and a lot of dirt around the nozzle opening can even result in excessive wetting and have to be avoided. In this thesis the excessive wetting is not investigated further. A printhead with 8 mm long channels and nozzles with a diameter of 30 μm in an electroformed nickel nozzle plate without any defects is used to study the dynamics of a layer of ink on the nozzle plate.

A source for wetting of the nickel nozzle plate can result from failure of the drop formation process as shown in figure 5.1. Often when the drop formation fails, the drop speed decreases slowly. When the drop speed becomes lower than a certain critical level, the adjacent drops will merge and a large amount of ink is collected just below the nozzle plate. The normal jetting direction is downwards, and gravity is pulling the ink away from the nozzle plate. However, after a while, this large amount of ink is attracted towards the nozzle plate. This whole sequence takes about 1000-10000 drop formation cycles, corresponding to $0.05 - 0.5\ s$ with a drop repetition rate of 20 kHz.

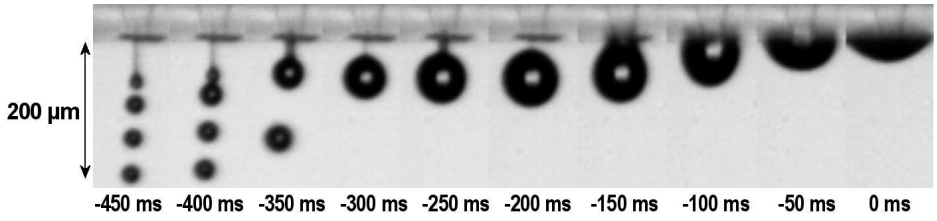

Figure 5.1: The recorded failure of the drop formation process during the last thousand drop formation cycles. As the drop speed decreases below a critical level, the adjacent drop will merge and a large amount of ink collects just below the nozzle opening. This large amount of ink is finally attracted to the nozzle plate and this results in wetting of the nozzle plate.

Several mechanisms can result in the attraction of the large blob of ink. First, the continuous firing of drops results in an increase of the blob radius which can be faster as the net displacement of the large amount of ink. So the surface of the blob grows towards the nozzle plate.

The second mechanism is the attraction force resulting from the surface tension of the ink. The tail does not pinch off anymore when the distance between the blob surface and the nozzle is short. The surface tension forces will then tend to merge the blob with the meniscus.

At some point the large blob of ink covers the whole nozzle opening and a third mechanism starts to play a role. The variable filling of the nozzle, which is the driving force behind the refill mechanism, changes to a complete filling of the nozzle. The asymmetric nozzle shape, which is now completely filled from the inside and the outside, starts to act as a micro-pump as long as long as the actuation continues. The micro-pump action of an asymmetric micro-channel in a changing pressure field is described in [128, 144]. The pumping direction is inwards, so that the large blob is attracted to the nozzle.

When the ink comes into contact with the nozzle plate surface around the nozzle opening, the wetting properties of the surface generate another force which attracts the ink to the nozzle plate. The observed contact angles of the ink on a nozzle plate are less than 20 degrees. The contact angle results from the balance of

forces at the contact line, figure 5.2a. The forces result from the surface tensions at the ink-air interface γ_l, the solid-air interface γ_s and the solid-ink interface γ_{sl}. The contact angle is defined by the Young equation:

$$\gamma_s = \gamma_l cos\theta + \gamma_{sl} \tag{5.1}$$

The capillary length scale is much larger than the nozzle diameter, section 4.1.1, so gravity plays no role on this scale. Without gravity, the drop has the shape of a sphere, and on a flat substrate the drop gets the shape of a spherical cap, cut-off at the contact angle. Using standard trigonometric formulas for the volume of a sphere and the volume of a spherical cap and making both volumes the same, we get for the spreading ratio SR, i.e. for the ratio between the contact radius R_c of the spherical cap on the substrate and the radius of the drop R_d:

$$SR = \frac{R_c}{R_d} = \left(\frac{4sin\theta(1+cos\theta)}{(1-cos\theta)(2+cos\theta)} \right)^{\frac{1}{3}} \tag{5.2}$$

The spreading ratio according to this formula is depicted as function of the contact angle in figure 5.2b. For contact angles less than 20 degrees the drop will spread over a large area.

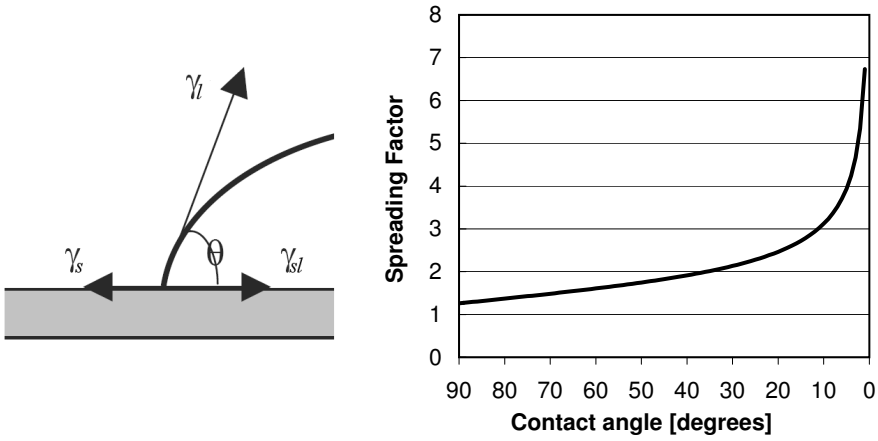

(a) (b)

Figure 5.2: (a) At the contact line the balance of forces from the surface tensions at the ink-air interface γ_l, the solid-air interface γ_s and the solid-ink interface γ_{sl} results in a contact angle θ. (b) The spreading ratio of a spherical cap as function of the contact angle. For contact angles less than 20 degrees, the drop will spread over a large area.

5.1.2 Wetting regimes and visualization

It is found that after a period of jetting (at least several seconds) a thin ink layer is formed on the nozzle plate [87]. The thickness of the layer is of the order of 10 μm, so we have to deal with the dynamics of thin films as described in [63, 129]. With our ink the Bond number $g\Delta\rho L^2/\eta$ and the Galileo number $gL^3\Delta\rho^2/\eta^2$ are both very small, meaning that gravity can be neglected with respect to viscous and surface tension forces. The observed velocities of the ink movement on the nozzle plate are of the order of 1 mm/s [14]. With our ink the Reynolds number $\rho uL/\eta$ and the Weber number $\rho u^2 L/\gamma$ are both very small, too, meaning that also inertia can be neglected with respect to viscous and surface tension forces. So, the flow phenomena are dominated by viscous and surface tension forces.

The wetting properties of a surface are determined by the surface energies of the ink and the nozzle plate material, but most of all by the interaction between the ink and the nozzle plate material [62]. An important parameter is the spreading coefficient S:

$$S = \gamma_s - \gamma_{sl} - \gamma_l \tag{5.3}$$

which give the energy difference between a dry and a wet surface. With a positive spreading coefficient, the nozzle plate and the ink are in a complete wetting regime, and with a negative one in a partial wetting regime. In a complete wetting regime the contact angle will become zero and a thin layer of liquid will be formed, the precursor film. In the partial wetting regime, drops exist with a certain contact angle. However, detailed knowledge of the energies involved is not present. Especially the data on interactions between the ink and the nozzle plate, which should be described with van-der-Waals interactions and polar interactions (for example comprised to Lewis acid-base interactions [171]) are missing. Therefore, a phenomenological investigation of the flow patterns on a nozzle plate is performed.

The nozzle plate has two arrays of nozzles. The nozzles within one row are at a spacing of 340 μm. The two arrays are located near the long edges of the nozzle plate and the distance between the two arrays is 8 mm, figure 5.3. The circular areas around the nozzles are due to a difference in material structure, which is found to be irrelevant for this study.

The flow pattern on the nozzle plate are visualized with a standard 25 fps video camera as with the visualization of the drop formation. Instead of a stroboscopic illumination, now an continuous light source (Olympus Highlight 3001) is used. A mirror is mounted at 45° just below the nozzle plate to obtain a top view of the nozzle plate. With a needle a localized air flow is applied to bend to drops away from the mirror without influencing the flow pattern on the nozzle plate. Particle Tracking Velocimetry with 2 μm melamine tracer particles with a density of 1510 kg/m^3 is used to measure the velocities in the ink layer. The density of the ink is 1090 kg/m^3. For the measurements of the flow phenomena in the ink layer around a single nozzle, the ink is directly deposit on the nozzle and actuation is started after the ink has reached an equilibrium situation, see [14] for more information.

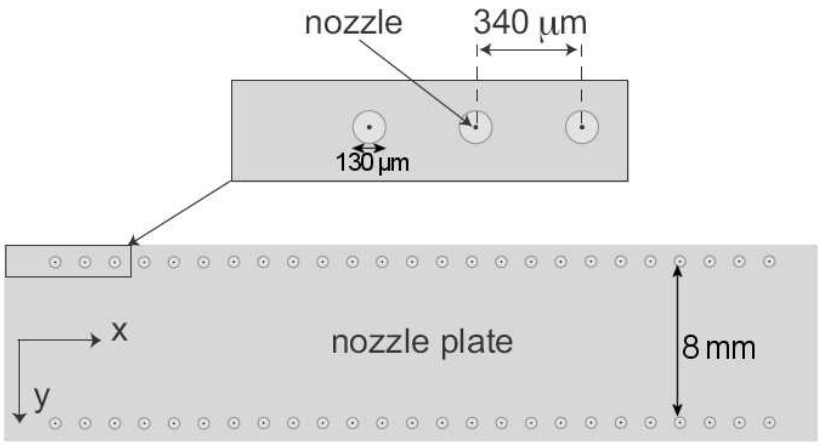

Figure 5.3: Drawing of the top view of the nozzle plate with two arrays of nozzles with a distance between the array of 8 mm. The distance between the nozzles is 340 μm and the nozzles have a diameter of 30 μm.

5.2 A wetted nozzle *

5.2.1 Jetting nozzle

With normal actuation, drops are jetted continuously, and measurements are performed up to a drop repetition rate of 30 kHz.

At a repetition rate of 20 kHz, a bi-directional flow pattern is visible as shown in figure 5.4a. The arrows are drawn following the movement of the tracer particles, the circular area around the nozzle has a diameter of 130 μm. The edge of the nozzle-plate is located at left side, so the ink layer is mainly present at the right side of the nozzle and the neighboring nozzles are disturbing the flow pattern above and below the jetting nozzle. So most tracer particle are moving at the right side of the nozzle.

The video recording shows that both directions occur at the same position, indicating a depth dependence of the velocity. The depth dependence of the velocity profile is measured by recording the nozzle plate surface also at an angle of 45°. Since the light is reflected on the nozzle plate surface, also the mirror images of the tracer particles are visible. From the distance between the particles themselves and the mirror images, the depth profile can be determined. It turns out that particles close the nozzle plate surface are moving away from the nozzle and particles near the ink-air interface are moving towards the nozzle. The resulting Couette velocity profile is shown in figure 5.4b.

*Part of this subsection has been published as: B. Beulen, J. de Jong, H. Reinten, M. van den Berg, H. Wijshoff, and R. van Dongen, *Flows on the nozzle plate of an inkjet printhead*, Exp. Fluids **42**, 217 (2007).

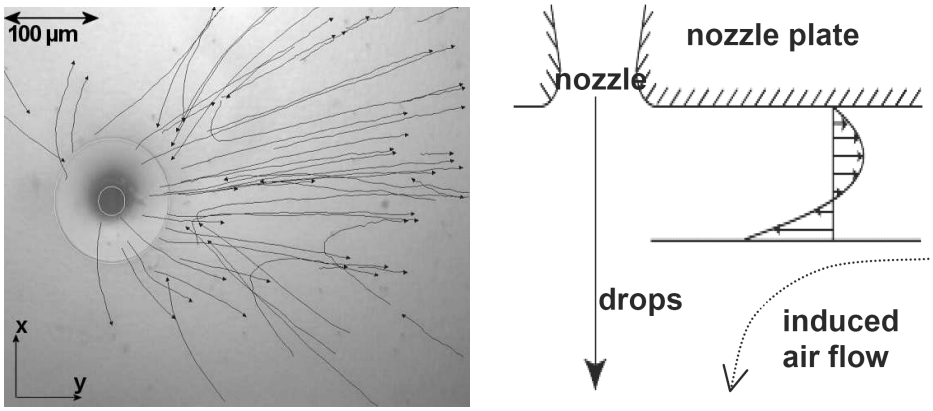

(a) (b)

Figure 5.4: (a) The streamlines in an ink layer around a nozzle, jetting at 20 kHz. Particles are moving in a radial pattern towards the nozzle and away from the nozzle, indicating a bi-directional flow. (b) The velocity profile in the ink layer near the nozzle. Ink is moving from the nozzle into the ink layer because of the overfilling of the nozzle and is dragged towards the nozzle by the induced air flow.

In section 3.4.1, we have seen that during normal operation the refill of the nozzle during jetting results in an overfilling of the nozzle. This overfilling results in a net ink flow from the nozzle into the ink layer near the nozzle plate surface. In section 4.3.1 we have seen that the momentum transfer to the surrounding air by the continuously jetted drop induces an air flow of several m/s along with the jetted drops. This induced air flow causes an acceleration of the surrounding air and subsequently a suction of air towards the jetted drops. So there is not only an air flow along with the jetted drops, but also an air flow towards the jetting nozzle. This drags the ink at the ink-air interface towards the nozzle [14]. Both mechanisms result in the observed Couette flow.

The radial velocity v_r and the circumferential velocity v_θ of the tracer particles are shown in figure 5.5 as a function of their distance r to the nozzle. The radial pattern results in circumferential velocities much lower than the radial velocities, only 0 ± 0.05 mm/s. The radial velocities decrease from a maximum of 0.1 mm/s at a distance of 50 μm from the center of the nozzle to 0.05 mm/s at a distance of 400 μm from the nozzle. The velocities of the traces particles are split into a group with a positive speed (towards the nozzle) and a group with a negative speed (away from the nozzle).

At a drop repetition rate of 25 kHz, a radial flow pattern is visible, too, but now only in one direction, towards the nozzle, figure 5.6a. The recorded speed is much higher, namely 0.4 mm/s at a distance of 400 μm and up to 0.7 mm/s at a distance of 250 μm. The tracer particles cannot be tracked completely up to the nozzle because their velocities become too high to be resolved with the

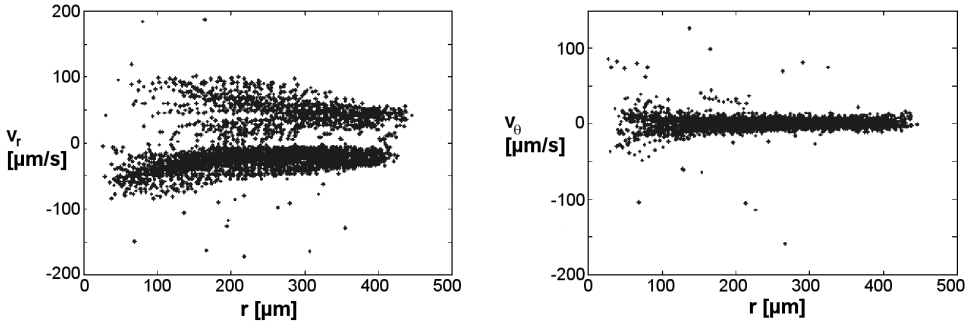

Figure 5.5: The radial velocity component v_r and the circumferential velocity component v_θ of the flow in the ink layer around a nozzle, which fires drops at a repetition rate of 20 kHz. The radial flow properties are confirmed, as $v_\theta \ll v_r$. The radial velocity distribution shows a group tracer particles moving away from the nozzle and another group moving towards the nozzle.

employed camera. In figure 5.6b the velocity amplitude $|v| = \sqrt{v_r^2 + v_\theta^2}$ is plotted on a double logarithmic scale as a function of the distance to the center of the nozzle. The cloud of data points is formed by rows of data points representing a recorded streamline.

From these data the r-dependency of the tracer particle velocities is determined for each streamline separately. The gives a relationship of $|v| \propto r^n$ with $n = -1.3$ with a standard deviation of 0.3. For an ideal 2D sink flow, $v_\theta = 0$ and v_r becomes $|v|$. The value of n can be derived directly from conservation of mass and flux at the velocity potential lines, which are perpendicular to the radial streamlines. The circumference of the potential lines scales with r, so the velocity must scale with r^-1 to keep the flux constant. The small deviations are caused by the non-uniform layer thickness.

There is only a flow towards the nozzle. This means that there is no flow from the nozzle to the ink layer anymore. The overfilling is too weak or even vanished. The overfilling is driven by the variation of the mass of ink inside the nozzle. The meniscus retraction is the cause of the variation of mass. However, with an ink layer, during the meniscus retraction ink will flow from the ink layer into the nozzle. When the meniscus protrudes, ink will flow from the nozzle into the ink layer. The variation of the mass of ink in the nozzle, which is the driving force behind the refill, will be less. The refill mechanism will be less strong and can even vanish completely.

When the ink layer is so thick that the nozzle area remains covered all the time, the nozzle will start to act as a micro-pump with the flow directed inwards, section 5.1.1. The ink layer thickness must be larger than 40 μm, as we will see in section 6.2.1. This can become an extra driving force and the flow in the ink

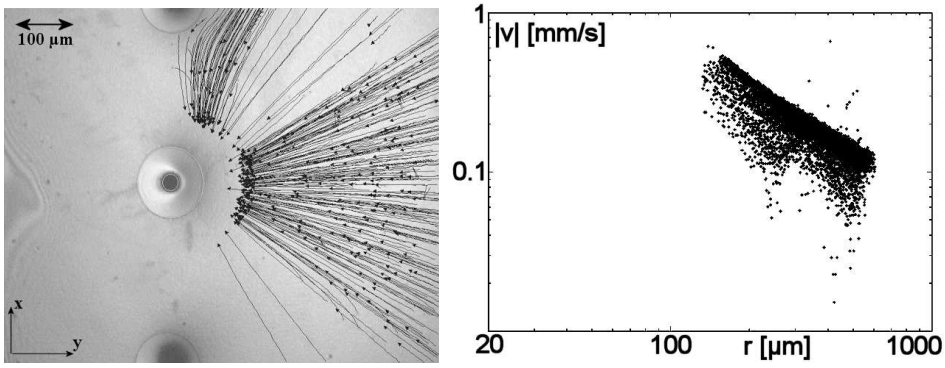

(a) (b)

Figure 5.6: (a) The streamlines in an ink layer around a nozzle, jetting at 20 kHz. Particles are moving in a radial pattern towards the nozzle, indicating a sink flow. (b) The velocity amplitude $|v| = \sqrt{v_r^2 + v_\theta^2}$ of the flow in the ink layer. The tracer particles follow a $|v| \propto r^n$ dependency with $n = -1.3$ with a standard deviation of 0.3.

layer towards the nozzle can become very strong.

A quantitative analysis of the weakening of the refill effect and the onset of the micro-pump action requires accurate data on the ink layer thickness distribution. However, these are not available. What is known, is that the ink layer thickness varies between 10-20 μm. The thickness of the ink layer is estimated by the number of fringes that arise from narrow-band LED illumination ($\lambda = 545$ nm) placed under an angle of 45°. The larger amount of ink is towards the middle of the nozzle plate, which is at the right of the actuated nozzle with the orientation shown in the figures.

At a drop repetition rate of 15 kHz the sink flow is very strong ($v_r > 1\ mm/s$), resulting in dewetting of the area around the nozzle as shown in figure 5.7. Within a few seconds an area of several hundred micrometers is depleted of ink. The dry surroundings even extend over the neighboring nozzles.

Measurements at a drop repetition rate of 5 and 10 kHz show a weak sink flow towards the nozzle, qualitatively comparable to the sink flow observed at 25 kHz. The observed flow pattern at the different drop repetition rates are now:

5 kHz: Weak sink flow, $v_\theta = 0$, $v_r \approx 0.1\ mm/s$

10 kHz: Very weak sink flow, $v_\theta = 0$, $v_r < 0.1\ mm/s$

15 kHz: Very strong sink flow, $v_\theta = 0$, $v_r > 1\ mm/s$

20 kHz: Couette flow, $v_\theta = 0$, $v_r \approx \pm 0.1\ mm/s$

25 kHz: Normal sink flow, $v_\theta = 0$, $v_r \approx 1\ mm/s$

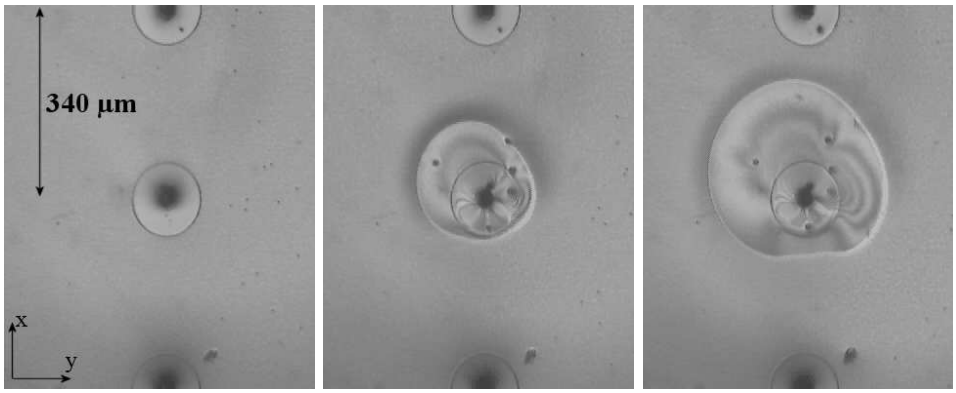

(a) 0 s (b) 1 s (c) 2 s

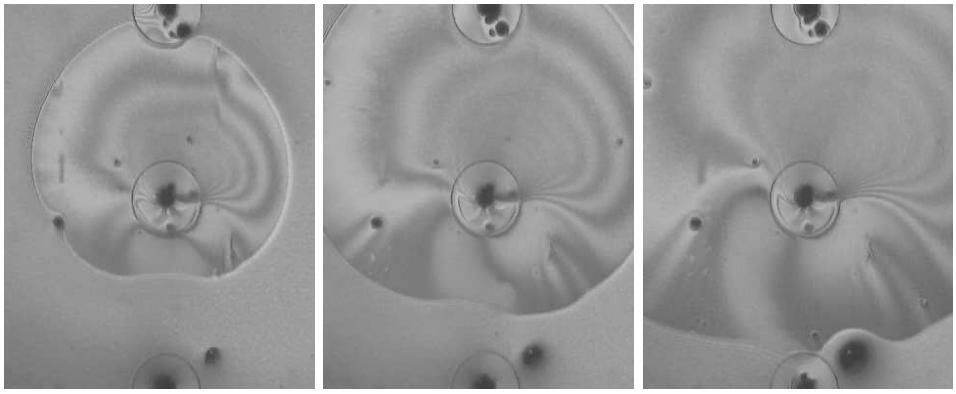

(d) 4 s (e) 8 s (f) 16 s

Figure 5.7: The dewetting of the area around the nozzle because of a very strong sink flow in the ink layer around the nozzle, when the nozzle jets with a repetition rate of 15 kHz. The pictures (a-f) are taken at 0, 1, 2, 4, 8 and 16 seconds after start of the jetting process.

5.2.2 Non-jetting nozzle

In this section, the flow patterns are observed in the non-jetting actuation regime. Reducing the actuation amplitude below the threshold for drop formation results in a meniscus movement only. The threshold for drop formation is about 50% of the nominal driving amplitude for a drop speed of 5 m/s. Without drop formation, there is no induced air flow anymore, which drags the ink towards the nozzle.

The measurements are performed at actuation frequencies up to 30 kHz. At very low driving voltages, less than 10% of the nominal driving amplitude for a drop speed of 5 m/s, no activity is seen. At moderate driving amplitude a source flow is observed at all actuation frequencies, most likely driven by the refill effect. The amplitude of the meniscus movement is now big enough to cause a significant variation of the mass of ink in the nozzle. This leads to overfilling of the nozzle

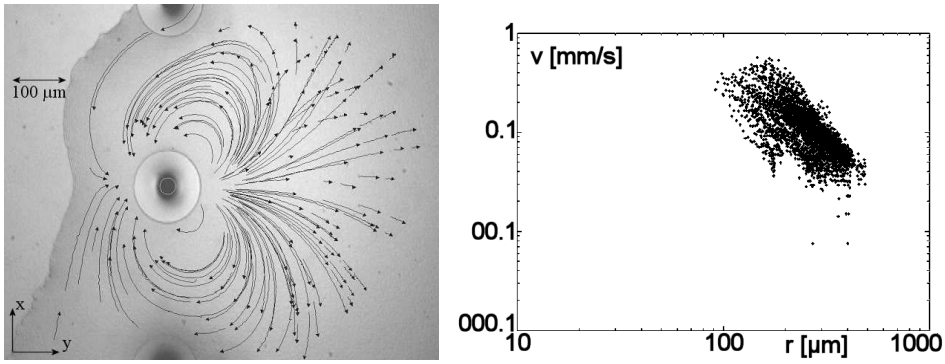

(a) (b)

Figure 5.8: (a) The streamlines in an ink layer around a nozzle, actuated at 20 kHz without drop formation. The tracer particles are moving in a dipole flow pattern. (b) The velocity amplitude $|v| = \sqrt{v_r^2 + v_\theta^2}$ of the flow in the ink layer. The tracer particles follow a $|v| \propto r^n$ dependence with $n = -2.3$ with a standard deviation of 0.3. Taken from [14].

and ink can flow from the nozzle into the ink layer around the nozzle.

At driving amplitudes just below the drop formation threshold, a dipole flow is observed for almost all driving frequencies. In figure 5.8a the streamlines of the flow in the ink layer with the nozzle actuated at a frequency of 20 kHz are shown. The direction of the dipole is along the gradient in the ink layer thickness. Left of the nozzle there is almost no ink and right of the nozzle there is a lot of ink. The velocity amplitudes are comparable with the sink and Couette flow in the jetting situation.

In figure 5.8b the velocity amplitude is plotted as a function of the distance to the center of the nozzle, in a double logarithmic plot. The r-dependency shows a $|v| \propto r^n$ relationship with $n = -2.3$ with a standard deviation of 0.3. For an ideal 2D dipole flow n should be -2. The deviation is most likely caused by the gradients in the ink layer thickness. So a vibrating meniscus can act as a source for a dipole flow.

At least two possible mechanisms can be responsible for this. First, the vibrating meniscus in the nozzle can excite capillary waves. When these wave are absorbed by viscous dissipation, flow patterns can be generated by acoustic streaming [102, 110, 143]. The driving force is the transfer of the time average momentum in an acoustic beam to either an increase of the time average pressure in the ink layer or a decrease of the layer thickness. Under ideal circumstances this leads to quadrupole like flow field, but the time average spatial distribution of the ink layer thickness, which is not known quantitative, will have a large impact.

A second mechanism results from possible variations in the surface tension of the ink. Gradients in the surface tension will lead to a Marangoni flow since

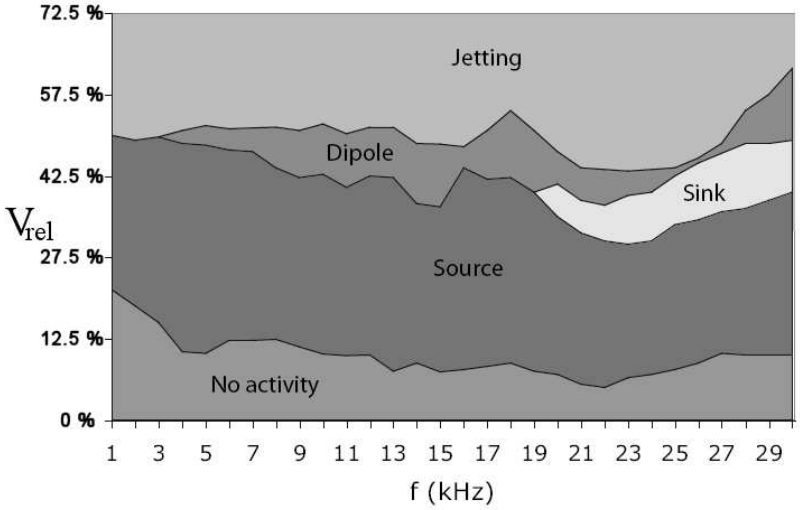

Figure 5.9: The observed flow pattern with a non-jetting nozzle (source, sink and dipole flow) as function of actuation amplitude and frequency. Taken from [14]. The actuation amplitude V_{rel} is given relative to the nominal driving amplitude.

the surface of the liquid tries to minimize the surface energy. In the next section we will see that the surface tension of the ink can change. The ink consists of a mixture of organic compounds in a polymer based resin and local changes in surface tension can occur through selective evaporation or through exposing such a liquid to a surface vibration [161]. The actuated nozzle acts as a source for vibration but also continuously supplies the ink layer with homogeneous mixed ink compounds.

In figure 5.9 an overview of the observed flow pattern is given. The measurements are performed with increasing driving amplitude from zero to jetting amplitudes for frequencies up to 30 kHz. At frequencies of 19 kHz and higher, a sink flow is observed at driving amplitudes just between the source flow regime and the dipole flow regime.

With these measurements the ink is deposit directly at the nozzle area to get more or less constant conditions for the experiments. Normally the nozzles are wetted by ink coming from the nozzle itself or form other places at the nozzle plate. We will look now at the wetting patterns on nozzle plate scale.

5.3 A wetted nozzle plate †

5.3.1 Long-range phenomena

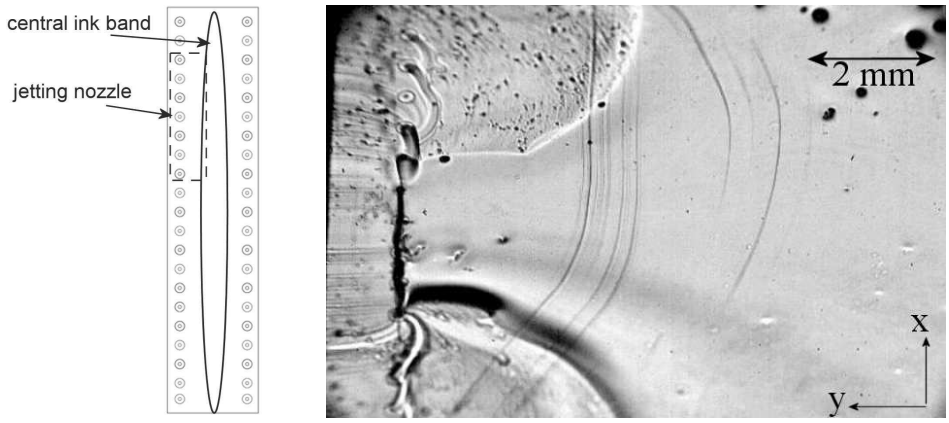

(a) (b)

Figure 5.10: (a) Schematic drawing of a top view on the nozzle plate and the central ink band. This is the normal starting situation when jetting starts. (b) Developed ink flow from the central ink band to a row of nozzles when seven nozzles are jetting with a repetition rate of 30 kHz.

Under normal operation conditions, the nozzle plate is prepared before the actual printing starts. It is impossible to remove all the ink from the nozzle plate. Therefore, there is always some ink at the nozzle plate, which accumulates in the middle of the nozzle plate in a stationary central ink band as shown in figure 5.10a. The thickness of the central ink band varies between 1 μm and 10 μm. This situation is the starting point for the observations on nozzle plate scale [87].

When a row of nozzles is jetting, an ink flow from the central ink band to the jetting nozzles is visible, figure 5.10b. This trunk flow even develops when a single nozzle is actuated without jetting i.e. at a low driving amplitude. The development of the ink flow from the central ink band towards a single actuated, but not jetting, nozzle is shown in figure 5.11. When the nozzle is actuated with a driving amplitude just below the jetting threshold, the central band starts to deform slowly and after a few minutes a streamer is developed which protrudes in the direction of the actuated nozzle. After the trunk has been formed it elongates rapidly and reaches the actuated nozzle within 0.2 s [87].

The measurement of the position of the front of the trunk is based on the fringes, which are visible with the narrowband (λ = 545 nm) LED illumination

†Part of this subsection is published as: J. de Jong, H. Reinten, H. Wijshoff, M. van den Berg, K. Delescen, R. van Dongen, F. Mugele, M. Versluis, and D. Lohse, *Marangoni flow on an inkjet nozzle plate*, Appl. Phys. Lett **91**, 204102 (2007).

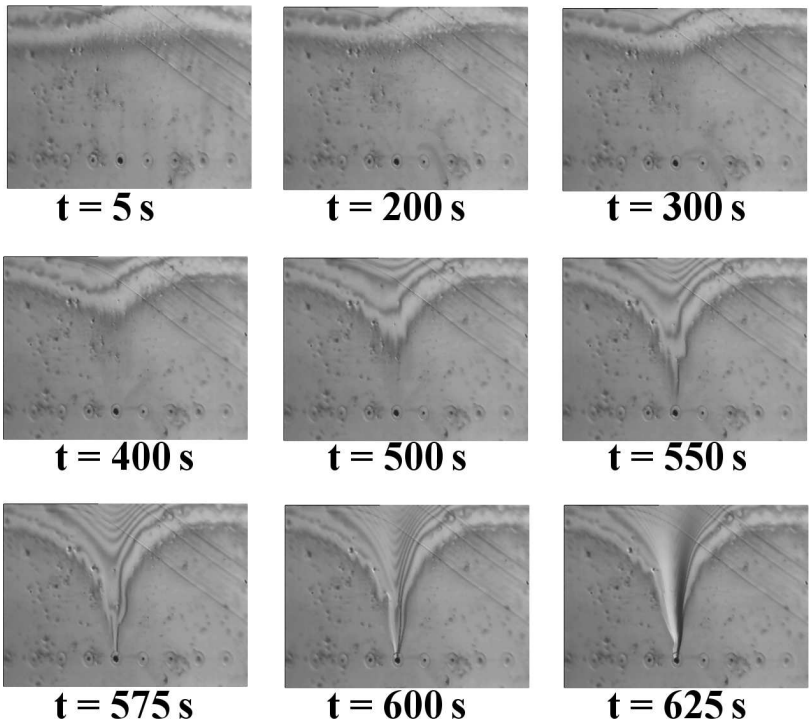

Figure 5.11: The development of the trunk flow from the central ink band towards an actuated, but non-jetting, nozzle. The central ink band is located just at the top of the pictures and a row of 9 nozzles with the middle nozzle actuated is located at the bottom of the pictures. Actuation is at a repetition rate of 30 kHz with an amplitude of 47.5 % of the nominal driving voltage. A similar picture with a jetting nozzle can be found in [87].

at an angle of 45°. The ink front position is defined through a layer thickness of 150 nm. Its position as a function of time after the streamer has developed is depicted in figure 5.12, together with an non-jetting actuation at only 40 % of the nominal driving amplitude and a jetting actuation. The position of the ink front follows a power law relationship with an exponent of 0.46 ± 0.06 for all three cases [87]. Only the pre-factor depends on the amplitude of the actuation.

$$y = c(t0 - t)^{0.46 \pm 0.06} \tag{5.4}$$

The error in the value of the exponent corresponds to a displacement error of 10 μm. The speed at which the front of the trunk moves is typical 5-10 $\mu m/s$.

5.3.2 Driving mechanisms

The question is what are the possible driving mechanisms for the trunk flow. The discussion below includes air flow, nozzle plate vibrations, electrostatic effects,

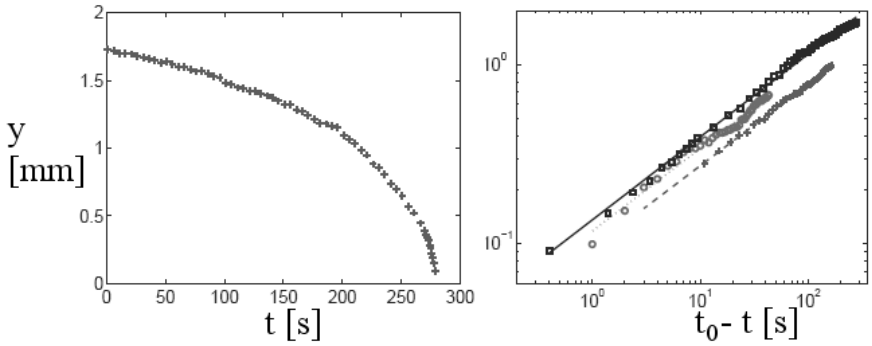

Figure 5.12: The position of the ink front with a jetting actuation (a and b-squares) and with non-jetting actuation at 47.5 % (b-circles) and at 40 % (b-pluses) of the nominal driving amplitude. In the loglog plot also the corresponding power law fits are drawn. The nozzle is located at $y = 0$ and t_0 is the time when the front arrives at the nozzle ($\approx$ 280 s). Taken from [87].

pressure differences, gravitational effects, thermal effects, and variations in surface tension from variations in nozzle plate composition or ink composition.

(i) Air flow as a driving force towards the nozzle. The air flow is induced by the drop formation process and accelerates the surrounding air towards the jetting nozzle, see section 4.3.1. Although this air flow drags the ink in a layer around the jetting nozzle towards the jetting nozzle [14], it can be ruled out as driving force on nozzle plate scale since the non-jetting cases shows almost the same velocity of the trunk flow.

(ii) Nozzle plate vibrations. The actuation with piezo elements can excite resonances in the printhead structure, section 2.3. The maximum amplitude of the nozzle plate vibrations, found with the finite element analysis of the dynamic behavior of the printhead structure, is about 5 nm. This is confirmed with measurements with a speckle interferometer. These oscillations could results in a net flow of ink. The average speed $\overline{u_y}$ of an ink layer with thickness h at a distance l is given by [7]:

$$\overline{u_y} = \frac{1}{12}\frac{a^2\omega^2\rho h}{2\eta l} \tag{5.5}$$

with a the amplitude of the vibration (maximum 5 nm) with angular frequency ω. With frequencies up to 100 kHz the maximum speed becomes about 10 nm/s at a distance of 1 mm, much lower than the observed velocities of almost 10 $\mu m/s$. As a final check experiments are performed with sealed nozzles. Even with many nozzles actuated, there is no ink flow observed anymore. So nozzle plate vibrations don't play any role of significance.

(iii) Electrostatic effects. The electrical resistivity of the nickel nozzle plate and the graphite based body of the printhead is measured to be less than 40 Ω.

This low value indicates that there are no thick and insulating oxide layers on the nickel nozzle plate. The resistivity of the ink is only 8 $k\Omega m$. These low values exclude electro-wetting as a possible source for the ink flow.

(iv) When there is an ink layer between the ink in the middle of the nozzle plate and the nozzle, a pressure difference can drive the ink towards the nozzle. This ink layer must have a thickness less than 100 nm, the lower limit of the optical recordings. Pressure differences can result directly from the refill effect and a micro-pump action of the nozzle, or from changing capillary pressures because of a variation in the curvature of the surface. The speed in a liquid film of thickness h driven by a pressure difference Δp over length l can be derived easily from Stokes' law, when applying the boundary condition of $u_y = 0$ at the solid interface and $\partial u/\partial z = 0$ at the air interface:

$$\overline{u_y} = \frac{h^2 \Delta p}{3\eta l} \tag{5.6}$$

To get the observed speed of 10 $\mu m/s$ in an layer with a thickness of maximum 100 nm, the pressure difference over 1 mm should be at least 10 bar, which is not realistic. For capillary pressure driven flow the pressure variation results from differences in curvature ($\Delta p \propto \gamma \Delta R^{-1}$), which leads with $\Delta R^{-1} \propto h/l^2$ to a h^3 dependency:

$$\overline{u_y} \propto \frac{\gamma h^3}{\eta l^3} \tag{5.7}$$

and also unrealistic curvatures to get a speed of 10 $\mu m/s$ over a distance of 1 mm. So pressure differences are not the main driving force behind the observed flow phenomena.

(v) Gravitational effects. on mm-scale the Bond number and the Galileo number are not very small anymore, meaning that gravity indeed cannot be neglected. This is also expressed in the capillary length L_γ, (equation 4.1), which is 1.7 mm with the transparent test ink. The gravitational forces with the nozzle plate in its normal position, upside down, can result in a pendant drops because of the Rayleigh-Taylor instability, which has a most unstable wavelength λ^* of [63]:

$$\lambda^* = 2\pi\sqrt{2} L_\gamma \tag{5.8}$$

This wavelength is 16 mm in our case, more than the width of the nozzle plate. Drops can become unstable and will detach from the nozzle plate when the diameter becomes larger than $2\pi L_\gamma$ [63], which is still larger than the width of the nozzle plate. So drops will not detach from the nozzle plate. The question is however, are gravitational forces the driving forces behind the observed flow phenomena? Therefore, an experiment is performed with the head turned upside down. This had no effect, the observed flow patterns remained the same, qualitative and quantitative. So gravitational forces seem not to be responsible for the observed flow phenomena

(vi) Thermal effects. Surface tension is temperature dependent and a thermal gradient can therefore result in differences in surface tension. Thermal measurements of the nozzle plate surface show a maximum difference in temperature of 4 K. For most liquids a typical relative surface tension dependency on temperature is found to be of order $-10^{-3}\ K^{-1}$ [107]. With the nozzles, which are located near the long edges of the nozzle plate, at the lowest temperature, this would result in a flow towards the nozzles. However, the measured temperature differences result in surface tension differences of only a few percent, which is not enough to generate any strong flow effects. Furthermore, the actuation of the nozzle has no influence on the temperature. So the observed temperature differences cannot play any role.

(vii) Differences in nozzle plate composition or ink composition can result in surface tension gradients which can drive an ink flow. This is called Marangoni flow [44, 80, 81, 112, 169]. Contact angle measurements on different places on the nozzle plate show no differences. So only differences in surface tension of the ink remain as possible driving force. The average speed resulting from a difference $\Delta\gamma$ over a distance l is [129]:

$$\overline{u_y} = \frac{h\Delta\gamma}{6\eta l} \tag{5.9}$$

The speed scales linearly with the layer thickness. Also for this driving force there must be a layer of ink between the middle of the nozzle plate and the nozzles. For a speed of 10 $\mu m/s$ at a distance of 1 mm in an ink layer with a maximum thickness of 100 nm, the required difference in surface tension is only 6 mN/m. This is possible with our ink, which consists of a mixture of multiple organic compounds in a polymer based-resin.

As a check, additional measurements were done with silicone oil. The silicone oil, which is used, is a pure single component liquid, not vulnerable to surfactants and selective evaporation of certain components. Therefore, the surface tension is constant within the oil film. With the silicone oil, which also shows good wetting on the nozzle plate, no surface flow is observed at all. This indicates that surface tension gradients are the main driving forces behind the observed flow phenomena.

With only surface tension gradients as possible driving force there must be a way of communication between the nozzle and the band of ink in the middle of the nozzle plate, i.e. a thin ink layer with a thickness less than the minimum visually observable thickness of 100 nm.

5.3.3 Complete wetting

The existence of an ink layer with a thickness less than 100 nm can only result from a complete wetting regime, i.e. a precursor film. A striking evidence that there is a precursor film together with macroscopic drops is demonstrated through the following experiment: A drop is deposit close to an array of nozzles on the nozzle plate without a visible ink layer, figure 5.13. The drop has a diameter of 130 μm and a thickness of 720 nm. The drop remains visible as a macro drop

with a contact angle of 15°. The arrows indicate the flow direction of the drop and the circles indicate which nozzle is actuated. As soon as a certain nozzle is actuated the drop moves towards the actuated nozzle and deforms.

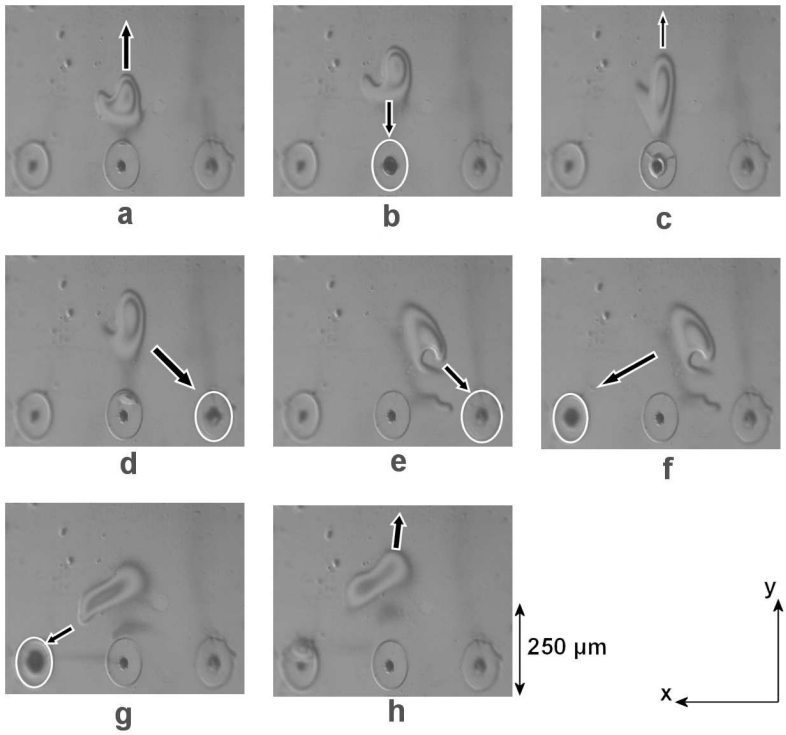

Figure 5.13: Pictures of a moving drop near an array of nozzles. The drop moves continuously. The flow direction is indicated by the arrows. The direction of the movement is determined by the fact whether a nozzle is actuated or not. The frames are in chronological order. (a, c, h) Without actuation the drop moves towards the middle, which is located at the upper side of the pictures. (b, d, e, f, g) The drop moves towards the actuated nozzle, which is indicated by a white circle. The communication between the drop and the nozzles is facilitated by a precursor film.

Without actuation, the drop moves towards the middle of the nozzle plate. This explains the existence of a central band of ink, because often the nozzles are not actuated for a long time. So most of the time, there is a flow of ink in the precursor film towards the middle of the nozzle plate, which maintains the central ink band.

For a direct observation of the precursor film ellipsometry is performed. The result is, that there is an ink layer with a thickness of only $13 \pm 1\ nm$ on the entire nozzle plate surface. This film facilitates the communication between the nozzles

near the long edges of the nozzle plate and the ink band in the middle of the nozzle plate and also Marangoni flow is enabled by the precursor film [66, 70, 157].

5.3.4 Marangoni flow

The most likely cause for creating a surface tension gradient are surfactants. The following discussion is adapted from [87]. When the meniscus in the nozzle oscillates, two effects can decrease the surfactant concentration at the surface. First, a moving meniscus will have on the average a larger surface area, between the minimum area of πR_n^2 and a maximum area of $2\pi R_n^2$ in the non-jetting case. The oscillation frequency of several tens kHz is too high for the surfactant concentration to equilibrate [107]. The surface will be on the average more depleted with surfactant molecules. A second effect is that an oscillating flow in the nozzle will mix the components of the ink. The surfactant molecules will be mixed more homogeneously with the other ink components. This reduces also the surfactant concentration on the surface. Hence, the surface tension will increase in an actuated nozzle.

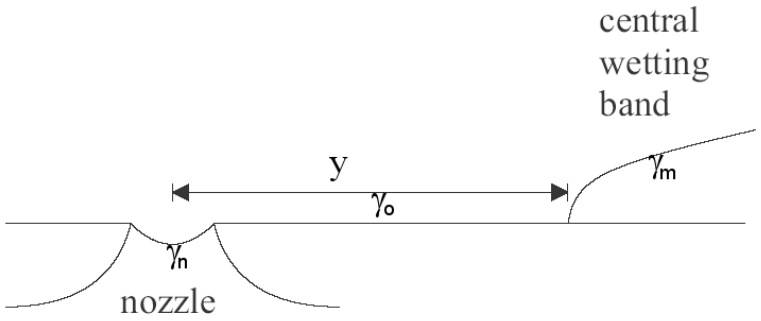

Figure 5.14: Drawing of the ink on the nozzle plate. The distance of the ink to the nozzle is y. The equilibrium surface tension of the ink is γ_0, the surface tension of the ink in the nozzle γ_n and γ_m for the ink in the middle of the nozzle plate.

So when a nozzle is actuated, the surface tension of the ink in the nozzle increases while the surface tension of the ink in the precursor film remains at its low equilibrium position, see also figure 5.14. This effect will be more pronounced for larger actuation. The resulting Marangoni flow is directed towards the nozzle. To get an expression for the speed of the ink front, we integrate equation 5.9 similar to [42, 43, 62, 161] to obtain:

$$y(t) = \sqrt{\frac{h\Delta\gamma}{3\eta}}(t_0 - t)^{\frac{1}{2}} \tag{5.10}$$

This equation is consistent with the experimental observations shown in figure 5.12 and described with equation 5.4. To match the pre-factor of equation 5.10

with the experimental data, the differences in surface tension become 20 mN/m with the actuation at 40 % of the nominal driving amplitude, 30 mN/m with the actuation at 47.5 % and 40 mN/m for the jetting case. These differences are rather high, but the order of magnitude is realistic, taking into account the simplicity of this model.

Without actuation, there is a movement towards the middle of the nozzle plate. This must be caused by the fact that the ink in the middle of the nozzle plate gets also a higher surface tension. Evaporation of the more volatile surfactant molecules results in an increase is surface tension of the ink which is for a longer time on the surface of the nozzle plate i.e. the ink in the middle of the nozzle plate. Both situations are depicted in figure 5.14, with the surface tension γ_m of the ink in the middle of the nozzle plate always larger than the surface tension γ_0 of the ink in the precursor film. Furthermore, γ_0 is less than the critical surface tension with a complete wetting regime as consequence, and γ_m is larger than the critical surface tension with partial wetting regime as consequence. The ink in the middle of the nozzle plate remains visible as a macro-drop. The surface tension γ_n of the ink in the nozzle is only higher than γ_0 when the nozzle is actuated.

5.4 Impact on drop formation

5.4.1 Drop properties

A layer of ink on the nozzle plate around a nozzle has a large effect on the drop formation process. In figure 5.15a-c the effect of an ink layer with increasing thickness on the drop formation is shown. The ink is supplied via static pressure through neighboring nozzles, see also [85]. During one second, a higher ambient pressure of 100 *mbar* is applied to the ink reservoir inside the printhead. This higher ambient pressure is much smaller than the acoustic pressure amplitudes generated by the actuation. The jetting nozzle keeps jetting with almost the same drop speed. From the non-actuated nozzles ink will flow out and spread over the nozzle plate, see also figure 6.2. As the ink layer reaches the jetting nozzle and the thickness of the layer around the jetting nozzle increases, the drop velocity decreases. The pictures are taken with a Phantom high speed camera. A quantitative measurement of the ink layer thickness is not possible, so the experiments can show only the general trends.

An ink layer results in a larger mass of ink at the nozzle. More mass of ink at the nozzle results in more inertia, which slows down the speed of the drop. The drop formation with different ink layer thickness is calculated with Flow3D, figure 5.15b. The pressure at the beginning of the nozzle is kept the same in these calculations, to demonstrate the effect of the ink layer around the nozzle on the drop formation process itself. The resulting drop speed decreases with 0.5 m/s per micrometer ink layer thickness and ceases at an ink layer thickness of 10 μm.

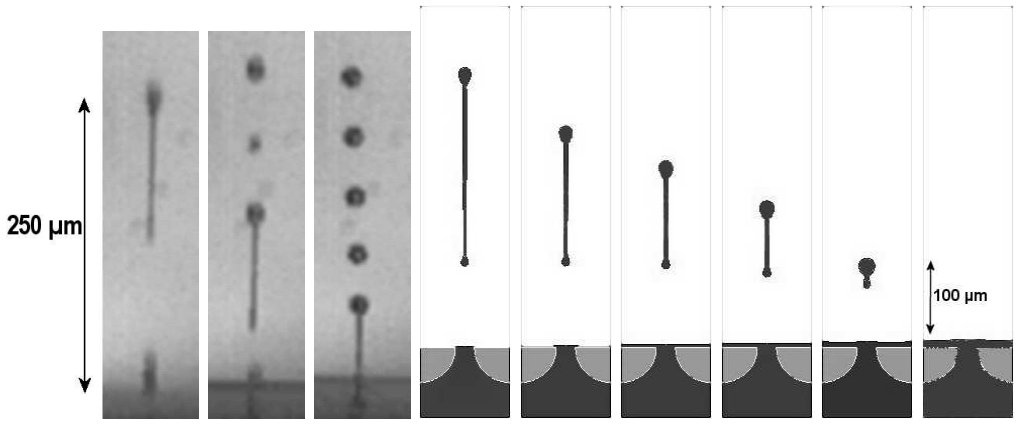

Figure 5.15: (a) The measured effect of an increasing ink layer thickness on the drop formation. The ink is supplied via a static pressure through neighboring nozzles at $t = 0$ [85]. (b, c) As the ink layer thickness increases after 35 and 40 ms, the drop speed decreases. (d-i) The calculated effect of an ink layer with a thickness of 0, 2, 4, 6, 8 and 10 μm. The pressure at the beginning of the nozzle is kept the same in the Flow3D calculations. The pictures show the drop shape at 60 μs after the start of the actuation. The drop speed is 7.5 to 6.5, 5.6, 4.7, 2.9 and 0 m/s respectively.

5.4.2 Channel acoustics

The extra mass of ink at the nozzle also changes the pressure waves inside the ink channels. Like with overfilling because of the refill effect, section 3.4.1, the impedance of the nozzle increases. The reflection of the pressure waves at the nozzle will result in higher pressure amplitudes. The effect is much stronger now. In figure 5.16a the effect of a disappearing ink layer on the pressure at the entrance of the nozzle is shown. With an ink layer thickness of 10 μm or more the pressure amplitude increases more than 50%. This compensates partly the effect of the increased resistance for the drop formation process. The drop speed decreases less slowly and the drop size increases because a part of the ink from the ink layer is dragged along with the drop formation. With a 50% higher pressure amplitude at the entrance of the nozzle, the drop formation fails only with an ink layer thickness more than 20 μm in the Flow3D simulation.

The impact of an ink layer around the nozzle is also visible in the Paint signal, see section 1.3.2. More ink around the nozzle results in a smaller amplitude of the Paint signal, figure 5.16.

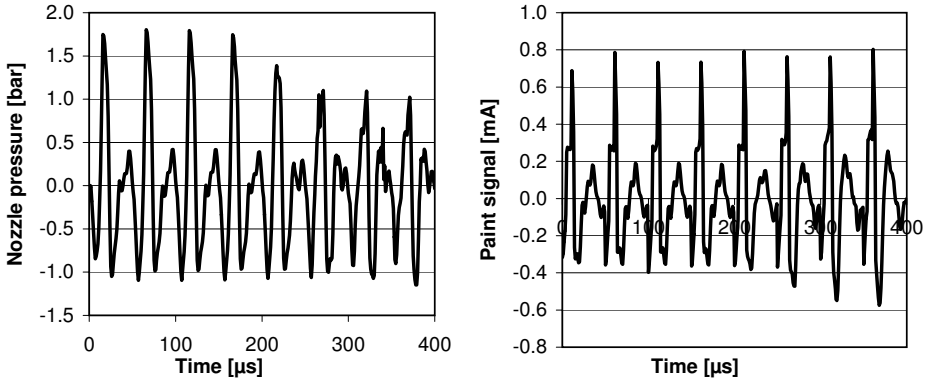

(a) (b)

Figure 5.16: The effect of a decreasing ink layer thickness. Eight drop formation cycles with a repetition rate of 20 kHz are simulated with Flow3D. The ink layer thickness is 20 μm at the start of the first drop formation cycle and decreases to 16, 12, 8, 4, 3, 2 and 1 μm at the beginning of the next cycles. (a) The nozzle pressure decreases from 1.75 MPa to 1.10 MPa and (b) the amplitude of the Paint signal increases.

5.5 Concluding remarks

In the previous chapters the actuation, the generation of the pressure waves and the drop formation process are discussed. In chapter 4 the satellite drop formation was a disturbing mechanism. This chapter is completely dedicated to another disturbing mechanism, i.e. the wetting of the nozzle plate.

The strong refill mechanism results in overfilling of the nozzle, with a risk on inducing wetting. Also the failure of the drop formation process can result in wetting of the nozzle plate. An ink layer around a jetting nozzle disturbs the drop formation. The drop formation is even blocked when the ink layer becomes more than 20 μm. A jetting nozzle induces several flow patterns in the ink layer. The continuous jetting of drops induces an air flow towards the nozzle. This air flow drags the outer part of the ink layer always towards the nozzle. As a consequence a strong sink flow can be visible or a Couette type of flow, when the overfilling of the nozzle adds ink to the inner part of the ink layer. Also an actuated, but non-jetting, nozzle induces all kind of flow phenomena. Dipole, source and sink flow patterns complete the observed phase diagram of possible flow pattern in the ink layer around an actuated nozzle.

The nickel nozzle plate and the ink are in a complete wetting regime. Older ink on the nozzle plate has other properties which results in a partial wetting regime. This older ink accumulates in the middle of the nozzle plate. The dynamic movement of the ink in an actuated nozzle results also in an increase of the surface

tension. The precursor film of fresh ink, which was measured to be 13 nm in thickness, provides a way of communication between the nozzles and the central band of ink. A trunk flow drives the ink from the middle of the nozzle plate towards actuated nozzles. Marangoni flow is the driving mechanism behind this flow pattern.

An ink layer can also have a negative impact on the jetting stability. This will be discussed in the next chapter.

Chapter 6

Bubble dynamics

In this chapter the main factors which determine the jetting stability are discussed. Even after removing large dirt particles and air bubbles from the ink, there are sometimes air bubbles generated during the drop formation process. We will see that because of the low acoustic pressures in the printheads, air entrainment is the only mechanism for the generation of air bubbles. Wetting and small dirt particles play a crucial role in this process. There is a critical ink layer thickness, which results directly in air entrainment. Dirt particles with a size of 20 μm *disturb the drop formation and can also induce the generation of air bubbles. Air bubbles can be measured directly in special transparent heads. The effect of air bubbles on the channel acoustics can be measured by using the piezo actuator also as a sensor. Then it will be discussed that a small air bubble oscillates at its natural frequency after the collapse. These oscillations are visible with the acoustic measurement and can even enhance the drop speed. If an air bubble can dissolve or be jetted out, no problem is generated. However, at the end of this chapter, we will see that an air bubble can also grow in an acoustic field by rectified diffusion. The air bubbles grow to a size comparable to the displacement by the acoustic pressure waves. A large air bubble will not oscillate at its natural frequency but counteracts the pressure build-up and the drop formation process ceases completely.*

6.1 Stability

6.1.1 Dirt and air entrapment

A major requirement for todays productive drop-on-demand inkjet printers is the stability of the droplet jetting process. Large dirt particles can block a nozzle opening completely and there will be no drop formation at all. A nozzle can also be partial blocked by a large dirt particle. This results in severe deviations of the drop speed and size, the jetting angles and the drop shape, see figure 6.1. The particles can originate from the head itself (e.g. graphite particles), dragged along with the ink (e.g. no good enough filtering or non-compatible ink components), or can come from outside (e.g. paper fibres and common dust). Under normal

operating conditions large dirt particles will be removed. This is not further investigated in this thesis.

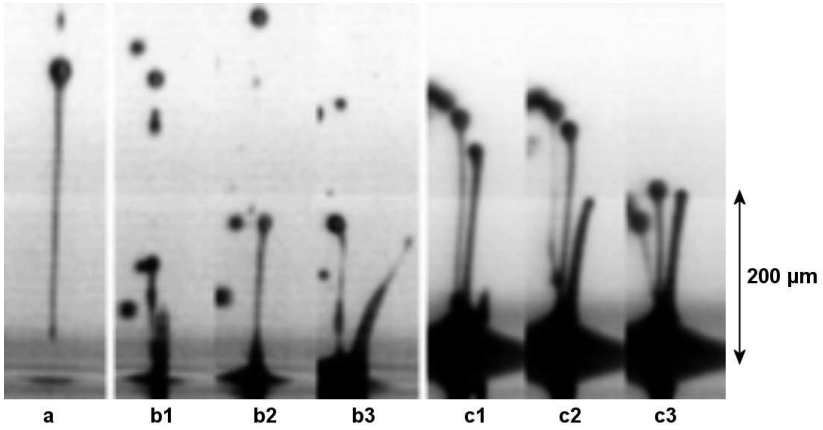

Figure 6.1: High speed camera recordings with (a) the undisturbed drop formation in the left picture. The drop formation with partial blocked nozzles are shown in the other pictures, (b) with drops still jetted away and (c) without jetted drop. The recordings are made with a Phantom V7 high speed camera at 60 μs after the start of the actuation.

Air bubbles will influence the acoustics and the drop formation process and can results in nozzle failure as we will see in this chapter. The ink can contain a lot of air bubbles before the drop formation starts. This air can originate from the ink manufacturing process or from failures in the ink supply system. For normal printhead operation these sources have to be eliminated and also these sources of instability are not a topic in this thesis. The research is concentrated on the generation of air bubbles during normal printhead operation.

Two possible sources for the generation of air bubbles during normal printhead operation are cavitation and air entrainment at the nozzle. Cavitation takes place when the negative acoustic pressure exceeds the Blake threshold at the cavitation nuclei. Cavitation can take place at small air bubbles, at non-wetted channel/nozzle-walls, at non-wetted dirt particles, or at inclusions by surfactants [100]. The acoustic design of the printheads is such that the acoustic negative pressure remains always above the threshold for cavitation. So air entrainment at the nozzle during printhead operation remains as only possible source for the generation of air bubbles.

6.1.2 Acoustic detection of air bubbles

The disturbance or the failure of the drop formation process itself is not suitable for quantitative measurements of the behavior of the bubble. The printheads

developed for application in a printer are opaque. A direct observation of air bubbles in these printheads is not possible. Only in a special transparent head, a direct observation of air bubbles is possible [83, 84, 86]. A way to measure the effect of air bubbles in the opaque heads is to use the piezo actuator also as a sensor. This is the Paint measurement, see section 1.3.2. With the Paint measurement, the electric current from the piezo elements is measured. The Paint current I_p from a piezo element with area A_p is given by the equation:

$$I_p = \frac{dQ}{dt} = A_p \frac{dD_3}{dt} \tag{6.1}$$

with D_3 the electric displacement or charge density in the polarization and actuation direction of the piezo element, see section 2.1. With equation 2.5 we get:

$$I_p = d_{33} A_p \frac{dT_3}{dt} + \epsilon_3 A_p \frac{dE_3}{dt} \tag{6.2}$$

The normal stress component T_3 is generated by the pressure P in the ink channel. The electric field is in the actuation direction $E_3 = V/h_p$, with h_p the height of the piezo element. With V the voltage on the electrodes, this equation becomes:

$$I_p = d_{33} A_p \frac{dP}{dt} + \frac{\epsilon_3 A_p}{h_p} \frac{dV}{dt} \tag{6.3}$$

The capacitance of the piezo element is given by $C_p = \epsilon_3 A_p / h_p$. After integrating the pressure, which can show local variations, over the length l_p of the piezo element we get:

$$I_p = C_p \frac{dV}{dt} + d_{33} b_p \int_0^{l_p} \frac{dP}{dt} dz \tag{6.4}$$

with b_p the width of the piezo element. The Paint current is now known in terms of the actuator voltage and the channel pressure. With the solution for the acoustic channel pressure in the frequency domain:

$$P(z,t) = P_r e^{i(\omega t - kz)} + P_l e^{i(\omega t + kz)} \tag{6.5}$$

we can express the Paint current or signal in terms propagating waves towards the nozzle and coming from the nozzle with wave number k and frequency ω. Inserting this equation in equation 6.4 results in:

$$I_p = i\omega C_p V + d_{33} b_p \frac{\omega}{k} \left(P_l e^{ikl_p} - P_r e^{-ikl_p} \right) \tag{6.6}$$

Not only the drop formation, the refill and the wetting of the nozzle plate changes the reflection of the acoustic pressure wave, but also an air bubble has a large influence on the pressure waves P_l coming from the nozzle.

6.2 Air entrainment

6.2.1 Wetting layer

Air entrainment is directly linked to the presence of an ink layer on the nozzle plate [14, 85–87]. An ink layer around the nozzle results in a lower drop speed, sections 5.4. Flow3D simulations show that the drop speed decreases with ink layer thickness up to 20 μm and the nozzle ceases to fire drops at ink layer thickness above 20 μm. The experiment with adding a layer of ink through the neighboring channels showed the same impact on the drop formation.

The same experiment also shows the formation of air bubbles. Four stages of this experiment are shown in a top view in figure 6.2a-d. First the normal jetting situation is depicted. In the second frame the supply of an ink layer through neighboring channels is shown. The stopping of the drop formation is shown in the third frame. Finally, the creation of air bubbles is depicted. After the drop formation has failed, small air bubbles are visible in the ink layer as indicated.

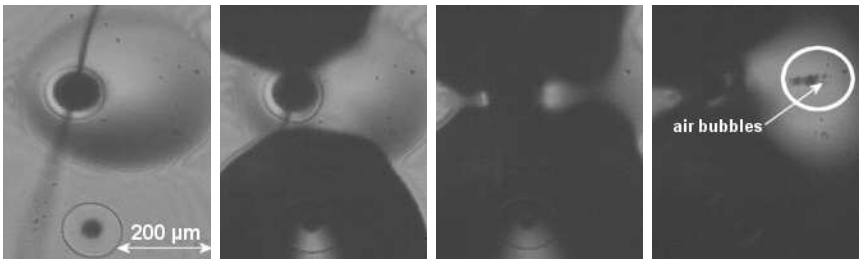

(a) $t = 0\ ms$ (b) $t = 15\ ms$ (c) $t = 45\ ms$ (d) $t = 180\ ms$

Figure 6.2: Top view of an experiment where ink is supplied at t = 0 ms through the neighboring nozzles via a static pressure. The pictures are taken with a high-speed camera with 10 $kfps$. The first frame shows the regular jetting. The second frame is taken at the moment when the ink layer reaches the jetting nozzle. The third frame shows the moment when jetting stops. The last frame shows the air bubbles, which are created. These bubbles are inside the white circle.

The ink layer is applied during 1 s. The ink layer covers a large part of the nozzle plate and is very thick. The drop formation fails, but the actuation continues at a repetition rate of 20 kHz. Air bubbles are visible in the ink layer after 0.2 s. After 1 s, the ink supply stops and the ink layer thickness decreases. After 1.5 s, jetting starts again. It turns out that an air bubble is also entrapped in the jetting nozzle [85].

Flow3D simulations are used for a qualitative check whether air entrainment can be induced by an ink layer on the nozzle plate. With an ink layer thickness of $0 - 20\ \mu m$, only the drop speed is lowered. With an ink layer thickness of more than 20 μm, no drops are generated anymore. In a simulation with an ink layer thickness of 30 μm on the nozzle plate air entrainment is visible as shown in figure

6.3a-d. With this simulation it is assumed that the influence of the ink layer on the pressure waves inside the printhead is negligible. Two actuation cycles at a repetition rate of 20 kHz are modeled. During the first cycle, which started with no fluid movement at all, no air is entrained. Air is entrained during the second cycle. The actual air entrainment occurs when the meniscus is pulling back and ink is already flowing into the nozzle. The void is then closed at the top, because of a lot of ink flows in from the layer around the nozzle. At an ink layer thickness of more than 40 μm, only a net inflow of ink is visible without a large deflection of the free surface.

(a) $t = 0\ \mu s$ (b) $t = 55\ \mu s$ (c) $t = 60\ \mu s$ (d) $t = 65\ \mu s$

Figure 6.3: (a) Flow3D simulation with an ink layer of 30 μm on the nozzle plate. (b-d) During the second actuation cycle, which started 50 μs after the first cycle, an air bubble is entrapped. Taken from [85]

.

The experiment with an ink layer supplied through the neighboring channels shows the formation of multiple bubbles in the ink layer. Because the ink layer thickness varies slowly on a seconds time scale, the critical ink layer is present during multiple drop actuation cycles. Each cycle air can be entrained. To determine the critical layer thickness, experiments are performed with additional nickel plates to create a well defined ink layer thickness around the jetting nozzle [85]. By firing only three drops in one sequence, the amount of ink around the nozzle is not changed significantly. The critical layer thickness turned out to be between 30 μm and 40 μm, in agreement with the simulations.

6.2.2 Small dirt particles [‡]

With a wetted nozzle plate, in most cases a flow towards the nozzle is observed during jetting, section 5.2.1. Relative small dirt particles, caught in the ink layer, are likely to reach the jetting nozzle and this can results in a distortion of the drop formation. This distortion also influences the Paint signal. Therefore the acoustics inside the ink channels are continuously monitored with the Paint signal. At a repetition rate of 20 kHz a time interval of 30 μs between the actuation pulses is taken for further analysis of the Paint signal. The amplitude of the current from

[‡]Part of this subsection has been published as: J. de Jong, H. Reinten, M. van den Berg, H. Wijshoff, M. Versluis, G. de Bruin and D. Lohse, *Air entrapment in piezo-driven inkjet printheads*, J. Acoust. Soc. Am. **120**, 1257 (2006).

the piezo element $I(t)$ during that time interval T is calculated, also called the amplitude of the Paint signal, is defined as [§]:

$$\sigma^2 = \frac{1}{T}\int_0^T [I(t)]^2\, dt \tag{6.7}$$

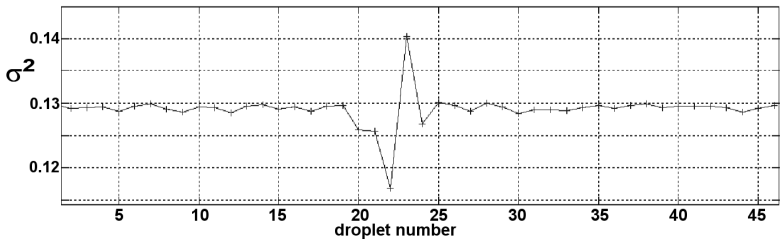

Figure 6.4: The amplitude of the Paint signal. During 25 drop formation cycles before and after a distortion the variance varies less than 0.5 %, the distortion leads to a deviation of 5-10 %.

The amplitude of the Paint signal varies by $5-10$ %, figure 6.4. The amplitude of the Paint signal over 25 drop formation cycles before and after the distortion varies by less than 0.5 %. The influence of the distortion on the Paint signal is used to trigger a high-speed camera to record the drop formation when the distortion takes place [104]. The correlation between the distorted drop formation and the variation in the Paint signal is published in more detail in [85].

The deviation of the amplitude can not only trigger a high-speed camera but also a piezo electric device that can move 60 μm within 1 ms. This device, with a tiny metal chisel attached to it, was placed under the nozzle plate at a distance of a few micrometers from the stream of jetted drops. When triggered, this device moves into the stream of drops to capture them, see figure 6.5. At the same trigger signal also the actuation is stopped, and only the last few drops are captured for further analysis. It turns out that the captured droplets contain relative large particles with a diameter of about 20 μm. These particles are not found in captured drops where no distortion occurred.

A variation of a few micrometers in the position of the meniscus results in a comparable variation of the Paint signal, see also section 3.4.1. To explain that the Paint amplitude is first several percent lower and then several percent larger, the meniscus must first be protruded out of the nozzle and second the meniscus must be retracted. Also a variation in the drop speed is observed during a distortion. The first droplet is 0.1-0.2 m/s faster and the second droplet up to 0.4 m/s slower, with often a deviating shape and jetting angle [85]. The variation in the drop speed, as a result of the different meniscus positions (because of a

[§]Note that in the published article $\sigma^2 - \sigma^2_{ref}$ is plotted in the figures.

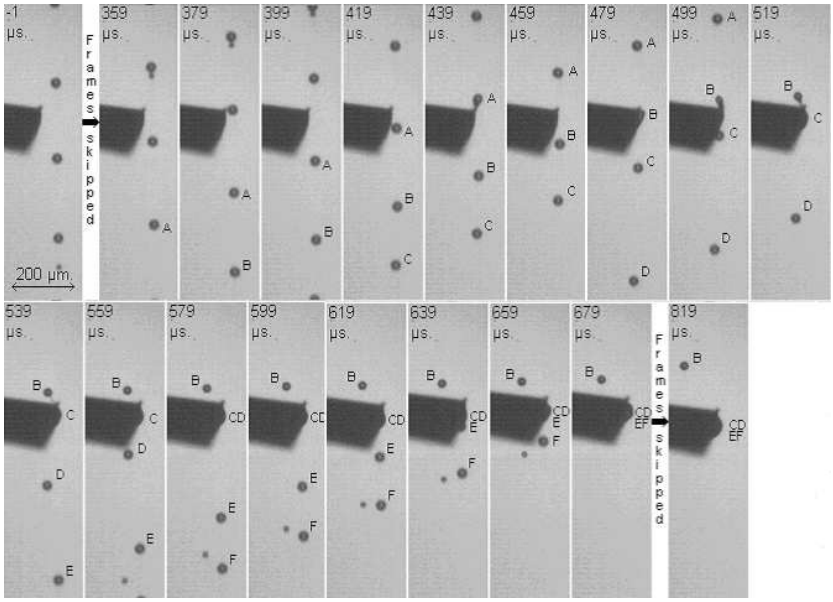

Figure 6.5: High-speed camera recording of the capture of the last jetted drops after a disturbance triggered the piezo electric device. A piezo element with a tiny metal chisel is visible at the left of the drop stream. After the trigger signal, the piezo electric device moves into the stream of drops. The times are given relative to the trigger moment. Four droplets, indicated with C, D, E and F, are caught. Jetting was stopped after droplet F.

variation in the refill level, section 3.4.1), corresponds to the observed variations during the distortion of the Paint signal.

The dirt particles itself can also be the source of the observed variations in drop speed. For a qualitative check, the drop formation is simulated with dirt particles at different positions. In figure 6.6 two examples are shown with a spherical particle at 10 μm and at 30 μm under the meniscus surface. The drop speed varies with the particle at different positions under the surface. With respect to the undisturbed drop speed, the variations are:

- at 5 μm, 1.9 m/s slower and particle is jetted away
- at 7.5 μm, 2.8 m/s slower and particle is jetted away
- at 10 μm, 1.3 m/s faster
- at 10 μm, 0.9 m/s faster
- at 30 μm, 0.4 m/s slower
- at 40 μm, 0.5 m/s faster

From the capturing of the drops, visually and with the piezo electric element, we know that the last drop in the distortion drags along the dirt particle. In the simulation this happens too, when the dirt particles are very close to the surface.

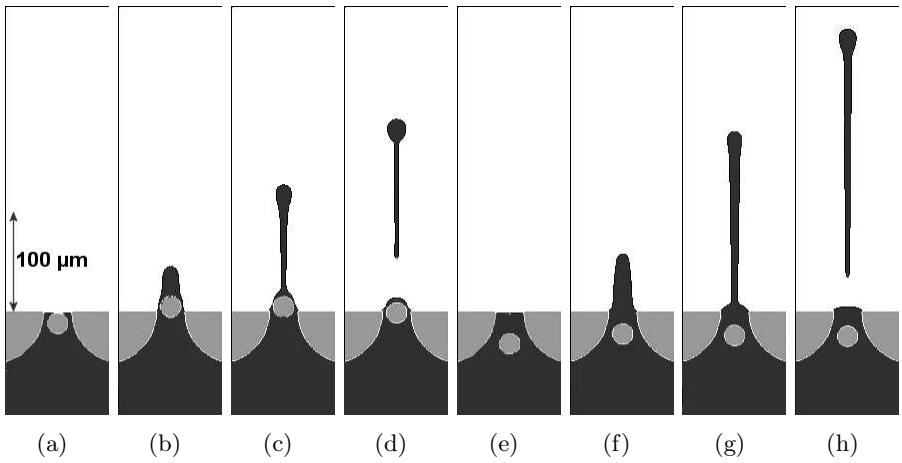

Figure 6.6: Simulation of the effect of a spherical particle with a diameter of 20 μm on the drop formation. The pressure in the channel is kept the same and the starting position of the meniscus is also at its original position. The drop formation is shown at 0, 15, 30 and 45 μs after start of the actuation. First with the particle at 10 μm under the meniscus surface (a,b,c,d) and second with the particle at 30 μm under the surface (e,f,g,h).

The variation of the amplitude of the Paint signal, shown in figure 6.4, is the most common example of a distortion. After the disturbance occurred, jetting keeps going on as usual. But sometimes after a disturbance, an air bubble is entrapped, which becomes later visible as a larger deviation of the Paint signal. After that, there is also a disturbance of the drop formation visible, with finally even the complete break down of the drop formation process. This will be shown in the next subsections. The entrainment of an air bubble is always preceded by a distortion. No air bubbles are detected without a distortion preceding it. So the described distortion is a necessary but not sufficient condition for air entrainment [85].

The exact mechanism of how air is entrained is still not known. In reality the dirt particle have irregular shapes, mostly in the shape of flakes. The drop formation model is a 2D model rotational symmetric model. To simulate irregular shapes a full 3D model is required, which leads to a very long calculation time. The particles are relative large. The particle size is typical 20 μm, the nozzle diameter is 30 μm. Partial blocking of the nozzle opening could be the origin of the air entrainment process. To check this, experiments are done with a 400 μm thick teflon wiper. During the jetting of a single nozzle, the 1 mm wide wiper partially moves over the nozzle with a speed of 3 $\mu m/\mu s$. So the nozzle is partially

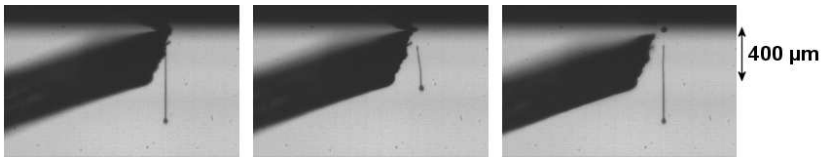

Figure 6.7: High-speed camera recording of the effect of a partial covering of the nozzle opening with a teflon wiper. Shown are the drop formation before, during (the wiper moves away from the camera), and after the covering. The drop formation during the partial coverage is distorted a lot. After the distortion, the drop formation is normal again.

blocked for several actuation cycles. The drop formation is distorted a lot during this period, figure 6.7. If partial blocking of the nozzle is the mechanism behind air entrainment, the experiment should lead to a deterministic generation of air bubbles. However, this is not the case.

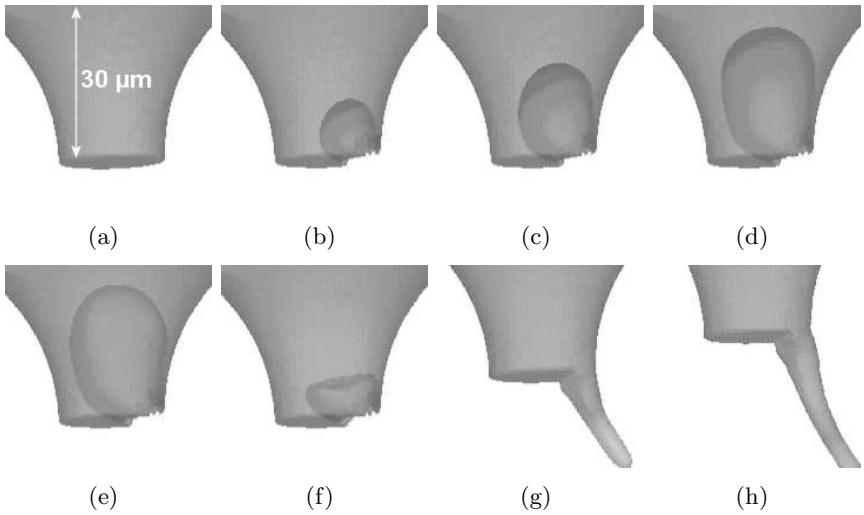

Figure 6.8: Simulation of the effect of a partial coverage of the nozzle opening. The nozzle opening, which has a diameter of 28 μm, is covered over 20 μm from the left. In the picture only the ink domain over the last 30 μm of the nozzle length is shown. Although the drop formation is distorted a lot as in the experiments, the meniscus retraction does not show an increased possibility to entrain air.

This is also qualitative confirmed with Flow3D simulations with a 3D drop formation model with a partial covered nozzle opening. In all the simulations the drop formation is also distorted a lot, with a large deviation of the jetting directions, but air entrainment is not seen. The asymmetric retraction of the meniscus does not give any clues on a larger chance to entrain air. In figure 6.8

an example is shown with the nozzle covered over 20 μm. Only a circle segment with a maximum width of 10 μm at the right remains as nozzle opening.

So the exact mechanism how air is entrained is not clear, but a distortion with a dirt particle with a size of typical 20 μm is necessary to have a chance that air is entrained.

6.3 The oscillating bubble

6.3.1 Size dynamics

The radius of an air bubble changes in an acoustic field. For a bubble in an infinite large volume the bubble radius R of a bubble with radius R_0 at ambient pressure is given by the Rayleigh-Plesset equation [19]:

$$R\ddot{R} + \frac{3}{2}\dot{R}^2 = \frac{1}{\rho}\left(\left(p_0 + \frac{2\gamma}{R_0} - p_\nu\right)\left(\frac{R_0}{R}\right)^{3\zeta} + p_\nu - \frac{2\gamma}{R} - \frac{4\eta\dot{R}}{R} - p_\infty\right) \tag{6.8}$$

The pressure p_ν is the vapor pressure, p_∞ is the imposed pressure at a distance where the pressure due to the inertia of the radial flow field around the bubble is negligible with respect to the imposed pressure fluctuations. It is assumed that the bubble oscillates isothermally, so that the polytropic index $\zeta = 1$ [71]. The imposed pressure fluctuation are calculated with the narrow channel model, see section 3.1. The resulting dynamic changes in bubble size for bubbles with a diameter of 20 μm and a 40 μm are shown in figure 6.9.

In figure 6.9 we can see that the bubble radius increases twice, at 9 μs and at 30 μs. This corresponds to the negative pressure peaks in the pressure at the entrance of the nozzle, see also figure 3.8. When the imposed pressure becomes higher than the ambient pressure, the bubbles collapses. After the collapse the bubble resonates with its natural frequency. The collapse and resonance of a bubble occurs when the frequency of the imposed pressure field is much lower than the natural frequency of the bubble [73]. The channel frequency of the 8 mm long pressure channel is 50 kHz and the natural frequencies of the bubbles are 150 and 300 kHz for the 40 μm and the 20 μm bubbles, respectively. The collapse of air bubbles plays an important role in sonoluminescense [23] and can be used for driving a micro-pump [89]. In our case, the oscillating bubble influences the channel acoustics and the drop formation.

6.3.2 Impact on channel acoustics

When air is entrained, the amplitude of the Paint signal will show an increasing deviation after the distortion, instead of remaining at the same value as shown in figure 6.4. At a repetition rate of 20 kHz, the variance will deviate more than 10% within 100 drop formation cycles , figure 6.10a. It turns out that the deviation is caused by a typical pattern. When looking at the shape of the Paint signal, figure

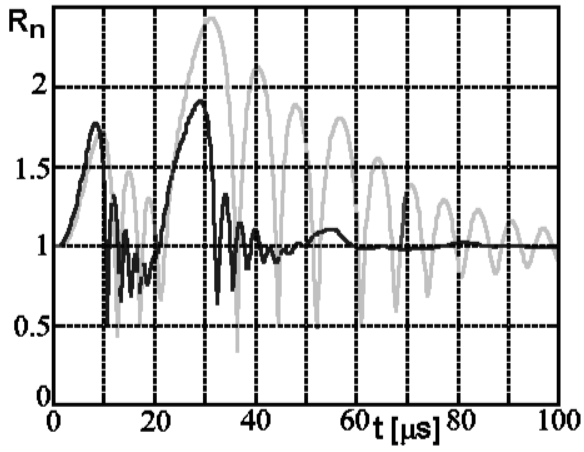

Figure 6.9: The change in bubble size (as normalized radius $R_n = R(t)/R_0$) of bubbles with a diameter of 20 μm (black) and 40 μm (grey). The calculations are done with the Rayleigh-Plesset equation and the pressure from the narrow channel model. The imposed pressure variation is large enough to generate a collapse with an oscillation after the collapse [72].

6.10b, it turns out that the deviation is caused by a distortion with a frequency of 170 kHz [85].

The acoustic waves, emitted by an oscillating bubble, are recorded as a 170 kHz distortion, figure 6.10b. We see the oscillation of a bubble as a 170 kHz distortion because this frequency is next to the basic channel resonance at 50 kHz the next strong peak in the frequency characteristics of this head. The frequency characteristics describe the relation between the electric activity in the actuator and the meniscus movement. This characteristic acts also as a filter for the Paint measurements.

The natural frequency f_0 of a free bubble, neglecting surface tension, viscosity, vapor pressure and advection, is called the Minnaert frequency [100]:

$$f_0^M = \frac{1}{\pi D_0}\sqrt{\frac{3\zeta p_0}{\rho}} \tag{6.9}$$

The resonance frequency of 170 kHz corresponds to a bubble diameter of 36 μm. However, an air bubble in an inkjet printhead is not a free bubble. The bubble is located within a confined space. The confined space is the semi-closed connection channel with a diameter of 250 μm and a small nozzle opening. The resonance frequency will be reduced by 30-50 % for a bubble with a diameter of 20-40 μm [61, 126]. So the diameter of the bubble causing the 170 kHz resonance is 18-25 μm. The volume of the air bubble is $2 - 8$ pl, much smaller than the volume displacement by the acoustic pressure field. This means that the results of the

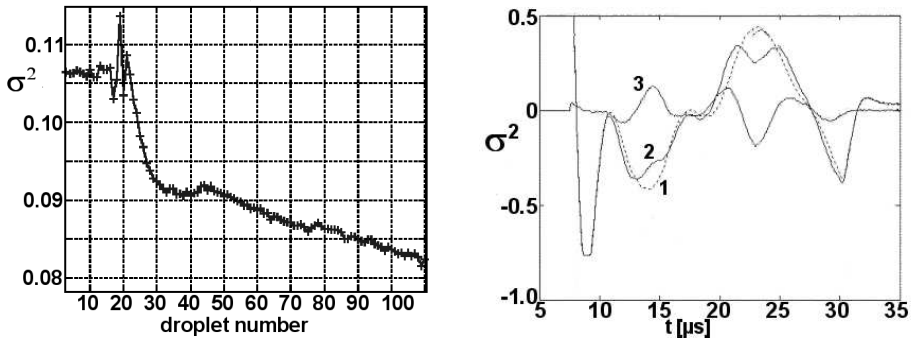

(a) (b)

Figure 6.10: (a) The amplitude of the Paint signal when a distortion occurs before cycle 20 and air is entrained. The amplitude of the Paint signal deviates more than 10 % within 100 drop formation cycles at a repetition rate of 20 kHz. The actuation amplitude is the nominal driving amplitude for a drop speed of 7 m/s. (b) The shape of the Paint signal without an air bubble (dotted line 1), with an air bubble (continuous line 2), and the difference between the two signals (continuous line 3). This shows a 170 kHz distortion after 100 drop formation cycles.

calculations without a two-way coupling to the channel acoustics, as shown in figure 6.9, give a good approximation.

When a bubble shows a collapse in the response to the imposed pressure field, also thermal and acoustic damping should be taken into account [23, 38]. This makes the description of the dynamical behavior of a bubble in an acoustic field rather complicated. This is not further investigated in this thesis.

6.3.3 Impact on drop formation ¶

The experiments with the opaque heads show no variation of the drop speed during the first 100 drop formation cycles [85]. In these heads, relative small bubbles with a diameter less than 20 μm, radiate sound waves, which give a deviation of the acoustic pressure inside the channel of more than 10%, figure 6.10a. However, this has no impact on the drop formation process.

A transparent head is developed for a direct visualization of the behavior of the air bubble [83], see also figure 6.12. A nozzle plate and a connection channel are made with powder-blasting out of glass plates. The transparent connection channel has a length of 400 μm and a hourglass shaped cross-section with a diameter between 80 μm and 250 μm. The 70 μm long conical shaped nozzle has

¶Part of this subsection has been published as: J. de Jong, R. Jeurissen, H. Borel, M. van den Berg, H. Wijshoff, H. Reinten, M. Versluis, A. Prosperetti and D. Lohse, *Entrapped air bubbles in piezo-driven inkjet printing: their effect on the droplet velocity*, Phys. Fluids **18**, 121511 (2006).

an entrance diameter of 50 μm and an outlet diameter of 30 μm, see also figure 6.9a. These glass plates replace the 50 μm nickel nozzle plate.

The pressure channel of this head has a length of 5 mm and there is also the normal connection channel with a length of 1 mm. The acoustic properties of this printhead are comparable with the opaque head. High speed camera recordings with a Phantom V7 camera at 40 $kfps$ and a continuous light source behind the glass plates show the relation between the behavior of an entrained air bubble and the impact on channel acoustics and the drop formation.

In the experiment with the transparent head, the oscillations of a bubble have an effect on the drop speed [86]. This is shown in figure 6.11a for a range of bubble diameters between 22-38 μm. The driving amplitude is low, which results in a drop speed of only 1 m/s without an air bubble. In the experiment the droplet velocity increases and reaches a maximum of 2.5 m/s. Then the droplet velocity gradually decreases to 1 m/s at 0.9 s. A small amplitude oscillation with $f = 50Hz$ is superimposed onto the droplet velocity, reflecting the AC frequency of the devices. This effect is negligible compared to the effect of the entrained air bubble on the drop speed.

The recorded images of the ejected droplets and oscillating bubbles are analyzed with a gray-level threshold to determine the location of the edges of the droplets and bubbles. The images of the bubbles only consist of some tens of pixels, limiting the accuracy of the size determination. Other sources of errors are the optical diffraction and the assumed sphericity of the bubbles in the digital image analysis. For the ejected drops and for the bubbles within the channel (away from the walls) we do not have any indication of deviations from sphericity. However, the air bubbles, when pushed against the glass nozzle plate, seem to be slightly non-spherical.

The scatter in the bubble radius is found to be quite large, due to the low contrast in the images and because multiple bubble radii are measured over one acoustic cycle. When we compensate for the latter by plotting the average radius (over 40 bubble radii), the bubble growth becomes more obvious. This is used in figure 6.11b where the two data sets are combined to get the drop speed as function of bubble size. The measured drop speed increases to 2.5 m/s with increasing bubble size until a diameter of 33 μm and than decreases very fast with increasing bubble size. Finally, jetting fails with a bubble diameter from 38 μm on.

A resonance effect of the bubble oscillation with the meniscus movement results in the increase of the velocity. This can be verified with a simple model [82], which is based on the approach used in [126]. The dynamic behavior of the bubble is based on the polytropic relation $pV^{\zeta} = constant$ between bubble volume and the pressure. The meniscus movement is based on Newton's second law with a Poiseuille flow profile in the nozzle. The continuity equation completes the set of equations. After linearization around the equilibrium volume, a forced harmonic oscillator equation for the meniscus speed is obtained. A sinusoidal velocity is imposed with the main channel resonance frequency, which is also 50 kHz for the

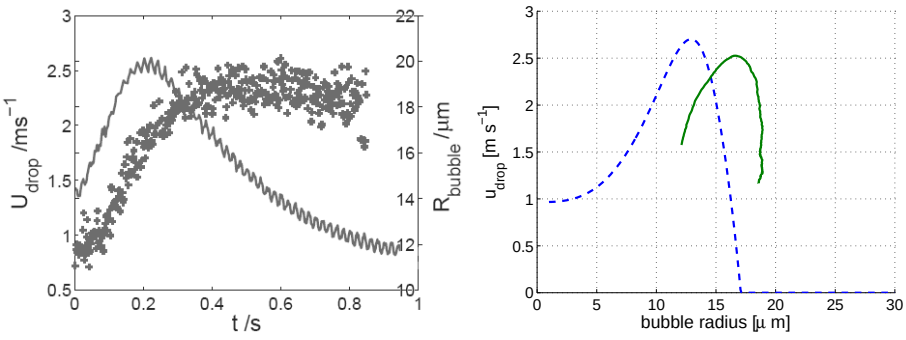

(a) (b)

Figure 6.11: (a) Simultaneously measured bubble radius and drop speed with the transparent head described in [86]. The actuation is started at t = 0 s. The bubble diameter increases from 22 to 38 μm and the drop speed increases from 1 to 2.5 m/s at 0.2 s and decreases again. (b) The resulting relationship between bubble diameter and drop speed as measured (solid line) and calculated with the simple harmonic oscillator model (dashed line). The measured drop speed shows a maximum at a bubble diameter of 33 μm. Jetting fails with a bubble diameter larger than 38 μm.

transparent head. The diameter of the bubble where the resonance effect takes place reads according to this model [86]:

$$D_0^{res} = \left(\frac{6\zeta \rho A_n^3 p_0}{\pi l_n (\rho^2 \omega^2 A_n^2 + 64\pi^2 \eta^2)} \right)^{\frac{1}{3}} \tag{6.10}$$

In the model, the conical nozzle shape is replaced by a straight nozzle with the same outlet diameter as the conical shaped nozzle, i.e. 30 μm. The conical nozzle has an entrance diameter of 50 μm and a length of 70 μm. This is transformed to a straight nozzle with the same acoustic impedance, see section 3.1.2 and equation 3.26. The length of the acoustic equivalent straight nozzle is 32 μm. The resulting drop speed is shown in figure 6.11b, together with the measured results. The drop speed is calculated with the energy balance as mentioned in section 3.2.2. The results of the simple model agree reasonable with the experimental data. Only the bubble diameter where the resonance effect takes place is a little smaller, 26 μm instead of 33 μm.

The natural frequency of a bubble with diameter D_0 which acts as a harmonic oscillator with the meniscus movement of a nozzle is:

$$f_0^H = \sqrt{\frac{3\zeta D_n^2}{8\pi \rho l_n D_0^3}} \tag{6.11}$$

The natural frequency of a bubble with diameter $D_0 = 33\ \mu m$ is 50 kHz, the same as the main channel resonance frequency.

For the opaque heads the resonance effect would take place for a bubble diameter of 40 μm. The volume of the bubble, 34 pl is than of the same order of magnitude as the displacement by the acoustic pressure field. In the calculations so far, the imposed acoustic pressure is not altered by the bubble. When the volume of the bubble is of the same order of magnitude as the displacement by the acoustic pressure, this assumption is not valid anymore. The impact on the channel acoustics will be very large. A two-way coupling between channel acoustics and the dynamic behavior of the bubble is necessary in order to get a model giving results in agreement with the experimental observations.

6.4 The moving bubble

6.4.1 Balance of forces [‖]

Many forces are acting on a bubble in an acoustic pressure field. First there is the primary Bjerknes force. The force acts in the direction of the acoustic pressure gradient. A small bubble will be pushed towards the pressure node, i.e. the small bubble will move towards the channel. A very large bubble will have a low natural resonance frequency and start to oscillate in anti-phase with the acoustic pressure field. The primary Bjerknes will now act in the opposite direction towards the pressure anti-node, i.e. the bubble will move towards the nozzle.

The secondary Bjerknes forces are generated by the acoustic pressure field emitted by the oscillating bubble itself. Due to a mirror effect this force will push bubbles against a rigid wall. These two forces can explain the main characteristics of the experimentally observed displacement of a bubble. This is the optical measurements with the transparent printhead [84]. A small bubble which is generated near the nozzle, moves with a speed of 5 mm/s towards the channel, because of the primary Bjerknes force, and is attracted against the (transparent) connection channel wall, because of the secondary Bjerknes force. After a while this bubble has grown in size to a diameter of 32 μm. The natural frequency of this bubble as harmonic oscillator, as described in the previous section, is reduced to 55 kHz and tends to become lower than the frequency of the main channel resonance. The bubble moves now with a speed of 20 mm/s in the opposite direction towards the nozzle plate.

Especially near the nozzle itself the drag force from the ink flow becomes important. This force tends to drag the bubble along with the ink flow, thus along with the drop formation. Buoyancy or gravity forces play no role in our case. Other forces which could play a role are lift forces from the radial flow field, the added mass and inertia forces and finally the Basset history force which results from the absorbed momentum in the boundary layer around the bubble [151]. These forces will results in complicated movement patterns.

[‖] Part of this subsection has been published as: J. de Jong, M. Versluis, G. de Bruin, D. Lohse, H. Reinten, M. van den Berg, H. Wijshoff and N. de Jong, *Acoustical and optical characterization of air entrapment in piezo-driven inkjet printheads*, Proc. IEEE-IUS **2**, 1270 (2005).

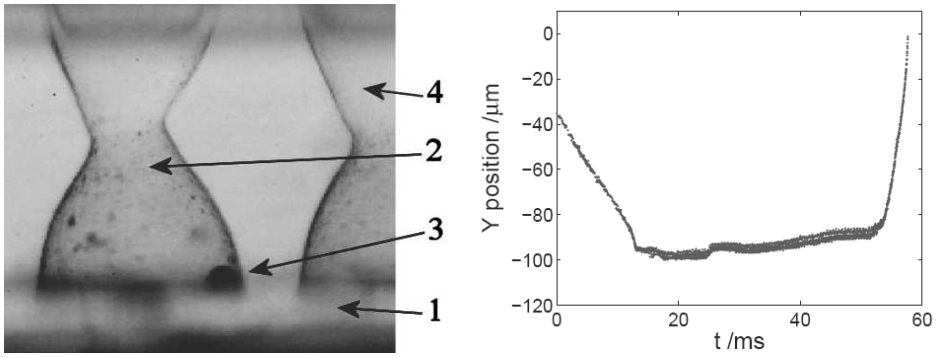

(a) (b)

Figure 6.12: (a) The transparent head, used for direct visual measurements of entrapped air bubbles with the nozzle plate 1, the connection channel 2, an air bubble 3, and a neighboring channel 4. (b) The y-position of the air bubble as a function of the time after the air entrapment. The bubble first moves into the channel. At t = 52 ms the Bjerknes force reverses sign and the air bubble is pushed back towards the nozzle. Taken from [84].

6.4.2 Net displacements

The forces on the bubble result in a displacement pattern, which can only be resolved numerically for an opaque printhead. In figure 6.13a the net displacement after one drop formation cycle is shown. The bubble has a diameter of 10 μm at different positions on the nozzle axis. The results are simulated with a 2D rotational symmetric drop formation model in Flow3D. So only bubbles at the nozzle axis can be simulated. The pressure inside the bubble is calculated with the polytropic equation. The initial pressure inside the bubble is equal to the ambient pressure enlarged with the Laplace pressure $2\gamma/R_0$. The pressure in the connection channel at a position 300 μm in the channel in front of the nozzle is kept the same. There is only a one-way coupling between the channel acoustics and the flow phenomena in the nozzle. The bubble cannot influence the pressure waves in the channels in these simulations.

Depending on the axial position, the bubble is either moved inwards or outwards after one drop formation cycle. There are four positions where the net axial displacement becomes zero. Two positions are unstable because the bubble at locations around this point moves further away from these positions. That are the position at 25 μm and 72.5 μm. But, the two axial positions at 62.5 μm and 105 μm are stable. The bubble at locations around points moves towards these positions. These two positions act as a bubble trap.

At axial positions between the meniscus and 20 μm behind the surface, the bubble is jetted out. Also experiments show that jetting out of an air bubble is a possible recovery mechanism. In figure 6.13b the amplitude of the Paint

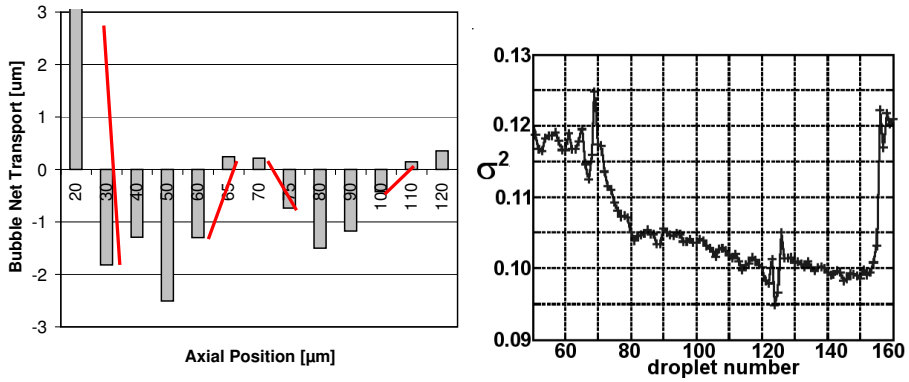

(a) (b)

Figure 6.13: (a) Simulation of the net bubble displacement after one drop formation cycle. Depending on the axial position the bubble with a diameter of 10 μm is moved outward or inward. At axial positions around 62.5 μm and 105 μm the bubble can be trapped. At axial positions between 0 μm and 20 μm the bubble is jetted out. (b) Measured amplitude of the Paint signal with distortions at drop formation cycles 70 and 124, air entrainment after drop formation cycle 70. The jetting out of a bubble is visible at drop formation cycle 155. This is a fast recovery mechanism, generated by the net displacement pattern inside the nozzle.

signal is shown. At drop formation cycle 70 a distortion occurs followed by air entrainment. At drop formation cycle 124 a second distortion is visible without any consequences. With drop formation cycle 155 the amplitude of the Paint signal returns in one cycle to its normal value, which can only be caused by jetting out of the bubble. The numerical simulation of the jetting out is shown in figure 6.14.

6.5 The growing bubble

6.5.1 Rectified diffusion and dissolution

A bubble in an acoustic pressure field will grow by rectified diffusion when the pressure variations are strong enough [19, 59, 71]. At pressure maxima, air is squeezed out of the bubble, but this loss is overcompensated at the pressure minima when the bubble expands. This results in a net gas diffusion into the bubble.

In the transparent head growth rates are optically measured. The net growth rate is 0.04 pl/ms when actuating at 10 kHz with a relative low driving amplitude for a drop speed of 1 m/s [86]. This is a net growth of 0.004 $pl/cycle$. With a very low non-jetting actuation amplitude at a repetition rate of 20 kHz, the net growth rate is 0.39 pl/ms or 0.02 $pl/cycle$ [84].

Without an acoustic field the bubble will dissolve. There is no net transport of ink and the ink around the bubble will saturate with dissolved air and the

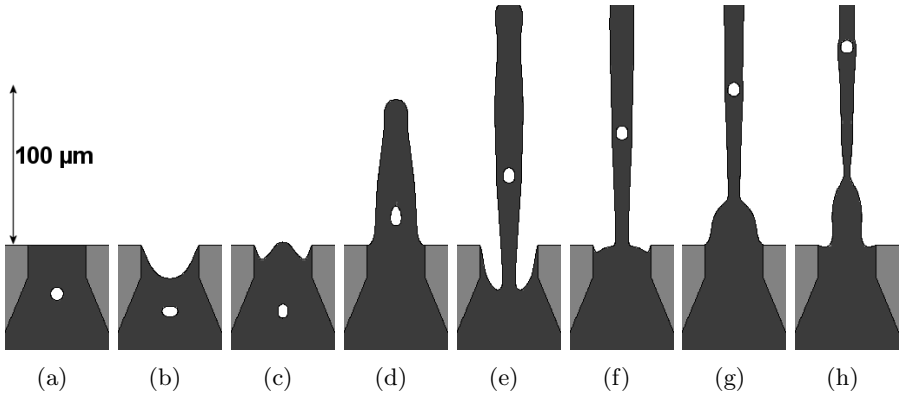

Figure 6.14: Simulation with Flow3D of the jetting out of a bubble. The bubble has a diameter of 10 μm at an axial position 20 μm under the meniscus. The frames show the drop formation with the bubble at 0, 8, 16 . . . 56 μs after start of the actuation. The channel length is 8 mm and nozzle diameter is 32 μm.

dissolution rate will be rather low. In the experiments without actuation with the transparent head [86], the dissolution rate of a 26 μm bubble is constant at 0.5 pl/s until the bubble is completely dissolved. This is shown in figure 6.15. The dissolution rate is 2 to 3 orders of magnitude slower than the growth by rectified diffusion. This can also be seen in the figure, where the bubble size increases much faster when the actuation starts again.

The bubble size increases fast and saturates at an equilibrium size of 20 pl within a second. After 1000-5000 actuation cycles, the growth by rectified diffusion is balanced by the dissolution of the bubble. This equilibrium is broken at the moment when jetting breaks down. Without drop formation the bubble size saturates at a much larger size of almost 70 pl.

With jetting, the ink around the bubble will be continuously refreshed. The ink around the nozzle and the air bubble will be less saturated with dissolved air. This results in higher dissolution rates. The saturation size in the jetting situations will be smaller than in the non-jetting situations. Experimental data are only obtained with a transparent head. In the jetting situations the bubble size saturates always at a diameter of 35-40 μm (20-33 pl) and in the non-jetting situations at a diameter of 45-50 μm (50-70 pl) [83, 84, 86].

Just after the air entrainment the bubble has a diameter of 12 μm (0.9 pl), as measured visually with the transparent heads [84]. In the opaque heads the bubble size is estimated at 20 μm (4 pl) after 100 drop formation cycles at a repetition rate of 20 kHz with a nominal driving amplitude for a drop speed of 7 m/s, section 6.3.2. We assume that the bubble size is the same as in the transparent heads just after the air entrainment. This gives an estimation of the net growth rate of 0.62 pl/ms or 0.03 $pl/cycle$.

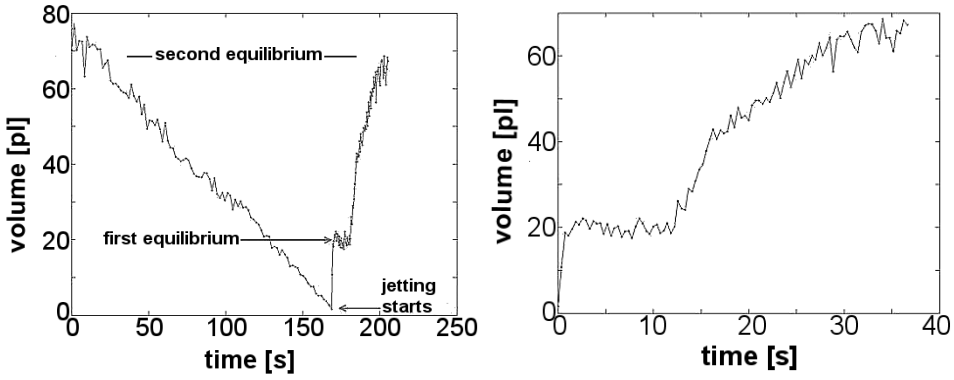

(a) (b)

Figure 6.15: Measured bubble size with actuation stopped at $t = 0$ s until $t = 165$ s. The dissolution rate is 0.46 pl/s. Then the actuator is turned on and droplets are jetted from the nozzle. The bubble size increases fast and saturates at an equilibrium size of 20 pl within a second. The equilibrium is broken after 12 seconds at the moment jetting breaks down. This is shown in the second figure, which shows only the first 40 s after the actuator is turned on again. Without drop formation the bubble size saturates at a much larger size of almost 70 pl.

6.5.2 Influence of the actuation

When turning off the actuation for a specific time interval, the bubble will either be entirely dissolved or only partly. This can be seen in the Paint signal after the actuation is started again. If the time interval is long enough, the bubble will be dissolved completely, and the Paint signal is normal again. When the time interval is not long enough, the bubble is dissolved only partly. The bubble is still present and the modification of the Paint signal by the bubble will still be visible. The bubble will again grow by rectified diffusion until it saturates at its equilibrium size.

This is in fact what happens in the experiment with the regular head, where the growing and dissolution cannot be measured optically. A bubble is created during an actuation at a high drop repetition rate. Then the repetition rate is lowered stepwise and the Paint signal is monitored until a new equilibrium is established. By lowering the repetition rate the bubble will get more and more time to dissolve until it is dissolved completely before the next drop is jetted. The results of this experiment are shown in figure 6.16.

The analysis of the Paint signal is this figure is as follows. The current from the piezo element $I(t)$ during a time interval T is compared with a reference $I_0(t)$ (i.e.

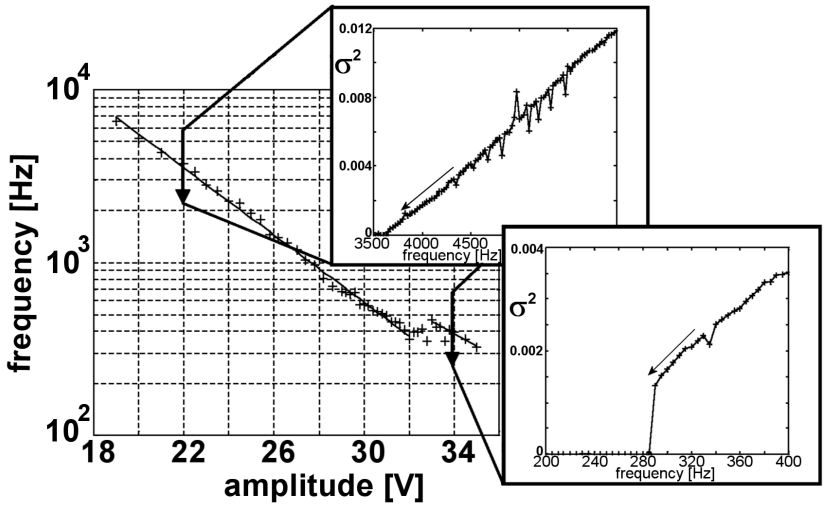

Figure 6.16: (a) Measured drop repetition rate at which the air bubble, which is created at a repetition rate of 20 kHz, dissolves completely when lowering the repetition rate. At low driving amplitude the rectified diffusion is weak and the bubble dissolves already at a high repetition rate. At a high actuation amplitude, the repetition rate must be lower before the bubble disappears. (b) The decrease of the deviation of the Paint signal (as variance of the difference with the reference Paint signal). At 22 V the bubble dissolves and the deviation decreases gradually to zero (upper picture). (c) At 35 V the bubble can be jetted out and the deviation decreases stepwise to zero (lower picture).

the signal without air bubbles) and the variance σ^2 of the difference is calculated:

$$\sigma^2 = \frac{1}{T}\int_0^T \left[I(t) - I_0(t)\right]^2 dt \tag{6.12}$$

At a low actuation amplitude, the rectified diffusion is slow and the bubble dissolves completely in a relative short time. Lowering the repetition rate to 1-7 kHz is already sufficient at actuation amplitudes of 50-80 % of the nominal amplitude, which is 35 V. At nominal actuation amplitude the repetition rate must be lowered to 200 Hz before the bubble dissolves completely.

Because of jetting out along with the drop, bubbles can disappear already at 400 Hz at the nominal driving amplitude. This is shown in figure 6.16b+c, where the variance of the difference between the Paint signal and the reference signal is depicted as a function of the decreasing repetition rate. In figure 6.16b, the decreasing deviation of the Paint signal is shown when a bubble dissolves completely between a repetition rate of 6 and 3.5 kHz. In the lower picture the decreasing deviation is shown when the bubble is jetted out at a repetition rate 285 Hz.

6.5.3 Impact on channel acoustics

At high repetition rates of 10-20 kHz and nominal actuation amplitudes, air bubbles grow during 1000-5000 actuation cycles to a bubble size of 50-70 pl. This volume is comparable to the total volume displacement by the acoustic pressure wave. The volume displacement of acoustic pressure field can be counteracted by the change in bubble size. This will change the acoustic properties of the channel completely.

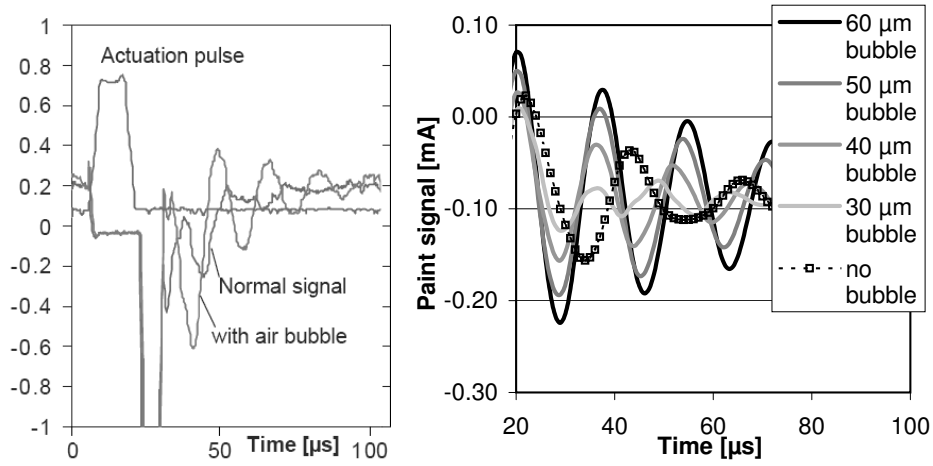

(a) (b)

Figure 6.17: Measured (a) and calculated (b) effect of a large air bubble on the Paint signal. A large air bubble acts as an open boundary condition for the pressure waves inside the channel. The acoustic properties of the channel shift to a $\frac{1}{2}\lambda$ resonator with a frequency of 65 kHz instead of 50 kHz. The frequency and also the amplitude of the acoustic pressure increase.

Without an air bubble, the nozzle acts as a partial closed boundary condition for the pressure waves inside the ink channel, see section 3.1.2. The channel will act almost as a $\frac{1}{4}\lambda$ resonator. A large bubble can counteract the pressure build-up. This results in a complete open reflection. The channel will act now as a $\frac{1}{2}\lambda$ resonator. The main resonance frequency will increase and also the amplitude of the pressure wave will increase. This is visible in the measured and in the calculated Paint signal, figure 6.17.

The variation of the Paint signal in the experiment with lowering of the repetition rate contains information on the behavior of a small air bubble and the behavior of a large air bubble. With FFT-transformation of the Paint signals we get the frequency components in the Paint signal. The amplitude and the phase of two important frequency components are shown in figure 6.18 as function of the drop repetition rate.

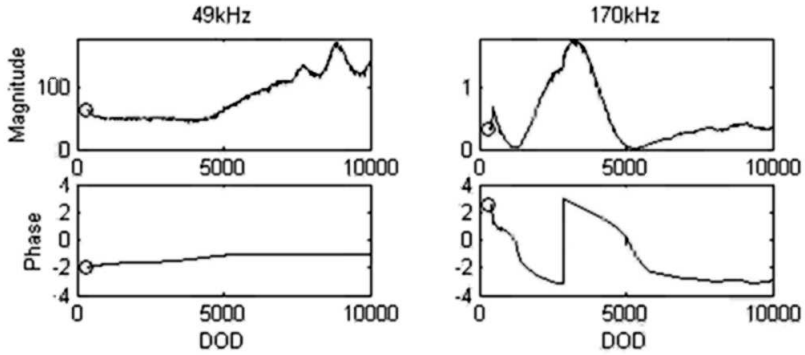

Figure 6.18: The amplitude and phase of the 50 and 170 kHz components in the Paint signal as function of the drop repetition rate. A large air bubble is created at high drop repetition rate. The Paint signal is measured after a stepwise lowering of the repetition rate, when the bubble is saturated at its new equilibrium size. FFT-transformation of the Paint signal results in the depicted amplitude and phase of the 50 and 170 kHz components. The 170 kHz component shows an oscillation, especially via the 2π phase shift. The amplitude and phase of the 50 kHz does not show an oscillation of the bubble.

A small air bubble will show a collapse and an oscillation at its natural frequency, section 6.3.2. With the frequency characteristics of the printhead this is measured as a distortion with a frequency of 170 kHz. This frequency component shows a 2π phase shift in figure 6.18. A large air bubble will change the main channel resonance at 50 kHz towards a $\frac{1}{2}\lambda$ resonator.

6.5.4 Impact on drop formation

When a distortion leads to air entrainment the bubble diameter is 20 μm after hundred drop formation cycles. The drop speed remains the same during the first 100 drop formation cycles in a regular head. The bubble continues to grow and the drop speed starts to decrease with 1 m/s during the next 300 drop formation cycles [85].

In the experiments with the transparent head [86] jetting breaks down at a bubble diameter of 38 μm. The bubble size is then of the same order as the volume displacement by the acoustic pressure field. The bubble counteracts the acoustic pressure variation. There is no driving force left for the ink movement in the nozzle. A large bubble changes the pressure waves inside the ink channel. For numerical simulations with Flow3D, we have to use the acoustic model. The drop formation process comes to an end as shown in figure 6.19.

The acoustic Flow3D simulation can only show the main trends for large bubbles. The minimum applicable grid size with the acoustic calculations is too coarse to model bubble sizes less than 30 μm. For bubbles sizes of 30-60 μm the accuracy

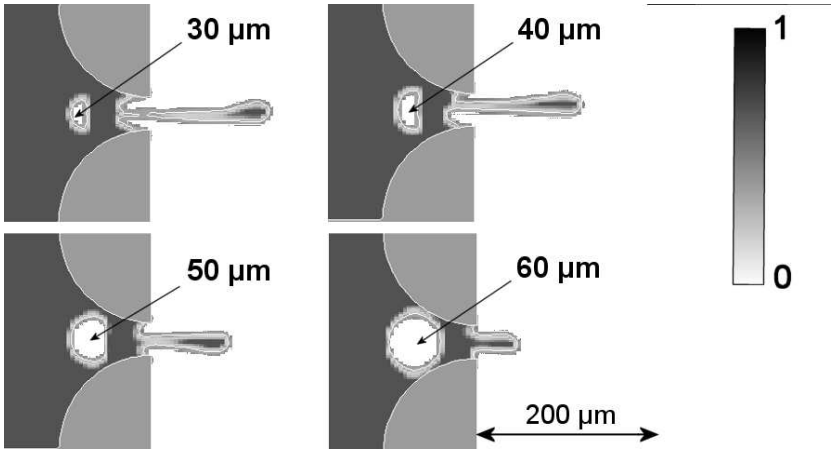

Figure 6.19: Breakdown of the drop formation process with large air bubbles. The channel length is 8 mm and the nozzle diameter 32 m. The drop speed without an air bubble is 7 m/s. The simulations of one drop formation cycle for bubble diameters of 30, 40, 50 and 60 μm are done with the acoustic model in Flow3D. Shown is the fraction of fluid. There are no sharp interfaces, because the minimum applicable grid size is too coarse for an accurate simulation.

is not very good as can be seen in the figure. We need another model to simulate the behavior of air bubbles and their impact on the acoustic properties of the printheads.

In [83] a one-dimensional model has been developed. This is based on the narrow channel theory for the channel acoustics. The bubble dynamics are described with a linearized Rayleigh-Plesset equation. Essential in the model is the two-way coupling between channel acoustics and bubble dynamics. The model shows the importance of the impact that large bubbles have on the acoustic properties. The air bubble acts back on the acoustic pressure field in the ink channel, thus on its own dynamics. An air bubble with a diameter of 46 μm reduces the nozzle pressure by a factor of four. This causes the collapse of the drop formation process. The counteraction on the pressure build-up also limits further bubble growth and thus determines the saturation size of the bubble. The model also shows the shift of the main channel resonance frequency towards the higher frequency of the $\frac{1}{2}\lambda$ resonator characteristics. Another important result is that the bubble collapse disappears and that the large bubble oscillates with the same frequency as the channel acoustics.

6.6 Concluding remarks

In chapter 5 the wetting of the nozzle plate was discussed. The wetting of the nozzle plate is also a source for jetting instability, the subject of this chapter.

There is a critical layer thickness, which directly leads to air entrainment. The generation of air bubbles is the mechanism, which can lead to nozzle failure. The wetting layer plays also a role in combination with 20 μm small dirt particles, caught in the ink layer and transported towards the nozzle. The distortion by a dirt particle can be detected with an acoustic measurement, which uses the piezo elements also as sensors.

An entrapped air bubble will oscillate in the acoustic pressure field. The acoustic properties of the ink channel act as a filter for this measurement. Therefore the oscillations of small air bubbles are recorded as a signal with a frequency of 170 kHz. Primary and secondary Bjerknes forces, drag forces and many other forces result in movement patterns of the air bubble. The movement of an air bubble can result in jetting out, thus in a fast recovery. The movement of air bubbles can be visualized with a special transparent head. Small air bubbles do not have a negative effect on the drop formation process. However, in the pressure field the bubbles will grow by rectified diffusion. The growth rate is much faster than the dissolution rate, the other recovery mechanism. The air bubbles grow in the pressure field to a size comparable with the drop size and the displacement by the acoustic pressure waves. The large air bubble will then counteract the pressure build-up and the drop formation process ceases completely.

Chapter 7

Conclusions

In the past decades, inkjet technology has evolved into a technology which plays an important role in the graphical printing industry and in many emerging new industrial and medical applications. The piezo inkjet technology has unique capabilities due to its ability to deposit a wide variety of materials on various substrates in well defined patterns. To comply with the increasing and diverging requirements for today's inkjet technology, a fundamental understanding of the underlying processes is very important. This justifies the research, reported in this thesis, which extends over the solid mechanics field and the fluid mechanics field.

The physics behind the chain of processes comprise the two-way coupling from the electrical to the mechanical domain through the piezo electric actuator, the coupling to the acoustic domain inside the ink channels, and the coupling to the fluid dynamic domain, the drop formation process. Furthermore, wetting of the nozzle plate and air bubbles can have a negative influence on the printhead performance. The five topics (actuation, channel acoustics, drop formation, wetting, and air bubbles) are the research topics of this thesis.

The first step is the actuation, chapter 2, which implies the transformation of an electric voltage to a deformation of the ink channels. With a piezoelectric bump mode actuator design, an efficient transformation of electric potential to mechanical deformations can be realized. However, mechanical constraints can result in cross-talk effects, and resonances in the printhead structure can be excited. The deformations inside the printhead cannot be measured. Modeling with the commercial finite element code Ansys is a way to resolve this. The numerical modeling provides the design rules for an efficient actuation, without generating cross-talk effects. The drive towards smaller printheads with more nozzles will push the balance between the operational demands and the manufacturability to its limits. A printhead design is a compromise between the two aspects, the functional requirements and the cost of production. The numerical modeling is the tool to match the often conflicting requirements for the different parts in the printhead. This leads to an optimal printhead design within known constraints. New actuation principles can also be explored, before starting the expensive and

time consuming manufacture of a new printhead design.

The deformation of the channel cross-section results in pressure waves. The pressure waves in the ink channels play a central role in the printhead operation, chapter 3. They connect the electrical-mechanical domain of the actuator to the fluid dynamic domain in and outside of the nozzles. The traveling wave provides an efficient acoustic mechanism to generate the required pressure for the drop formation process, when the acoustic impedance of the nozzle matches the impedance of the ink channel. Also refill, the filling of the nozzle for the next drop formation cycle, is driven by the acoustic pressure waves. However, residual vibrations in the ink channel must be as low as possible before the next drop formation cycle starts. Another disturbing effect is acoustic cross-talk, which is the traveling of pressure waves through the reservoir towards neighboring channels. This can be avoided with a thin foil on the ink supply. Measurements are done with the laser-Doppler setup and an acoustic measurement (Paint), which uses the piezo elements also as sensors. Details of the phenomena inside the ink channels, such as local pressure variations, are available through modeling. The acousto-elastic interaction plays an important role in the "narrow-channel" model and acoustic modeling with Ansys provides the details of the interactions with the structure dynamics of the printhead. With fundamental knowledge of the acoustic properties, new printhead concepts can be developed successfully into an operating printhead that can fire billions of drops with constant size and velocity and a reliability as high as possible. The flow and pressure at the nozzle sets the boundary condition in the acoustic modeling. The pressure at the entrance of the nozzle is the coupling to the final stage of the printhead operation, the drop formation.

The application of the traveling wave principle leads to the drop formation process, which takes several tens of microseconds. The drop formation process is the subject of chapter 4. Optical measurements and modeling provide the information, which leads to its better understanding. The tail break-off process is not affected by the actuation. Up to four satellite drop formation mechanisms can generate extra drops, which have a negative impact on the printing result. An important application is drop size modulation. With the knowledge of the drop formation process, eight drop size modulation techniques are identified. For the modeling of the free surface flow with surface tension and its impact on channel acoustics we use the commercial volume of fluid code Flow3D. The calculations provide also information on the meniscus retraction, the internal distribution of the speed of the ink, and the impact of the drop formation process on the pressure waves inside the ink channels. The Flow3D software is adapted to incorporate flexible walls, which is not feasible in the standard code. We can predict the resulting drop properties accurately. This will be used to investigate the jetting behavior of many new liquids, which are used in the different new applications. The critical material properties can be defined and this will be used as a guide for the development of new jetting materials. The jetting of smaller drops is more sensitive to the influence of the surrounding air. This is a new challenge for the modeling of the drop formation, requiring the development of new models.

The flow of ink on the nozzle plate is important. Wetting of the nozzle plate can influence the drop formation and the pressure waves inside the ink channels. The material interactions, which determine the wetting properties, are not known in detail. Therefore, an experimental study of the wetting phenomena is performed with a nickel nozzle plate, chapter 5. An actuated nozzle induces several flow patterns in an ink layer around the nozzle opening. When jetting, an induced air flow also influences the flow pattern around a nozzle. The nozzle plate and the ink are in the complete wetting regime, except for a central band of (older) ink in the middle of the nozzle plate, which is in the partial wetting regime. The precursor film provides a means of communication between the central band of ink and the nozzles. Differences in surface tension of the ink result in Marangoni flow over the entire nozzle plate. The experimental observations can be understood with theories found in the literature. A numerical model, which can predict the wetting properties, is not available. The molecular interactions have to be taken into account. However, molecular modeling will only provide the interaction parameters. The parameters must be translated into a macroscopic flow pattern with additional models. This is closely related to the research on the interactions of ink with the media. The impact, spreading, and solidification of drops onto a solid surface is the final stage of the printing process. New applications require the depositions of various kinds of liquids on different types of substrates. Numerical modeling of the wetting phenomena, which can take into account the material interactions, would be a very powerful tool in the development of new inkjet applications. The final goal is to control the wetting properties of the nozzle plate. Either a uniform thin layer of ink or no ink layer at all will improve the jetting behavior of the printhead.

Wetting, without or with dirt particles, can also result in air entrainment. Air bubbles play an important role in the jetting stability. The theoretical and experimental research on the generation and the behavior of air bubbles and their impact on the printhead performance is the subject of chapter 6. The resulting drop properties, the Paint measurement and visualization with a special transparent head are the experimental tools. Various aspects of the generation and the behavior of air bubbles are clarified. An air bubble oscillates in the acoustic pressure field. The oscillations can result in an enhanced drop speed and also the acoustic pressure waves are altered, as measured with Paint. Many forces act on an air bubble, which results in complicated movement pattern. The air bubble grows in the acoustic pressure field by rectified diffusion, with a growth rate much faster then the dissolution rate. Large air bubbles disturb the drop formation. The ultimate goal is to prevent the generation of air bubbles, or to control the behavior of air bubbles. Small air bubbles, which do not have a negative influence the drop formation, can be manipulated with acoustic pressure waves. Either a controlled jetting out or a fast dissolution would remove an air bubble before the drop formation is disturbed. The air bubble also influences the acoustic properties of the ink channels. Therefore, a numerical model will have to incorporate a full two-way coupling between the dynamic behavior of an air bubble and the pressure

waves inside the ink channels. Only with numerical modeling the results of the acoustic measurements can be translated into bubble properties such as bubble radius, position, velocity, etc.

The requirements for the inkjet printing technology will increase. The near future demands for smaller drops, higher drop velocities, higher drop repetition rates, smaller printhead designs, a maximum jetting stability, complex fluids, etc. To meet these challenges, inkjet research will continue towards high integration densities in the printhead, zero cross-talk levels, zero variation of the resulting drop properties, and the elimination of nozzle failure. This makes the development of new inkjet technologies an exciting environment, where scientific research and industrial development can reinforce each other for many years to come.

References

[1] S. Allaman and G. Desie, *Improved ink jet in situ visualization strategies*, Proc. IS&T's NIP20, 383 (2004).

[2] R.R. Allen, *Inkjet printing with large pagewide arrays: issues and challenges*, Proc. IS&T's NIP12, 43 (1996).

[3] B.V. Antohe and D.B. Wallace, *Acoustic phenomena in a demand-mode piezoelectric inkjet printer*, Proc. IS&T's NIP17, 885 (2001).

[4] B.V. Antohe and D.B. Wallace, *Acoustic phenomena in a demand-mode piezoelectric inkjet printer*, J. Imaging Sci. & Technol. **46**, 409 (2002).

[5] A. Ballato, *Piezoelectricity: Old effect, new thrust*, IEEE Transactions on Ultrasonics, Ferroelectrics and Frequency Control **42**, 916 (1995).

[6] O.A. Basaran, *Small-scale free surface flows with breakup: Drop formation and emerging applications*, AIChE J. **48**, 1842 (2002).

[7] G.K. Batchelor, *An introduction to fluid dynamics*, Cambridge University Press (1970).

[8] R. Beesom, *The ABCs of HP's SPT (Scalable Printhead Technology)*, IMI 13th Annual European Inkjet Conference (2005).

[9] M. Beltman, P. van de Hoogt, R. Spiering, and H. Tijdeman, *Air loads on a rigid plate oscillating normal to a fixed surface*, J. Sound & Vibr. **206**, 217 (1997).

[10] M. Beltman, *Viscothermal wave propagation including acousto-elastic interaction*, PhD thesis, University of Twente, Enschede (1998).

[11] R. Bennett, *Precision industrial ink-jet printing technology for full color PLED display and TFT-LCD manufacturing*, Proc. of the 3rd International Display Manufacturing Conference, Japan (2003).

[12] S.S. Berger, R.F. Burr, J.D. Padgett, and D.A. Tence, *Ink manifold design of phase change piezoelectric ink jets*, Proc. IS&T's NIP13, 703 (1997).

[13] W.T. Berggren, M.S. Westphall, and L.M. Smith, *Single-pulse nano- electrospray ionization*, Anal. Chem. **74**, 3443 (2002).

[14] B. Beulen, J. de Jong, H. Reinten, M. van den Berg, H. Wijshoff, and R. van Dongen, *Flows on the nozzle plate of an inkjet printhead*, Exp. Fluids **42**, 217 (2007).

[15] G. Beurer and J. Kretschmer, *Function and performance of a shear mode piezo printhead*, Proc. IS&T's NIP13, 621 (1997).

[16] A. Bietsch, J. Zhang, M. Hegner, H.P. Lang, and C. Gerber, *Rapid functionalization of cantilever array sensors by inkjet printing*, Nanotechnology **15(8)**, 873 (2004).

[17] D.B. Bogy and F.E. Talke, *Experimental and theoretical study of wave propagation phenomena in drop-on-demand ink jet devices*, IBM J. Res. Develop. **28**, 314 (1984).

[18] A.L. Brady, M. McDonald, S.N. Theriault, and B. Smith, *The impact of Silicon MEMS on the future of ink jet printhead design and performance*, Proc. IS&T's NIP21, 264 (2005).

[19] C.E. Brennen, *Cavitation and bubble dynamics*, Oxford University Press (1995).

[20] M.P. Brenner, X.D. Shi, and S.R. Nagel, *Iterated instabilities during droplet fission*, Phys. Rev. Letters **73**, 3391 (1994).

[21] M.P. Brenner, J.R. Lister, and H.A. Stone, *Pinching threads, singularities and the number 0.0304. . .*, Phys. Fluids **8**, 2827 (1996).

[22] M.P. Brenner, J. Eggers, K. Joseph, S.R. Nagel, and X.D. Shi, *Breakdown of scaling in droplet fission at high Reynolds number*, Phys. Fluids **9**, 1573 (1997).

[23] M.P. Brenner, S. Hilgenfeldt, and D. Lohse, *Single-bubble sonoluminescense*, Rev. Mod. Physics **74**, 425 (2002).

[24] J.D. Brock, I.M. Cohen, I.P. Ivanov, H.P. Le, and J. Roy, *Oscillations of an air bubble in an ink jet*, J. Imaging Sci. Technol. **10**, 127 (1984).

[25] J. Brünahl, *Physics of Piezoelectric Shear Mode Inkjet Actuators*, PhD Thesis Royal Institute of Technology Stockholm (2003).

[26] D. Bruijnen, R. van de Molengraft, A. Draad, and T. Heeren, *Productivity analysis of a scanning inkjet printer*, Proc. IS&T's NIP21, 129 (2005).

[27] W.L. Buehner, J.D. Hill, T.H. Williams, and J.W. Woods, *Application of ink-jet technology to a word processing output printer*, IBM J. Res. Dev. **21**, 1968 (1977).

[28] N. Bugdayci, D.B. Bogy, and F.E. Talke, *Axisymmetric Motion of Radially Polarized Piezoelectric Cylinders Used in Ink Jet Printing*, IBM J. Res. Develop. **27**, 171 (1983).

[29] R.F. Burr, D.A. Tence, and S.S. Berger, *Multiple dot size fluidics for phase change piezoelectric ink jets*, Proc. IS&T's NIP12, 12(1996).

[30] R.F. Burr, S.S. Berger and D.A. Tence, *Overview of phase change piezoelectric ink jet fluids modeling and design*, Proc. ASME **239**, 545(1996).

[31] J.C. Charter, R.M. Alvis, S.B. Brown, K.C. Langry, T.S. Wilson, M.T. McBride, M.L. Myrick, W.R. Cox, M.E. Grove, and B.W. Colston, *Fabricating optical fiber imaging sensors using inkjet printing technology: A pH sensor proof-of-concept*, Biosens. Bioelectron. **21(7)**, 1359 (2006).

[32] M. Chee, R. Yang, E. Hubbell, A. Berno, X.C. Huang, D. Stern, J.Winkler, D.J. Lockhart, M.S. Morris, and S.P.A. Fodor, *Accessing genetic information with high-density DNA arrays*, Science **274**, 610 (1996).

[33] A.U. Chen and O. Basaran, *A new method for significantly reducing drop radius without reducing nozzle radius in drop-on-demand drop production*, Physics of Fluids **14**, L1 (2002).

[34] A.U. Chen, P.K. Notz, and O.A. Basaran, *Computational and experimental analysis of pinch-off and scaling*, Phys. Rev. Lett. **88**, 174501 (2002).

[35] H.H. Chen and M.P. Brenner, *The optimal faucet*, Phys. Rev. Letters **92**, 166106 (2004).

[36] T. Chen, W.R. Cox, D. Lenhard, and D.J. Hayes, *Microjet printing of high precision microlens array for packaging of fiber-optic components*, Proc. SPIE Optoelectronic Interconnects, Integrated Circuits and Packaging **4652**, 136 (2002).

[37] T. Chen, *Piezoelectric Inkjet Print Head Technology for Precision Dispensing Application*, Proc. DF2006, 66 (2006).

[38] X.M. Chen and A. Prosperetti, *Thermal processes in the oscillations of gas bubbles in tubes*, J. Acoust. Soc. Am. **104**, 1389 (1998).

[39] J.M. Cittadino, E. Mendes, and A. Soucemarianadin, *A Tool for Monitoring Piezoelectric Micro-pumps*, Proc. IS&T's NIP21, 278 (2005).

[40] P.W. Cooley, D.B. Wallace, and B.V. Antohe, *Application of inkjet printing technology to biomems and microfluidic systems*, Proc. SPIE Conference on Microfluidics and BioMEMS **4560**, 177 (2001).

[41] W.R. Cox, T. Chen, D. Ussery, D.J. Hayes, J.A. Tatum, and D.L. MacFarlane, *Microjetted lenslet triplet fibers*, Optics Communications **123**, 492 (1996).

[42] A.A. Darhuber, W.W. Reisner, and S.M. Troian, *Dynamics of capillary spreading along hydrophilic microstripes*, Phys. Rev. **64**, 031603 (2001).

[43] A.A. Darhuber, J.M. Davis, W.W. Reisner, and S.M. Troian, *Thermocapillary actuation of liquid flow on chemically patterned surfaces*, Phys. Fluids **15**, 1295 (2003).

[44] A.A. Darhuber and S.M. Troian, *Principles of microfluidic actuation by modulation of surface stresses*, Ann. Rev. Fluid Mech. **37**, 425 (2005).

[45] D.D. Darling, *Driving Waveforms to Reduce Voltage Requirements of Inkjets*, Proc. IS&T's NIP20, 851 (2004).

[46] D.D. Darling, *Frequency dependent fluidic inductance and resistance in inkjet passages*, Proc. IS&T's NIP20, 877 (2004).

[47] R.F. Day, E.J. Hinch, and J.R. Lister, *Self-similar capillary pinchoff of an inviscis liquid*, Phys. Rev. Letters **80**, 704 (1998).

[48] J.F. Dijksman, *Hydrodynamics of small tubular pumps*, J. Fluid. Mech. **139**, 173 (1984).

[49] J.F. Dijksman, *Hydro-acoustics of piezoelectric driven ink-jet print heads*, Flow Turb. & Comb. **61**, 211 (1999).

[50] T.G. Duby, *Performance improvements for commercial piezo prinhead*, Proc. IS&T's NIP17, 328 (2001).

[51] J. Eggers and T.F. Dupont, *Drop formation in a one-dimensional approximation of the Navier-Stokes equation*, J. Fluid Mech. **161**, 205 (1994).

[52] J. Eggers, *Nonlinear dynamics and breakup of free-surface flows*, Rev. Mod. Phys. **69**, 865 (1997)

[53] L. Euler, *Principes géneraux du mouvementdes fluides*, Mem.Acad.Sci.Berlin **11**, 274 (1755).

[54] J.Q. Feng, *A general fluid dynamic analysis of drop ejection in drop-on-demand ink jet devices*, J. Imaging Sci. & Techn. **46**, 398 (2002).

[55] R.J. Furbank and J.F. Morris, *Droplet formation from particulate suspensions*, Proc. IS&T's NIP17, 304 (2001).

[56] R.J. Furbank and J.F. Morris, *An experimental study of particle effects on drop formation*, Phys. Fluids **16**, 1777 (2004).

[57] E.P. Furlani, *Temporal instability of viscous liquid microjets with spatially varying surface tension*, J. Physics A **38**, 263 (2005).

[58] E.P. Furlani, *Thermal modulation and instability of Newtonian liquid microjets*, Proc. Nanotech2005 **1**, 668 (2005).

[59] M.M. Fyrillas and A.J. Szeri, *Dissolution or growth of soluble spherical oscillating bubbles*, J. Fluid Mech. **277**, 381 (1994).

[60] B.J. de Gans, P.C. Duineveld, and U.S. Schubert, *Inkjet printing of polymers: state of the art and future developments*, Adv. Materials **16**, 203 (2004).

[61] X. Geng, H. Yuan, H.N. Oguz, and A. Prosperetti, *The oscillation of gas bubbles in tubes: Experimental results*, J. Acoust. Soc. Am. **106**, 674 (1999).

[62] P.G. de Gennes, *Wetting: statics and dynamics*, Rev. Mod. Phys. **57(3)**, 827 (1985).

[63] P.G. de Gennes, F. Brochard-Wyart, and D. Quéré, *Capillarity and wetting phenomena*, Spinger, Berlin, 2003.

[64] M.B. Groot Wassink, *Enabling higher fetting frequencies for inkjet printheads using Iterative Learning Control*, Proc. IS&T's NIP 21, 273 (2005).

[65] M.B. Groot Wassink, *Inkjet printhead performance enhancement by feedforward input design based on two-port modeling*, PhD thesis, Delft University of Technology (2007).

[66] W.B. Hardy, *The spreading of fluids on glass*, Philosoph. Mag. **38**, 49 (1919).

[67] E.I. Haskal, M. Buechel, and J.F. Dijksman, *Ink jet printing of passivematrix polymer light emitting displays*, Proc. Int. Symp. Soc. for Information Display **33**, 776 (2002).

[68] J. Heilmann, *The applications of inkjet for the printing of PDLC display cells*, Proc. IS&T's NIP21, 48 (2005).

[69] J. Heinzl, *Printing with ink droplets from a multi-nozzle device*, Advances in non-impact printing technologies for computer abd office applications, Joseph Gaynor Ed., 1191 (1981).

[70] F. Heslot, N. Fraysse, and A.M. Cazabat, *Molecular layering in the spreading of wetting liquid drops*, Nature **338**, 640 (1989).

[71] S. Hilgenfeldt, D. Lohse, and M.P. Brenner, *Phase diagrams for sonoluminiscescing bubbles*, Phys. Fluids **8**, 2808 (1996).

[72] S. Hilgenfeldt, M. P. Brenner, S. Grossmann, and D. Lohse, *Analysis of Rayleigh-Plesset dynamics for sonoluminescing bubbles*, J. Fluid Mech. **365**, 171 (1998).

[73] S. Hilgenfeldt and D. Lohse, *Predictions for upscaling sonoluminescence*, Phys. Rev. Letters **82**, 1086 (1999).

[74] N.P. Hine, *Deaeration system for a high-performance drop-on- demand ink jet*, J. Imaging Technol. **17**, 223 (1991).

[75] A. Hirota, N. Aichi, and S. Ishikura, *Development of drop-on-demand piezoelectric line inkjet printhead*, Proc. IS&T's NIP21, 257 (2005).

[76] C.W. Hirt and B.D. Nichols, *Volume of Fluid (VOF) method for the dynamics of free boundaries*, J. Comput. Phys. **39**, 201 (1981).

[77] S.D. Howkins, C.A. Willis, and H. Nishimura, *Cross-talk reduction by smart delay firing*, Proc. IS&T's NIP20, 845 (2004).

[78] I.M. Hutchings, G.D. Martin, S.D. Hoath, and R.H. Morgan, Proc. IS&T's NIP22, 91 (2006).

[79] P. James and R. Papen, *Nanolitre dispensing: a new innovation in robotic liquid handling*, Drug Discovery Today **3(9)**, 429 (1998).

[80] O.E. Jensen and J.B. Grotberg, *Insoluble surfactant spreading on a thin viscous film: shock evolution and film rupture*, J. Fluid Mech. **240**, 59 (1992).

[81] O.E. Jensen and J.B. Grotberg, *The spreading of heat or soluble surfactant on a thin liquid film*, Phys. Fluids **A5**, 58 (1993).

[82] R. Jeurissen, J. de Jong, H. Borel, M. Versluis, M. van den Berg, H. Wijshoff, H. Reinten, A. Prosperetti, and D. Lohse, *Sound Absorption of Bubbles in Inkjet-printer Microchannels*, Proc. 6th EFMC, 340 (2006).

[83] R. Jeurissen, J. de Jong, H, Reinten, M. van den Berg, H. Wijshoff, M. Versluis, and D. Lohse, *The effect of an entrained air bubble on the acoustics of an ink channel*, J. Acoust. Soc. Am. (in press 2007).

[84] J. de Jong, M. Versluis, G. de Bruin, D. Lohse, H. Reinten, M. van den Berg, H. Wijshoff, and N. de Jong, *Acoustical and optical characterization of air entrapment in piezo-driven inkjet printheads*, Proc. IEEE-IUS **2**, 1270 (2005).

[85] J. de Jong, H. Reinten, M. van den Berg, H. Wijshoff, M. Versluis, G. de Bruin, and D. Lohse, *Air entrapment in piezo-driven inkjet printheads*, J. Acoust. Soc. Am. **120**, 1257 (2006).

[86] J. de Jong, R. Jeurissen, H. Borel, M. van den Berg, H. Wijshoff, H. Reinten, M. Versluis, A. Prosperetti, and D. Lohse, *Entrapped air bubbles in piezo-driven inkjet printing: their effect on the droplet velocity*, Phys. Fluids **18**, 121511 (2006).

[87] J. de Jong, H. Reinten, H. Wijshoff, M. van den Berg, K. Delescen, R. van Dongen, F. Mugele, M. Versluis, and D. Lohse, *Marangoni flow on an inkjet nozzle plate*, Appl. Phys. Lett **91**, 204102 (2007).

[88] M. Kanaya, *MACH for pigment ink*, Proc. IS&T's NIP19, 280 (2003).

[89] B.C. Khoo, E. Klaseboer, and K.C. Hung, *A collapsing bubble-induced micro-pump using the jetting effect*, Senors and Actuators **118**, 152 (2004).

[90] T. Kitahara, *Ink jet head with multi-layer piezoelectric actuator*, Proc. IS&T's NIP11, 346 (1995).

[91] A. Knobloch, *Printed RFID labels based on polymer electronics*, Proc. DF2005, 121 (2005).

[92] H.S. Koo, M. Chen, and P.C. Pan, *LCD-based color filter films fabricated by a pigment-based photo resist inks and printing technology*, Thin Solid Films **515**, 896 (2006).

[93] S. Korol and Chr. Greb, *Solid ink printing with dynamic drop size modulation*, Proc IS&T's NIP16, 61 (2000).

[94] T.A. Kowalewski, *On the separation of droplets from a liquid jet*, Fluid. Dyn. Res. **17**, 121 (1996).

[95] J. Kretschmer and G. Beurer, *Design parameters of a shear mode piezo printhead for a given resolution*, Proc. IS&T's NIP13, 626 (1997).

[96] P.S. Laplace, *Mechanique celeste, supplement au X libre*, Courier, Paris (1805).

[97] H.P. Le, *Progress and trends in ink-jet printing technology*, J. Imaging Sci. & Technol. **42**, 49 (1998).

[98] H.C. Lee, *Boundary layer around a liquid jet*, IBM J. Res. Develop. **21**, 48 (1977).

[99] H.H. Lee, K.S. Chou, and K.C. Huang, *Inkjet printing of nanosized silver colloids*, Nanotechnology **16(10)**, 2436 (2005).

[100] T.G. Leighton, *The acoustic bubble*, Academic Press London (1994).

[101] W. Letendre, S. Halwawala, and B. Smith, *Jetting and Imaging Performance of the M-300/10 Jet Module*, Proc. IS&T's NIP22, 83(2006).

[102] M.J. Lighthill, *Waves in fluids*, Cambridge University Press (1978).

[103] J.R. Lister and H.A. Stone, *Capillary breakup of a viscous thread surrounded by another viscous fluid*, Phys. Fluids **10**, 2758 (1998).

[104] D. Lohse, J. de Jong, M. Versluis, M. van den Berg, H. Wijshoff, and H. Reinten, *Disturbing bubbles in piezo-acoustic printing*, Proc. 6th EFMC, 369 (2006).

[105] B. Lopez, D. Vadillo, P. Pierron, and A. Soucemarianadin, *Transient phenomena during drop formation in DOD printing*, Proc. IS&T's NIP18, 170 (2002).

[106] C.Y. Lung, M.D. Barnes, N. Lermer, W.B. Whitten, and J.M. Ramsey, *Single-molecule analysis of ultradilute solutions with guided streams of 1-mwater droplets*, Appl. Opt. **38**, 1481 (1999).

[107] J. Lyklema, *Fundamentals of interface and colloid science vol. III: Liquid-fluid interfaces*, Academic Press (2000).

[108] E. Manini and A. Scardovi, *Experimental evaluation of reflections of acoustic waves in DOD systems*, SPSE Proc. Adv. N.I.P Techn, 1092 (1982).

[109] H. J. Manning and R. A. Harvey, *Xaar greyscale technology*, Proc. IS&T's NIP15, 35 (1999).

[110] P. Marmottant and S. Hilgenfeldt *Controlled vesicle deformation and lysis by single oscillating bubbles*, Nature **423**, 153 (2003).

[111] G. Martin, *Jet formation and late-stage ligament instability in Drop-on-demand printing*, Proc. IS&T's NIP22, 96 (2006).

[112] O.K. Matar, *Nonlinear evolution of thin free viscous films in the presence of soluble surfactant*, Phys. Fluids **14**, 4216 (2002).

[113] M. McDonald, *Scaling of piezoelectric drop-on-demand jets for high resolution applications*, Proc. IS&T's NIP12, 53 (1996).

[114] M. McDonald, *Crosstalk study of a high speed shear mode piezo inkjet printhead*, Proc. IS&T's NIP15, 40 (1999).

[115] M. McDonald, *Continuous improvement: Performance and reliability in shear mode piezo ink jet printing*, Proc. IS&T's NIP17, 287 (2001).

[116] J.M. Meacham, M.J. Varady, F.L. Degertekin, and A.G. Fedorov, *Droplet formation and ejection from a micromachined ultrasonic droplet generator: Visualization and scaling*, Phys. Fluids **17**, 100605 (2005).

[117] C.D. Meinhart and H. Zhang, *The flow structure inside a microfabricated inkjet printhead*, J. MEMS Systems **9**, 67 (2000).

[118] Chr. Menzel, A. Bibl, and P. Hoisington, *MEMS solutions for precision micro-fluidic dispensing application*, Proc. IS&T's NIP20, 169 (2004).

[119] T. Mimura and S. Sakai, *Micro piezoelectric head technology of color inkjet printer*, Proc. DPP2001, 230 (2001).

[120] T. Nakanishi, I. Ohtsu, M. Furuta, E. Ando, and O. Nishimura, *Direct MS/MS analysis of proteins blotted on membranes by a matrix-assisted laser desorption/ionization-quadrupole ion trap-time-of-flight tandem mass spectrometer*, J. Proteome Research **4**, 743 (2005).

[121] C.L.M.H. Navier, *Memoires sur les lois du movement des fluides*, Mem.Acad.Sci.Inst.France **6**, 389 (1822).

[122] J.A. Nollet, *Reserches sur les causes particulieres des phenomenes electriques*, Les Freres Guerin, Paris (1749).

[123] J.A. Nollet and Mr. Watson, *An examination of certain phenomena in electricity*, Philosophical Transactions **46**, 368 (1749).

[124] N. Noto, T. Torii, S. Suematsu, and K. Kugai, *A new compact high resoluation solid ink print head and its application to a plate making printer*, Proc. IS&T's NIP14, 50 (1998).

[125] P.K. Notz, A.U. Chen, and O.A. Basaran, *Satellite drops: unexpected dynamics and change of scaling during pinch-off*, Phys. Fluid **13**, 549 (2001).

[126] H.N. Oguz and A. Prosperetti, *The natural frequency of oscillation of gas bubbles in tubes*, J. Acoust. Soc. Am. **103**, 3301 (1998).

[127] I. Ohtsu, T. Nakanisi, M. Furuta, E. Ando, and O. Nishimura, *Direct matrix-assisted laser desorption/ionization time-of-flight mass spectrometric identification of proteins on membrane detected by western blotting and lectin blotting*, J. Proteome Research **4**, 1391 (2005).

[128] A. Olsson, G. Stemme, and E. Stemme, *A valve-less planar fluid pump with two pump chambers*, Sensors and Actuators **A46-47**, 549 (1995).

[129] A. Oron, S.H. Davis, and S.G. Bankoff, *Long-scale evolution of thin liquid films*, Rev. Mod. Phys. **69(3)**, 931 (1997).

[130] D.H. Peregrine, G. Shoker, and A. Symon, *The bifurcation of liquid bridges*, J. Fluid. Mech. **212**, 25 (1990).

[131] P. Pierron, S. Alleman, and A. Soucemarianadin, *Dynamics of jetted liquid filaments*, Proc. IS&T's NIP17, 308 (2001).

[132] J.A.F. Plateau, *On the recent theories of the constitution of jets of liquid issuing from circular orifices*, Philosophical Magazine **12**, 286 (1856).

[133] J.F. Pond, *Inkjet Technology and Product Development Strategies*, Torrey Pines Research (2000).

[134] S.A.N. Prasad *Two-port electroacoustic model of a piezoelectric composite circular plate*, PhD Thesis, University of Florida (2002).

[135] D. Radulescu and et al., *3d printing of biological materials for drug delivery and tissue engineering applications*, Proc. DF2005, 96 (2005).

[136] Lord Rayleigh, *On the instability of jets*, Proc. of the London math. soc. **10**, 4 (1878).

[137] S. Sakai, *Dynamics of Piezoelectric Inkjet Printing Systems*, Proc. IS&T's NIP26, 15 (2000).

[138] F. Savart, *Memoire sur la constitution des veines liquides lancees par des orifices circulaires en mince parol*, Ann.Chim. **53**, 337 (1833).

[139] H. Schlichting, *Boundary layer theory*, McGraw-Hill book company, New York (1979),

[140] M. Schoeppler, *Diverging Ink Jet Technologies and Applications*, Proc. IS&T's NIP22, 1 (2006).

[141] X.D. Shi, M.P. Brenner, and S.R. Nagel, *A cascade of structure in a drop falling from a faucet*, Science **265**, 219 (1994).

[142] D.Y. Shin, P. Grassia, and B. Derby, *Oscillatory limited compressible fluid flow induced by the radialmotion of a thick-walled piezoelectric tube*, J. Acoust. Soc. Am. **114**, 1314 (2003).

[143] T.M. Squires and S.R Quake, *Microfluidics: Fluid physics at nanoliter scale*, Rev. Mod. Phys **77(3)**, 977 (2005).

[144] E. Stemme and G. Stemme, *A valveless diffuser/nozzle-based fluid pump*, Sensors and Actuators **A39**, 159 (1993).

[145] G.G. Stokes, *On the theories of the internal friction of fluids in motion, and of the equilibrium and motion of elastic solids*, Trans. Cambr. Phil. Soc. **IIX**, 287 (1849).

[146] J. Sumurel, *Digital printing of bioinks*, Proc. DF2006, 93 (2006).

[147] R.G. Sweet, *High frequency recording with electrostatically deflected ink-jets*, Rev. Sci. Instrum. **36**, 131 (1965).

[148] J. Szczech, J. Zhang, K. Kalyan, P. Brazis, and D. Gamota, *Printed electronic using traditional graphic arts printing technologies*, Proc. DF2005, 213 (2005).

[149] T. Takahashi, *Adaptability of piezoelectric inkjet head*, Proc. IS&T's NIP17, 323 (2001).

[150] H. Tijdeman, *On the propagation of sound waves in cylindrical tubes*, J. Sound and Vibr. **39**, 1 (1975).

[151] R. Toegel, S. Luther, and D. Lohse, *Viscosity destabilizing sonoluminescing bubbles*, Phys. Rev. Letters **96**, 114301 (2006).

[152] C. Tracy and D. Grose, *The quality plan for the manufacture of an ink jet print assembly with 1536 jets*, Proc. IS&T's NIP18, 157 (2002).

[153] S. Umezu, H. Suzuki, and H. Kawamoto, *Droplet Formation and Dropping Position Control in Electrostatic Inkjet Phenomena*, Proc. IS&T's NIP21, 283 (2005).

[154] S. Umezu, R. Nakazawa, and H. Kawamoto, *Cross-Talk of Multi-Nozzle in Electrostatic Inkjet System*, Proc. IS&T's NIP22, 66 (2006).

[155] M. Usui, H. Hayashi, K. Hara, and T. Kitahara, *Development of the new MACH (MACH with MLCips*, Proc. IS$T's NIP12, 50, (1996).

[156] M. Usui et al., *The Development of Pigment Ink for Plain Paper*, Proc. IS&T's NIP18, 369 (2002).

[157] M.P. Valignat, G. Oshanin, S. Villette, A.M. Cazabat, and M. Moreau, *Molecular weight dependence of spreading rates of ultrathin polymeric films*, Phys. Rev. Lett. **80**, 5377 (1998).

[158] W. Voit, W. Zapka, L. Belova, and K.V. Rao, *Application of inkjet technology for the deposition of magnetic nanoparticles to form micronscale structures*, IEEE Proc Science Measurement and Technology **150(5)**, 252 (2003).

[159] J.W. Waanders, *Piezoelectric Ceramics. Properties and applications*, Philips Components, Eindhoven (1991).

[160] D.B. Wallace, W.R. Cox, and D.J. Hayes, *Direct write using inkjet techniques*, Direct-Write technologies for rapid prototyping applications - sensors, electronics, and integrated power sources, 177227. Academic Press, San Diego (2002).

[161] D.T. Wasan, A.D. Nikolov, and H. Brenner, *Droplets speeding on surfaces*, Science **291**, 605 (2001).

[162] H.M.A. Wijshoff, *Free surface flow and acousto-elastic interaction in piezo inkjet*, Proc. Nanotech2004 **2**, 215 (2004).

[163] H.M.A. Wijshoff, *Manipulating drop formation in piezo acoustic inkjet*, Proc. IS&T's NIP22, 79 (2006).

[164] H.M.A. Wijshoff, *Modeling the drop formation process in inkjet printheads*, Flow3D News spring2007, 4 (2007). Flow3D is CFD software developed by Flow Science Inc., Santa Fe, New Mexico.

[165] H.M.A. Wijshoff, *Drop formation mechanisms in piezo-acoustic inkjet*, Proc. Nanotech2007 **3**, 448 (2007).

[166] H.M.A. Wijshoff, *Better printheads via simulation: Flow3D helped double the speed of a new wide-format printer without sacrificing quality*, Desktop Engineering **13(2)**, 46 (2007).

[167] Chr. Williams, *Ink-jet printers go beyond paper*, Phys. World **19**, 24 (2006).

[168] J.C. Yang, W. Chien, M. King and W.L. Grosshandler, *A simple piezoelectric droplet generator*, Exp. Fluids **23**, 445 (1997).

[169] L.Y. Yeo, O.K. Matar, E.S.P. Ortiz and G.F. Hewitt, *The dynamics of Marangoni-driven local film drainage between two drops*, J. Colloid Interface Sci. **241**, 233 (2001).

[170] W.Y. Yeong, C.K. Chua, K.F. Leong, and M. Chandrasekaran, *3D inkjet printing for rapid prototyping: development of a physical model*, Proc. Int. Conf. Materials Processing for Properties and Performance, 379 (2004).

[171] I. Yildrim, *Surface free energie characterization of powders*, PhD thesis, Virginia State University (1998).

[172] T. Young, *Cohesion of fluids*, Phil.Trans.R.Soc.London **95**, 65 (1804).

[173] W. Zapka, R. Kaack, W. Voit, M. Schulz, M. Zimmermann, L. Levin and W. Ahlemeir, *Large drop volumes from Xaar-type inkjet printheads*, Proc. IS&T's NIP18, 161 (2002).

[174] W. Zapka, M. Crankshaw, W. Voit, J. Brünahl, U. Herrmann and G. Münchow, *Increased inkjet printing frequency from offset channel printheads*, proc. IS&T's NIP19, 272 (2003).

[175] J. Zhang, *New developments in Epson's inkjet head technology*, Proc. IS&T's NIP21, 269 (2005)

[176] X. Zhang and O.A. Basaran, *An experimental study of dynamics of drop formation*, Phys. Fluids **7**, 1184 (1995).

[177] Y. Zhou, *A coupled field analysis of an ink jet printhead with shear mode piezo transducer*, Proc. IS&T's NIP13, 809 (1997).

[178] Y. Zhou, *Measurement of the displacement of a shear mode piezoelectric transducer using laser Doppler vibrometer*, Proc. IS&T's NIP14, 23 (1998).

[179] Y. Zhou, *The application of piezo ink jet technology to high-speed dod single pass printing*, Proc. IS&T's NIP16, 28 (2000).

[180] Y. Zhou, *Recent advances in highle durable piezoelectric inkjet print head technology*, Proc. IS&T's NIP20, 855 (2004).

Summary

In the first chapter a general introduction on inkjet is presented, describing that not only printing onto paper but many other applications have emerged the last years. The drops coming out of the nozzle can be measured with all kind of optical measurements. Single drops can even be captured for further analysis. What is happening inside the printhead is much more difficult to measure. The most important measurement uses the piezo actuator also as a sensor, which is especially in the research on jetting stability an important measurement. The measurement gives only the average pressure inside the ink channels. Therefore, the modeling of the physical phenomena with available commercial codes and the development of dedicated special models is an essential part of this research. Added to the measurements, the modeling reveals the chain of processes, which lead to the drop formation. The physics behind the chain of processes comprise (i) the two-way coupling from the electrical to the mechanical domain (i.e., the piezo electric actuator), (ii) the coupling to the acoustic domain inside the ink channels, and (iii) finally the coupling to the fluid dynamic domain, i.e. the drop formation. Furthermore, (iv) wetting of the nozzle plate and (v) air bubbles can have a negative influence on the printhead performance. These are the five research topics of this thesis.

In the second chapter, the coupling between the electrical and mechanical domain is described. Piezo-electric materials generate an efficient transformation of an electric potential to a mechanical displacement. The bump mode design with the actuation parallel to the polarization direction of the piezo-electric material provide an efficient actuator design. The channel cross-sections must be deformed to generate the pressure waves for firing drops from the nozzles. The substrate provides the reaction forces. Both mechanical constraints result in a complicated deformation pattern with local cross-talk as negative consequence. Components of local cross-talk are the direct, the pressure induced, and the electric cross-talk. Doubling the number of piezo elements can reduce the local cross-talk, because the extra piezo elements can then guide the reaction force to the channel walls. Another disturbing effect is that, when actuating many channels simultaneously, resonances in the printhead structure can be excited. The frequency and shape of the resonance modes are important for the amount of excitation.

In the third chapter, the acoustics inside the ink channels are discussed. The acoustics play a central role in the printhead operation. The dynamics of the print-

head structure are coupled through the acoustics to the drop formation process in the nozzle. The derivation of the governing equations of the channel acoustics is given, with the acousto-elastic coupling as an essential part. The elasto-acoustic coupling between the pressure waves inside the ink channel and the flexible channel walls, reduces the effective speed of sound from 1250 m/s to 850 m/s. The resulting frequency characteristics and the application of the traveling wave principle are then described. The interface with the nozzle is treated as a boundary condition: a good acoustic coupling between the nozzle and the ink channel results in low pressure amplitudes and a high velocity of the ink in the nozzle. The resulting drop size depends mainly on the size of the nozzle cross-section, the drop velocity, and the channel length. At the other end of the channel, a thin foil results in a high compliance of the ink supply. This reduces the acoustic cross-talk, i.e., the traveling of acoustic waves through the ink reservoir towards neighboring channels. The residual vibrations inside the ink channel and the variable mass of ink in the nozzle, result in a strong refill, which is necessary to supply the nozzles with ink for the next drop formation cycle. However, the residual vibrations have an influence on the drop properties at high drop repetition rates. The variations of the drop speed and the drop volume can become large when the residual vibrations interfere with local cross-talk effects. Furthermore, a spatial and temporary overlap between the resonances in the printhead structure and acoustic resonances in the ink domain must be avoided to keep the negative influence on the drop formation process as low as possible.

The topic of chapter four are the flow phenomena outside the printhead. The free surface flow, resulting in drop formation, is the ultimate goal of the inkjet process. The application of the traveling wave principle leads to a drop formation process, which takes several tens of microseconds. The fill-before-fire action retracts the meniscus during the first 10-20 μs. Then the head of the drop appears outside the nozzle. Because of the viscosity of the ink, a long tail is formed, which slows down the speed of the head of the drop from 20 m/s to 7 m/s. Important drop properties are drop size and speed and the formation of satellites. The tail breaks off after $45 - 60$ μs. At tail break-off a secondary tail is formed. The secondary tail forms a mist of very small droplets with a volume less than 1 pl. The mist of droplets is dragged along with the main drops, due to the induced air flow. The resulting dynamics at the end of the tail are mainly determined by the ink properties and not by the shape and amplitude of the driving waveform. Long tails will be formed when the speed of the head exceeds the speed of the end of the tail. A long tail will break-up in small satellite droplets through the Rayleigh breakup mechanism. Another satellite drop can be generated by the small mass of ink in the nozzle, which can result in a supercritical acceleration. This means that surface tension forces cannot compete anymore with unsteady inertia. This results in the formation of a fast satellite drop, out of the head of the drop. The formation of slow satellites out of the tail of the drop is another satellite drop formation mechanism. This occurs when the distribution of mass in the tail has a minimum between the head of the drop and the middle of the tail. An important

application is drop size modulation. With the knowledge of the drop formation process up to eight drop size modulation techniques are identified. The mechanisms are (i) varying the driving pulse width and (ii) the fill-before-fire level, (iii) using pre-actuation, (iv) multiple drops or (v) break pulses, (vi) the fast satellite drop formation mechanism with split and block pulse, and (vii) exciting meniscus oscillations and (viii) drop formation oscillations.

In chapter five the observed wetting phenomena on the nozzle plate are described. Wetting of the nozzle plate plays an important role in the printhead performance. The strong refill mechanism results in overfilling of the nozzle, with a risk on inducing wetting. The failure of the drop formation process can also result in wetting of the nozzle plate. An ink layer around a jetting nozzle disturbs the drop formation. The drop formation is even blocked when the ink layer thickness becomes more than 20 μm. Also observed is that a jetting nozzle induces several flow patterns in the ink layer around the nozzle opening. The continuous jetting of drops induces an air flow towards the nozzle. This air flow drags the outer part of the ink layer always towards the nozzle. As a consequence either a strong sink flow can be visible or a Couette flow, when the overfilling of the nozzle adds ink to the inner part of the ink layer. Also an actuated, but non-jetting, nozzle induces several flow patterns. Dipole, source and sink flow complete the observed phase diagram of possible flow patterns in the ink layer. The wetting properties of the nozzle plate are determined by the material interactions between the ink and the nozzle plate material. This results either in a partial wetting regime or a complete wetting regime. The nickel nozzle plate and the ink are in a complete wetting regime. Older ink on the nozzle plate has other properties which results in a partial wetting regime. The older ink accumulates in the middle of the nozzle plate. The movement of the ink in an actuated nozzle results also in an increase of the surface tension. The precursor film of fresh ink, which is measured to be 13 nm in thickness, provides a way of communication between the nozzles and the central band of ink. A trunk flow drives the ink from the middle of the nozzle plate towards the actuated nozzles. Differences in the surface tension of the ink, which results in Marangoni flow, are the driving mechanism behind this flow pattern.

In the last chapter of this thesis, the main factors which determine the jetting stability are discussed. The stability of the drop formation process is crucial. Many sources for jetting instabilities can be eliminated by a proper printhead and actuation design. But even then sometimes air is entrained during the normal printhead operation, with an important role of the ink layer around the nozzle. There is a critical wetting layer thickness, which directly leads to air entrainment. A second mechanism is caused by typical 20 μm small dirt particles, caught in the ink layer and transported towards the nozzle. The distortion by a dirt particle can be detected with the acoustic measurement. An entrapped air bubble oscillates in the acoustic pressure field, which can also be measured acoustically. The acoustic properties of the ink channel act as a filter for this measurement. Therefore, the oscillations after the collapse of small air bubbles are recorded in the heads

with 8 mm long channels as a signal with a frequency of 170 kHz. Primary and secondary Bjerknes forces, and drag forces result in a movement of the air bubble. The jetting out of an air bubble is a fast recovery, but in some cases the air bubble stays inside the ink channel. The movement of air bubbles can be visualized with a special transparent head. Small air bubbles do not have a negative effect on the drop formation process. However, in the pressure field, the bubbles grow by rectified diffusion. The growth rate is much faster than the dissolution rate. The air bubbles grow to a size comparable to the volume displacement by the acoustic pressure waves. The large air bubble will then counteract the pressure buildup. This has a large effect on the drop formation and finally the drop formation process ceases completely.

Samenvatting

De laatste jaren zijn naast het printen op papier veel nieuwe inkjet toepassingen ontstaan, hetgeen is beschreven in de algemene inleiding in het eerste hoofdstuk. De druppels die uit de nozzles komen, kunnen met allerlei optische technieken worden gemeten. Afzonderlijke druppels kunnen zelfs worden opgevangen en verder worden geanalyseerd. Wat binnen in de printkop gebeurt, is echter veel moeilijker te meten. Bij de belangrijkste meetmethode wordt de piezo actuator ook als een sensor gebruikt. Deze meting wordt vooral gebruikt bij het onderzoek naar jetstabiliteit. Deze meetmethode geeft echter alleen maar informatie over de gemiddelde druk in het inktkanaal. Daarom zijn het modelleren van de fysische verschijnselen met commercieel verkrijgbare rekenpakketten, en het ontwikkelen van speciale rekenmodellen, een essentieel onderdeel van dit onderzoek. Met de rekenmodellen als aanvulling op de metingen wordt de reeks van processen, die tot druppelvorming leidt, opgehelderd. De fysica omvat (i) de tweeweg koppeling tussen het elektrische en het mechanische domein in de piezo-elektrische actuator, (ii) de koppeling naar het akoestische domein in de inktkanalen en tenslotte (iii) de koppeling naar het vloeistof dynamica domein, ofwel de druppelvorming. Verder kunnen (iv) de bevochtiging van de nozzleplaat, en (v) luchtbellen, een negatieve invloed hebben op het jetgedrag van de printkop. Deze vijf onderzoeksonderwerpen zijn beschreven in de opeenvolgende hoofdstukken van dit proefschrift.

In het tweede hoofdstuk wordt de koppeling tussen het elektrische en het mechanische domein beschreven. Elektrische potentialen kunnen met piezo-elektrische materialen zeer efficient worden omgezet in mechanische verplaatsingen. Een bump actuator, met de actuatierichting parallel aan de polarisatie richting van het piezo-elektrisch material, levert een efficient actuator ontwerp op. De kanaaldoorsnedes moeten worden vervormd om de drukgolven op te wekken, die nodig zijn om druppels uit de nozzles te jetten. Het substraat zorgt voor de reactiekracht. De inklemming van de piezo elementen tussen de kanalen en het substraat leidt tot een gecompliceerd patroon van vervormingen, met lokale overspraak als negatieve consequentie. De direkte, de indirekte en de elektrische overspraak zijn de drie componenten van de lokale overspraak. Met het verdubbelen van het aantal piezo elementen kan de lokale overspraak worden verminderd. De extra piezo elementen worden dan gebruikt om de reactiekracht naar de kanaalwanden te leiden. Een ander verstorend effekt is dat, wanneer er zeer veel kanalen tegelijk worden geactueerd, er resonanties in de constructie van de printkop kunnen worden aanges-

lagen. De frequentie en de vorm van de eigentrillingen zijn bepalend voor de mate waarin ze worden aangeslagen.

In het derde hoofdstuk wordt de akoestiek in de inktkanalen besproken. De akoestiek speelt een centrale rol in de werking van de printkop. De dynamica van de printkop constructie wordt via de akoestiek gekoppeld aan het druppelvormingsproces in de nozzle. De afleiding van de, voor de kanaalakoestiek bepalende, vergelijkingen wordt gegeven, waarbij de elastische-akoestische wisselwerking een belangrijke rol speelt. De elastische-akoestische wisselwerking tussen de drukgolven in het kanaal en de flexibele wanden van het kanaal verlaagt de effektieve geluidsnelheid van 1250 m/s naar 850 m/s. De resulterende frequentie karakteristieken en de toepassing van het lopende golf principe worden vervolgens beschreven. Het uiteinde met de nozzle wordt beschreven met randvoorwaarden. Een goede akoestische koppeling tussen de nozzle en het kanaal leidt tot lage drukken in het kanaal en een hoge snelheid van de inkt in de nozzle. De resulterende druppelgrootte hangt met name af van de nozzle doorsnede, de druppelsnelheid en de kanaallengte. Aan het andere uiteinde van het kanaal verhoogt een dunne folie de vervormbaarheid van de inkttoevoer. Dit vermindert de akoestische overspraak, ofwel het door het reservoir heenlopen van drukgolven naar de andere kanalen. De resterende drukgolven in het kanaal leiden samen met de variabele inktmassa in de nozzle tot een sterke vulling, hetgeen noodzakelijk is om de nozzle met inkt te voorzien voor de volgende druppelvormingscyclus. Echter, de resterende drukgolven kunnen ook de druppeleigenschappen bij hoge jetfrequenties beinvloeden. Wanneer er een wisselwerking is tussen de resterende drukgolven en de effekten van lokale overspraak, kunnen de variaties in druppel snelheid en volume groot worden. Bovendien moet de overlap in tijd en ruimte tussen de resonanties in de constructie van de printkop en de akoestische resonanties in het inktdomein worden vermeden om de negatieve invloed op de druppelvorming zo laag mogelijk te houden.

Het onderwerp van het vierde hoofdstuk zijn de stromingsverschijnselen buiten de printkop. De vrije-oppervlaktestroming, welke resulteert in druppelvorming, is het uiteindelijke doel van het inkjet procédé. De toepassing van het lopende golf principe leidt tot een druppelvormingsproces dat enkele tientallen microsecondes duurt. De "fill-before-fire" actie trekt de meniscus terug gedurende de eerste $10-20$ μs. Dan komt de kop van de druppel naar buiten. Door de viscositeit van de inkt, wordt er een lange staart gevormd, die de snelheid van de kop afremt van 20 m/s naar 7 m/s. Belangrijke druppeleigenschappen zijn de druppelgrootte, de snelheid, en de vorming van satelliet druppels. De staart breekt af na $45-60$ μs. Bij het afbreken van de staart ontstaat er een secundaire staart. De secundaire staart vormt een nevel van zeer kleine druppels, met een volume kleiner dan 1 pl. De nevel van druppels wordt door een opgewekte luchtstroom meegesleurd met de hoofddruppels. Het gedrag van het staartuiteinde wordt hoofdzakelijk bepaald door de inkteigenschappen en niet door de vorm en de amplitude van de aanstuur golfvorm. Lange staarten worden gevormd wanneer de snelheid van de kop groter wordt dan de staartsnelheid. Een lange staart vormt vervolgens kleine

satelliet druppels vanwege de Rayleigh instabiliteit. Een ander satelliet druppelvormingsmechanisme wordt gegenereerd door de kleine inktmassa in de nozzle, welke een bovenkritische versnelling tot gevolg kan hebben. Dit betekent dat de oppervlaktespanningskrachten niet meer in staat zijn om de instationaire traagheidskrachten op te vangen. Als gevolg hiervan wordt er een snelle satelliet druppel uit de kop van de druppel gevormd. De vorming van langzame satelliet druppels uit de staart van de druppel is nog een ander satelliet druppelvormingsmechanisme. Dit vindt plaats wanneer de massaverdeling in de staart een minimum heeft tussen de kop van de druppel en het midden van de staart. Een belangrijke optie is druppelgrootte modulatie. Met de kennis van het druppelvormingsproces zijn er acht druppelgrootte modulatie technieken geidentificeerd. Deze mechanismes zijn (i) het varieren van de pulsbreedte en (ii) het "fill-before-fire" niveau, (iii) het opslingeren van de actuatie, (iv) het gebruik van meerdere druppels, (v) het gebruik van rempulsen, (vi) het snelle satelliet druppelvormingsmechanisme met een splits en een blokker puls, (vii) het aanslaan van oscillaties in de meniscus en (viii) het aanslaan van oscillaties in de druppelvorming zelf.

In hoofdstuk vijf worden de waargenomen bevochtigingsverschijnselen op de nozzleplaat beschreven. De bevochtiging van de nozzleplaat speelt een belangrijke rol in het gedrag van de printkop. Het sterke vulmechanisme leidt tot een overvolle nozzle, met een risico op bevochtiging als gevolg. Het falen van het druppelvormingsproces kan ook tot bevochtiging van de nozzleplaat leiden. Een inktlaag rond de nozzle verstoort de druppelvorming. De druppelvorming wordt zelfs geblokkeerd wanneer de inktlaagdikte meer is dan 20 μm. Ook is waargenomen dat een jettende nozzle verschillende stromingspatronen opwekt in de inktlaag rondom de nozzle opening. Het continu jetten van druppels wekt een luchtstroom op in de richting van de nozzle. Deze luchtstroom sleurt het buitenste deel van de inktlaag mee, in de richting van de nozzle. Als gevolg kan er ofwel een sterke afvoerstroming zichtbaar zijn ofwel een Couette stroming, wanneer het vullen van de nozzle sterk genoeg is om inkt aan te voeren naar het binnenste deel van de inktlaag. Een geactueerde, maar niet jettende nozzle, wekt ook verschillende stromingspatronen op. Dipool, bron en afvoerstromingen maken het plaatje compleet van waargenomen stromingspatronen. De bevochtigingseigenschappen van de nozzleplaat worden bepaald door de materiaal interacties tussen de inkt en het materiaal van de nozzleplaat. Dit resulteert in ofwel een "partial wetting" regime ofwel in een "complete wetting" regime. De nikkel nozzleplaat en de inkt bevinden zich in het "complete wetting" regime. Verouderde inkt heeft andere eigenschappen, hetgeen resulteert in een "partial wetting" regime. De verouderde inkt vloeit samen in het midden van de nozzleplaat. De beweging van de inkt in een geactueerde nozzle resulteert ook in een toename van de oppervlaktespanning. De precursor laag van verse inkt, welke een gemeten laagdikte heeft van 13 nm, voorziet in een communicatie mogelijkheid tussen de nozzles en de centrale inktband. Er ontstaat een stroming die de inkt aanvoert vanuit de centrale inktband naar de geactueerde nozzles. De verschillen in de oppervlaktespanning van de inkt zijn de drijvende kracht achter dit stromingspatroon.

In het laatste hoofdstuk worden de belangrijkste factoren besproken die bepalend zijn voor de jetstabiliteit. De stabiliteit van het druppelvormingsproces is van cruciaal belang. Veel bronnen van jetinstabiliteit kunnen worden weggenomen met een goed ontwerp van de printkop en de actuatie. Maar zelfs dan, wordt er tijdens de normale printkopwerking soms lucht ingehapt. De inktlaag op de nozzleplaat speelt hierbij een belangrijke rol. Er bestaat een kritische laagdikte, welke altijd tot luchtinhappen leidt. Een tweede mechanisme wordt veroorzaakt door typisch 20 μm grote vuildeeltjes, die, gevangen in de inktlaag, in de richting van de nozzle worden getransporteerd. De verstoring door een vuildeeltje kan worden gemeten met de akoestische meetmethode. Een ingesloten luchtbel oscilleert in een akoestisch drukveld, wat ook met de akoestische meetmethode kan worden gemeten. De akoestische eigenschappen van het inktkanaal werken als een filter voor de akoestische metingen. Daarom worden de oscillaties, na het in elkaar klappen van een kleine luchtbel, in printkoppen met 8 mm lange kanalen gemeten als een signaal met een frequentie van 170 kHz. De eerste en tweede Bjernes krachten en de krachten van de inktstroming verplaatsen de luchtbel. Het naar buiten jetten is een snel herstelmechanisme, maar in sommige gevallen blijft de luchtbel in het kanaal zitten. De beweging van de luchtbellen kan zichtbaar worden gemaakt met een speciale tranparante printkop. Kleine luchtbellen hebben geen nadelige invloed op het druppelvormingsproces. Echter, de luchtbellen groeien in een akoestisch veld door "rectified diffusion". De groeisnelheid is veel sneller dan de oplossnelheid. De luchtbellen groeien tot afmetingen die vergelijkbaar zijn met de volume verplaatsing van het akoestisch drukveld. De grote luchtbellen werken dan de drukopbouw tegen. Dit heeft een grote invloed op de druppelvorming en uiteindelijk valt de druppelvorming volledig stil.

Acknowledgements

The research, described in this thesis, is done at the R&D department of Océ Technologies B.V., in close cooperation with the Physics of Fluids research group of the faculty of Science and Technology of the University of Twente. I want to thank all the people who have contributed to this research. Doing research in an industrial product development environment is by no means possible without the help and support of many people from Océ R&D itself and from other groups. Beforehand I want to apologize to the people who I may have forgotten.

First of all, I would like to thank my promotor Prof. dr. Detlef Lohse for giving me the opportunity to add the scientific aspects to the more product development driven research. I also want to acknowledge the support of Océ Technologies B.V., allowing me to extend my regular job to become a "PhD student" and for letting me using research results for writing this thesis.

Many thanks go to my Océ colleagues, especially Hans Reinten and Marc van den Berg, for their scientific discussions, experimental expertise, and being persons which make work a very stimulating and pleasant part of my life. This holds also for all other colleagues who directly or indirectly contributed to this work: Henk Stolk, Jan Simons, Mark Gröninger, Wim de Zeeuw, Jos Hollands, Pieter van Groos, Jan van Stiphout, Jos Ummels, Frans Blom, René Ramekers, Hans Gollatz, Rob van Loon, Pierre Klerken, Aart Polderman, Rob Koper, Vincent Peters, Aswin Draad, Jack Bisshop, Hugo Boesten, Joost Anne Veerman, Ron Berghs, and Rob Faessen.

I want to express my gratitude to the people in Enschede for the very interesting discussions and meetings we have. This make the journeys to Enschede another enjoyable part of my research. In particular, many thanks to Michel Versluis, Gerrit de Bruin, Frieder Mugele, and the PhD students Jos de Jong for his experimental work on air bubbles and getting me started with writing a thesis, he is an Océ colleague now, Roger Jeurissen, for his contributions to the modeling aspects and many deep thoughts on the theoretical aspects, and Arjan van der Bos, for carrying on the experimental work on bubble dynamics.

Important contributions came also from the master students. Therefore I would like to thank them, too. From the University of Twente in chronological order Jos de Jong, Ferdy Migchelbrink, Roger Jeurissen, Huub Borel, and Jacco Hettinga. From the Eindhoven University of Technology, Bart Beulen and Koos Delescen, for their research on wetting phenomena. For that, I would also like to

thank Rini van Dongen for his significant contributions on this topic.

Thanks also to the group of Henk Tijdeman from the University of Twente, for their work on the narrow-channel model. This was the starting point for many years of modeling, which is a very important part of this research.

I want to thank the group of Daniel Rixen of the Technical University Delft for their work on the streamfunction vorticity model, which was the basis for the development of the first own numerical models on bubble dynamics.

Tanks also to Mustafa Megahed of Logica-PDV in Bochum (D), for his work on the Flow3D models, Ken Williams of Flow Simulation Services in Albuquerque (NM), for his work on flex-walls in Flow3D, and Wybo Wagenaar of Infinite Simulation Systems in Breda, for his work on the Ansys models.

Writing a thesis also means that you need some people who are willing to read the text from cover to cover. Without the comments, corrections, and motivating suggestions of Detlef, Marc, Jos, Roger, and Hans, this thesis would never be become to what it is now. I gratefully appreciate this support, which took a lot of their time.

Finally, I want to thank my wife Jacqueline and my daughters Veerle en Jenske, for their support, love, and most of all, for their patience during the writing of the thesis. Having a man, sitting most of his time behind a laptop, is not always the same as having an ideal husband and father.

List of publications

2004

- H.M.A. Wijshoff, *Free surface flow and acousto-elastic interaction in piezo inkjet*, Proc. Nanotech2004 **2**, 215 (2004).

2005

- J. de Jong, M. Versluis, G. de Bruin, D. Lohse, H. Reinten, M. van den Berg, H. Wijshoff, and N. de Jong, *Acoustical and optical characterization of air entrapment in piezo-driven inkjet printheads*, Proc. IEEE-IUS **2**, 1270 (2005).

- M.A. Gröninger, M.J. van den Berg, and H.M.A. Wijshoff, *Inkjet system, method of making this system and use of said system*, US Patent 20050285908.

2006

- H.M.A. Wijshoff, *Piezo inkjet printer*, US Patent 20060207332.

- J. de Jong, H. Reinten, M. van den Berg, H. Wijshoff, M. Versluis, G. de Bruin, and D. Lohse, *Air entrapment in piezo-driven inkjet printheads*, J. Acoust. Soc. Am. **120**, 1257 (2006).

- H.M.A. Wijshoff, *Inkjet printer*, US Patent 20060221150.

- J. de Jong, R. Jeurissen, H. Borel, M. van den Berg, H. Wijshoff, H. Reinten, M. Versluis, A. Prosperetti, and D. Lohse, *Entrapped air bubbles in piezo-driven inkjet printing: their effect on the droplet velocity*, Phys. Fluids **18**, 121511 (2006).

- H.M.A. Wijshoff, *Printing method and printer used for applying this method*, US Patent 20060244773.

- R. Jeurissen, J. de Jong, H. Borel, M. Versluis, M. van den Berg, H. Wijshoff, H. Reinten, A. Prosperetti, and D. Lohse, *Sound Absorption of Bubbles in Inkjet-printer Microchannels*, Proc. 6th EFMC, 340 (2006).

- D. Lohse, J. de Jong, M. Versluis, M. van den Berg, H. Wijshoff, and H. Reinten, *Disturbing bubbles in piezo-acoustic printing*, Proc. 6th EFMC, 369 (2006).
- H.M.A. Wijshoff, *Inkjet printhead and inkjet printer containing the same printhead*, US Patent 0274115.
- H.M.A. Wijshoff, *Manipulating drop formation in piezo acoustic inkjet*, Proc. IS&T's NIP22, 79 (2006).

2007

- B. Beulen, J. de Jong, H. Reinten, M. van den Berg, H. Wijshoff, and R. van Dongen, *Flows on the nozzle plate of an inkjet printhead*, Exp. Fluids **42**, 217 (2007).
- H.M.A. Wijshoff, *Modeling the drop formation process in inkjet printheads*, Flow3D News spring2007, 4 (2007).
- H.M.A. Wijshoff, *Drop formation mechanisms in piezo-acoustic inkjet*, Proc. Nanotech2007 **3**, 448 (2007).
- H.M.A. Wijshoff, *Printhead and inkjet printer comprising such a printhead*, US Patent 20070236541.
- H.M.A. Wijshoff, *Better printheads via simulation: Flow3D helped double the speed of a new wide-format printer without sacrificing quality*, Desktop Engineering **13(2)**, 46 (2007).
- J. de Jong, H. Reinten, H. Wijshoff, M. van den Berg, K. Delescen, R. van Dongen, F. Mugele, M. Versluis, and D. Lohse, *Marangoni flow on an inkjet nozzle plate*, Appl. Phys. Lett **91**, 204102 (2007).

2008

- R. Jeurissen, J. de Jong, H, Reinten, M. van den Berg, H. Wijshoff, M. Versluis, and D. Lohse, *The effect of an entrained air bubble on the acoustics of an ink channel*, J. Acoust. Soc. Am. (in press 2008).

About the author

Herman Wijshoff was born September 3, 1961, in Grevenbicht, the Netherlands. He graduated from high school (Gymnasium) at "Het Bisschoppelijk College" in Sittard. In September 1979 he started to study Applied Physics at the Eindhoven University of Technology, the Netherlands. He did his traineeship at the Plasma and Materials Processing group at the university [†]. In 1986, he received his M.Sc. degree in Physics on the behavior of two dimensional electron gases at semiconductor heterojunctions [‡]. In that same year, he joined the Research and Development department of Océ Technologies B.V. in Venlo, the Netherlands. The main focus was on materials research, especially the viscoelastic behavior of polymers and elastomers. Since 1997 he has been involved in the inkjet research program. He has focussed primarily on the modeling of the functional behavior of inkjet printheads. This research program is in close cooperation with prof. dr. Detlef Lohse.

[†]Published as: B. van der Sijde, O. Abu-Zeid, and H.M.A. Wijshoff, *Measured collisional radiative coefficients of the 4p groups of the argon I and argon II systems*, Physics Letters **A101(9)**, 491, (1984).

[‡]Published as: R.G. van Welzenis, H.M.A. Wijshoff, and K. Ploog, *Hot electron Hall effect in a two-dimensional electron gas*, Physica B **134B**, 347, (1985).